School of Civil and Mechanical Engineering

Dynamic Analyses and Vibration Mitigation of Offshore Monopile Wind Turbines

Haoran Zuo

This thesis is presented to the Degree of
Doctor of Philosophy
of
Curtin University

April 2019

Declaration

To the best of my knowledge and belief this thesis contains no material previously published by any other person except where due acknowledgement has been made.

This thesis contains no material which has been accepted for the award of any other degree or diploma in any university.

Signature: ……..

Date: ……...

ABSTRACT

Offshore wind turbines have become a main contributor to produce electrical energy nowadays. To more effectively extract the vast wind resource in marine areas, offshore wind turbines are designed and constructed with slender tower and large rotors. These thin-walled high-rise structures are susceptible to external vibration sources such as wind, wave and seismic loadings. The excessive vibrations can compromise the wind energy output and decrease the fatigue life of wind turbines and may even lead to collapse in some extreme conditions. It is therefore important to understand the dynamic behaviours of offshore wind turbines and mitigate the adverse vibrations.

The dynamic responses of offshore wind turbines under wind, wave and/or seismic loadings have become a hotly debated topic recently. A number of studies have been reported in the literature. However, in most of the previous studies, the wind turbines were normally assumed in the parked condition and the blades were considered as a lumped mass located at the tower top, and generally only the responses of the tower were considered. In reality, the geometrical characteristics and rotational velocity of the blades can directly influence the wind loads acting on them. Moreover, the centrifugal stiffness generated by the large rotating blades can alter the structural stiffness and vibration frequencies, which in turn affects the structural responses. The simplified analyses with lumped mass model and parked condition therefore may not be able to accurately capture the structural responses of offshore wind turbines. In addition, the onshore earthquake ground motions were often used as inputs in seismic response analyses of offshore wind turbines owing to the lack of offshore earthquake ground motion data. This may lead to inaccurate predictions of seismic responses of offshore wind turbines because onshore and offshore ground motions have different characteristics since sea water can significantly suppress the vertical seafloor motions near the P wave resonant frequencies of sea water layer, and sea water layer further changes the water saturation level and pore pressure of subsea soil layers and hence influences the wave propagation in the soil media and the ground motions. Due to these limitations of previous studies, it is imperative to develop more sophisticated numerical models to accurately estimate the dynamic behaviours of offshore wind turbines. This comprises the research aim of the first part of this thesis.

Extensive research efforts have also been made on the vibration mitigation of offshore wind turbines. Most of the previous studies focused on mitigating the vibration of the tower only by installing a single large control device (e.g. tuned mass damper (TMD)) in the nacelle. This practice is effective to suppress the fundamental vibration mode of the tower, in which the maximum displacement occurs at the tower top. It is thus reasonable when wind and wave loads are considered since the energies of these two loads concentrate in the low frequency

range and only the first vibration mode of the tower can generally be excited. However, when offshore wind turbines are located in the regions with high seismic activities, earthquake load can be another potential vibration source during their service lives, and higher vibration modes might be also excited due to the broader frequency range of earthquake ground motions. In this case, installing the control device only in the nacelle may not be effective to control vibrations from second or higher modes. More control devices therefore should be installed at certain locations along the tower. Moreover, the spare space in the nacelle is actually limited, and installing a single large control device inside is not straightforward. It is more practical to divide the single large control device into multiple smaller ones. Furthermore, damages of the blades were also observed in many wind turbine accidents, therefore it is also important to suppress the excessive vibrations of the blades. The vibration mitigation of the blades was however rarely considered in the previous studies.

The primary objectives of this thesis are to develop more sophisticated numerical models to more realistically capture the dynamic responses of offshore wind turbines and to propose more practical passive control strategies to mitigate their excessive vibrations under wind, wave and/or seismic loadings. This thesis therefore can be broadly divided into two parts, with the first part focusing on the structural responses and the second part on the vibration control. Particularly, in Chapter 2, a detailed three-dimensional (3D) finite element (FE) model of the NREL 5 MW wind turbine is developed by using the commercially available FE code ABAQUS. The tower and blades are explicitly modelled and soil-structure interaction (SSI) is considered. The influences of parked and operating conditions, SSI and rotational velocity on the dynamic responses of offshore wind turbines are investigated. This numerical model is then used to investigate the responses of wind turbines subjected to onshore and offshore earthquake ground motions (Chapter 3) and construct the fragility curves of the wind turbine subjected to the combined actions of wind and wave (Chapter 4).

In the second part, multiple TMDs (MTMDs) are proposed to be installed along the tower to control the first and higher vibration modes of the tower induced by the wind, wave and seismic loads (Chapter 5). This concept is then further extended to control the out-of-plane vibrations of the tower and blades (Chapter 6) and the simultaneous in-plane and out-of-plane vibrations of the tower and blades (Chapter 7). The numerical results demonstrate the proposed control method can effectively mitigate the vibrations of both the tower and blades with high robustness.

ACKNOWLEDGEMENTS

First and foremost, I would like to extend my sincere gratitude and respect to my supervisor Prof. Hong Hao and co-supervisor Dr. Kaiming Bi, who have been giving me invaluable guidance and persistent encouragement during my research study. I would never accomplish this thesis without their generous helps.

Many thanks go to the staff and postgraduate students in the School of Civil and Mechanical Engineering and Centre for Infrastructure Monitoring and Protection (CIMP) for their friendship and kind help during my study at Curtin University.

I would like to acknowledge Curtin University for the Curtin International Postgraduate Research Scholarship (CIPRS) for me to pursue this study.

Last but not least, I wish to express my deep appreciation to my parents and family, for their unconditional love and support.

LIST OF PUBLISHED WORK AND/OR WORK PREPARED FOR PUBLICATION

This thesis contains published work and/or work prepared for publication, which has been co-authored. The bibliographical details of the work and where it appears in the thesis are outlined below.

Chapter 2

Zuo, H., Bi, K. & Hao, H. (2018). Dynamic analyses of operating offshore wind turbines including soil-structure interaction. *Engineering Structures*, *157*, 42-62. https://doi.org/10.1016/j.engstruct.2017.12.001

Chapter 3

Zuo, H., Bi, K., Hao, H. & Li, C. (2019). Influence of earthquake ground motion modelling on the dynamic responses of offshore wind turbines. *Soil Dynamics and Earthquake Engineering*, *121*, 151-167. https://doi.org/10.1016/j.soildyn.2019.03.008.

Chapter 4

Zuo, H., Bi, K., Hao, H., Li, J., Xin, Y. & Li, C. (2019). Fragility analyses of offshore wind turbines subjected to aerodynamic and sea wave loadings. (Under review).

Chapter 5

Zuo, H., Bi, K. & Hao, H. (2017). Using multiple tuned mass dampers to control offshore wind turbine vibrations under multiple hazards. *Engineering Structures*, *141*, 303-315. https://doi.org/10.1016/j.engstruct.2017.03.006.

Chapter 6

Zuo, H., Bi, K. & Hao, H. (2019). Mitigation of tower and out-of-plane blade vibrations of offshore monopile wind turbines by using multiple tuned mass dampers. *Structure and Infrastructure Engineering*, *15*(2):269-284. https://doi.org/10.1080/15732479.2018.1550096.

Chapter 7

Zuo, H., Bi, K., & Hao, H. (2019). Simultaneous out-of-plane and in-plane vibration mitigations of offshore monopile wind turbines by tuned mass dampers. (Under review).

STATEMENT OF CONTRIBUTION OF OTHERS

The works presented in this thesis were primarily designed, numerically executed, interpreted and written by the candidate and also the first author of the publications (Haoran Zuo). Significant input to the works was also provided by co-authors. Contributions of the co-authors are described below. The signed contribution form is attached in the appendix.

Chapters 2 and 5-7

Hong Hao and Kaiming Bi defined the overall scope and objectives of the works and suggested research methodologies and approaches. All the numerical simulations were carried out by Haoran Zuo. The manuscripts were written by Haoran Zuo with revisions and editions from Kaiming Bi and Hong Hao, both of whom also provided additional intellectual input in the discussions of the results.

Chapter 3

All the numerical simulations were carried out by Haoran Zuo. Chao Li helped simulate onshore and offshore ground motions used in this study. The manuscript was written by Haoran Zuo, which was thoroughly revised by Kaiming Bi and Hong Hao.

Chapter 4

The fragility analyses of offshore wind turbines were investigated by Haoran Zuo. Jun Li and Yu Xin provided random variables by using the Latin Hypercube sampling technique. Chao Li participated in the discussion of the analysis method. The manuscript was written by Haoran Zuo, which was thoroughly revised by Kaiming Bi and Hong Hao.

LIST OF RELEVANT ADDITIONAL PUBLICATIONS

The additional publications relevant to the thesis with the bibliographical details are listed below.

1. Bi, K., Hao, H. & **Zuo, H.** (2016). Using MTMD system to control wind turbine vibrations under combined wind and seismic loadings. *2nd Huixian International Forum on Earthquake Engineering for Young Researchers*, 19-21 August, Beijing, China.
2. **Zuo, H.**, Bi, K. & Hao, H. (2017). Influence of operational condition on the dynamic behaviours of offshore wind turbines. *The 15th East Asia-Pacific Conference on Structural Engineering & Construction*, 11-13 October, Xi'an, China.
3. **Zuo, H.**, Bi, K. & Hao, H. (2018). Influence of soil-structure interaction on the dynamic behaviours of offshore wind turbines. *13th International Conference on Steel, Space and Composite Structures*, 31 January-2 February, Perth, Australia.
4. **Zuo, H.**, Bi, K. & Hao, H. (2018). Using multiple tuned mass dampers to mitigate out-of-plane vibrations of offshore wind turbines. *7th World Conference on Structural Control and Monitoring*, 22-25 July, Qingdao, China.
5. Hao, H., Bi, K., **Zuo, H.**, Nikoo, M., Zhou, T. & Ma, R. (2018). Recent research on passive control of offshore structural vibrations in the Centre for Infrastructure Monitoring and Protection (CIMP) at Curtin University. *7th World Conference on Structural Control and Monitoring*, 22-25 July, Qingdao, China.
6. Bi, K., **Zuo, H.** & Hao, H. (2018). Performance of offshore wind turbine under aerodynamic and sea wave loadings and its vibration control. *The 15th International Symposium on Structural Engineering*, 25-27 October, Hangzhou, China.
7. Ni, P., Xia, Y., Li, J., Hao, H., Bi, K. & **Zuo, H.** (2018). Multi-scale stochastic dynamic analysis of offshore risers with lognormal uncertainties. (Under review)

TABLE OF CONTENTS

LIST OF FIGURES

LIST OF TABLES

CHAPTER 1 INTRODUCTION

1.1 Background

Offshore wind turbines have been widely used to produce electrical energy nowadays. As reported by the Global Wind Energy Council (GWEC, 2018), a historical record of 4,334 MW of new offshore wind power was installed worldwide in 2017, with an 87% increase compared to that in 2016, and the cumulative offshore wind capacity in 2017 reached 18,814 MW. To more efficiently extract the vast wind resources in marine areas throughout the lifetimes of offshore wind turbines, they are erected with slender tower and large rotors. For example, the tower height and rotor diameter of the conceptual Haliade-X 12 MW offshore wind turbine reach 150 m and 220 m respectively (GWEC, 2018). These thin-walled high-rise structures are vulnerable to the external excitations such as wind, wave and/or seismic loads. The excessive vibrations can compromise the wind energy output and decrease the fatigue life and may even lead to the catastrophic collapse of wind turbines in some harsh conditions. To ensure the safety and serviceability of offshore wind turbines, it is important to accurately understand their dynamic behaviours and mitigate the adverse vibrations.

Extensive research works have been carried out to investigate the dynamic responses of wind turbines under wind, wave and/or seismic loads (Alati et al., 2015; Bazeos et al., 2002; Bisoi & Haldar, 2014, 2015; De Risi et al., 2018; Hacıefendioğlu, 2012; Harte et al., 2012; Kjørlaug & Kaynia, 2015; Lavassas et al., 2003; Murtagh et al., 2005; Santangelo et al., 2016; Wang et al., 2018). However, in most of the previous studies (Bazeos et al., 2002; Bisoi & Haldar, 2014, 2015; De Risi et al., 2018; Hacıefendioğlu, 2012; Lavassas et al., 2003; Wang et al., 2018), the wind turbines were assumed in the parked condition and the blades were modelled as a lumped mass located at the tower top by ignoring the geometries of the blades and the interaction between the tower and blades. Only the responses of the tower were therefore investigated in these studies. In reality, the geometrical configurations and rotational velocity of the blades can directly influence the wind loads acting on them (Hansen, 2008). Moreover, the centrifugal stiffness generated by the rotating blades can increase the stiffness and natural frequencies (Murtagh et al., 2005), which in turn indirectly affect the dynamic responses of the wind turbines. The simplified analyses with lumped mass model and parked condition may not be able to accurately capture the dynamic responses of offshore wind turbines.

Furthermore, earthquake ground motions at the onshore site were used as inputs in the seismic response analyses of offshore wind turbines owing to the lack of seafloor earthquake recordings (Alati et al., 2015; De Risi et al., 2018; Hacıefendioğlu, 2012; Kaynia, 2018; Wang et al., 2018), which may lead to inaccurate structural response estimations. This is due to the fact that the existence of sea water can significantly suppress the vertical seafloor seismic

motions near the P wave resonant frequencies of the sea water layer (Li et al., 2015) and the characteristics of seafloor seismic motions are thus different from those of the onshore ground motions. In addition, the sea water layer changes the water saturation level and pore pressure of subsea soil layers and hence the seafloor ground motions (Yang & Sato, 2000). Li et al. (2015) theoretically derived the ground motion transfer functions at the offshore site by taking the influence of sea water layer into account based on the fundamental hydrodynamic formulas and one-dimensional (1D) wave propagation theory, and proposed methods to stochastically simulate the offshore ground motions at the site surface and different soil depths of a single site (Li et al., 2018c), and spatially varying ground motions at multiple sites (Li et al., 2017, 2018a). Previous studies on the buried offshore pipelines (Bi et al., 2017) and bridges (Li et al., 2018b) indicated that the seismic responses of these structures obtained based on the offshore earthquake ground motions are very different from those obtained by using the onshore data as inputs. For the offshore wind turbines, their seismic responses may be also very sensitive to the ground motion types (especially to the vertical component) due to their high-rise structural layouts. However, to the author's best knowledge, this issue has not yet been addressed in the open literature.

Besides the above deterministic analyses, some researchers adopted the probabilistic approach by employing fragility analysis to further assess the reliability of wind turbines. For example, Kim et al. (2014) analysed the seismic fragility of offshore wind turbines considering the interaction between the monopile foundation and surrounding soil; Patil et al. (2016) compared the influence of near- and far-fault ground motions on the seismic fragility of wind turbine tower; Mardfekri and Gardoni (2013) developed the probabilistic models to predict the deformation, shear and moment demands on the wind turbine tower subjected to wind and wave loads. However, it should be noted that most of these studies assumed the wind turbines were in the parked condition (Kim et al., 2014) and the mass of the blades was lumped at the tower top (Patil et al., 2016; Mardfekri & Gardoni, 2013). The influence of the rotating blades therefore cannot be considered. Moreover, study of the fragilities of the blades has never been reported.

Extensive efforts have also been devoted to the vibration mitigation of offshore wind turbines. Most of the previous studies focused on the vibration control of the tower, and various control devices have been proposed. These control devices can be broadly divided into the *passive* (Buckley et al., 2017; Colwell & Basu, 2009; Chen & Georgakis, 2013a, 2013b; Chen et al., 2015a; Dezvareh et al., 2016; Ghassempour et al., 2019; Hussan et al., 2018; Lackner & Rotea, 2011; Mensah & Dueñas-Osorio, 2014; Murtagh et al., 2008; Stewart & Lackner, 2014; Sun & Jahangiri, 2018, 2019; Zhang et al., 2013, 2016, 2019a, 2019b; Zhao et al., 2018; Zheng et al., 2017), *semi-active* (Caterino, 2015; Sarkar & Chakraborty, 2017; Sun, 2017, 2018) and

active (Brodersen et al., 2017; Fitzgerald et al., 2018; Stewart & Lackner, 2011) categories depending on whether external power is needed. Compared to the semi-active and active control devices, passive control techniques need no power input and therefore they have been widely used in the vibration mitigation of wind turbines. The effectiveness of these proposed methods were either *numerically* (Brodersen et al., 2017; Buckley et al., 2017; Colwell & Basu, 2009; Dezvareh et al., 2016; Fitzgerald et al., 2018; Ghassempour et al., 2019; Hussan et al., 2018; Lackner & Rotea, 2011; Mensah & Dueñas-Osorio, 2014; Murtagh et al., 2008; Sarkar & Chakraborty, 2017; Stewart & Lackner, 2011, 2014; Sun, 2017, 2018; Sun & Jahangiri, 2018, 2019; Zhang et al., 2019a; Zheng et al., 2017) or *experimentally* (Caterino, 2015; Chen & Georgakis, 2013a, 2013b; Chen et al., 2015a; Zhang et al., 2013, 2016, 2019b; Zhao et al., 2018) studied. The results confirmed these control devices can be used to mitigate the adverse vibrations of the tower. It should be noted that the control device was suggested installing in the nacelle in almost all the previous studies. This practice is reasonable when wind and/or wave loads are considered since the energies of these loads concentrate in the low frequency range and only the fundamental vibration mode of the tower can be excited, in which the maximum displacement occurs at the tower top. However, when offshore wind turbines are located in the regions with high seismic activities, earthquake load can be another potential vibration source during their service lives, and higher vibration modes might be also excited due to the broader frequency range of earthquake ground motions. In this case, only installing the control device in the nacelle may not be effective to control vibrations induced by higher vibration modes. More control devices therefore should be installed at certain locations along the height of the tower. Moreover, the spare space in the nacelle is limited and installing a single large control device inside may not be possible. It will be more practical to divide the large control device into multiple smaller ones.

Damages to blades were observed in many wind turbine accidents and it is also imperative to suppress the excessive vibrations of the blades. The blade vibrations can occur in both the in-plane and out-of-plane directions. The studies on the in-plane vibration control of the blades are relatively extensive (Basu et al., 2016; Chen et al., 2015b; Staino et al., 2012; Zhang et al., 2014, 2015a, 2015b). Similar to the tower, the control methods can be divided into the *passive* (Basu et al., 2016; Zhang et al., 2014, 2015a, 2015b), *semi-active* (Chen et al., 2015b) and *active* (Staino et al., 2012) categories. However, very limited research works on the out-of-plane vibration control of the blades were performed. Arrigan et al. (2011) proposed using semi-active tuned mass dampers (TMDs) to control the out-of-plane vibrations of the blades. Significant reduction was achieved for both the steady and turbulent wind loads, which highlighted the viability of TMDs in mitigating the vibrations of the blades in the out-of-plane direction. Using semi-active and active control strategies can achieve reasonable structural

response reduction, but both methods need relatively complicated controller configurations and external power input, which impedes their applications in the blades since the space in the blades is even smaller than that in the nacelle. Therefore using multiple small TMDs (MTMDs) will be more practical.

1.2 Research objectives

The primary goals of this study is to develop more sophisticated numerical models to more accurately capture the dynamic responses of offshore wind turbines, and to propose more practical passive control strategies to mitigate their excessive vibrations under wind, wave and/or seismic loads. The specific objectives of this research are:

1. To develop a detailed 3D finite element (FE) model of the NREL 5 MW wind turbine by taking the geometrical configurations of the tower and blades, and the rotation of the blades into account.
2. To investigate the influence of different types of earthquake ground motions (i.e. the onshore/offshore and uniform/depth-varying ground motions) on the seismic responses of offshore wind turbines.
3. To perform fragility analyses of offshore wind turbines under wind and wave loads.
4. To investigate the effectiveness of using MTMDs to control the fundamental and higher vibration modes of the tower.
5. To study the feasibility of using MTMDs to control the vibrations of the tower and blades in the out-of-plane direction.
6. To examine the control effectiveness of using bi-directional TMD systems to simultaneously control the in-plane and out-of-plane vibrations of the tower and blades.

1.3 Research outline

This thesis comprises eight chapters. The contents of the seven chapters following this introductory chapter are described below:

The detailed 3D FE model of the NREL 5 MW wind turbine is developed by using the commercially available FE code ABAQUS in Chapter 2. The tower and blades are explicitly modelled and soil-structure interaction (SSI) is considered. The influences of parked and operating conditions, SSI and rotational velocity on the dynamic responses of offshore wind turbines are investigated.

In Chapter 3, onshore and offshore seismic motions are stochastically simulated including the direct and indirect effects of sea water layer. In particular, special emphasises are placed on investigating the influences of offshore and depth-varying ground motions on the seismic responses of offshore wind turbines.

In Chapter 4, the uncertainties of the structural mass, stiffness and damping are considered to derive the probabilistic demand model of the wind turbine as a function of wind speed. The dynamic behaviours of the wind turbine subjected to the combined wind and wave loads are investigated in a probabilistic frame and the fragility curves for both the tower and blades in the parked and operating conditions are developed.

In Chapter 5, MTMDs are proposed to control the vibrations of the wind turbine tower induced by the fundamental and higher vibration modes when it is subjected to the combined wind, wave and seismic excitations. The responses of the original wind turbine (without control device) are compared with those controlled by single TMD and MTMDs. The robustness of the proposed method is also discussed by arbitrarily assuming some dampers lose their control capabilities.

As an extension of Chapter 5, in which MTMDs are only used to control the vibrations of the wind turbine tower, MTMDs are installed in both the tower and blades to control the out-of-plane vibrations of the wind turbine in Chapter 6. The responses of the parked and operating wind turbines under wind and wave loads are compared and discussed, and the effectiveness and robustness of the proposed method are investigated.

In Chapter 7, a bi-directional TMD system is proposed to simultaneously control the in-plane and out-of-plane vibrations of offshore wind turbines. The control effectiveness of the proposed method is numerically investigated.

The conclusions of the current study and recommendations for the future research are presented in Chapter 8.

It should be noted that this thesis is compiled by combining the technical papers prepared by the candidate during his PhD study. Therefore, Chapters 2 to 7 can be read independently. On the other hand, to make each technical paper complete, the numerical model development, and the wind, wave and/or earthquake loading simulations were introduced in almost every chapter (i.e. in each independent chapter). These parts thus might be slightly repetitive with each other.

1.4 References

Alati, N., Failla, G., & Arena, F. (2015). Seismic analysis of offshore wind turbines on bottom-fixed support structures. *Philosophical Transactions Royal Society A*, *373*, 20140086.

Arrigan, J., Pakrashi, V., Basu, B., & Nagarajaiah, S. (2011). Control of flap-wise vibrations in wind turbine blades using semi-active tuned mass dampers. *Structural Control and Health Monitoring*, *18*(8), 840-851.

Basu, B., Zhang, Z., & Nielsen, S. R. K. (2016). Damping of edgewise vibration in wind turbine blades by means of circular liquid dampers. *Wind Energy*, *19*(2), 213-226.

Bazeos, N., Hatzigeorgiou, G., Hondros, I., Karamaneas, H., Karabalis, D., & Beskos, D. (2002). Static, seismic and stability analyses of a prototype wind turbine steel tower. *Engineering Structures*, *24*(8), 1015-1025.

Bi, K., Hao, H., Li, C., & Li, H. (2017). Stochastic seismic response analysis of buried onshore and offshore pipelines. *Soil Dynamics and Earthquake Engineering*, *94*, 60-65.

Bisoi, S., & Haldar, S. (2014). Dynamic analysis of offshore wind turbine in clay considering soil-monopile-tower interaction. *Soil Dynamics and Earthquake Engineering*, *63*, 19-35.

Bisoi, S., & Haldar, S. (2015). Design of monopile supported offshore wind turbine in clay considering dynamic soil-structure-interaction. *Soil Dynamics and Earthquake Engineering*, *73*, 103-117.

Brodersen, M. L., Bjørke, A. S., & Høgsberg, J. (2017). Active tuned mass damper for damping of offshore wind turbine vibrations. *Wind Energy*, *20*(5):783-796.

Buckley, T., Watson, P., Cahill, P., Jaksic, V., & Pakrashi, V. (2018). Mitigating the structural vibrations of wind turbines using tuned liquid column damper considering soil-structure interaction. *Renewable Energy*, *120*, 322-341.

Caterino, N. (2015). Semi-active control of a wind turbine via magnetorheological dampers. *Journal of Sound and Vibration*, *345*, 1-17.

Chen, J., & Georgakis, C. T. (2013a). Tuned rolling-ball dampers for vibration control in wind turbines. *Journal of Sound and Vibration*, *332*(21), 5271-5282.

Chen, J., & Georgakis, C. T. (2013b). Spherical tuned liquid damper for vibration control in wind turbines. *Journal of Vibration and Control, 21*(10), 1875-1885.

Chen, J., Liu, Y., & Bai, X. (2015a). Shaking table test and numerical analysis of offshore wind turbine tower systems controlled by TLCD. *Earthquake Engineering and Engineering Vibration*, *14*(1), 55-75.

Chen, J., Yuan, C., Li, J., & Xu, Q. (2015b). Semi-active fuzzy control of edgewise vibrations in wind turbine blades under extreme wind. *Journal of Wind Engineering and Industrial Aerodynamics*, *147*, 251-261.

Colwell, S., & Basu, B. (2009). Tuned liquid column dampers in offshore wind turbines for structural control. *Engineering Structures*, *31*(2), 358-368.

De Risi, R., Bhattacharya, S., & Goda, K. (2018). Seismic performance assessment of monopile-supported offshore wind turbines using unscaled natural earthquake records. *Soil Dynamics and Earthquake Engineering*, *109*, 154-172.

Dezvareh, R., Bargi, K., & Mousavi, S. A. (2016). Control of wind/wave-induced vibrations of jacket-type offshore wind turbines through tuned liquid column gas dampers. *Structure and Infrastructure Engineering*, *12*(3), 312-326.

Fitzgerald, B., Sarkar, S., & Staino, A. (2018). Improved reliability of wind turbine towers with active tuned mass dampers (ATMDs). *Journal of Sound and Vibration*, *419*, 103-122.

Ghassempour, M., Failla, G., & Arena, F. (2019). Vibration mitigation in offshore wind turbines via tuned mass damper. *Engineering Structures*, *183*, 610-636.

Global Wind Energy Council (GWEC). (2018). Global wind report-Annual market update 2017.

Hacıefendioğlu, K. (2012). Stochastic seismic response analysis of offshore wind turbine including fluid-structure-soil interaction. *The Structural Design of Tall and Special Buildings*, *21*(12), 867-878.

Hansen, M. O. L. (2008). Aerodynamics of wind turbines 2nd ed. London: Earthscan.

Harte, M., Basu, B., & Nielsen, S. R. K. (2012). Dynamic analysis of wind turbines including soil-structure interaction. *Engineering Structures*, *45*, 509-518.

Hussan, M., Rahman, M. S., Sharmin, F., Kim, D., & Do, J. (2018). Multiple tuned mass damper for multi-mode vibration reduction of offshore wind turbine under seismic excitation. *Ocean Engineering*, *160*, 449-460.

Kaynia, A. M. (2018). Seismic considerations in design of offshore wind turbines. *Soil Dynamics and Earthquake Engineering*.

Kim, D. H., Lee, S. G., & Lee, I. K. (2014). Seismic fragility analysis of 5 MW offshore wind turbine. *Renewable Energy*, *65*, 250-256.

Kjørlaug, R. A., & Kaynia, A. M. (2015). Vertical earthquake response of megawatt-sized wind turbine with soil-structure interaction effects. *Earthquake Engineering & Structural Dynamics*, *44*(13), 2341-2358.

Lackner, M. A., & Rotea, M. A. (2011). Passive structural control of offshore wind turbines. *Wind Energy*, *14*(3), 373-388.

Lavassas, I., Nikolaidis, G., Zervas, P., Efthimiou, E., Doudoumis, I., & Baniotopoulos, C. (2003). Analysis and design of the prototype of a steel 1-MW wind turbine tower. *Engineering Structures*, *25*(8), 1097-1106.

Li, C., Hao, H., Li, H., & Bi, K. (2015). Theoretical modeling and numerical simulation of seismic motions at seafloor. *Soil Dynamics and Earthquake Engineering*, *77*, 220-225.

Li, C., Hao, H., Li, H., Bi, K., & Chen, B. (2017). Modeling and Simulation of Spatially Correlated Ground Motions at Multiple Onshore and Offshore Sites. *Journal of Earthquake Engineering*, *21*(3), 359-383.

Li, C., Li, H., Hao, H., & Bi, K. (2018a). Simulation of Spatially Varying Seafloor Motions Using Onshore Earthquake Recordings. *Journal of Engineering Mechanics*, *144*(9), 04018085.

Li, C., Li, H., Hao, H., Bi, K., & Chen, B. (2018b). Seismic fragility analyses of sea-crossing cable-stayed bridges subjected to multi-support ground motions on offshore sites. *Engineering Structures*, *165*, 441-456.

Li, C., Li, H., Hao, H., Bi, K., & Tian, L. (2018c). Simulation of multi-support depth-varying earthquake ground motions within heterogeneous onshore and offshore sites. *Earthquake Engineering and Engineering Vibration*, *17*(3), 475-490.

Mardfekri, M., Gardoni, P. (2013). Probabilistic demand models and fragility estimates for offshore wind turbine support structures. *Engineering Structures*, 52, 478-487.

Mensah, A. F., & Dueñas-Osorio, L. (2014). Improved reliability of wind turbine towers with tuned liquid column dampers (TLCDs). *Structural Safety*, *47*, 78-86.

Murtagh, P. J., Basu, B., & Broderick, B. M. (2005). Along-wind response of a wind turbine tower with blade coupling subjected to rotationally sampled wind loading. *Engineering Structures*, *27*(8), 1209-1219.

Murtagh, P. J., Ghosh, A., Basu, B., & Broderick, B. M. (2008). Passive control of wind turbine vibrations including blade/tower interaction and rotationally sampled turbulence. *Wind Energy*, *11*(4), 305-317.

Patil, A., Jung, S., & Kwon, O. S. (2016). Structural performance of a parked wind turbine tower subjected to strong ground motions. *Engineering Structures*, *120*, 92-102.

Santangelo, F., Failla, G., Santini, A., & Arena, F. (2016). Time-domain uncoupled analyses for seismic assessment of land-based wind turbines. *Engineering Structures*, *123*, 275-299.

Sarkar, S., & Chakraborty, A. (2017). Optimal design of semiactive MR-TLCD for along-wind vibration control of horizontal axis wind turbine tower. *Structural Control and Health Monitoring*, *25*(2), e2083.

Staino, A., Basu, B., & Nielsen, S. R. K. (2012). Actuator control of edgewise vibrations in wind turbine blades. *Journal of Sound and Vibration*, *331*(6), 1233-1256.

Stewart, G. M., & Lackner, M. A. (2011). The effect of actuator dynamics on active structural control of offshore wind turbines. *Engineering Structures*, *33*(5), 1807-1816.

Stewart, G. M., & Lackner, M. A. (2014). The impact of passive tuned mass dampers and wind-wave misalignment on offshore wind turbine loads. *Engineering Structures*, *73*, 54-61.

Sun, C. (2017). Mitigation of offshore wind turbine responses under wind and wave loading: Considering soil effects and damage. *Structural Control and Health Monitoring*, *25*(3), e2117.

Sun, C. (2018). Semi-active control of monopile offshore wind turbines under multi-hazards. *Mechanical Systems and Signal Processing*, *99*, 285-305.

Sun, C., & Jahangiri, V. (2018). Bi-directional vibration control of offshore wind turbines using a 3D pendulum tuned mass damper. *Mechanical Systems and Signal Processing*, *105*, 338-360.

Sun, C., & Jahangiri, V. (2019). Fatigue damage mitigation of offshore wind turbines under real wind and wave conditions. *Engineering Structures*, *178*, 472-483.

Wang, P., Zhao, M., Du, X., Liu, J., & Xu, C. (2018). Wind, wave and earthquake responses of offshore wind turbine on monopile foundation in clay. *Soil Dynamics and Earthquake Engineering*, *113*, 47-57.

Yang, J., & Sato, T. (2000). Interpretation of seismic vertical amplification observed at an array site. *Bulletin of the Seismological Society of America*, *90*(2), 275-285.

Zhang, R., Zhao, Z., & Dai, K. (2019a). Seismic response mitigation of a wind turbine tower using a tuned parallel inerter mass system. *Engineering Structures*, *180*, 29-39.

Zhang, Z., Basu, B., & Nielsen, S. R. K. (2015a). Tuned liquid column dampers for mitigation of edgewise vibrations in rotating wind turbine blades. *Structural Control and Health Monitoring*, *22*(3), 500-517.

Zhang, Z., Basu, B., & Nielsen, S. R. K. (2019b). Real-time hybrid aeroelastic simulation of wind turbines with various types of full-scale tuned liquid dampers. *Wind Energy*, *22*(2), 239-256.

Zhang, Z., Chen, J., & Li, J. (2013). Theoretical study and experimental verification of vibration control of offshore wind turbines by a ball vibration absorber. *Structure and Infrastructure Engineering*, *10*(8), 1087-1100.

Zhang, Z., Li, J., Nielsen, S. R. K., & Basu, B. (2014). Mitigation of edgewise vibrations in wind turbine blades by means of roller dampers. *Journal of Sound and Vibration*, *333*(21), 5283-5298.

Zhang, Z., Nielsen, S. R. K., Basu, B., & Li, J. (2015b). Nonlinear modeling of tuned liquid dampers (TLDs) in rotating wind turbine blades for damping edgewise vibrations. *Journal of Fluids and Structures, 59*, 252-269.

Zhang, Z., Staino, A., Basu, B., & Nielsen, S. R. K. (2016). Performance evaluation of full-scale tuned liquid dampers (TLDs) for vibration control of large wind turbines using real-time hybrid testing. *Engineering Structures, 126*, 417-431.

Zhao, B., Gao, H., Wang, Z., & Lu, Z. (2018). Shaking table test on vibration control effects of a monopile offshore wind turbine with a tuned mass damper. *Wind Energy*, *21*(12), 1309-1328.

Zheng, M., Yang, Z. J., Yang, S., & Still, B. (2017). Modeling and mitigation of excessive dynamic responses of wind turbines founded in warm permafrost. *Engineering Structures, 148*, 36-46.

CHAPTER 2 DYNAMIC ANALYSES OF OPERATING OFFSHORE WIND TURBINES INCLUDING SOIL-STRUCTURE INTERACTION

ABSTRACT[1]

In the dynamic analyses of offshore wind turbines subjected to external vibration sources, the wind turbines are normally assumed in the parked condition and the blades are considered by a lumped mass located at the tower top. In reality, the geometrical characteristics and rotational velocity of the blades can directly influence the wind loads acting on the blades. Moreover, the centrifugal stiffness generated by the rotating blades can increase the stiffness and natural frequencies of the blades, which in turn can further affect the structural responses. The lumped mass model, therefore, may lead to inaccurate structural response estimations. On the other hand, monopile, a long hollow steel member inserting into the water and seabed, is generally designed as the foundation of an offshore wind turbine. The soil-monopile interaction can further alter the vibration characteristics and dynamic responses of offshore wind turbines. In the present study, the dynamic responses of the modern NREL 5 MW wind turbine subjected to the combined wind and sea wave loadings are numerically investigated by using the finite element code ABAQUS. The blades are explicitly modelled and soil-structure interaction (SSI) is considered. The influences of operational condition and rotor velocity on the dynamic behaviours are systematically investigated. It is found that the responses of the wind turbine in the operating condition are much larger than those in the parked condition; SSI can affect the tower vibrations substantially, while it has a negligible effect on the in-plane vibrations of the blades.

2.1 Introduction

Offshore wind turbines play an important role in producing electrical energy. Multi-megawatt offshore wind turbines with slender tower and large rotor are widely adopted in the state-of-the-art designs to more efficiently extract the vast wind resource. For example, the tower height and rotor radius of the modern NREL 5 MW horizontal axis wind turbine reach 87.6 m and 63 m respectively (Jonkman et al., 2009). These flexible wind turbines are vulnerable to the external vibration sources. For example, wind and sea wave loadings, which are experienced constantly during the whole lifetime of an offshore wind turbine, can result in excessive vibrations to the structures. These adverse vibrations may compromise the wind

[1] This chaper was published in *Engineering Structures* with the full bibliographic citation as follows: Zuo, H., Bi, K., & Hao, H. (2018). Dynamic analyses of operating offshore wind turbines including soil-structure interaction. *Engineering Structures*, *157*, 42-62. https://doi.org/10.1016/j.engstruct.2017.12.001.

energy output, cause the fatigue damage to the structural components, and even direct structural damage under extreme conditions. To ensure the safe and effective operations of these offshore wind turbines, it is important to accurately understand the dynamic behaviours when they are subjected to the external vibration loadings.

Extensive research works have been conducted by different researchers to investigate the dynamic behaviours of wind turbines under wind, sea wave and/or seismic loadings. To simplify the analysis, the wind turbines were normally assumed in the parked condition, and the blades were modelled as a lumped mass located at the top of the tower (Bazeos et al., 2002; Bisoi & Haldar, 2014, 2015; Chen & Georgakis, 2013; Colwell & Basu, 2009; Lavassas et al., 2003; Zuo et al., 2017) by neglecting the geometrical configurations of the blades and the interaction between the tower and blades. In reality, the geometrical characteristics and rotational velocity of the blades can directly influence the wind loads acting on the blades (Hansen, 2008). Moreover, the geometry of the rotor can influence the vibration characteristics of the wind turbine especially when it is in the operating condition since the locations of the blades are changing periodically and the centrifugal stiffness generated by the rotating blades can increase the stiffness and the natural frequencies of the blades (Murtagh et al., 2005), which in turn can indirectly affect the dynamic responses of wind turbines. The simplified lumped mass model therefore may lead to the inaccurate structural response estimations.

To investigate the influence of blades on the dynamic behaviours of wind turbines, Prowell et al. (2009), Kjørlaug and Kaynia (2015), and Santangelo et al. (2016) considered the geometrical characteristics of the blades and explicitly developed the finite element (FE) models of the blades in the seismic analyses of wind turbines. However, only the parked condition was considered in these studies, rotating induced blades location changes and stiffness increment therefore were not considered. To investigate the dynamic behaviours of operating wind turbines, Prowell et al. (2014) performed shaking table tests to investigate its seismic responses, additional damping in the fore-aft direction was observed compared to the parked condition. Some researchers simplified each blade as a single (Harte et al., 2012; Quilligan et al., 2012) or two (Fitzgerald & Basu, 2016) degrees-of-freedom (DOF) system, and the structural responses were estimated by using the home-made programs (e.g. in MATLAB). A lot of mathematics are involved in the calculations, these methods are therefore not convenient for other researchers/engineers to use. Moreover, wind loads acting along the height of the tower and the length of the blades are inevitably different, hence the structural responses may not be realistically captured by these simplified models. Some other researchers modelled the wind turbines by using the commercially available software such as FAST (Yuan et al., 2017) or validated their models against FAST (Kim et al., 2014). The structural components can be explicitly developed and the blades rotation can be considered by using

FAST. However, as indicated in the user's guide (Jonkman & Buhl Jr, 2005), FAST employs a combination of modal and multi-body dynamics formulations and models the blades and tower as flexible elements using a linear modal representation that assumes small deflections. In other words, FAST can only simulate the elastic response of wind turbines. Under the extreme loading conditions, the wind turbine may experience nonlinear deformations, which may not be realistically considered by FAST.

On the other hand, the monopile is widely designed as the foundation of offshore wind turbines due to its simplicity (Damgaard et al., 2014; Kuo et al., 2011). A typical monopile is a long hollow steel member with 3-6 m outer diameter and 22-40 m length (Bisoi & Haldar, 2014), inserting into the sea water and seabed. It can be regarded as an extension of the wind turbine tower. For such a slender flexible foundation, the interaction between the monopile and the surrounding soil is inevitable and can reduce the vibration frequencies or even vibration modes of the structure, which in turn may further influence the dynamic behaviours of offshore structures (Mostafa & El Naggar, 2004). Many numerical (Andersen et al., 2012; Arany et al., 2016) and experimental (Bhattacharya & Adhikari, 2011; Lombardi et al., 2013) studies have been carried out to investigate the influence of soil-structure interaction (SSI) on the vibration characteristics of wind turbines. Andersen et al. (2012) and Arany et al. (2016) investigated the effect of soil uncertainty on the first natural frequency of offshore wind turbine; Bhattacharya and Adhikari (2011) and Lombardi et al. (2013) conducted laboratory tests on a scaled wind turbine model and found that the natural frequencies of wind turbine were strongly related to the foundation flexibility. Some researchers also investigated the influence of SSI on the dynamic responses of wind turbines (Bisoi & Haldar, 2014, 2015; Damgaard et al., 2014; Fitzgerald & Basu, 2016; Hacıefendioğlu, 2012; Harte et al., 2012; Kjørlaug & Kaynia, 2015; Santangelo et al., 2016). However, it should be noted that in all these studies the wind turbines were either assumed in the parked condition (Kjørlaug & Kaynia, 2015; Santangelo et al., 2016) and the blades were lumped at the tower top (Bisoi & Haldar, 2014, 2015; Hacıefendioğlu, 2012), or the rotation of the blades was considered by the simplified 1- or 2-DOF system (Damgaard et al., 2014; Fitzgerald & Basu, 2016; Harte et al., 2012). The influence of blades on the structural responses was therefore not realistically considered as discussed above.

In the present study, a detailed FE model of the modern NREL 5 MW wind turbine is developed by using the commercially available FE code ABAQUS. The tower and blades are explicitly modelled. Compared to the previous simplified models, the present numerical model can realistically consider the influence of geometrical configurations of the blades on the wind loads, as well as the centrifugal stiffness variations of the blades generated by the blades rotation. Moreover, the possible nonlinear behaviour of the tower and blades can also be

conveniently considered. This FE model can be readily used by other researchers/engineers. This detailed FE model is used to systematically investigate the influences of operational conditions and SSI on the wind turbine responses when subjected to the combined actions of wind and sea wave loadings. The structure of this chapter is organized as follows: the NREL 5 MW wind turbine and the development of the FE model is presented in Section 2.3; Section 2.4 defines the vibration sources including the wind and sea wave loadings which are used in the analyses; the numerical results are discussed in Section 2.5 and some concluding remarks are made in Section 2.6.

2.2 Numerical model

2.2.1 NREL 5 MW wind turbine

The modern NREL 5 MW three-bladed wind turbine is selected as an example in the present study. The wind turbine is selected simply because its properties are well defined in many previous studies such as in (Jonkman et al., 2009). The outer diameters at the top and bottom of the tower are 3.87 m and 6 m, and the corresponding wall thickness are 0.019 m and 0.027 m respectively. The outer diameter and wall thickness decrease linearly from the bottom to the top of the tower. The total length of the monopile is 75 m, in which 20 m and 45 m are in the water and seabed respectively and another 10 m is above the mean sea level (Kooijman et al., 2003). The diameter and wall thickness of the monopile foundation are the same as the bottom cross section of the tower. The radius of the hub is 1.5 m and the length of the blade is 61.5 m. The distance from the hub centre to the tip of the blade is therefore 63 m.

The pre-twisted blade is made up of eight unique airfoil sections and the geometries can be found in (Jonkman et al., 2009). The mass of each blade is 17,740 kg as reported (Jonkman et al., 2009), but the wall thickness of the blade is not given in (Jonkman et al., 2009). A uniform wall thickness is assumed in the present study and a thickness of 0.019 m is computed to ensure that the mass of the blade is the same as that reported in (Jonkman et al., 2009). Figure 2-1 shows the main dimensions of the wind turbine and Table 2-1 tabulates the detailed information.

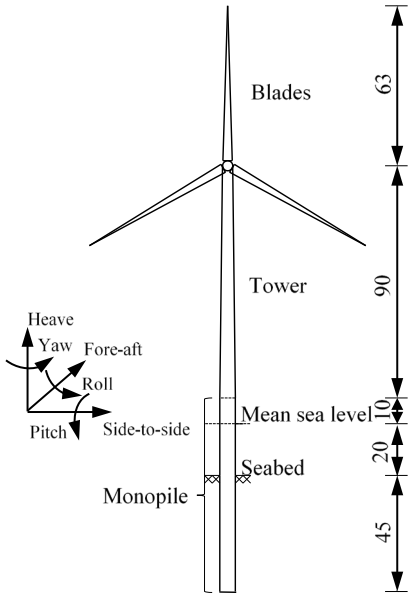

Figure 2-1 Offshore wind turbine model (Front view, dimensions in m)

Table 2-1 Properties of NREL 5MW wind turbine (Jonkman et al., 2009)

NREL 5 MW baseline wind turbine properties		
Basic description	Max. rated power	5 MW
	Rotor orientation, configuration	Upwind, 3 blades
	Rotor diameter	126 m
	Hub height	90 m
	Cut-in, rated, cut-out wind speed*	3 m/s, 11.4 m/s, 25 m/s
Blade	Cut-in, rated rotor speed	6.9 rpm, 12.1 rpm
	Length	61.5 m
	Overall (integrated) mass	17,740 kg
	Structural damping ratio	0.48%
	Hub diameter	3 m
Hub and Nacelle	Hub mass	56,780 kg
	Nacelle mass	240,000kg
	Height above water	87.6 m
Tower	Overall (integrated) mass	347,460 kg
	Structural damping ratio	1%

*In Table 2-1, cut-in wind speed means that wind turbine starts to rotate at a (cut-in) rotor speed of 6.9 rpm; rated wind speed means the maximum energy output of wind turbine will be achieved at a (rated) rotor speed of 12.1 rpm and cut-out wind speed is the speed above which the wind turbine stops working in order to protect the electrical and mechanical components.

2.2.2 Finite element model

The detailed three-dimensional (3D) FE model of the NREL 5 MW wind turbine is developed by using the finite element code ABAQUS. The tower and monopile above and in the sea water are modelled by the shell elements (S4 in ABAQUS), while the monopile buried in the soil medium is modelled by the beam elements (B31 in ABAQUS). The nacelle and hub are fixed at the top of the tower, only the masses of them are considered in the numerical model, and they are modelled by the point mass element in ABAQUS and is lumped at the tower top.

To ensure the deformation continuity at the connection between the tower and the monopile, the cross sections of the bottom of the tower and the top of the monopile are tied with each other. To consider the influence of blades on the dynamic behaviours of offshore wind turbines, the blades are explicitly developed and they are modelled by the shell elements again. A hinge connection between the tower and blades is defined to simulate the rotation of the blades and the rotational DOF along the out-of-rotor-plane direction is released.

The cross sections of the blades, tower and monopile in the water are divided into 24 elements as suggested in (Bi & Hao, 2016). A convergence test shows that an element size of 1 m along the blades, tower and monopile in the water and soil yields a good balance between the computational time and accuracy, an element size of 1 m is therefore selected in these directions. As mentioned above, the monopile above and in the sea water is modelled by the shell elements while the monopile in the soil is modelled by the beam elements in order to conveniently consider SSI. To make sure the same deformations of the beam element and shell elements at the seabed level, the node of the beam element and nodes of the shell elements are coupled with each other at this cross section. Figure 2-2 shows FE model of the wind turbine except the monopile in the soil medium, the modelling of which will be discussed in Section 2.3.3. In the numerical model, the three blades are labelled as #1 to #3 in an anticlockwise direction as shown in Figure 2-2.

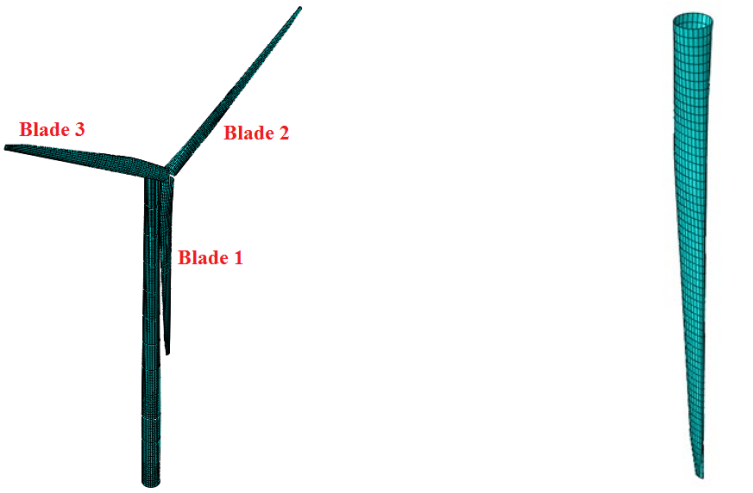

(a) wind turbine in the parked condition (b) blade

Figure 2-2 FE model of the wind turbine (the monopile in the soil medium is not shown)

The blades are made of polyester with a density of 1850 kg/m^3 (Burton et al., 2001). The tower and monopile are made of steel. For the monopile above the mean sea level and buried in the soil medium, the density is 7850 kg/m^3, while the density of the tower is taken as 8500 kg/m^3 (Jonkman et al., 2009) to account for the paint, welds, bolts and flanges that are not directly considered in the numerical model. For the monopile in the sea water, the vibrating monopile

can impart an acceleration to the surrounding sea water. The water-monopile interaction is modelled by the added mass method (Bi & Hao, 2016) in the present study, in which the effective mass m_e of the monopile can be expressed as

$$m_e = m_p + m_a \tag{2.1}$$

where m_p is the monopile physical mass and m_a denotes the added mass which can be calculated as (DNV, 2010)

$$m_a = C_a \frac{\pi}{4} d_p^2 \rho_w \tag{2.2}$$

where d_p is the outer diameter of the monopile, ρ_w=1030 kg/m^3 is the sea water density and C_a is the added mass coefficient, which is assumed as 1.0 in the present study (DNV, 2010). Table 2-2 tabulates the material properties of the blades, tower and monopile. The polyester and steel are assumed as ideal elastic-plastic materials and the relationship between stress and strain is shown in Figure 2-3. As shown in Figure 2-3, f_y is the yield strength, ε_1 is the elastic strain and ε_2 is the strain which equals to the sum of the elastic and plastic strains.

Table 2-2 Material properties of the wind turbine (Burton et al., 2001; Jonkman et al., 2009)

Component	Material	Density (kg/m^3)	Young's modulus (GPa)	Poisson's ratio	Yield strength (MPa)	Plastic strain
Blade	Polyester	1850	38	0.3	700	0.02
Tower	Steel	8500	210	0.3	235	0.01
Monopile	Steel	7850	210	0.3	235	0.01

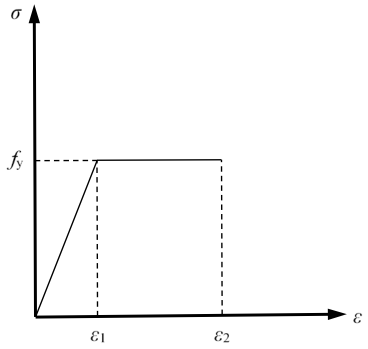

Figure 2-3 Ideal elastic-plastic stress-strain relationship of polyester and steel

Some previous studies (Jonkman et al., 2009; Kim et al., 2014) calculated the vibration frequencies and vibration modes of the NREL 5 MW wind turbine in the parked condition and without considering SSI. To examine the accuracy of the developed FE model, the natural frequencies and vibration modes of the wind turbine are calculated and compared with those in a previous study (Jonkman et al., 2009). For a fair comparison, the parked condition is considered and the bottom of the tower is fixed (i.e. SSI is not considered) in this section.

Table 2-3 tabulates the first 12 natural frequencies, the corresponding vibration modes and the differences of the vibration frequencies between these two studies. It can be seen that in general good agreements are observed. Slightly larger differences are obtained when the frequencies are corresponding to the vibration modes of the blades. This is because the strengthening webs in the blades are not included in the numerical model due to the lack of the detailed geometry and material properties. The first flap-wise and edgewise vibration mode shapes of the blade are compared with those in another study (Fitzgerald & Basu, 2014) and the results are shown in Figure 2-12 in Section 2.4.2. Good agreements are obtained again and the slightly larger amplitudes in the present model are because the strengthening webs are not modelled as discussed above.

Table 2-3 Natural frequencies of NREL 5 MW wind turbine in the parked condition and without considering SSI

Mode	Description	(Jonkman et al., 2009) (Hz)	Current study (Hz)	Diff.
1	1st tower side-to-side	0.312	0.300	-3.85%
2	1st tower fore-aft	0.324	0.316	-2.47%
3	1st blade flap-wise yaw	0.666	0.490	-26.43%
4	1st blade flap-wise pitch	0.668	0.541	-19.01%
5	1st blade collective flap	0.699	0.607	-13.16%
6	1st blade edgewise pitch	1.079	1.172	8.62%
7	1st blade edgewise yaw	1.090	1.210	11.01%
8	2nd blade flap-wise yaw	1.934	1.729	-10.60%
9	2nd blade flap-wise pitch	1.922	1.970	2.50%
10	2nd blade collective flap	2.021	2.252	11.43%
11	2nd tower side-to-side	2.936	2.705	-7.87%
12	2nd tower fore-aft	2.900	2.855	-1.55%

2.2.3 Soil springs

As discussed above, the interaction between the monopile foundation and the surrounding soil may significantly influence the dynamic behaviours of offshore wind turbine. To more accurately perform dynamic analysis, SSI is considered in the present study. Many different methods have been adopted by different researchers to consider SSI (Bisoi & Haldar, 2014; Kjørlaug & Kaynia, 2015; Lombardi et al., 2013). Due to the simplicity and accuracy, the nonlinear soil springs are adopted in the present study.

In the nonlinear soil spring method, the lateral resistances of the soil against the foundation movements are depicted by the springs in the directions perpendicular and parallel to the rotor plane (the *p-y* springs in Figure 2-4), and the vertical springs attached to the monopile are applied to simulate the shaft friction (*t-z* spring) and end bearing capacity at the tip of the monopile (*Q-z* spring). The space between each group of soil springs is selected as 1 m as suggested in (Bisoi & Haldar, 2014), and they are modelled by the ground spring elements in ABAQUS. Figure 2-4 shows the model of the monopile foundation attached with soil springs.

The properties of the soil springs are described by the *p-y*, *t-z* and *Q-z* curves as recommended in API (2014) and DNV (2014), which are briefly introduced in this section.

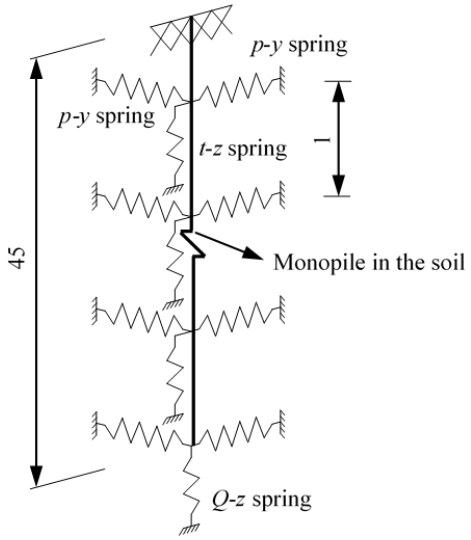

Figure 2-4 SSI modelling (not to scale, dimensions in m)

In the present study, only the undrained clay is considered. As recommended in API (2014) and DNV (2014), the lateral force per unit length of the monopile (p) is related to the undrained shear strength of soil s_u and the transition depth Z_R, which is expressed by

$$Z_R = 6s_u d_p / \left(\gamma' d_p + J s_u\right) \tag{2.3}$$

where d_p is the outer diameter of the monopile, γ' is the effective unit weight of soil and it is 8 kN/m^3 and J is a dimensionless empirical constant, and the value of 0.5 is adopted in the present study (Bisoi & Haldar, 2014).

When $s_u \leq 100$ kPa and the depth below the seabed $Z > Z_R$, the lateral force per unit length of the monopile can be calculated as

$$p = \begin{cases} 0.5 p_u (y/y_c)^{1/3} & \text{for } y \leq 3y_c \\ 0.72 p_u & \text{for } y > 3y_c \end{cases} \tag{2.4}$$

where y is the lateral displacement of the monopile and y_c is the deformation at which the strength of the soil reaches one-half of the ultimate soil resistance, which is estimated as

$$y_c = 2.5 \varepsilon_c d_p \tag{2.5}$$

in which, ε_c is the strain corresponding to one-half of the maximum stress in laboratory undrained compression tests of undisturbed soil. The relationship between s_u and ε_c proposed by Ashour et al. (1998) is used in the present study. Three soil undrained shear strengths (25, 50 and 100 kPa) are considered in this study, the corresponding values of ε_c are 0.02, 0.008 and 0.006 respectively.

In Eq. (2.4), p_u is the ultimate lateral soil resistance per unit length of the monopile, which can be calculated as

$$p_u = \begin{cases} (3s_u + \gamma' Z)d_p + Js_u Z & \text{for } 0 < Z \leq Z_R \\ 9s_u d_p & \text{for } Z > Z_R \end{cases} \quad (2.6)$$

When $Z \leq Z_R$, p becomes

$$p = \begin{cases} 0.5p_u(y/y_c)^{1/3} & \text{for } y \leq 3y_c \\ 0.72p_u(1-(1-Z/Z_R)(y-3y_c)/12y_c) & \text{for } 3y_c < y \leq 15y_c \\ 0.72p_u(Z/Z_R) & \text{for } y > 15y_c \end{cases} \quad (2.7)$$

The axial resistance of the soil is modelled by a combination of shaft friction and end bearing capacity at the monopile tip as shown in Figure 2-4. The relationship between the mobilized soil-monopile shear transfer and monopile displacement at any depth can be represented by the *t-z* curve (API, 2014). Similarly, *Q-z* curve is used to describe the relationship between the end bearing resistance and axial tip deflection (API, 2014). In API (2014), the t/t_{max} versus z/z_{peak} and Q/Q_p versus z/d_p relationships are tabulated. In which z is the monopile axial deflection at any depth below the seabed; z_{peak} is the displacement corresponding to the maximum soil-monopile adhesion and the value of z_{peak} is typically 1% of the monopile outer diameter d_p; t and t_{max} are the mobilized and maximum soil-monopile adhesion respectively; Q and Q_p are the mobilized and end bearing capacities respectively. The values of t_{max} and Q_p are dependent on the undrained soil shear strength s_u and can be calculated as suggested in API (2014). Substituting t_{max}, z_{peak}, Q_p and d_p into the tables in API (2014), the t versus z and Q versus z relationships can be obtained.

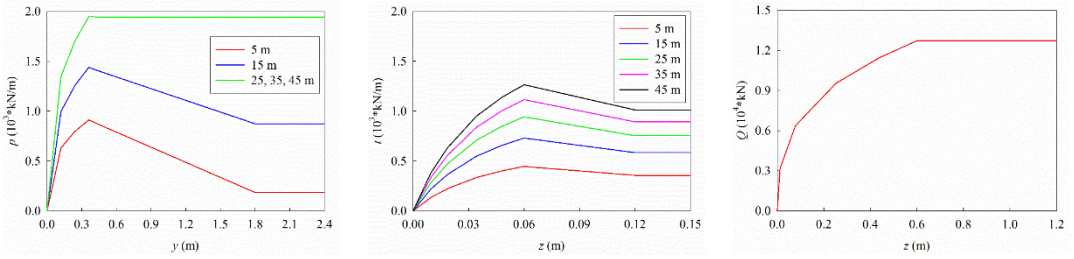

(a) *p-y* curve (b) *t-z* curve (c) *Q-z* curve

Figure 2-5 *p-y*, *t-z* and *Q-z* curves

Figure 2-5 shows the *p-y*, *t-z* and *Q-z* curves at different depths (5 to 45 m with an increment of 10 m) below the seabed with s_u=50 kPa (corresponds to a typical medium clay). As shown in Figure 2-5(a), p is not influenced by the depth when it is larger than 25 m. Figure 2-5(c) shows the relationship at the monopile tip, the depth is fixed and therefore only one curve is included in Figure 2-5(c).

2.2.4 Vibration characteristics

After the nonlinear soil springs are defined, the vibration frequencies and vibration modes of the wind turbine with the consideration of SSI are calculated. As discussed above, three undrained shear strengths of soil are considered in the present study. For conciseness, only the results when s_u=50 kPa are reported. Table 2-4 tabulates the first ten natural frequencies and Figure 2-6 shows the corresponding vibration modes. To show the mode shape more clearly, the blades are not shown when the mode is dominated by the tower vibration.

Table 2-4 First ten natural frequencies of the wind turbine with SSI (s_u=50 kPa)

Mode	Description	f (Hz)
1	tower fore-aft (1st order)	0.154
2	tower side-to-side (1st order)	0.156
3	blade flap-wise yaw (1st order)	0.474
4	blade flap-wise pitch (1st order)	0.536
5	blade collective flap (1st order)	0.596
6	tower side-to-side (2nd order)	1.096
7	tower fore-aft (2nd order)	1.121
8	blade edgewise pitch (1st order)	1.206
9	blade edgewise yaw (1st order)	1.250
10	blade flap-wise yaw (2nd order)	1.626

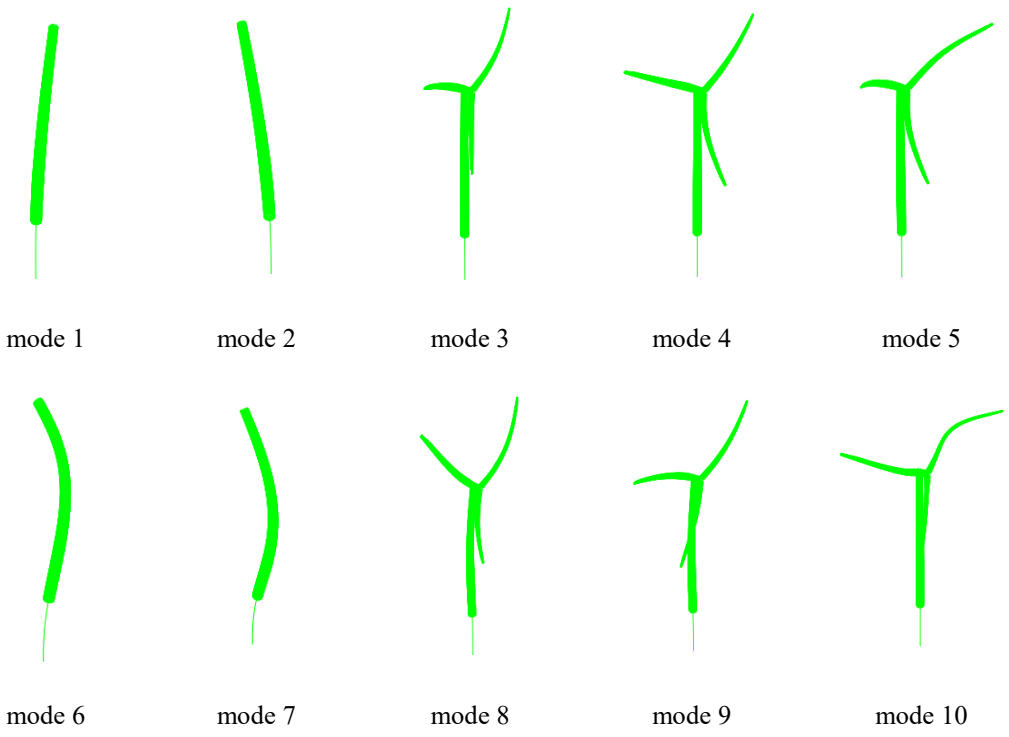

Figure 2-6 Vibration modes of the wind turbine with SSI

2.2.5 Damping

The damping mechanism of an offshore wind turbine is quite complicated and it normally comprises structural damping, aerodynamic damping, hydrodynamic damping and soil

damping, which account for the contributions of the structure itself, wind, surrounding sea water and supporting soil respectively (Arany et al., 2016). The structural damping ratios of the blades and the tower are 0.48% and 1% respectively as suggested in (Jonkman et al., 2009). Aerodynamic damping results from the relative velocity between the wind and the rotating blades, which depends on the wind velocity, rotor speed, the geometrical configurations of the blades and the flow around the blades (Hu et al., 2015). It is not easy to accurately obtain the aerodynamic damping. The aerodynamic damping in the fore-aft direction for an operating wind turbine is normally within the range of 1-6% (Valamanesh & Myers, 2014). Without loss of generality, a constant value of 3.5% is adopted in the present study as suggested by Bisoi and Haldar (2014, 2015). For a parked wind turbine or in the side-to-side direction, previous studies (Arany et al., 2016; Valamanesh & Myers, 2014) revealed that the aerodynamic damping ratio is almost zero, and zero is adopted in the present study. The hydrodynamic damping results from the drag between the tower and the surrounding water. The upper limit of hydrodynamic damping ratio is about 0.23% (Arany et al., 2016) and this value is used in this study. The soil damping develops from SSI and it includes the material damping of the soil and the wave radiation damping which may go up to as high as 20% for the subgrade medium in some cases (Bisoi & Haldar, 2014). However, as will be demonstrated in Sections 2.4.1 and 2.4.3, the frequency contents of wind and sea wave loads are very low (up to 0.2 and 0.8 Hz respectively), and as indicated in (Andersen, 2010) very little energy is dissipated by the radiation of waves when the excitation frequency is below 1 Hz, the wave radiation damping is therefore neglected in the numerical model. The material damping is thus dominant in the soil damping and 1% is assumed in the present study (Arany et al., 2016). Therefore, summing all the components together, the damping ratio is 3.98% in the fore-aft direction for the rotating blades; for the parked blades or in the side-to-side direction, the value is 0.48%; and the damping ratio of the tower taking into account SSI is 2.23%. The damping of offshore wind turbine is considered by means of Rayleigh damping and the first out-of-plane and in-plane vibration frequencies of the tower and blades are used to calculate the mass and stiffness coefficients for the tower and blades respectively (Chopra, 2012).

2.3 Vibration sources

In the present study, the wind and sea wave loadings, which are experienced during the whole lifetime of an offshore wind turbine, are considered as the external vibration sources. The wind and sea wave loads are stochastically simulated based on the sophisticated simulation techniques, and they are briefly introduced in this section for completeness of the paper.

2.3.1 Wind load on the tower

The wind load can be decomposed into a constant mean wind load and a fluctuating component. The Kaimal spectrum (Murtagh et al., 2005) is used to model the power spectral density (PSD) function of the fluctuating wind velocity along the tower, which is given by

$$S_{vv}(h,f) = \frac{v_*^2}{f}\frac{200c}{(1+50c)^{5/3}} \tag{2.8}$$

where

$$c = fh/\bar{v}(h) \tag{2.9}$$

and

$$\bar{v}(h) = v_* \ln(h/z_0)/K \tag{2.10}$$

in which h is the height of the location where wind load is calculated, f is the frequency in Hz, $\bar{v}$ is the mean wind velocity, v_* is the friction velocity, c is the Monin coordinate, K is the von-Karman's constant, which is generally taken as 0.4 (Benowitz & Deodatis, 2015) and z_0 is the roughness length.

For a continuous line-like structure, like the tower, the wind loads at different locations along the tower are different but with certain similarities, which is known as the spatial correlation effect. The spatial correlation effect is normally described by a spatial coherency loss function. The modal fluctuating drag force power spectrum, which considers the influence of spatial correlation effect, can be calculated by (Murtagh et al., 2005)

$$S_{f,j}(f) = (C_{dt}\rho)^2 \sum_{k=1}^{N}\sum_{l=1}^{N} S_{v_k v_l}(f) A_k A_l \bar{v}_k \bar{v}_l \phi_j(k)\phi_j(l) \tag{2.11}$$

in which C_{dt} is the drag coefficient of the tower, ρ is the air density, A_k, A_l and $\bar{v}_k$, $\bar{v}_l$ are the areas exposed to the wind and the mean wind velocities at locations k and l respectively, $\phi_j(k)$ and $\phi_j(l)$ are the jth mode shape at locations k and l. As will be demonstrated in the following analysis, the energy of wind load mainly concentrates in the low frequency range (see Figure 2-7) and normally the first vibration mode of the tower can be excited by the wind, j=1 is therefore used in the simulation. S_{vkvl} is the cross PSD function of wind velocity between locations k and l, which can be expressed as

$$S_{v_k v_l}(f) = \sqrt{S_{v_k v_k}(f) S_{v_l v_l}(f)}\, coh(k,l;f) \tag{2.12}$$

where $S_{v_k v_k}$ and $S_{v_l v_l}$ are the wind velocity auto PSDs as given by Eq. (2.8), $coh(k, l; f)$ is the spatial coherency loss function between locations k and l and the model as proposed by Huang et al. (2013) is adopted in the present study

$$coh(k,l;f) = exp\left(-\frac{D\omega|k-l|}{2\pi\hat{v}}\right)exp\left(-i\frac{k-l}{v_{app}}\omega\right) \quad (k>l) \tag{2.13}$$

in which, $|k\text{-}l|$ and $\hat{v}$ are the distance and average mean wind velocity between locations k and l respectively, D is a decay constant, ω is angular frequency in rad/s and v_{app} is the apparent wave velocity. For $k<l$, the spatial coherency loss function is the complex conjugate of that with $k>l$.

The time histories of the fluctuating drag force with zero mean then can be simulated by using the Inverse Fast Fourier transform (IFFT) technique (Bi & Hao, 2012; Hao et al., 1989).

The mean wind drag force can be calculated by

$$\bar{f}_{mean,i} = \frac{1}{2}C_{dt}A_i\rho\bar{v}_i^2 \tag{2.14}$$

in which, A_i and $\bar{v}_i$ are the area associated with location i and the mean wind velocity at location i respectively.

The wind loads at different locations along the tower are different. To simplify the analysis, the tower is divided into nine segments in the simulation and the drag force is assumed to be the same within each segment. The lengths of the top and bottom segments are 5 and 15 m respectively and other segments are 10 m length. The mean wind velocity at the top of the tower is taken as 15 m/s, and the roughness length, air density, drag coefficient, decay constant and apparent wave velocity are 0.005, 1.2 kg/m^3, 1.2, 0.04 and 10 m/s respectively. Figure 2-7 shows the fluctuating wind velocity PSDs in segments S1 (85-90 m along the tower) and S5 (45-55 m) and the corresponding model values. The model and simulated coherency loss functions between segments S1and S5 are presented in Figure 2-8. As shown in Figure 2-7 and Figure 2-8, the simulated results are in well agreement with the corresponding model values. For brevity, not all the drag forces along the tower are shown. Only the time histories in two example segments (S1 and S5) are shown in Figure 2-9.

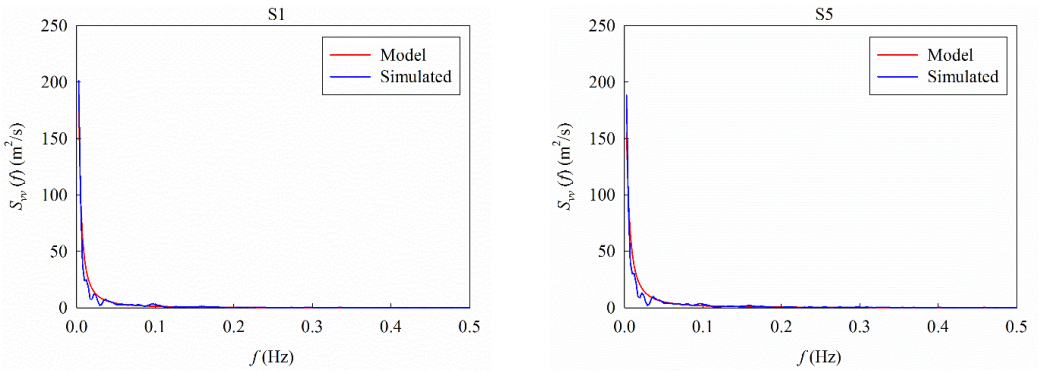

Figure 2-7 Comparisons of the simulated wind velocity with the model PSDs

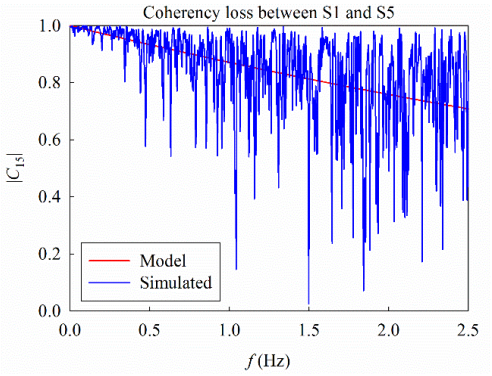

Figure 2-8 Comparison between the simulated and model coherency loss functions

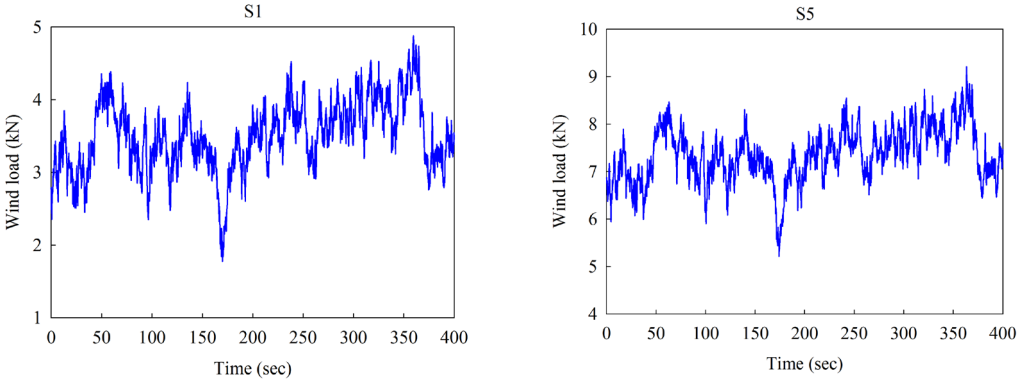

Figure 2-9 Wind loads in segments S1 and S5

2.3.2 Wind load on the blades

The wind loads on the blades are influenced by the wind velocity, rotor velocity, pitch angle, the number of blades and geometrical configurations of the blade (e.g. blade profile, twist and chord distribution) (Harte et al., 2012). To more realistically estimate the wind loads on the rotating blades, the blade element momentum (BEM) method, which couples the momentum theory with the local events taking place at the actual blades (Hansen, 2008), is adopted in the present study. In the BEM method, it is assumed that all sections are independent along the rotor, i.e. no aerodynamic interaction between different sections. Each blade therefore can be divided into several elements and wind load on each element can be calculated separately (Hansen, 2008).

The relative wind velocity on each element of the blade, v_{rel}, is given by

$$v_{rel}(r,t_s)=\sqrt{\left(\bar{v}(r,t_s)(1-a)+v_f(t_s)\right)^2+\left(\Omega r(1+a')\right)^2} \tag{2.15}$$

where r is a radial distance of the element from the centre of the hub, t_s is time, a and a' are the axial and tangential induction factors respectively, Ω is the rotor velocity in rad/s, $\bar{v}$ is the

mean wind velocity and v_f is the fluctuating wind velocity, the calculations of which are discussed below.

The height of each blade element $h(r,t_s)$ experiences a sinusoidal variation in magnitude as the rotation of the blades and the frequency of this variation is the same as the rotor frequency. With the definition of blade numbers in Figure 2-2, $h(r,t_s)$ can be expressed as

$$h(r,t_s) = H_{hub} + r\cos(\Omega t_s + \theta_i) \tag{2.16}$$

$$\theta_i = \pi - \frac{2\pi}{3}(i-1) \quad i = 1,2,3 \tag{2.17}$$

where H_{hub} is the hub height and θ_i is the phase difference between blades. By submitting $h(r,t_s)$ into Eq. (2.10), the mean wind velocity $\bar{v}$ in Eq. (2.15) therefore can be obtained.

Due to the rotation of the blades, the PSD of the fluctuating wind velocity v_f is not a constant but varies with time, namely it is a time-variant rotational sampled spectrum. However, not to further complicate the problem, an isotropic, homogeneous turbulence at the hub height is assumed to represent the turbulence over the rotor field in the present study as suggested by many previous studies (Harte et al., 2012). Based on this assumption, the fluctuating wind velocity v_f in Eq. (2.15) can be estimated by using the PSD of wind velocity at the hub height defined in Eq. (2.8).

After the relative wind velocity is determined (Eq. (2.15)), the local lift and drag forces on each element can be calculated as follows (Hansen, 2008)

$$p_l(r,t_s) = \frac{1}{2}\rho v_{rel}^2(r,t_s) l(r) C_{lb}(\alpha) \tag{2.18}$$

$$p_d(r,t_s) = \frac{1}{2}\rho v_{rel}^2(r,t_s) l(r) C_{db}(\alpha) \tag{2.19}$$

in which, l is the chord length, C_{lb} and C_{db} are the lift and drag coefficients of the blade respectively and it is related to the local angle of attack, which is defined by

$$\alpha(r,t_s) = \varphi(r,t_s) - \beta(t_s) - \kappa(r) \tag{2.20}$$

where β is the pitch angle and it is 10º in the present study and κ is the pre-twist angle of each element with respect to the hub, which decreases from the bottom of 13.3º to the tip of 0º (Jonkman et al., 2009). $\varphi(r,t_s)$ is the flow angle and it can be calculated as

$$\varphi(r,t_s) = \tan^{-1}\left(\frac{(1-a)\bar{v}(r,t_s) + v_f(t_s)}{(1+a')\Omega r}\right) \tag{2.21}$$

Figure 2-10 shows the lift and drag coefficients of the blade with respect to the angle of attack. The local wind loads in the directions parallel and perpendicular to the rotor plane therefore

can be calculated by projecting the local lift and drag forces along the edgewise and flap-wise directions respectively as shown in Figure 2-11, which can be expressed as

$$\begin{Bmatrix} p_t(r,t_s) \\ p_n(r,t_s) \end{Bmatrix} = \begin{bmatrix} \sin(\varphi(r,t_s)) & -\cos(\varphi(r,t_s)) \\ \cos(\varphi(r,t_s)) & \sin(\varphi(r,t_s)) \end{bmatrix} \begin{Bmatrix} p_l(r,t_s) \\ p_d(r,t_s) \end{Bmatrix} \tag{2.22}$$

The total in-plane and out-of-plane wind loads on the blade then can be obtained by integrating the wind loads on each blade element over the entire rotor length as

$$F_t(t_s) = \int_0^R p_t(r,t_s)\phi_{e,1}(r)dr \tag{2.23}$$

$$F_n(t_s) = \int_0^R p_n(r,t_s)\phi_{f,1}(r)dr \tag{2.24}$$

where R is rotor radius, $\phi_{e,1}$ and $\phi_{f,1}$ are the fundamental vibration mode shapes of the blade in the edgewise and flap-wise directions respectively, which are obtained by carrying out an eigenvalue analysis and they are shown in Figure 2-12.

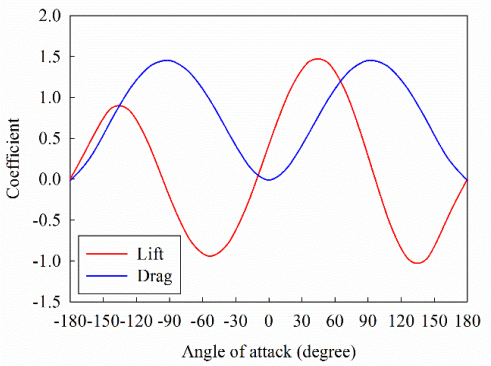

Figure 2-10 Lift and drag coefficients of the blade

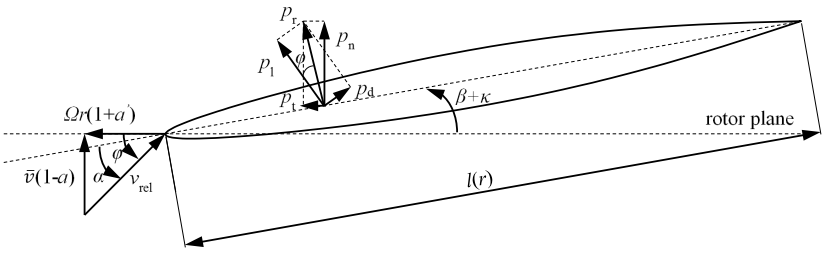

Figure 2-11 Wind loads on the blade element

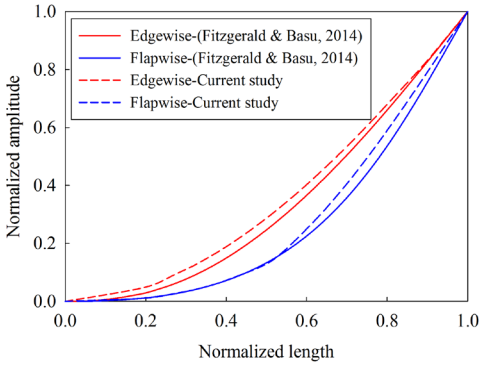

Figure 2-12 First edgewise and flap-wise vibration mode shapes of the blade

Based on the BEM method discussed above, the total in-plane and out-of-plane wind loads of a rotating blade can be calculated. When the parked condition is of interest, the same procedure can be followed, and the above equations can be simplified by submitting Ω=0 into Eqs. (2.15), (2.16) and (2.21).

The wind loads acting on the parked and rotating blades of the wind turbine therefore can be simulated respectively and Figure 2-13 shows the edgewise and flap-wise wind loads on blade 2 under different conditions. In this simulation, the mean wind velocity at the tower top is 15 m/s and the rotor speed is 12.1 rounds per minute. For conciseness, the wind loads on other two blades are not shown. As shown in Figure 2-13(a), the flap-wise wind loads are slightly larger than the edgewise wind loads when the wind turbine is in the parked condition, this is because the flow angle is a constant and equals to $\pi/2$ based on Eq. (2.21) when Ω=0 and the angle of attack is between 67 and 80 degrees, therefore the lift and drag coefficients have a small difference as shown in Figure 2-10, which in turn lead to non-significant difference between the flap-wise and edgewise wind loads on the parked blades. When the wind turbine is in the operating condition, the wind loads in the edgewise and flap-wise directions are obviously different and the wind load in the flapwsie direction is larger than that in the edgewise direction. Moreover, comparing Figure 2-13(a) with Figure 2-13(b), it is obvious that the wind loads on the rotating blades are much larger than those on the parked blades since the relative wind velocity becomes larger based on Eq. (2.15) due to the rotation of the blades.

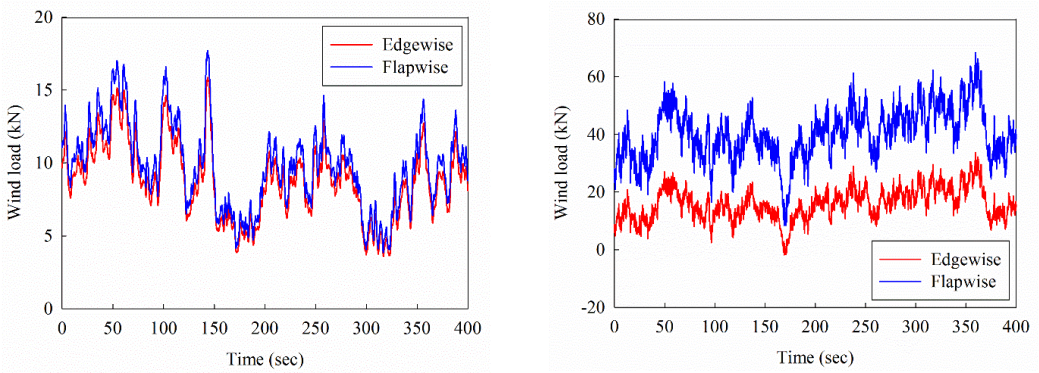

(a) parked condition (b) operating condition

Figure 2-13 Edgewise and flap-wise wind loads on blade 2

2.3.3 Sea wave load on the monopile

To calculate the sea wave load acting on the monopile, the JONSWAP spectrum, which has the following form (Hasselmann et al., 1973) is used to simulate the sea surface elevation

$$S_{\eta\eta}(f) = \alpha_P g^2 (2\pi)^{-4} f^{-5} exp\left[-\frac{5}{4}\left(\frac{f_m}{f}\right)^4\right] \gamma^{exp\left[-\frac{(f-f_m)^2}{2\sigma^2 f_m^2}\right]} \tag{2.25}$$

where η is the sea surface elevation, g is the gravitational acceleration, γ is the peak enhancement factor (typically 3.3) and f is frequency in Hz. α_P, f_m and σ are three constants, which are (Colwell & Basu, 2009)

$$\alpha_P = 0.076(Fg/v_{10}^2)^{-0.22} \tag{2.26}$$

$$f_m = 11(v_{10}F/g^2)^{-1/3}/\pi \tag{2.27}$$

and

$$\sigma = \begin{cases} 0.07 & f \le f_m \\ 0.09 & f > f_m \end{cases} \tag{2.28}$$

in which v_{10} is the mean wind velocity at 10 m above sea surface and F is the fetch length.

The sea surface elevation $\eta(t_s)$ in the time domain then can be simulated as

$$\eta(t_s) = \sum_{i=1}^{n} \sqrt{2d\omega S_{\eta\eta}(\omega_i)} \cos\left(\omega_i t_s + \Phi(\omega_i)\right) \tag{2.29}$$

where Φ is the random phase angle uniformly distributed over the range of $[0, 2\pi]$.

The velocity and acceleration of water particles in the horizontal direction can be expressed as (Sorensen, 2005)

$$v_x = \frac{H\omega}{2}\frac{\cosh k_w(d_w + z_w)}{\sinh k_w d_w}\cos(k_w x_w - \omega t_s + \varphi) \tag{2.30}$$

$$a_x = \frac{H\omega^2}{2}\frac{\cosh k_w(d_w + z_w)}{\sinh k_w d_w}\sin(k_w x_w - \omega t_s + \varphi) \tag{2.31}$$

in which x_w and z_w denote the horizontal and vertical coordinates respectively, d_w is water depth, which is 20 m in the present study, H is the wave height, which is two times of the amplitude of the sea surface elevation, ω is angular frequency in rad/s and k_w is the sea wave number, which can be estimated based on the following equation (Sorensen, 2005)

$$\omega^2 = g k_w \tanh(k_w d_w) \tag{2.32}$$

In the present study, the following parameters are used: g=9.8 m/s^2, v_{10}=11.5 m/s and F=40,000 m. The peak wave frequency f_m is therefore 0.208 Hz based on Eq. (2.27) and the wave period is T=1/f_m= 4.81 s. The wave length can be calculated as $\lambda = gT^2/2\pi$=36 m (Sorensen, 2005), and it is larger than five times of the diameter of the monopile. Based on the specifications in DNV (2010), the Morison formula can be used to calculate the sea wave load. According to the Morison equation, the transverse sea wave load per unit length of the monopile can be calculated as

$$F_w = \frac{1}{2}\rho_w C_{dp} d_p |v_x| v_x + \rho_w C_m A_p a_x \tag{2.33}$$

$$C_m = C_a + 1 \tag{2.34}$$

where A_p is the cross section area of the monopile, C_{dp}, C_m are the drag and inertia coefficients respectively, and C_{dp}=1.2, C_m=2.0 are adopted in the simulation. It should be noted that the first term represents the contribution of the quadratic drag force, and the second term is the inertia force.

In the simulation, the monopile in the water is divided into two segments and the length of each segment is 10 m. Figure 2-14 shows the PSDs of the simulated sea surface elevation and the given model, good match is observed. Figure 2-15 shows the simulated sea wave load time history at the mean sea level, and the sea wave loads at other locations along the monopile are not shown for conciseness.

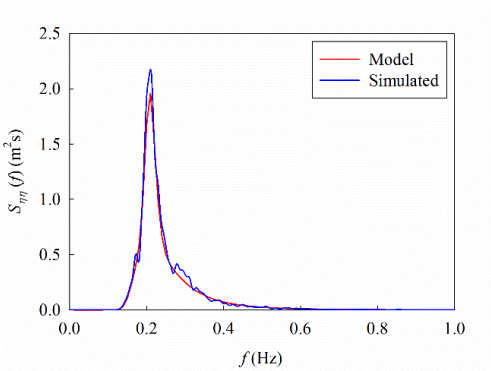

Figure 2-14 Comparison between the simulated sea surface elevation and the model PSDs

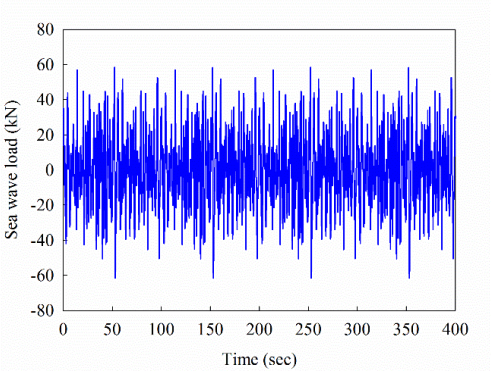

Figure 2-15 Sea wave load time history at mean sea level

As mentioned above, the blade, tower and monopile in the sea water are divided into a few segments. In the FE model, a reference point is defined in each segment and coupled with the cross section of the corresponding segment, the simulated wind and sea wave loadings are applied on these reference points.

2.4 Numerical results

2.4.1 Influence of operational conditions

To examine the influence of operational conditions of wind turbine on the structural responses, two cases are investigated in this section. In the first case, the wind turbine is in the parked condition, with the locations of the blades shown in Figure 2-2(a). In the second case, the blades are rotating with a uniform angular velocity of Ω=1.27 rad/s, which corresponds to the rated rotor speed of NREL 5 MW wind turbine (12.1 rpm). The wind and sea wave loads shown in Figure 2-9 and Figure 2-15 are applied to the tower respectively in both cases. For the wind loads on the blades, they depend on the rotor velocity as discussed in Section 2.4.2. Different wind loads as shown in Figure 2-13 are applied in different cases. In both cases, a duration of 400 s is considered for all the external vibration sources. Not to further complicate

the problem, SSI is not considered in this section, i.e. the wind turbine is fixed at the seabed level.

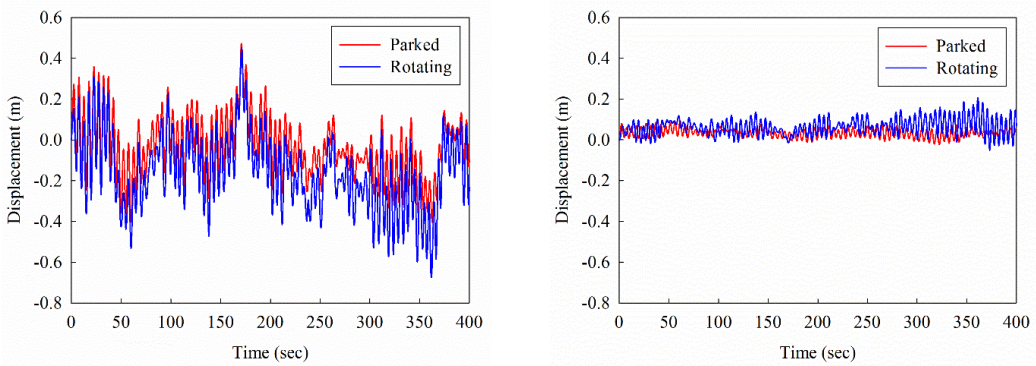

(a) fore-aft (b) side-to-side

Figure 2-16 Fore-aft and side-to-side displacement time histories at the tower top

It is obvious that the responses along the tower are different and the maximum responses occur at the tower top. For conciseness, only the maximum responses are discussed in the present study. Figure 2-16 shows the displacement time histories at the top of the tower in the fore-aft and side-to-side directions. The red curves are the results when the blades are in the parked condition, and the blue curves are the displacements when they are rotating. It shows that the displacements in the operating condition are larger than those in the parked condition in both directions. As shown in Figure 2-16(a), the maximum fore-aft displacement at the top of the tower is 0.473 m occurring at t=171 s when the wind turbine is still. When the blades are rotating, a larger maximum displacement of 0.674 m occurs at t=362 s. For the side-to-side displacement at the top of the tower, the maximum values are 0.093 and 0.206 m respectively when the wind turbine is in the parked and operating conditions (Figure 2-16(b)). These results are actually expected since as shown in Figure 2-13, when the blades are rotating, the wind loads acting on the blades are larger compared to the parked condition. Larger wind loads on the blades result in more severe interaction between the tower and blades and therefore larger tower responses. These results indicate that previous studies by assuming the wind turbines in the parked condition may result in non-conservative structural response estimations, which in turn may lead to the unsafe design of structural components.

Comparing Figure 2-16(a) with Figure 2-16(b), it is obvious that the side-to-side displacements of the tower are much smaller than the fore-aft responses in both cases. Two reasons lead to these results. The first one is that the wind and sea wave loads are only applied in the fore-aft direction on the tower in the numerical simulation, and no external vibration sources are acted in the side-to-side direction. The other reason is that as shown in Figure 2-13, the wind loads on the blades in the flap-wise (fore-aft direction corresponds to tower) and edgewise (side-to-side) directions are almost the same when the wind turbine is in the parked

condition (Figure 2-13(a)), while when it is in the operating condition, the wind loads in the flap-wise direction are much larger than those in the edgewise direction (Figure 2-13(b)). The larger wind loads on the blades result in more severe interaction between the tower and blades, and lead to the larger tower responses in the fore-aft direction as discussed above.

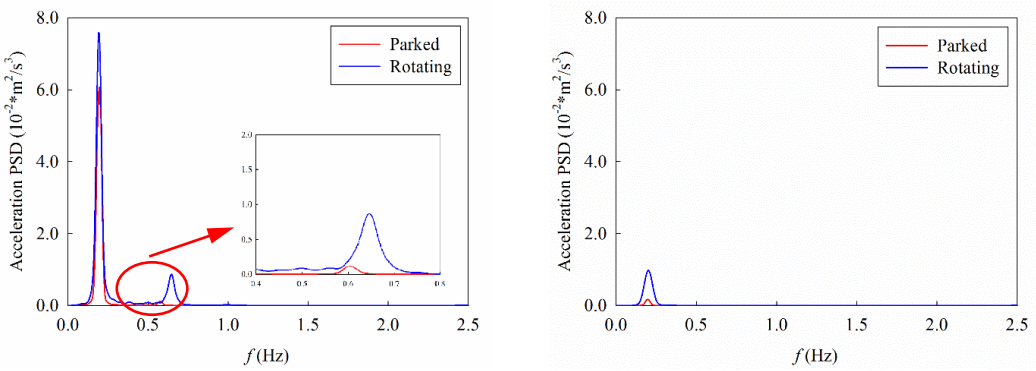

(a) fore-aft (b) side-to-side

Figure 2-17 Fore-aft and side-to-side acceleration PSDs at the tower top

Figure 2-17 shows the PSDs of the acceleration responses at the top of the tower in the fore-aft and side-to-side directions when the blades are in the parked and operating conditions. To more clearly obtain the dominant frequencies of the structural responses, an *N*/4-point Hamming window is used to smooth the PSDs in the present study, in which *N* is the number of the data to be analysed. As shown in Figure 2-17(a), an obvious peak appears at 0.204 Hz. As shown in Table 2-5 in Section 2.5.2, this value corresponds to the first vibration mode of the tower in the fore-aft direction, which means the first vibration mode is excited by the external vibration sources. Figure 2-17 also shows that another peak occurs at 0.603 and 0.647 Hz respectively when the wind turbine is in the parked and operating conditions. As shown in Table 2-5, 0.603 Hz is the first collective flap vibration mode of the blades when the wind turbine is in the parked condition. For 0.647 Hz, this frequency cannot be directly found in Table 2-5, this is because the rotating condition cannot be directly considered in the modal analysis by using ABAQUS. This frequency corresponds to the first collective flap vibration mode of the blades when the wind turbine is in the operating condition. These results indicate again that the interaction between the tower and blades makes the vibrations of the blades contribute to the tower responses. Compared to the parked condition, the first collective flap vibration frequency of the blades is slightly larger when it is in the operating condition as shown in Figure 2-17(a). This is because the centrifugal stiffness of the blades is generated when the wind turbine is operating, which in turn leads to large structural stiffness and vibration frequency of the blades. For the PSDs in the side-to-side direction, Figure 2-17(b) shows that only one peak appears at 0.208 Hz, and this peak corresponds to the first vibration mode of the tower in the side-to-side direction as shown in Table 2-5. Comparing the results

in Figure 2-17(b) with those in Figure 2-17(a), it is obvious that the energies are much smaller in the side-to-side direction, which results in the smaller tower responses in this direction as shown in Figure 2-16. Similarly, compared to the red curve, the values in the blue curve are larger, and this explains the larger structural responses in the operating condition as shown in Figure 2-16.

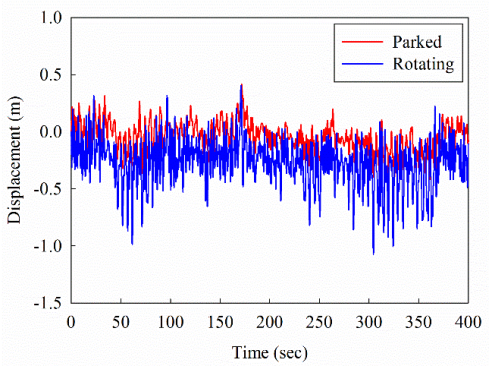

(a) blade 1

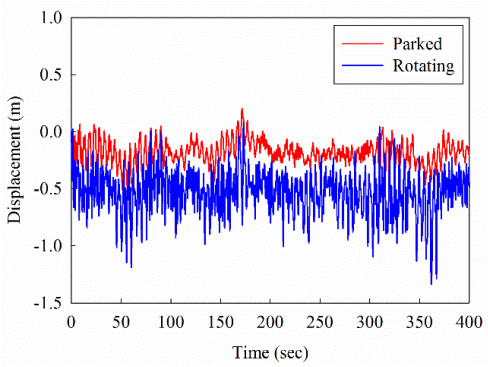

(b) blade 2

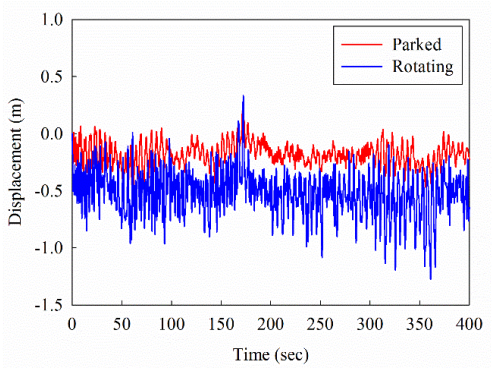

(c) blade 3

Figure 2-18 Flap-wise displacement time histories at the blade tips

Figure 2-18 shows the displacement (relative to the tower top) time histories at the tips of blades in the flap-wise direction. Wind load acting on the blade can be decomposed into a constant mean and a fluctuating component as discussed in Section 2.4. The mean value of the fluctuating term is zero. However, the total wind load on the blade has a non-zero mean because of the constant component of the wind pressure as shown in Figure 2-13, which results in the non-zero baseline of the structural responses shown in Figure 2-18. As shown, the maximum flap-wise displacements at the tips of blades 1, 2 and 3 are 0.429, 0.544, 0.544 m respectively when the wind turbine is in the parked condition. The displacements at the tips of blades 2 and 3 are the same. This is because the geometrical configurations and locations of blades 2 and 3 are the same as shown in Figure 2-2 and the same excitations are applied on these two blades, which in turn lead to the same structural responses. The result also shows that the maximum flap-wise displacement on blade 1 is smaller than that on blades 2 and 3,

this is because blade 1 is lower than blades 2 and 3 (see Figure 2-2), and the wind loads on blade 1 are smaller than those on blades 2 and 3. Figure 2-18 also shows that the maximum displacements are much larger when the blades are rotating and the corresponding values are 1.074, 1.338, 1.274 m respectively. When the wind turbine is in the operating condition, the flap-wise vibrations of the blades are not the same and they are influenced by the original locations of the blades.

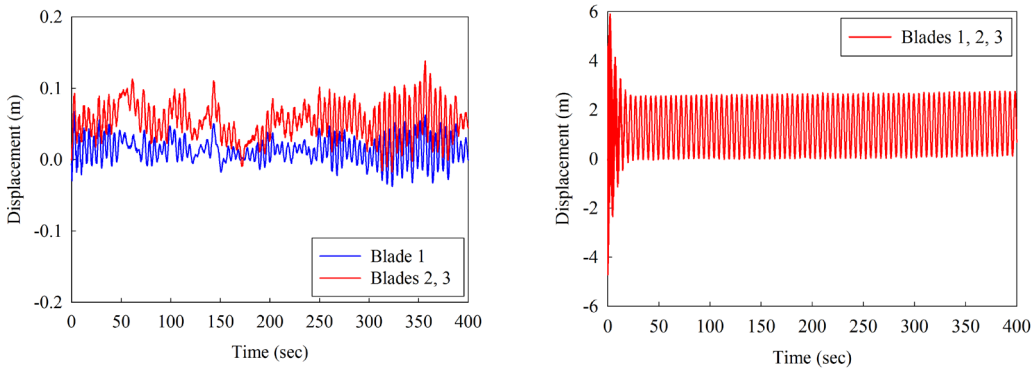

(a) parked (b) rotating

Figure 2-19 Edgewise displacement time histories at the blade tips

Figure 2-19 shows the edgewise displacements of the blades when they are in the parked and operating conditions. Again, the non-zero baseline of the edgewise displacements is due to the contribution of the mean term of the wind loads acting on the blades. As shown in Figure 2-19(a), the maximum edgewise displacements at the tips of blades 1, 2 and 3 are 0.067, 0.138 and 0.138 m respectively when the turbine is in the parked condition. When the blades are rotating, as shown in Figure 2-19(b), the edgewise responses of the three blades are identical because of the same geometrical and structural parameters in the rotor plane. Compared to the parked condition, the edgewise displacements of the blades are much larger when they are rotating. The edgewise displacements at the tips of the blades experience a sinusoidal variation in magnitude after about 25 s and the frequency of this variation equals to the rotor frequency of 0.202 Hz (1.27 rad/s). At the first 25 s, the amplitudes of the edgewise displacements are larger than those after 25 s since the blades rotate immediately from the parked state at t=0 s and the whole wind turbine system is unstable during this period (Staino & Basu, 2013). Due to the structural and aerodynamic damping of the blades, the displacements decrease to an almost constant value from t=25 s. These results are consistent with those reported in (Fitzgerald & Basu, 2014; Staino & Basu, 2013).

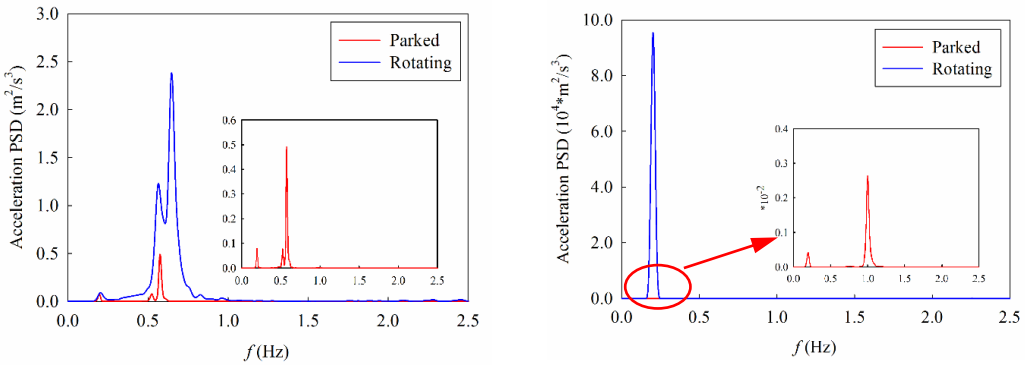

(a) flap-wise (b) edgewise

Figure 2-20 Flap-wise and edgewise acceleration PSDs at the tip of blade 2

To further explain the above results, Figure 2-20 shows the PSDs of the acceleration responses at the tip of blade 2 in the flap-wise and edgewise directions respectively. The acceleration PSDs of other blades are similar with those of blade 2, they are therefore not shown for brevity. As shown in Figure 2-20(a), three obvious peaks appear at 0.204, 0.544 and 0.603 Hz respectively when the wind turbine is in the parked condition. The first peak corresponds to the first fore-aft vibration mode of the tower, because of the interaction between the tower and blades as discussed above. Another two peaks correspond to the first flap-wise pitch and collective flap vibration modes of the blades as shown in Table 2-5 in Section 2.4.2. It should be noted that the first flap-wise yaw vibration mode of the blades is not excited since the locations of the blades and wind loads acting on the blades are symmetric and the flap-wise yaw vibration mode is antisymmetric as shown in Figure 2-6. The antisymmetric vibration mode cannot be excited by the symmetric load when it is acting on a symmetric structure. When the blades are rotating, the three peaks occur at 0.204, 0.565 and 0.647 Hz respectively. Again the last two vibration frequencies cannot be obtained from Table 2-5 due to the blades rotation cannot be directly considered in the modal analysis as discussed above. For the PSDs in the edgewise direction, Figure 2-20(b) shows that two peaks appear at 0.208 and 1.176 Hz respectively when the wind turbine is in the parked condition and these two peaks correspond to the first vibration modes of the tower and blades in the edgewise direction (side-to-side direction for the tower) as shown in Table 2-5. However, when the wind turbine is operating, only one peak occurs at the rotor frequency of the blades (0.202 Hz). This result well explains that the edgewise displacements of the rotating blades are governed by the rotor rotation as shown in Figure 2-19(b). Figure 2-20 also clearly shows the operating condition of wind turbine leads to larger responses of the blades as shown in Figure 2-18 and Figure 2-19 in both the flap-wise and edgewise directions.

2.4.2 Influence of SSI

Table 2-5 Vibration frequencies of the wind turbine without and with SSI

Mode	Description	w/o SSI	s_u=25 kPa		s_u=50 kPa		s_u=100 kPa	
		(Hz)	Freq. (Hz)	Diff. (%)	Freq. (Hz)	Diff. (%)	Freq. (Hz)	Diff. (%)
1	1st tower fore-aft	0.204	0.141	-30.9	0.154	-24.5	0.163	-20.1
2	1st tower side-to-side	0.208	0.142	-31.7	0.156	-25.0	0.165	-20.7
3	1st blade flap-wise yaw	0.488	0.474	-2.9	0.474	-2.9	0.474	-2.9
4	1st blade flap-wise pitch	0.544	0.532	-2.2	0.536	-1.5	0.538	-1.1
5	1st blade collective flap	0.603	0.594	-1.5	0.596	-1.2	0.598	-0.8
6	1st blade edgewise pitch	1.176	1.189	1.1	1.206	2.6	1.145	-2.6
7	1st blade edgewise yaw	1.206	1.231	2.1	1.250	3.6	1.154	-4.3
8	2nd tower fore-aft	1.562	1.036	-33.7	1.121	-28.2	1.242	-20.5
9	2nd tower side-to-side	1.630	1.003	-38.5	1.096	-32.8	1.279	-21.5
10	2nd blade flap-wise yaw	1.700	1.625	-4.4	1.626	-4.4	1.626	-4.4

To investigate the effect of SSI on the dynamic behaviours of the wind turbine, three different soils with undrained shear strength of s_u=25, 50 and 100 kPa are considered in the present study and are used to represent the typical soft, medium and stiff soils. As discussed above, the rotation of the blades cannot be explicitly considered in the modal analysis by using ABAQUS, only the parked condition is considered when the vibration characteristics (vibration frequencies and vibration modes) of the wind turbine are calculated. Table 2-5 tabulates the vibration frequencies of the wind turbine without and with the consideration of SSI. The corresponding differences between the vibration frequencies obtained without and with SSI are also given in the table. As shown in Table 2-5, SSI can significantly decrease the vibration frequencies of the tower especially for the soft soil condition, this is because the monopile inserts into the seabed and is surrounded by the soil when SSI is considered, which makes the tower more flexible compared to the case of the wind turbine fully fixed at the seabed level. Since the stiffness of the tower becomes smaller, the vibration frequencies of the tower therefore decrease. For example, when the undrained shear strength of the soil s_u is 25 kPa, the first vibration frequency of the tower in the fore-aft direction is 0.141 Hz, and it is 0.204 Hz when SSI is not considered. The reduction ratio reaches 30.9%. It should be noted that the energy of the wind load concentrates within the range of 0-0.1 Hz as shown in Figure 2-7, when SSI is considered, the first vibration frequency of the tower is closer to the dominant frequency of the wind load. In this case, resonance might occur and larger structural responses are expected. Therefore, SSI should be considered to more accurately predict the dynamic responses of the wind turbine.

Different from modal analysis, the wind turbine is assumed in the operating condition when the structural responses are calculated. In this section, a rotor angular velocity of Ω=1.27 rad/s is considered.

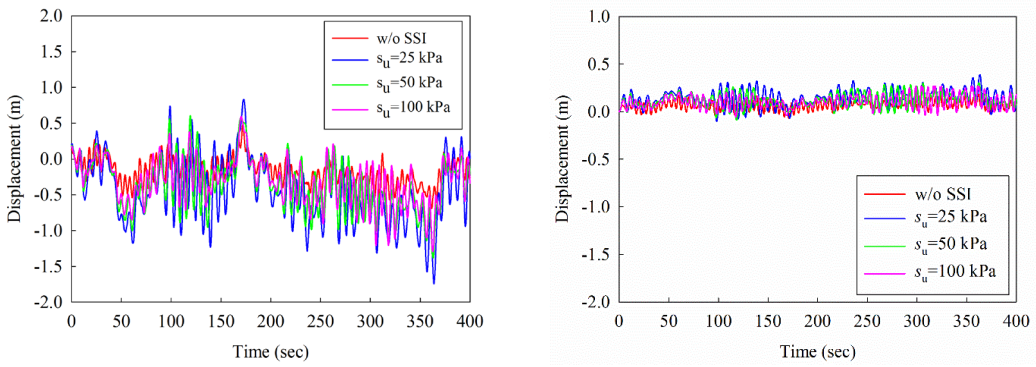

(a) fore-aft (b) side-to-side

Figure 2-21 Fore-aft and side-to-side displacement time histories at the tower top without and with SSI

Table 2-6 Maximum displacements at the tower top without and with SSI

Direction	w/o SSI (m)	s_u=25 kPa		s_u=50 kPa		s_u=100 kPa	
		Disp. (m)	Diff. (%)	Disp. (m)	Diff. (%)	Disp. (m)	Diff. (%)
Fore-aft	0.674	1.742	158.5	1.383	105.2	1.297	92.4
Side-to-side	0.206	0.388	88.3	0.301	46.1	0.269	30.6

Figure 2-21 shows the displacement time histories at the top of the tower in the fore-aft and side-to-side directions without and with the consideration of SSI. Table 2-6 tabulates the maximum fore-aft and side-to-side displacements at the tower top, and the corresponding differences between the peak displacements without and with SSI are given in the table as well. As shown in Figure 2-21, the tower vibrations are much larger in both the fore-aft and side-to-side directions when SSI is considered, and with the increment of soil shear strength, the lateral stiffness of soil increases and the deflection of monopile decreases (Ashour, et al., 1998). As shown in Figure 2-21(a) and Table 2-6, the maximum fore-aft displacements at the top of the tower are 1.742, 1.383 and 1.297 m respectively when s_u=25, 50 and 100 kPa, which increase by 158.5%, 105.2% and 92.4% respectively compared to that when the wind turbine is fixed at the seabed level, i.e. neglecting the interaction between the monopile foundation and the surrounding soil. Figure 2-21(b) and Table 2-6 also show that the peak displacements at the tower top in the side-to-side direction are 0.388, 0.301 and 0.269 m respectively. Compared to the case in which SSI is not considered, these values are increased by 88.3%, 46.1% and 30.6%.

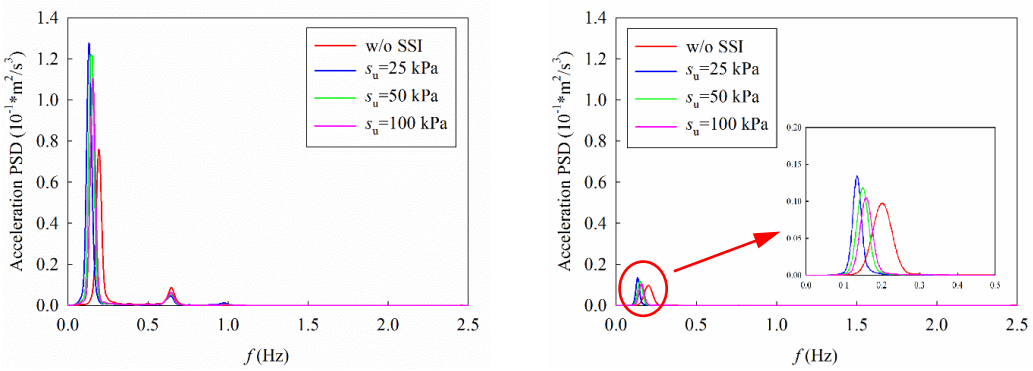

(a) fore-aft (b) side-to-side

Figure 2-22 Fore-aft and side-to-side acceleration PSDs at the tower top without and with SSI

Figure 2-22 shows the PSDs of the acceleration responses at the top of the tower in the fore-aft and side-to-side directions without and with the effect of SSI. As shown in Figure 2-22(a), the first vibration frequency of the tower in the fore-aft direction shifts to a lower value when SSI is considered, and they are 0.141, 0.154 and 0.163 Hz respectively when s_u=25, 50 and 100 kPa. It should be noted that the second peak appearing at 0.647 Hz corresponds to the first collective flap vibration mode of the blades and this frequency is almost not influenced by SSI as shown in Figure 2-22, which well agrees with the observations in Table 2-5 that SSI has almost no effect on the vibration frequencies of the blades. Similarly, as shown in Figure 2-22(b), the first vibration frequency of the tower in the side-to-side direction decreases as well when the effect of SSI is included. The corresponding vibration frequencies are 0.142, 0.156 and 0.165 Hz respectively when s_u=25, 50 and 100 kPa. Figure 2-22 also shows that more energies are obtained for the softer soil, which in turn result in the larger tower responses as shown in Figure 2-21.

Figure 2-23 shows the displacement time histories at the tips of the blades in the flap-wise direction. Table 2-7 tabulates the maximum flap-wise displacements at each blade tip and the corresponding differences when SSI is considered or not. As shown in Table 2-7, the largest displacements at the tip of blade 1 are 1.536, 1.231 and 1.220 m respectively when s_u=25, 50 and 100 kPa. For blade 2, the maximum values are 1.745, 1.648 and 1.632 m respectively, and the corresponding values are 1.701, 1.529 and 1.486 m respectively for blade 3. It can be seen that the flap-wise displacement responses of the blades are influenced by SSI but the extents are smaller than those of the tower (refer to Table 2-6). This is because the soil springs are directly connected to the monopile foundation of the tower while the influence of SSI on the blades is mainly through the (indirect) interaction between the tower and blades. As discussed above, softer soil leads to larger fore-aft vibrations of the tower, which in turn leads to the more severe interaction between the tower and blades, and therefore the larger flap-wise displacements of the blades.

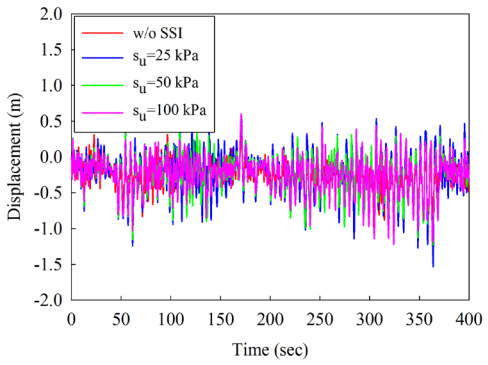

(a) blade 1

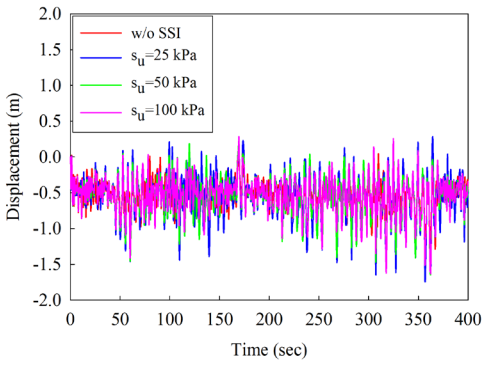

(b) blade 2

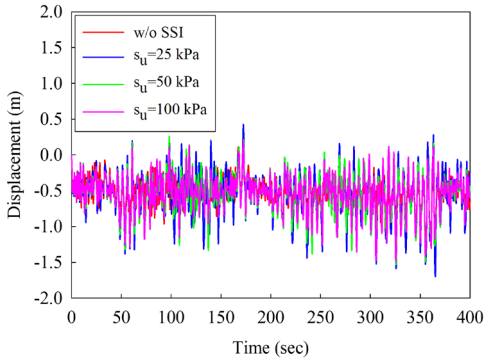

(c) blade 3

Figure 2-23 Flap-wise displacement time histories at the blade tips without and with SSI

Table 2-7 Maximum flap-wise displacements at the blade tip without and with SSI

Location	w/o SSI (m)	s_u=25 kPa		s_u=50 kPa		s_u=100 kPa	
		Disp. (m)	Diff. (%)	Disp. (m)	Diff. (%)	Disp. (m)	Diff. (%)
Tip of blade 1	1.074	1.536	43.0	1.231	14.6	1.220	13.6
Tip of blade 2	1.338	1.745	30.4	1.648	23.2	1.632	22.0
Tip of blade 3	1.274	1.701	33.5	1.529	20.0	1.486	16.6

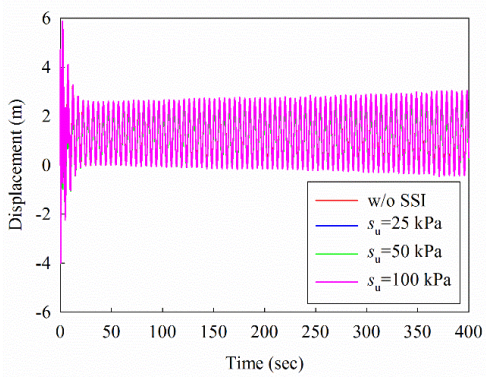

Figure 2-24 Edgewise displacement time histories at the tip of blade 2 without and with SSI

Figure 2-24 shows the edgewise displacement time histories at the tip of blade 2, and the displacements at other two blades are not shown since they are the same as discussed above.

As shown, again the edgewise displacements of the rotating blades are governed by the rotor rotation and SSI has a negligible effect on the displacement responses of the blades in the edgewise direction. This is because the vibrations of the tower in the side-to-side direction are very small as shown in Figure 2-21(b), which results in the negligible interactions between the tower and blades in the side-to-side direction. The results are consistent with those reported by Fitzgerald and Basu (2016).

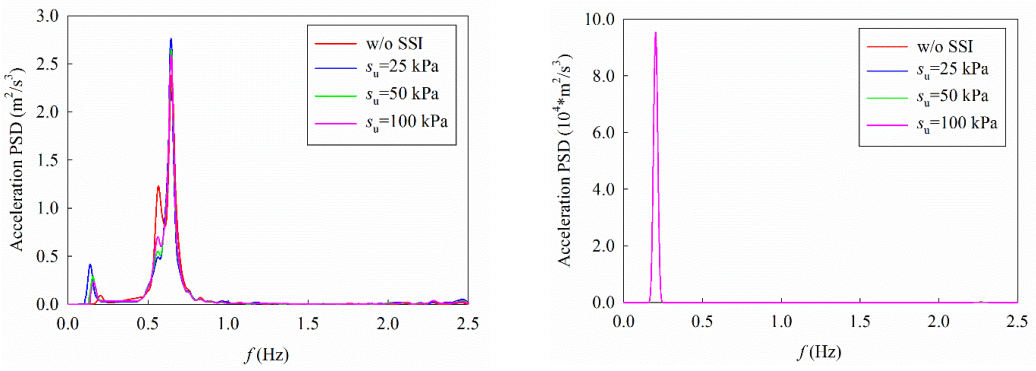

(a) flap-wise (b) edgewise

Figure 2-25 Flap-wise and edgewise acceleration PSDs at the tip of blade 2 without and with SSI

Figure 2-25 shows the PSDs of the acceleration responses at the tip of blade 2 in the flap-wise and edgewise directions. As shown in Figure 2-25(a), three obvious peaks appear in the PSD curves and they correspond to the first fore-aft vibration mode of the tower, the first flap-wise pitch and collective flap vibration modes of the blades respectively as discussed in Section 2.5.1. As shown, the frequency corresponding to the first peak changes when SSI is considered and the value becomes smaller when softer soil is considered. This is easy to understand, when softer soil is considered, the system becomes more flexible. For the second and third peaks, they correspond to the vibration modes of the blades and they are almost not influenced by SSI. Figure 2-25(b) shows that only one peak occurs at the rotor frequency of the blades (0.202 Hz) and the energies included in the PSD curves are the same when s_u=25, 50 and 100 kPa. This result again explains the results that SSI has no effect on the edgewise responses of the blades as shown in Figure 2-24.

2.4.3 Influence of rotor velocity

The rotor velocity may also significantly influence the structural responses. The designed cut-in and rated rotor velocities of the NREL 5 MW wind turbine are 6.9 and 12.1 rpm respectively as tabulated in Table 2-1. In other words, the wind turbine starts to rotate at a (cut-in) rotor speed of 6.9 rpm and the maximum energy output of the wind turbine will be achieved at a (rated) rotor speed of 12.1 rpm. To examine the influence of rotor velocity, the rotor velocity of 8 rpm (0.84 rad/s) and 12.1 rpm (1.27 rad/s) are investigated, which are within the designed

rotor velocity range. Another rotor velocity of 16 rpm (1.68 rad/s) is also considered to represent a worst rotating condition in the present study. SSI is also considered in this section and the undrained shear strength of soil is taken as 50 kPa.

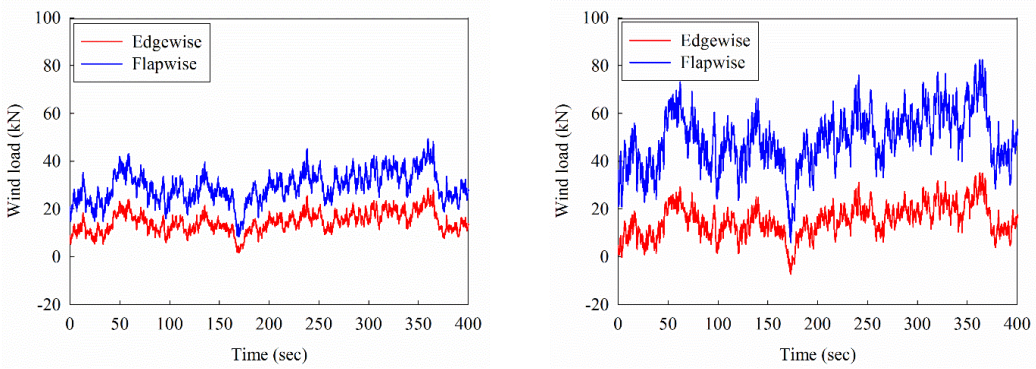

(a) Ω=0.84 rad/s (b) Ω=1.68 rad/s

Figure 2-26 Wind loads on blade 2 under different rotor velocities

As discussed in Section 2.4.2, the wind loads on the blades are influenced by the rotor velocity. Figure 2-26 shows the simulated wind loads on blade 2 in the flapwsie and edgewise directions when the rotor velocities are 0.84 and 1.68 rad/s respectively. Together with the wind loads shown in Figure 2-13(b) (the wind loads when Ω=1.27 rad/s), it can be seen that larger rotor velocity results in larger wind loads acting on the blade. For conciseness, the wind loads acting on the other two blades are not plotted in the figure. Similar trend is obtained.

Figure 2-27 shows the displacement time histories at the top of the tower in the fore-aft and side-to-side directions and the maximum displacements are tabulated in Table 2-8. As shown in Figure 2-27 and Table 2-8, the displacement responses at the top of the tower are increased in both directions with the increment of rotor velocity. The maximum fore-aft displacements at the tower top are 1.226, 1.383 and 1.523 m respectively when Ω=0.84, 1.27 and 1.68 rad/s, and the corresponding values in the side-to-side direction are 0.258, 0.301 and 0.329 m. This is because wind loads acting on the blades are larger with the increment of the rotor velocity as discussed above, and larger loads result in larger structural responses.

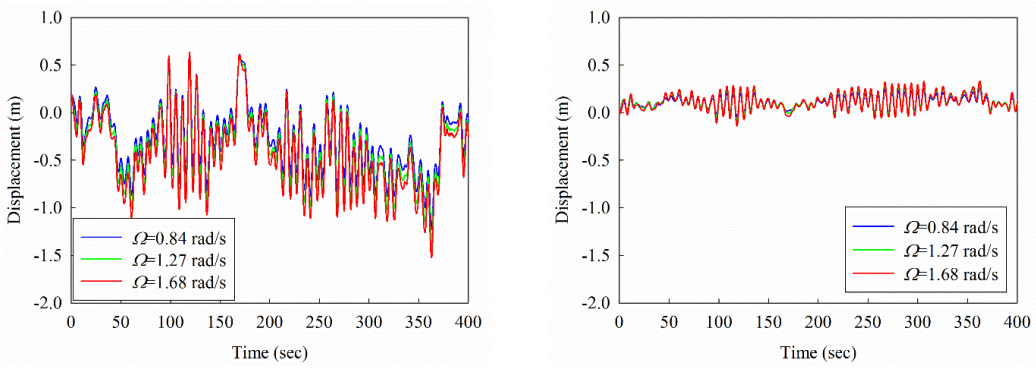

(a) fore-aft (b) side-to-side

Figure 2-27 Fore-aft and side-to-side displacement time histories at the tower top under different rotor velocities

Table 2-8 Maximum displacements at the tower top under different rotor velocities (Unit: m)

Direction	Ω=0.84 rad/s	Ω=1.27 rad/s	Ω=1.68 rad/s
Fore-aft	1.226	1.383	1.523
Side-to-side	0.258	0.301	0.329

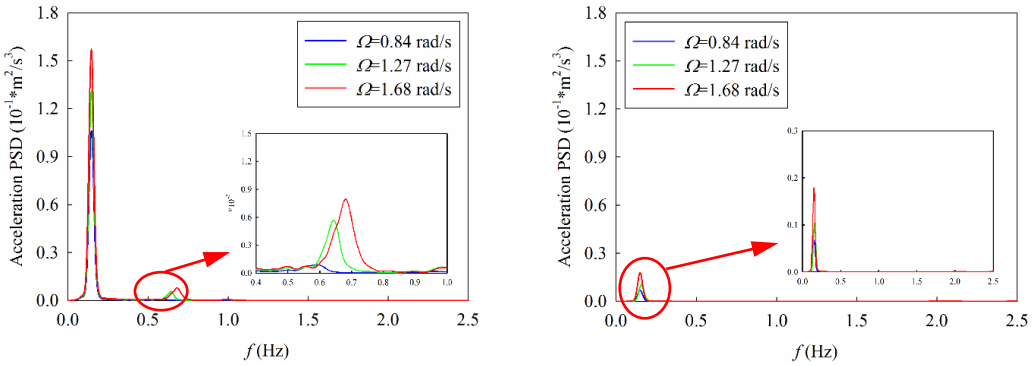

(a) fore-aft (b) side-to-side

Figure 2-28 Fore-aft and side-to-side acceleration PSDs at the tower top under different rotor velocities

Figure 2-28 shows the PSDs of the fore-aft and side-to-side acceleration responses at the top of the tower. As shown in Figure 2-28(a), the first peak appears at 0.154 Hz, which corresponds to the first fore-aft vibration frequency of the tower and is not influenced by the rotor velocity. The second peak corresponds to the first collective flap vibration mode of the blades and the frequencies are 0.598, 0.647 and 0.684 Hz respectively when Ω= 0.84, 1.27 and 1.68 rad/s, which are 0.4%, 8.1% and 14.7% greater than the frequency of 0.596 Hz when the wind turbine is in the parked condition as tabulated in Table 2-5. This is because the geometric stiffness arising out of centrifugal stiffening in the flap-wise direction can increase the stiffness and vibration frequencies of the blades (Fitzgerald & Basu, 2014; Murtagh et al., 2005). In the side-to-side direction, only one peak occurs at 0.156 Hz as shown in Figure 2-28(b). This value

corresponds to the first vibration frequency of the tower in the side-to-side direction as tabulated in Table 2-5. Figure 2-28 also shows that more energies concentrate in the PSD curves when the blades rotate at a larger velocity, which in turn lead to larger tower responses as shown in Figure 2-27.

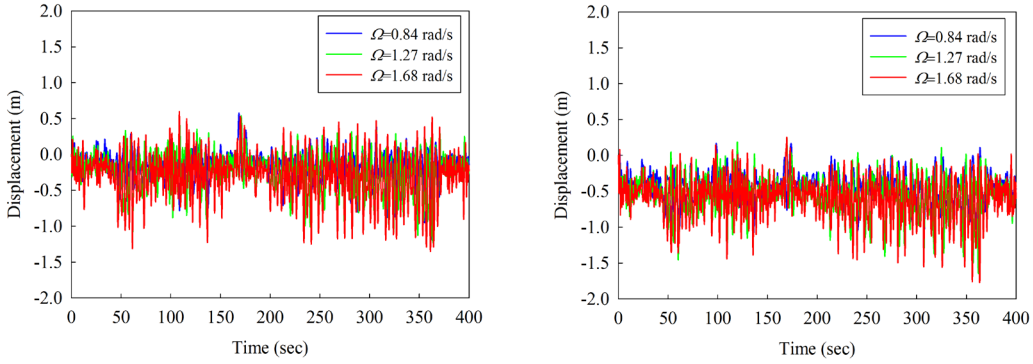

(a) blade 1 (b) blade 2

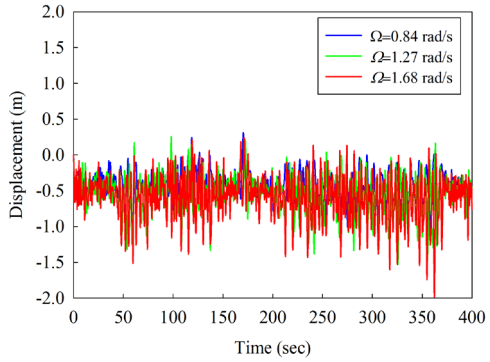

(c) blade 3

Figure 2-29 Flap-wise displacement time histories at the blade tips under different rotor velocities

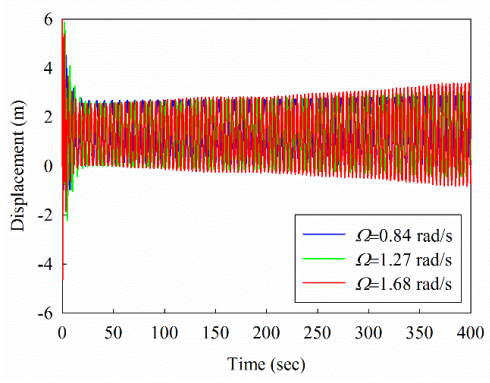

Figure 2-30 Edgewise displacement time histories at the tip of blade 2 under different rotor velocities

Figure 2-29 shows the displacement time histories at the tips of blades in the flap-wise direction and Figure 2-30 shows the edgewise displacements at the tip of blade 2. As shown in Figure 2-29 and Figure 2-30, both the flap-wise and edgewise displacement responses of the blades increase with the increment of the rotor velocity. This is because, as discussed above,

the wind loads acting on the blades are larger as shown in Figure 2-13(b) and Figure 2-26, which in turn lead to the larger responses of the blades. Table 2-9 tabulates the maximum flap-wise displacements at each blade tip. The maximum displacements at the tip of blade 1 in the flap-wise direction are 1.186, 1.124 and 1.155 m respectively when Ω=0.84, 1.27 and 1.68 rad/s; for blade 2, the peak values are 1.231, 1.648 and 1.529 m respectively; and the corresponding values are 1.352, 1.773 and 1.984 m respectively for blade 3. It is interesting to note that, as shown in Figure 2-30, the displacements at the blade tip in the edgewise direction is not a constant as that shown in Figure 2-19(b) but increase slightly from about t=200 s especially when Ω=1.68 rad/s. This is because the edgewise wind loads acting on the blades become larger in the time duration of 200-400 s as shown in Figure 2-26.

Table 2-9 Maximum flap-wise displacements at the blade tip under different rotor velocities (Unit: m)

Location	Ω=0.84 rad/s	Ω=1.27 rad/s	Ω=1.68 rad/s
Tip of blade 1	1.186	1.231	1.352
Tip of blade 2	1.124	1.648	1.773
Tip of blade 3	1.155	1.529	1.984

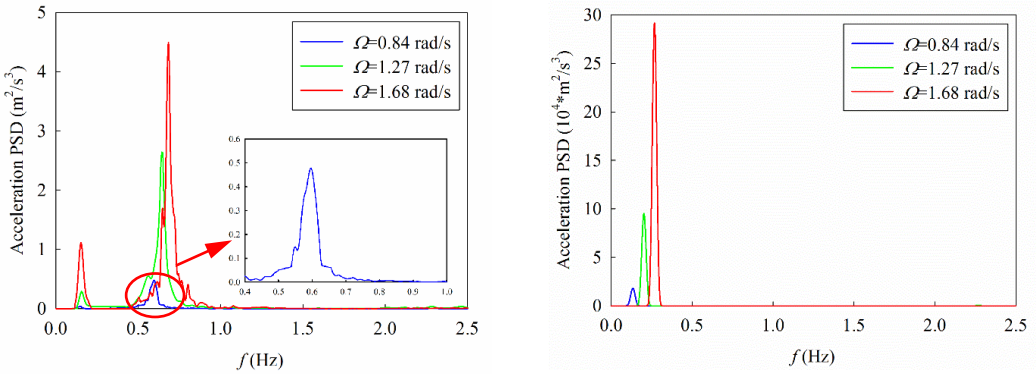

(a) flap-wise (b) edgewise

Figure 2-31 Flap-wise and edgewise acceleration PSDs at the tip of blade 2 under different rotor velocities

Figure 2-31 shows the PSDs of the acceleration responses at the tip of blade 2 in the flap-wise and edgewise directions. As shown in Figure 2-31(a), the first peak corresponding to the first vibration frequency of the tower (0.154 Hz) is not influenced by the rotor velocity, while the second peak corresponds to the first flap-wise pitch vibration mode of the blades and they are 0.549, 0.565 and 0.644 Hz respectively when Ω=0.84, 1.27 and 1.68 rad/s; the third peak is related to the first collective flap vibration mode of the blades, which are 0.598, 0.647 and 0.684 Hz respectively. As shown in Figure 2-31(b), only one obvious peak occurs and the frequencies are 0.134, 0.202 and 0.267 Hz respectively, which are the rotor velocities (0.84, 1.27 and 1.68rad/s). Figure 2-31 also clearly shows that much more energies are included in the PSD curves with the increment of the rotor velocity, which lead to the larger responses of

the blades in both the flap-wise and edgewise directions as shown in Figure 2-29 and Figure 2-30.

2.5 Conclusions

This chapter carries out numerical studies on the dynamic responses of the NREL 5 MW wind turbine subjected to the combined wind and sea wave loadings. The influences of operational conditions, soil-monopile interaction and rotor velocity on the tower and blades are systematically investigated. Numerical results reveal that:

(1) The maximum displacements at the top of the tower in the fore-aft and side-to-side directions when the wind turbine rotates with a rotor velocity of 1.27 rad/s are 142% and 222% larger than those when the wind turbine is in the parked condition. The peak flap-wise displacement of the blades is about 2.5 times of that of the parked wind turbine. Previous studies by assuming the wind turbines in the parked condition may result in non-conservative structural response estimations and unsafe design of structural components. In the current design codes, safety factors are normally used to account for the uncertainties and variabilities in loads, analysis methods and the importance of structural components for the wind turbines (IEC, 2005, 2009). It will be interesting to develop a uniform safety factor that can be used in the operating response estimation based on the parked results. However, more comprehensive research works are needed.

(2) The vibration frequencies of the tower are significantly decreased when SSI is considered, while SSI only marginally affects the natural frequencies of the blades. The out-of-rotor-plane displacement responses of the tower and blades are substantially influenced by SSI. However, SSI has a negligible effect on the displacements of the blades in the edgewise direction.

(3) The out-of-rotor-plane displacements of the tower and blades increase with the increment of the rotor velocity. The displacements of the blades in the edgewise direction increase slightly when the rotor velocity becomes larger.

It should be noted that wind is the dominant load in the present study by comparing Figure 2-9 with Figure 2-15. Moreover, sea wave is applied near to the bottom of the structure, the influence of the sea wave load on the structural responses is less evident compared to the wind load. When the wind turbine is located in the medium to deep water, the effect of the sea wave load might be obvious. Investigation of the influence of water depth on the structural responses is out of the scope of the present study. Furthermore, all the above conclusions are obtained based on the latest NREL 5 MW wind turbine, which is the largest wind turbine in the world currently. These conclusions may only be applicable to this group of wind turbines. To apply

the present results in engineering practice and to guide the designs for the whole wind turbine groups (i.e. including the small and medium groups of wind turbines as well), more comprehensive analyses are needed.

2.6 References

Andersen, L. (2010). Assessment of lumped-parameter models for rigid footings. *Computers & Structures*, *88*(23), 1333-1347.

Andersen, L. V., Vahdatirad, M., Sichani, M. T., & Sørensen, J. D. (2012). Natural frequencies of wind turbines on monopile foundations in clayey soils-A probabilistic approach. *Computers and Geotechnics*, *43*, 1-11.

American Petroleum Institute (API). (2014). Petroleum and natural gas industries-specific requirements for offshore structures. Part 4-geotechnical and foundation design considerations ISO 19901-4:2003 (Modified); 2011.

Arany, L., Bhattacharya, S., Macdonald, J. H., & Hogan, S. J. (2016). Closed form solution of Eigen frequency of monopile supported offshore wind turbines in deeper waters incorporating stiffness of substructure and SSI. *Soil Dynamics and Earthquake Engineering*, *83*, 18-32.

Ashour, M., Norris, G., & Pilling, P. (1998). Lateral loading of a pile in layered soil using the strain wedge model. *Journal of Geotechnical and Geoenvironmental Engineering*, *124*(4), 303-315.

Bazeos, N., Hatzigeorgiou, G., Hondros, I., Karamaneas, H., Karabalis, D., & Beskos, D. (2002). Static, seismic and stability analyses of a prototype wind turbine steel tower. *Engineering Structures*, *24*(8), 1015-1025.

Benowitz, B. A., & Deodatis, G. (2015). Simulation of wind velocities on long span structures: A novel stochastic wave based model. *Journal of Wind Engineering and Industrial Aerodynamics*, *147*, 154-163.

Bhattacharya, S., & Adhikari, S. (2011). Experimental validation of soil-structure interaction of offshore wind turbines. *Soil Dynamics and Earthquake Engineering*, *31*(5), 805-816.

Bi, K., & Hao, H. (2012). Modelling and simulation of spatially varying earthquake ground motions at sites with varying conditions. *Probabilistic Engineering Mechanics*, *29*, 92-104.

Bi, K., & Hao, H. (2016). Using pipe-in-pipe systems for subsea pipeline vibration control. *Engineering Structures*, *109*, 75-84.

Bisoi, S., & Haldar, S. (2014). Dynamic analysis of offshore wind turbine in clay considering soil-monopile-tower interaction. *Soil Dynamics and Earthquake Engineering*, *63*, 19-35.

Bisoi, S., & Haldar, S. (2015). Design of monopile supported offshore wind turbine in clay considering dynamic soil-structure-interaction. *Soil Dynamics and Earthquake Engineering*, *73*, 103-117.

Burton, T., Sharpe, D., Jenkins, N., & Bossanyi, E. (2011). Wind energy handbook 2nd ed. John Wiley & Sons.

Chen, J., & Georgakis, C. T. (2013). Tuned rolling-ball dampers for vibration control in wind turbines. *Journal of Sound and Vibration*, *332*(21), 5271-5282.

Chopra, A. K. (2012). Dynamics of structures 4th ed. New Jersey: Prentice Hall.

Colwell, S., & Basu, B. (2009). Tuned liquid column dampers in offshore wind turbines for structural control. *Engineering Structures*, *31*(2), 358-368.

Damgaard, M., Zania, V., Andersen, L. V., & Ibsen, L. B. (2014). Effects of soil-structure interaction on real time dynamic response of offshore wind turbines on monopiles. *Engineering Structures*, *75*, 388-401.

Det Norske Veritas (DNV). (2010). DNV-RP-C205: Environmental conditions and environmental loads. Norway: DNV.

Det Norske Veritas (DNV). (2014). DNV-OS-J101: Design of offshore wind turbine structures. Copenhagen, Denmark: DNV.

Fitzgerald, B., & Basu, B. (2014). Cable connected active tuned mass dampers for control of in-plane vibrations of wind turbine blades. *Journal of Sound and Vibration*, *333*(23), 5980-6004.

Fitzgerald, B., & Basu, B. (2016). Structural control of wind turbines with soil structure interaction included. *Engineering Structures*, *111*, 131-151.

Hacıefendioğlu, K. (2012). Stochastic seismic response analysis of offshore wind turbine including fluid-structure-soil interaction. *The Structural Design of Tall and Special Buildings, 21*(12), 867-878.

Hansen, M. O. L. (2008). Aerodynamics of wind turbines 2nd ed. London: Earthscan.

Hao, H., Oliveira, C., & Penzien, J. (1989). Multiple-station ground motion processing and simulation based on SMART-1 array data. *Nuclear Engineering and Design*, *111*(3), 293-310.

Harte, M., Basu, B., & Nielsen, S. R. K. (2012). Dynamic analysis of wind turbines including soil-structure interaction. *Engineering Structures*, *45*, 509-518.

Hasselmann, K., Barnett, T., Bouws, E., Carlson, H., Cartwright, D., Enke, K., Walden, H. (1973). Measurements of wind-wave growth and swell decay during the Joint North Sea Wave Project (JONSWAP). Hamburg: Deutches Hydrographisches Institut.

Hu, W., Thöns, S., Rohrmann, R. G., Said, S., & Rücker, W. (2015). Vibration-based structural health monitoring of a wind turbine system. Part I: Resonance phenomenon. *Engineering Structures*, *89*, 260-272.

Huang, G., Liao, H., & Li, M. (2013). New formulation of Cholesky decomposition and applications in stochastic simulation. *Probabilistic Engineering Mechanics*, *34*, 40-47.

IEC 61400-1. (2005). Wind turbines-Part 1: design requirements 3rd ed. Geneva (Switzerland): International Electrotechnical Commission.

IEC 61400-3. (2009). Wind turbines-Part 3: design requirements for offshore wind turbines 1st ed. Geneva (Switzerland): International Electrotechnical Commission.

Jonkman, J., Butterfield, S., Musial, W., & Scott, G. (2009). Definition of a 5-MW reference wind turbine for offshore system development. (Technical Report No. NREL/TP-500-38060). Golden, CO: National Renewable Energy Laboratory.

Jonkman, J., & Buhl Jr, M. L. (2005). FAST user's guide. Golden, CO: National Renewable Energy Laboratory.

Kim, D. H., Lee, S. G., & Lee, I. K. (2014). Seismic fragility analysis of 5 MW offshore wind turbine. *Renewable Energy*, *65*, 250-256.

Kjørlaug, R. A., & Kaynia, A. M. (2015). Vertical earthquake response of megawatt-sized wind turbine with soil-structure interaction effects. *Earthquake Engineering & Structural Dynamics*, *44*(13), 2341-2358.

Kooijman, H., Lindenburg, C., Winkelaar, D., van der Hooft, E. (2003). Aero-elastic modelling of the DOWEC 6 MW pre-design in PHATAS DOWEC-F1W2-HJK-01-046/9.

Kuo, Y. S., Achmus, M., & Abdel-Rahman, K. (2011). Minimum embedded length of cyclic horizontally loaded monopiles. *Journal of Geotechnical and Geoenvironmental Engineering*, *138*(3), 357-363.

Lavassas, I., Nikolaidis, G., Zervas, P., Efthimiou, E., Doudoumis, I., & Baniotopoulos, C. (2003). Analysis and design of the prototype of a steel 1-MW wind turbine tower. *Engineering Structures*, *25*(8), 1097-1106.

Lombardi, D., Bhattacharya, S., & Wood, D. M. (2013). Dynamic soil-structure interaction of monopile supported wind turbines in cohesive soil. *Soil Dynamics and Earthquake Engineering*, *49*, 165-180.

Mostafa, Y. E., & El Naggar, M. H. (2004). Response of fixed offshore platforms to wave and current loading including soil-structure interaction. *Soil Dynamics and Earthquake Engineering*, *24*(4), 357-368.

Murtagh, P. J., Basu, B., & Broderick, B. M. (2005). Along-wind response of a wind turbine tower with blade coupling subjected to rotationally sampled wind loading. *Engineering Structures*, *27*(8), 1209-1219.

Prowell, I., Elgamal, A., Uang, C. M., Enrique Luco, J., Romanowitz, H., & Duggan, E. (2014). Shake table testing and numerical simulation of a utility-scale wind turbine including operational effects. *Wind Energy*, *17*(7), 997-1016.

Prowell, I., Veletzos, M., Elgamal, A., & Restrepo, J. (2009). Experimental and numerical seismic response of a 65 kW wind turbine. *Journal of Earthquake Engineering*, *13*(8), 1172-1190.

Quilligan, A., O'Connor, A., & Pakrashi, V. (2012). Fragility analysis of steel and concrete wind turbine towers. *Engineering Structures*, *36*, 270-282.

Santangelo, F., Failla, G., Santini, A., & Arena, F. (2016). Time-domain uncoupled analyses for seismic assessment of land-based wind turbines. *Engineering Structures*, *123*, 275-299.

Sorensen, R. M. (2005). Basic coastal engineering. New York: Springer Science & Business Media.

Staino, A., & Basu, B. (2013). Dynamics and control of vibrations in wind turbines with variable rotor speed. *Engineering Structures*, *56*, 58-67.

Valamanesh, V., & Myers, A. (2014). Aerodynamic damping and seismic response of horizontal axis wind turbine towers. *Journal of Structural Engineering*, *140*(11), 04014090.

Yuan, C., Chen, J., Li, J., & Xu, Q. (2017). Fragility analysis of large-scale wind turbines under the combination of seismic and aerodynamic loads. *Renewable Energy*, *113*, 1122-1134.

Zuo, H., Bi, K., & Hao, H. (2017). Using multiple tuned mass dampers to control offshore wind turbine vibrations under multiple hazards. *Engineering Structures*, *141*, 303-315.

CHAPTER 3 INFLUENCE OF EARTHQUAKE GROUND MOTION MODELLING ON THE DYNAMIC RESPONSES OF OFFSHORE WIND TURBINES

ABSTRACT[2]

Offshore wind turbines (OWTs) are more and more widely used to produce electrical energy nowadays. Besides the constant wind and wave loads, earthquake excitation can be another important vibration source to the OWTs since many OWTs have been/will be constructed in the seismic prone areas. Extensive research works have been carried out to understand the dynamic behaviours of OWTs when they are subjected to multi-hazards (e.g. the simultaneous wind, wave and/or earthquake loadings). However, when seismic excitations are considered, the onshore earthquake records are normally used as inputs in the analyses due to the lack of offshore data and the difficulty in synthesizing the offshore seismic motions. This practice may lead to inaccurate structural response estimations since it is well known that the sea water can significantly suppress the seafloor vertical motions near the P wave resonant frequencies of the sea water layer, which in turn results in the different characteristics of onshore and offshore earthquake recordings. Moreover, the earthquake motions along the pile of OWTs are different from those at the ground surface, i.e. the earthquake motions vary with the soil depth. Recently, a method to stochastically simulate the earthquake ground motions on the offshore site was proposed, in which the influence of sea water layer was considered and the earthquake motions at any soil depth could be obtained. This chapter carries out numerical simulations on the dynamic behaviours of OWTs subjected to the combined wind, wave and earthquake loadings, and the depth-varying offshore seismic motions are used as inputs in the analyses. The seismic responses of OWTs obtained from the onshore and offshore earthquake motions are calculated and compared. The influence of depth-varying ground motions on the dynamic responses of OWTs is discussed.

3.1 Introduction

Offshore wind turbines (OWTs) are becoming an important contributor to the electricity generation. The growth and expansion of offshore wind farms increased rapidly in the past decade around the world (GWEC, 2018). The power generated by the wind turbine is

[2] This chapter was published in *Soil Dynamics and Earthquake Engineering* with the full bibliographic citation as follows:
Zuo, H., Bi, K., Hao, H. & Li, C. (2019). Influence of earthquake ground motion modelling on the dynamic responses of offshore wind turbines. *Soil Dynamics and Earthquake Engineering*, *121*, 151-167. https://doi.org/10.1016/j.soildyn.2019.03.008.

proportional to the wind speed and rotor diameter, which leads to the multi-megawatt wind turbines with large rotor diameter and slender tower for allowing more wind resource in the marine areas to be captured throughout the lifetimes of OWTs. These structures are very flexible and lightly damped since they are usually constructed with light-weight and high-strength materials, and the fundamental vibration periods of OWTs are generally larger than 3.0 s (Bhattacharya & Goda, 2016). As such, they are vulnerable to the external excitations, like wind and wave loads, which constantly act on the OWTs. Moreover, many wind turbines are located in the earthquake prone areas such as China, Japan and the United States (Katsanos et al., 2016). Seismic load can be another possible vibration source in these regions. In other words, OWTs might be subjected to the simultaneous wind, wave and earthquake loads. Some design codes (DNV, 2014; IEC, 2009) clearly stated that wind turbines need to be designed to resist seismic load when they are located in the regions with high seismic activities. These external vibration sources can lead to excessive vibrations to the OWTs, which can slow down the wind energy output, reduce the fatigue life of the structural components or even result in the structural collapse under extreme conditions. To mitigate these adverse vibrations, various control strategies have been proposed by different researchers (Sun & Jahangiri, 2018; Zhang et al., 2016; Zhao et al., 2018; Zuo et al., 2017, 2019).

Extensive research works have been conducted to investigate the structural responses of wind turbines subjected to the wind, wave and/or seismic loads (Alati et al., 2015; Bisoi & Haldar, 2014; De Risi et al., 2018; Díaz & Suárez, 2014; Hacıefendioğlu, 2012; Kaynia, 2018; Kim et al., 2014; Kjørlaug & Kaynia, 2015; Patil et al., 2016; Prowell et al., 2009, 2014; Santangelo et al., 2016; Wang et al., 2018; Witcher, 2005; Zuo et al., 2017, 2018). However, it should be noted that earthquake ground motions at the onshore site were normally used as inputs to calculate the seismic responses of OWTs (Alati et al., 2015; De Risi et al., 2018; Hacıefendioğlu, 2012; Kaynia, 2018; Kim et al., 2014; Kjørlaug & Kaynia, 2015; Patil et al., 2016; Wang et al., 2018; Zuo et al., 2017) due to the lack of seafloor earthquake recordings and the difficulty to predict seafloor seismic motions. These approaches may lead to inaccurate structural response estimations since the characteristics of seafloor seismic motions (especially the vertical component) are different from those of the onshore ground motions due to the fact that the existence of sea water can significantly suppress the vertical seafloor seismic motions near the P wave resonant frequencies of the sea water layer (Li et al., 2015). Moreover, the sea water layer can also indirectly influence the seafloor motions by changing the water saturation level and pore pressure of subsea soil layers (Yang & Sato, 2000). Recently, Li et al. (2015) theoretically derived the ground motion transfer functions at the offshore site by taking the influence of sea water layer into consideration based on the fundamental hydrodynamic equations and one-dimensional (1D) wave propagation theory, and proposed methods to

stochastically simulate the offshore ground motions at the ground surface and different soil depths (i.e. depth-varying seismic motions) of a single site (Li et al., 2018c), and spatially varying offshore ground motions at multiple sites (Li et al., 2017, 2018a). Based on the theoretical offshore site transfer function, Bi et al. (2017) compared the seismic responses of buried onshore and offshore pipelines. The analytical results revealed the sea water can significantly suppress the vertical motion induced bending stress and slightly increase the axial stress (Bi et al., 2017). Li et al. (2018b) investigated the seismic fragility of sea-crossing cable-stayed bridges by using the onshore and offshore seismic motions, and the influence of depth-varying ground motions on the seismic responses was also discussed. The numerical results showed that the component fragility of the bridge can be underestimated by up to 40% by using onshore seismic motions, and considering the depth-varying ground motions can impact both the component and system fragilities of the bridge (Li et al., 2018b). For the OWT, due to its high-rising structural layout, its dynamic responses may be very sensitive especially to the vertical earthquake component. However, to the best knowledge of the authors, no open literature reports the dynamic responses of OWTs by using offshore seismic motions in the analysis.

Furthermore, due to the simplicity and lower construction cost at the shallow sea, the monopile is commonly designed as the foundation of OWTs, and Arany et al. (2017) introduced a 10-step method to design the monopiles of OWTs to resist wind and wave loads. The typical monopile is a long hollow steel member, which inserted into the sea water and subsea soil layers. The interaction between the monopile and surrounding soil is inevitable and can alter the vibration frequencies of OWTs, which in turn affects the dynamic behaviours of OWTs (Zuo et al., 2018). In the seismic analyses of OWTs, the seismic motions along the height of the monopile were assumed to be the same as those at the seabed level in almost all the previous studies, and the variation of the ground motions along the monopile was not considered. In reality, the seismic motions at different soil depths are different because of the ground motion amplification effect of the soil. To consider the influence of depth-varying earthquake motions, only Kim et al. (2014) considered two types of earthquake loadings (uniform and depth-varying) on the seismic fragilities of an OWT, and they found that the fragility curves might be underestimated if the uniform earthquake loadings are applied compared to the depth-varying motions. However, it should be noted that the influence of sea water was not considered in this study (Kim et al., 2014).

Moreover, in the previous studies, the wind turbines were usually assumed in the parked condition, and the blades were simplified as a lumped mass located at the top of the tower (Bisoi & Haldar, 2014; De Risi et al., 2018; Hacıefendioğlu, 2012; Patil et al., 2016; Wang et al., 2018; Zuo et al., 2017). The influence of the rotation of the blades was therefore not

considered in these studies. In reality, the wind loads on the blades are related to the geometrical characteristics and rotational velocity of the blades (Hansen, 2008). In addition, the centrifugal stiffness induced by the rotation of the blades can increase the stiffness and vibration frequencies of the blades compared to those in the parked condition (Murtagh et al., 2005), which in turn may indirectly affect the structural responses of OWTs.

As an extension of the authors' previous study (Zuo et al., 2018), the dynamic responses of a typical OWT (the NREL 5 MW wind turbine) subjected to the combined wind, wave and earthquake loadings are numerically investigated in the present study. The detailed three-dimensional (3D) finite element (FE) model of the wind turbine is developed in ABAQUS, and the influence of the rotating blades is considered. In particular, special emphasises are placed on investigating the influences of using onshore ground motions to represent offshore earthquake motions and depth-varying seismic motions on the responses of OWTs. The dynamic behaviours of the wind turbine subjected to different types of earthquake excitations together with the wind and wave loads are compared and discussed in detail. The structure of this chapter is organized as follows: Section 3.3 briefly introduces the NREL 5 MW wind turbine and the development of the FE model; Section 3.4 presents the simulation of wind, wave loads and depth-varying offshore earthquake motions; the numerical results are discussed in Section 3.5 and some concluding remarks are made in Section 3.6.

3.2 Numerical modelling

The NREL 5 MW wind turbine is selected as an example in the present study since its properties are well defined in the open literature (Jonkman et al., 2009). The total length of the monopile foundation is 60 m, in which 20 m and 30 m are in the sea water and seabed respectively and another 10 m is above the mean sea level. The height of the tower from the mean sea level to the hub centre is 90 m. The length of the blade is 61.5 m and the radius of the hub is 1.5 m, the distance from the hub centre to the blade tip is therefore 63 m. The outer diameters at the bottom and top of the tower are 6 m and 3.87 m with the wall thickness of 0.027 m and 0.019 m respectively. The wall thickness of the blade is not given in (Jonkman et al., 2009), a uniform thickness is assumed to ensure the mass of the blade is the same as that defined in (Jonkman et al., 2009), and this thickness is calculated as 0.019 m. More detailed information regarding the wind turbine is tabulated in Table 3-1.

Table 3-1 Properties of the NREL 5 MW wind turbine (Kooijman et al., 2003; Jonkman et al., 2009)

Blade	Rotor diameter	126 m
	Hub height	90 m
	Cut-in, rated and cut-out wind speed	3 m/s, 11.4 m/s, 25 m/s
	Cut-in and rated rotor speed	6.9 rpm, 12.1 rpm
	Length	61.5 m
	Overall (integrated) mass	17,740 kg
	Structural damping ratio	0.5%
Hub and Nacelle	Hub diameter	3 m
	Hub mass	56,780 kg
	Nacelle mass	240,000kg
Tower	Height above water	87.6 m
	Bottom and top outer diameters	6 m, 3.87 m
	Bottom and top wall thicknesses	0.027 m, 0.019 m
	Overall (integrated) mass	347,460 kg
	Structural damping ratio	1%
Monopile	Total length	60 m
	Outer diameter	6 m
	Wall thickness	0.060 m

3.2.1 Finite element model

The detailed 3D FE model of the NREL 5 MW wind turbine is developed in ABAQUS. The tower and monopile above the seabed are modelled by shell elements, while the monopile inserted into the seabed is modelled by beam elements. To ensure the deformation continuity at the seabed level, the node of the beam element and the nodes of the shell elements are coupled with each other. A tie constraint is applied to connect the cross sections at the bottom of the tower and the top of the monopile to make sure the deformations are the same at the connection between the tower and monopile. The blades are also directly modelled by the shell elements and a hinge connection between the top of the tower and the root of the blades is defined and the rotational degree-of-freedom (DOF) in the out-of-rotor-plane direction (Y direction shown in Figure 3-7) is released to consider the rotation of the blades. It should be noted that the rotation of the blades should be only partially released in engineering practice in order to avoid the rigid body motion. In the numerical simulations, a uniform angular velocity is applied to the blades as a boundary condition when the operating condition is considered, and no rigid body motion problem will occur. For the hub and nacelle, only the masses are considered, and they are modelled by the point mass element lumped at the top of the tower. Figure 3-1 shows the FE model of the wind turbine, in which the three blades are labelled as #1 to #3 in an anticlockwise direction.

The materials of the tower, blades and monopile are assumed as ideal elastic-plastic materials and the detailed properties are tabulated in Table 3-2. For the monopile in the sea water, the vibrating monopile can impart an acceleration to the surrounding sea water. The added mass method is adopted in the present study to consider the interaction between the monopile and sea water (Zuo et al., 2018).

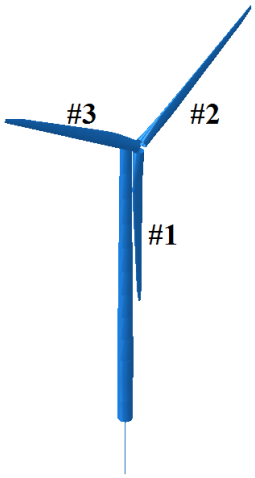

Figure 3-1 FE model of the NREL 5 MW OWT in ABAQUS

Table 3-2 Material properties of the NREL 5 MW wind turbine

Component	Material	Density (kg/m^3)	Young's modulus (GPa)	Poisson's ratio	Yield strength (MPa)	Plastic strain
Blade	Polyester	1850	38	0.3	700	0.02
Tower	Steel	8500	210	0.3	235	0.01
Monopile	Steel	7850	210	0.3	235	0.01

3.2.2 SSI modelling

The interaction between the monopile foundation and the subsea soil layers may significantly influence the vibration characteristics of OWTs. To more accurately analyse the structural responses of OWTs, soil-structure interaction (SSI) should be considered. Three different methods are widely adopted to simulate SSI: (1) the soil is directly modelled by solid elements in the FE model and the Mohr-Coulomb contact between the monopile and soil layers is used to consider the interaction (Fitzgerald & Basu, 2016); (2) the monopile foundation inserted into the seabed is simplified as the translational and rotational springs (Bhattacharya & Adhikari, 2011); and (3) the nonlinear soil springs attached to the monopile are used to consider the interaction (Bisoi & Haldar, 2014; Boulanger et al., 1999; Kim et al., 2014; Rendon & Manuel, 2014; Wang et al., 2018).

In the present study, the nonlinear soil springs are adopted to consider SSI due to its simplicity. In the numerical model, the lateral resistances provided by the soil layers against the monopile foundation movements are described by the springs in the directions parallel and perpendicular to the rotor plane (the *p-y* spring in Figure 3-2), and the vertical springs are defined to simulate the axial friction (the *t-z* spring) and tip bearing capacity (the *Q-z* spring). The space between two soil spring locations is selected as 3 m in the present study. The length of the monopile foundation inserted into the soil layers is 30 m, 11 groups of spring are therefore included in the FE model, and they are modelled by spring elements in ABAQUS. Figure 3-2 shows the

monopile in the seabed with soil springs. The properties of the soil springs can be depicted by the *p-y, t-z* and *Q-z* curves (API, 2014; DNV, 2014), which depend on the soil properties at the corresponding depth. Figure 3-3 shows the *p-y, t-z* and *Q-z* curves at different depths ranging from 3-30 m with an increment of 12 m below the seabed with the soil properties shown in Figure 3-7. The detailed calculations of these curves are out of the scope of this study, interested readers can refer to (Zuo et al., 2018) for more information.

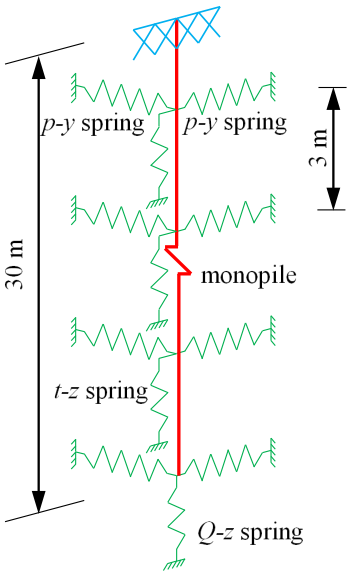

Figure 3-2 SSI modelling

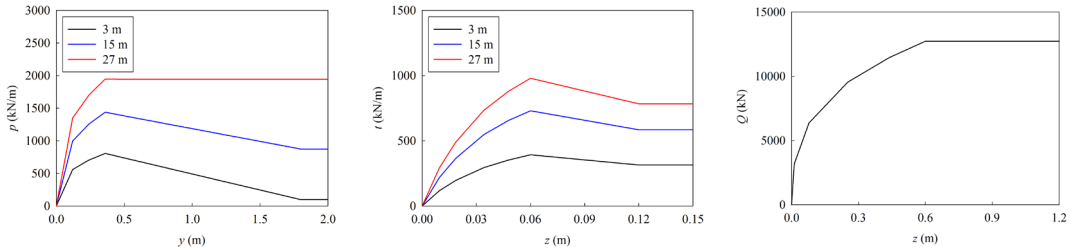

(a) *p-y* curve (b) *t-z* curve (c) *Q-z* curve

Figure 3-3 The properties of soil springs at different depths

It should be noted that the soil may lose part of its stiffness during earthquake shaking especially when liquefaction occurs (Dash et al., 2009, 2017), and a gap might be formed between the monopile and surrounding soil under cyclic loadings (Boulanger et al., 1999). This simplified soil spring model adopted in the present study cannot accurately consider these effects, and it in turn may result in slight inaccurate structural response estimations. To more accurately model the interaction between the monopile and surrounding soil, the more refined models proposed by Dash et al. (2009, 2017) and Boulanger et al. (1999) might be good options. On the other hand, it is worth noting that this simplified model provided in the design guides was actually widely adopted in many previous studies (Bisoi & Haldar, 2014; Kim et

al., 2014; Rendon & Manuel, 2014; Wang et al., 2018) to consider the SSI effect of wind turbines. Owing to the primary objective of the present study is to examine the suitability and accuracy of using onshore earthquake ground motions in seismic response analysis of offshore wind farms, instead of SSI effect, the simplified soil spring model is adopted in the analysis to avoid complicating the problem.

3.2.3 Vibration frequencies and damping ratios

The vibration frequencies of the NREL 5 MW wind turbine with the consideration of SSI can be obtained by carrying out an eigenvalue analysis after the soil springs are defined. It is well known that the eigenvalue analysis is a linear procedure, only the initial tangent stiffness of the soil springs will be used in the analysis though the soil springs are not linear as shown in Figure 3-3. Table 3-3 tabulates the vibration frequencies and the corresponding vibration modes. It can be seen that the first mode corresponds to the vibration of the tower in the side-to-side direction with a frequency of 0.195 Hz, and the first mode of the blades is in the out-of-plane direction and the vibration frequency is 0.595 Hz.

Table 3-3 Vibration frequencies of the wind turbine

Mode description	Frequency (Hz)
1st tower side-to-side	0.195
1st tower fore-aft	0.196
1st blade out-of-plane	0.595
1st blade in-plane	1.236
2nd tower fore-aft	1.088
2nd tower side-to-side	1.318

The damping of an OWT is composed of soil damping, hydrodynamic damping, structural damping and aerodynamic damping (Arany et al., 2016). The soil and hydrodynamic damping are assumed as 5% and 1.5% respectively in the present study (Li et al., 2018b). The structural damping ratios of the tower and blades are 1% and 0.5% as tabulated in Table 3-1. The aerodynamic damping of the operating wind turbine results from the relative velocity between the rotating blades and surrounding wind, and is assumed as 3.5% in the out-of-plane direction as suggested by Bisoi and Haldar (2014). Previous studies (Valamanesh & Myers, 2014) also revealed that the aerodynamic damping is almost zero when the wind turbine is in the parked condition. The same assumption is adopted in the present study. Summing up all the components, the damping ratio of the tower is 7.5%. The value is 4% in the out-of-plane direction for the rotating blades and 0.5% for the parked blades.

3.3 Simulation of external vibration sources

In the present study, the dynamic responses of the wind turbine subjected to the simultaneous wind, wave and earthquake loads are investigated. All these loadings are stochastically simulated based on the sophisticated simulation techniques and are briefly introduced in the following sections. More detailed information regarding the wind and wave load simulation can be found in (Zuo et al., 2018), and the details for the earthquake inputs can refer to (Li et al., 2015).

3.3.1 Wind and wave loads

The wind load on the tower is composed of a mean and a fluctuating component. The fluctuating wind loads at different locations along the height of the tower are different but with certain similarities. The Kaimal spectrum is adopted to calculate the power spectral density (PSD) of the fluctuating wind speed along the tower, and the similarities are described by a spatial coherency loss function. For simplicity, the tower is divided into nine segments and the wind load is assumed to be the same within each segment. Figure 3-4 shows the wind loads on the top segment when the mean wind speeds at the hub height are 11.4 m/s and 25 m/s respectively, which corresponds to the rated and cut-out speeds of the NREL 5 MW wind turbine, i.e. when the wind turbine is in the operating and parked conditions. The wind loads in the other segments are not presented for conciseness.

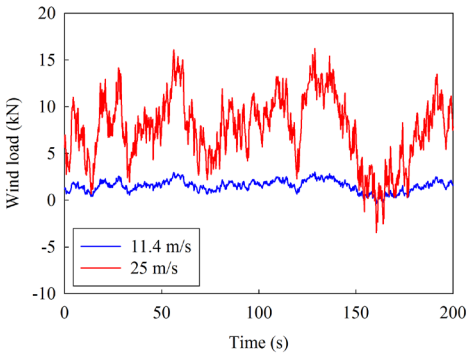

Figure 3-4 Wind load time histories at the tower top when the wind turbine is in the operating (11.4 m/s) and parked (25 m/s) conditions

The wind loads on the blades are different from those on the tower. They are related to the wind speed, rotational velocity and geometrical configurations of the blades. In the present study, the blade element momentum (BEM) method (Hansen, 2008) is used to simulate the wind loads on the blades. In this method, it is assumed that no interaction between different sections along the length of the rotor, the blades therefore can be divided into several elements and the wind load on each element can be calculated separately.

In the simulation of wind loads on the blades, the relative wind speed v_{rel} on each element of the blades should be defined first, which is given by

$$v_{\mathrm{rel}}(r) = \sqrt{(\bar{v}(1-a) + v_{\mathrm{f}})^2 + \left(\Omega r(1+a')\right)^2} \tag{3.1}$$

where r is a radial distance of the element from the hub centre, a and a' are the axial and tangential induction factors respectively, Ω is the rotational velocity in rad/s, and $\bar{v}$ and v_{f} are the mean and fluctuating wind speeds respectively. It should be noted that the oscillation of the blades under external excitations is not considered in Eq. (3.1) since the aerodynamic damping is included in the present study (Valamanesh & Myers, 2014). After the relative wind speed is determined, the lift and drag forces (p_{l} and p_{d} respectively) on each element can be calculated as follows

$$p_{\mathrm{l}}(r) = \frac{1}{2}\rho v_{\mathrm{rel}}^2(r) l(r) C_{\mathrm{lb}} \tag{3.2}$$

$$p_{\mathrm{d}}(r) = \frac{1}{2}\rho v_{\mathrm{rel}}^2(r) l(r) C_{\mathrm{db}} \tag{3.3}$$

in which ρ is the air density, l is the chord length and C_{lb} and C_{db} are the lift and drag coefficients of the blade respectively.

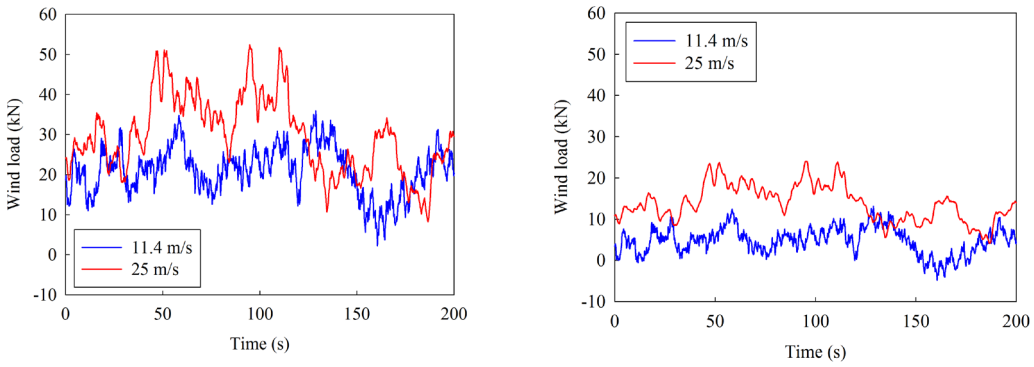

(a) out-of-plane (b) in-plane

Figure 3-5 Out-of-plane and in-plane wind load time histories on blade #2

Figure 3-5 shows the total out-of-plane and in-plane wind loads on blade #2 when the blades are parked (25 m/s) and rotating with a uniform velocity of 12.1 rounds per minute (rpm) and the wind speed at the hub height is 11.4 m/s.

For the wave load on the monopile, the JONSWAP spectrum is used to estimate the sea surface elevation and it has the following form

$$S_{\eta\eta}(f) = \alpha_P g^2 (2\pi)^{-4} f^{-5} exp\left[-\frac{5}{4}\left(\frac{f_m}{f}\right)^4\right] \gamma^{exp\left[-\frac{(f-f_m)^2}{2\sigma^2 f_m^2}\right]} \tag{3.4}$$

$$\alpha_P = 0.076(Fg/v_{10}^2)^{-0.22} \tag{3.5}$$

$$f_m = 11(v_{10}F/g^2)^{-1/3}/\pi \tag{3.6}$$

$$\sigma = \begin{cases} 0.07 & f \le f_m \\ 0.09 & f > f_m \end{cases} \tag{3.7}$$

where g is the gravitational acceleration, γ is the peak enhancement factor, F is the fetch length and v_{10} is the mean wind speed at 10 m above the sea surface.

The sea wave length is normally larger than the dimension of the monopile, Morison formula is then adopted to calculate the wave load. Similar to the tower, the monopile in the sea water is equally divided into two segments. Figure 3-6 shows the simulated wave load time histories at the mean sea level when the mean wind speeds at the hub height are 11.4 m/s and 25 m/s respectively.

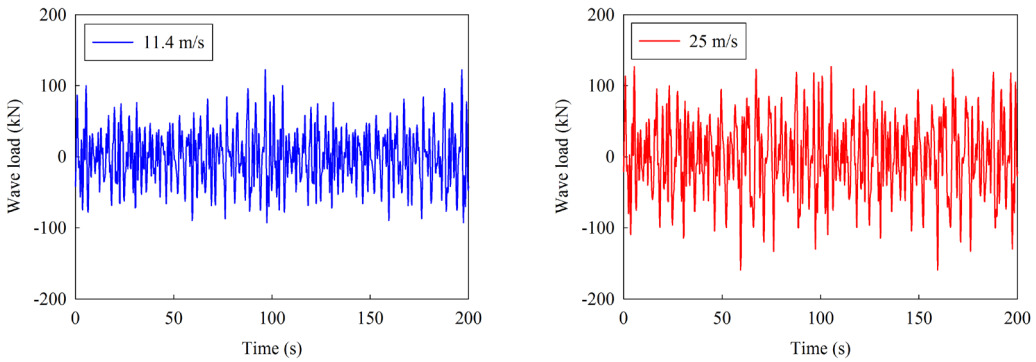

(a) 11.4 m/s (b) 25 m/s

Figure 3-6 Wave load time histories at the mean sea level

3.3.2 Depth-varying offshore earthquake ground motions

The 1D wave propagation theory proposed by Wolf (1985) has been widely used to investigate the influence of multiple soil layers on the seismic wave propagation (Bi & Hao, 2012). In this theory, it is assumed that the seismic waves, which are composed of out-of-plane shear horizontal (SH) wave and in-plane combined P and shear vertical (SV) waves, propagate into the site with an incident angle at the base rock and soil layer interface. The dynamic equilibrium equations of the site in the frequency domain then can be expressed by

$$[K_{\mathrm{SH}}][u_{\mathrm{SH}}] = [F_{\mathrm{SH}}] \text{ and } [K_{\mathrm{P-SV}}][u_{\mathrm{P-SV}}] = [F_{\mathrm{P-SV}}] \tag{3.8}$$

where $[K_{\mathrm{SH}}]$ and $[K_{\mathrm{P\text{-}SV}}]$ are the out-of-plane and in-plane stiffness matrices of the site respectively, $[u_{\mathrm{SH}}]$ and $[F_{\mathrm{SH}}]$ are the out-of-plane displacements and load vector corresponding to the incident SH wave, and $[u_{\mathrm{P\text{-}SV}}]$ and $[F_{\mathrm{P\text{-}SV}}]$ are the in-plane displacements and load vector of the combined P and SV waves.

For the offshore site, the sea water can significantly suppress the seafloor vertical motion near the P wave resonant frequencies of the sea water layer (Li et al., 2015). Moreover, the sea water can indirectly influence the seafloor motions by changing the water saturation level and pore pressure of the subsea soil layers, which in turn can significantly affect the propagation of seismic P wave at the offshore site (Yang & Sato, 2000). These direct and indirect influences of sea water layer, however, could not be considered by the conventional 1D wave propagation theory (Wolf, 1985). Recently, Li et al. (2015) extended this theory and theoretically derived the stiffness of the sea water by taking the direct and indirect influences of sea water into consideration, and further derived the stiffness matrices of the offshore site, i.e. $[K_{SH}]$ and $[K_{P\text{-}SV}]$ in Eq. (3.8).

By solving Eq. (3.8) at every discrete frequency, the relationship of the displacements between the base rock and each soil layer can be formed, and the site transfer functions in the three directions ($|H_X(i\omega)|$, $|H_Y(i\omega)|$ and $|H_Z(i\omega)|$ respectively) at each soil layer can be estimated.

The base rock motions of the offshore and onshore sites are assumed to have the same intensity and frequency contents and are represented by a filtered Tajimi-Kanai function $S_g(\omega)$, the PSD functions of the seismic motions at different soil depths then can be calculated as

$$S_{\mathrm{off},j}(\omega) = S_g(\omega)\left|H_{\mathrm{off},j}(i\omega)\right|^2 \text{ and } S_{\mathrm{on},j}(\omega) = S_g(\omega)\left|H_{\mathrm{on},j}(i\omega)\right|^2 \tag{3.9}$$

in which the subscripts off and on represent the offshore and onshore sites respectively, and j=X, Y and Z are the three different directions. After the PSD functions at different locations are estimated, the corresponding acceleration time histories can be generated based on the traditional spectral representation method (Bi & Hao, 2012; Hao et al., 1989). It should be noted that the generated acceleration time history is a stationary process, to obtain the non-stationary time histories, an envelope function $\zeta(t)$ is normally applied, and the envelope function generally has the following form

$$\zeta(t) = \begin{cases} (t/t_0)^2 & 0 \le t \le t_0 \\ 1 & t_0 < t \le t_n \\ exp[-0.155(t-t_n)] & t_n < t \le T \end{cases} \tag{3.10}$$

in which t_0=2 s and t_n=10 s are adopted.

In the present study, the OWT is located at a typical offshore site with the properties of each soil layer shown in Figure 3-7(a) (Li et al., 2018b, 2018c). In which K, ρ_w and ξ_w are the bulk modulus, density and damping ratio of the sea water respectively. For the soil layers and base rock, G is the shear modulus, ρ_s the density, n the porosity, S_r the degree of saturation, ξ_s the damping ratio and v the Poisson's ratio. For comparison, the onshore site is constructed by removing the sea water layer from the offshore site and the 20 m fully saturated soft clay is

replaced by partially saturated clay with the same thickness, and Figure 3-7(b) shows the soil conditions for the corresponding onshore site.

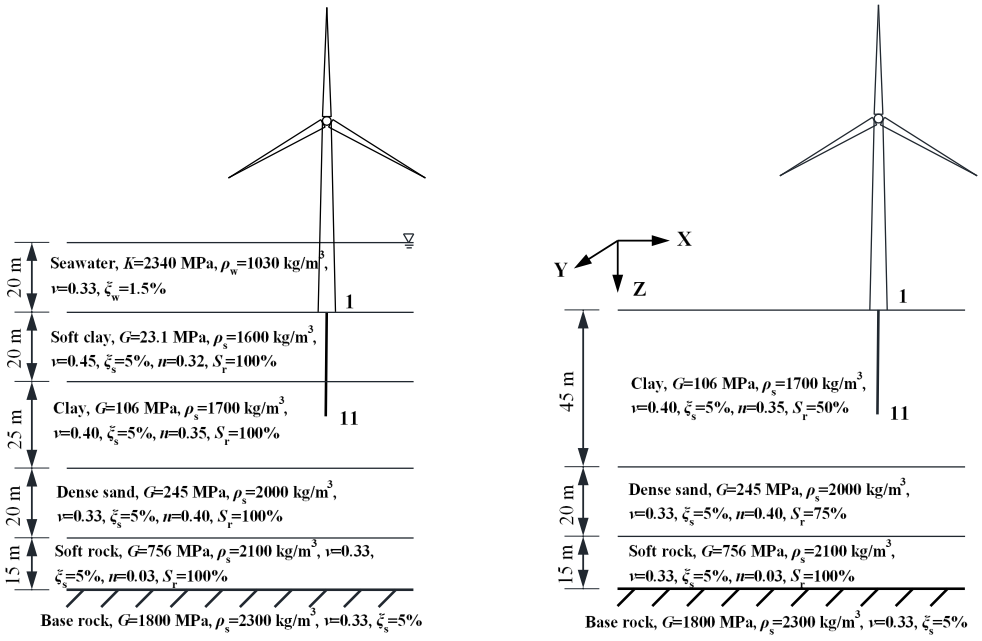

(a) offshore site (b) onshore site

Figure 3-7 The exampled (a) offshore and (b) onshore sites

The filtered Tajimi-Kanai PSD function used to represent the base rock motions has the following form

$$S_{\mathrm{g}}(\omega)=\frac{\omega^4}{\left(\omega_{\mathrm{f}}^2-\omega^2\right)^2+4\xi_{\mathrm{f}}^2\omega_{\mathrm{f}}^2\omega^2}\frac{\omega_{\mathrm{g}}^4+4\xi_{\mathrm{g}}^2\omega_{\mathrm{g}}^2\omega^2}{\left(\omega_{\mathrm{g}}^2-\omega^2\right)^2+4\xi_{\mathrm{g}}^2\omega_{\mathrm{g}}^2\omega^2}\Gamma \tag{3.11}$$

where ω_{f}, ξ_{f} and ω_{g}, ξ_{g} are the central frequencies and damping ratios of the high pass filter and the Tajimi-Kanai PSD function respectively, and Γ is the scaling factor. The parameters of the horizontal motion are assumed as ω_{f}=0.5π rad/s, ω_{g}=10π rad/s, ξ_{f}= ξ_{g}=0.6 and Γ=0.0034 $\mathrm{m^2/s^3}$. These parameters correspond to a ground motion time history with peak ground acceleration (PGA) of 0.2g and duration of T=20 s based on the standard random vibration method (Der Kiureghian, 1980). The corresponding peak ground displacement (PGD) is 0.082 m. The vertical motion on the base rock is also modelled by the filtered Tajimi-Kanai PSD function, but the amplitude is assumed to be 2/3 of the horizontal component.

In the present study, an incident angle of 60° is assumed. With all the above information, the transfer functions of the offshore and onshore sites at different locations can be calculated. Figure 3-8 shows the transfer functions at the ground surface (Point-1 in Figure 3-7) and the end of the monopile (Point-11) on the offshore and onshore sites in the three directions. For the transfer functions at other locations, they are not shown for conciseness. It can be seen from Figure 3-8 that the base rock motions are amplified at a variety of frequencies

corresponding to the respective vibration modes of the local sites. For the transfer function at the ground surface (Point-1), the horizontal transfer functions ($|H_X(i\omega)|$ and $|H_Y(i\omega)|$) at the offshore site are larger than those at the onshore site. This is because the offshore site is much softer than the onshore site due to the soft clay layer as shown in Figure 3-7. It should be noted that S wave cannot propagate in the sea water, so if the soil layers and soil conditions of the offshore and onshore sites are the same, the transfer function in the out-of-plane direction ($|H_Y(i\omega)|$) will be exactly the same. In the present study, due to the soil properties at the first 45 m for the two sites are different, the site transfer functions $|H_Y(i\omega)|$ are different for the two cases. For the transfer functions in the vertical direction ($|H_Z(i\omega)|$), the values obtained from the onshore site are, however, much larger than those from the offshore site due to the suppression effect from the sea water layer as discussed above. As a result, an almost zero value appears at the P wave resonant frequency of the sea water layer (20.95 Hz). At Point-11, the differences of the transfer functions between the offshore and onshore sites become less evident compared to Point-1, and the values are smaller than those at Point-1. This is because Point-11 is closer to the base rock compared to Point-1, the site amplification effect is therefore less evident.

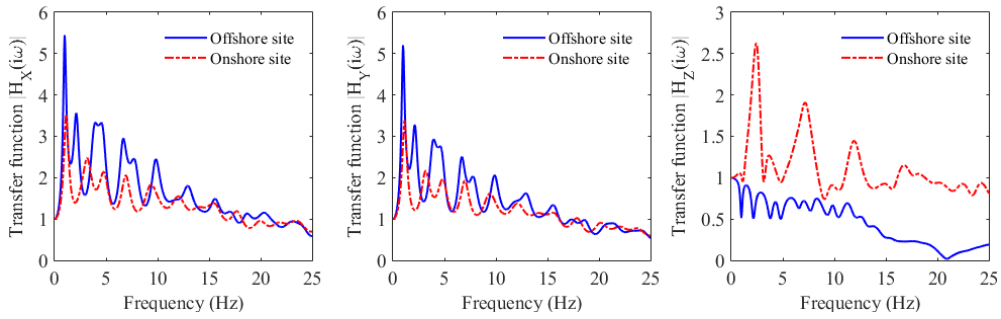

(a) transfer functions at Point-1

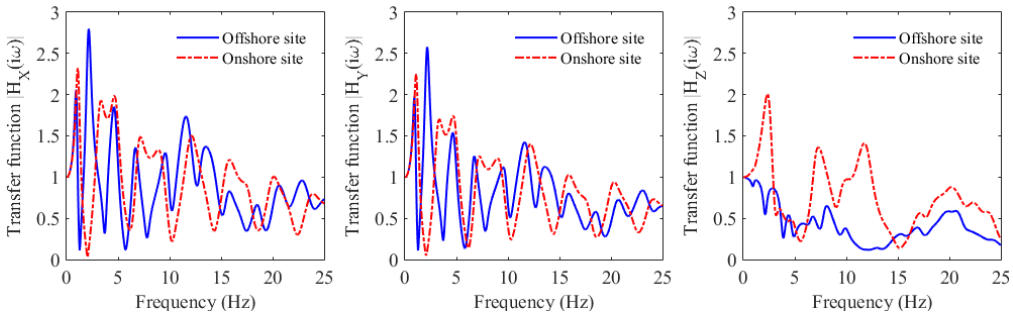

(b) transfer functions at Point-11

Figure 3-8 Ground motion transfer functions in the X, Y and Z directions at the offshore and onshore sites

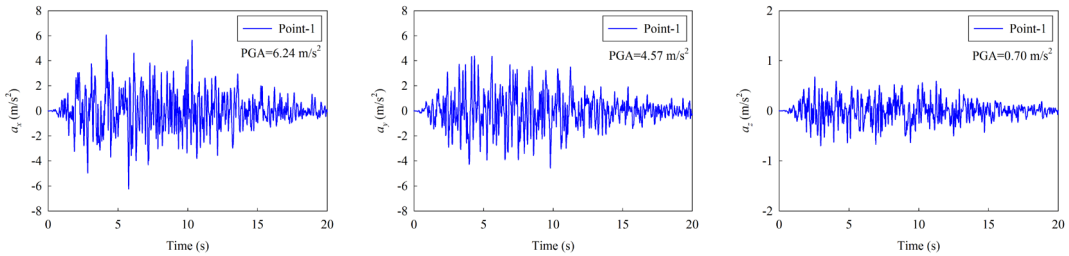

(a) at the site surface (Point-1)

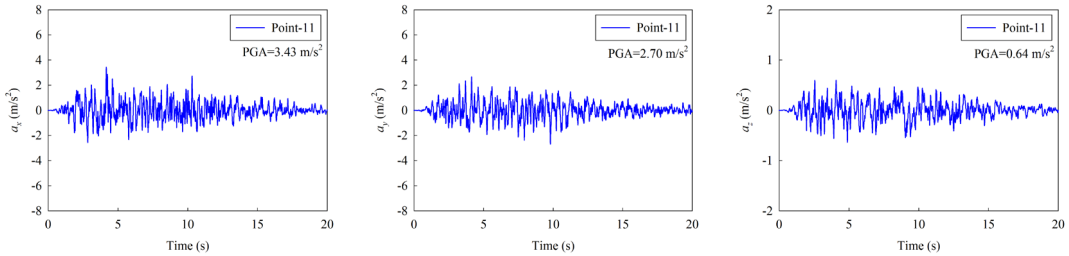

(b) at the end of the monopile (Point-11)

Figure 3-9 Acceleration time histories at the offshore site

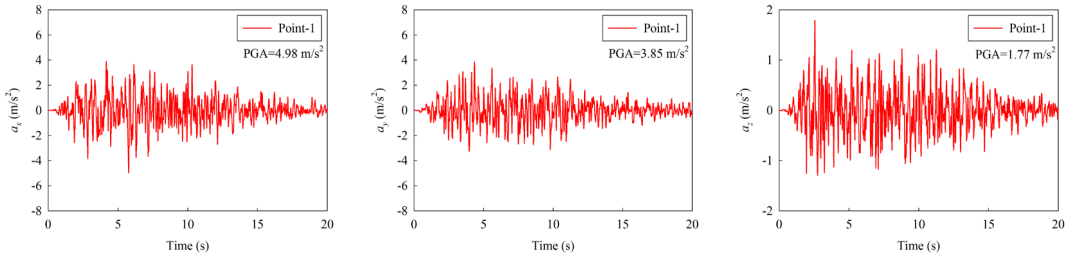

(a) at the site surface (Point-1)

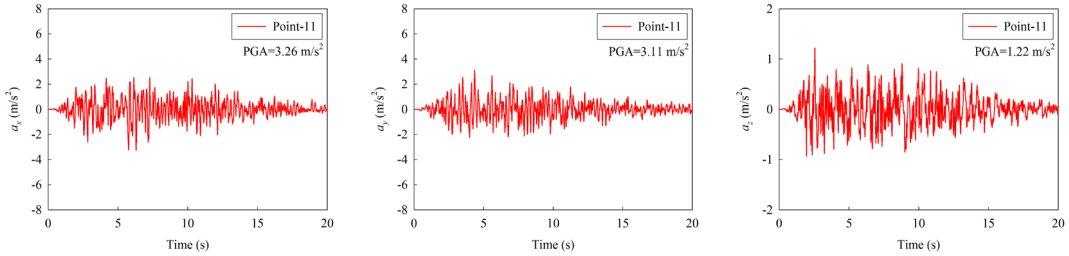

(b) at the end of the monopile (Point-11)

Figure 3-10 Acceleration time histories at the onshore site

With the above mentioned method, the offshore and onshore seismic motions at different locations in the three directions can be simulated, and Figure 3-9 and Figure 3-10 show the acceleration time histories. As shown, the offshore and onshore sites lead to different acceleration time histories, and the differences are most evident in the vertical direction. Moreover, the acceleration time histories at different locations along the monopile foundation are different. All these data can be explained by the different local site transfer functions as

presented in Figure 3-8. Figure 3-11 and Figure 3-12 compare the PSDs of the generated acceleration time histories with the corresponding theoretical curves. Good matches are obtained as shown.

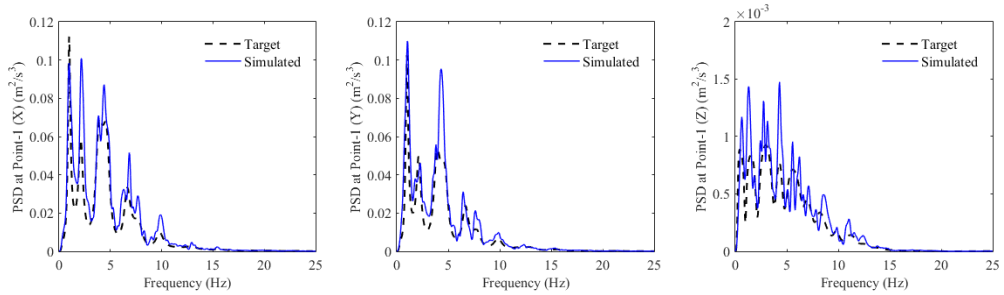

(a) at the site surface (Point-1)

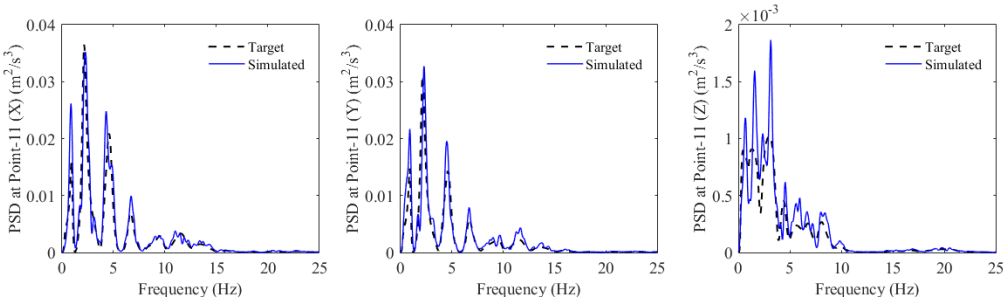

(b) at the end of the monopile (Point-11)

Figure 3-11 Comparisons between the PSD functions of the generated seismic motions and the corresponding target PSDs at the offshore site

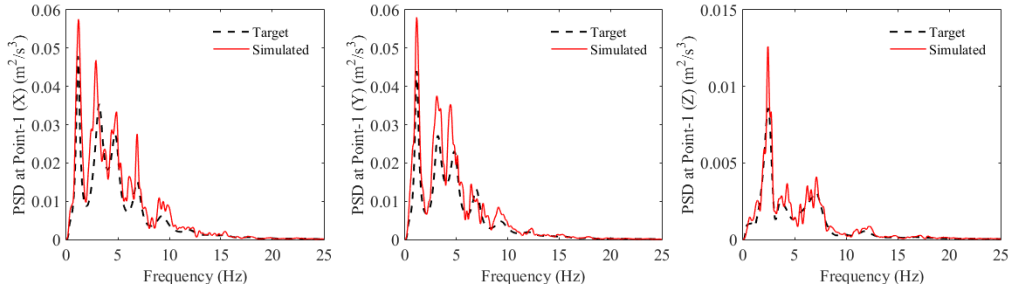

(a) at the site surface (Point-1)

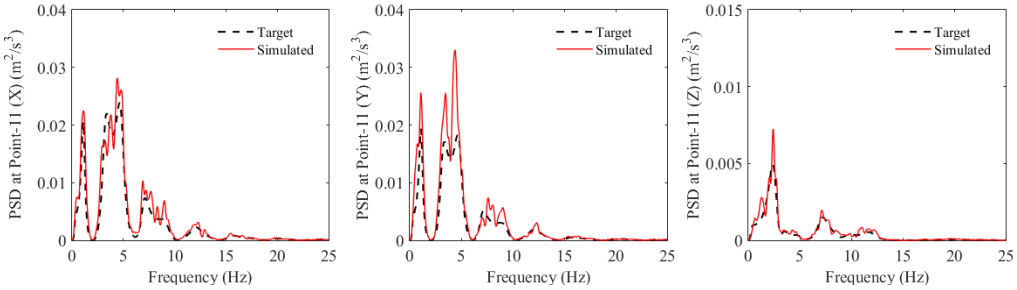

(b) at the end of the monopile (Point-11)

Figure 3-12 Comparisons between the PSD functions of the generated seismic motions and the corresponding target PSDs at the onshore site

The above results show that the seismic motions at the offshore and onshore sites are different and the motions vary with soil depth. By adopting the onshore seismic record at the ground surface may result in erroneous structural response estimations. The influence of the seismic inputs on the dynamic behaviours of the exampled OWT is discussed in detail in the next section.

3.4 Numerical results

As tabulated in Table 3-1, the blades rotate at a rated uniform velocity of 12.1 rpm (1.27 rad/s) when the mean wind speed at the hub height is 11.4 m/s. When the wind speed reaches 25 m/s, the wind turbine will be in the parked state to protect the electrical and mechanical components. These two operational scenarios are considered in the present study. The wind and wave loads as shown in Figure 3-4, Figure 3-5 and Figure 3-6 are applied to the tower and blades correspondingly. The seismic motions as shown in Figure 3-9 and Figure 3-10 are applied to the free ends of the nonlinear spring elements to simulate the earthquake loads acting on the structure. In all the simulations, the time duration is assumed as 200 s and earthquake loads come in at 100 s and end at 120 s. It should be noted that seismic loads may lead to sea water sloshing, which in turn can result in different water pressure along the height of the monopile foundation. This effect is however neglected in the present study, and this simplification is believed reasonable because only seismic P wave can propagate in the sea water, while most seismic energy is associated with S wave. Therefore the additional wave load induced by the seismic excitation is believed small.

3.4.1 Influence of seafloor ground motions

To investigate the influence of earthquake ground motions on the dynamic responses of OWTs, two cases are considered in each operational condition in this section. In the first case, the offshore seismic motions as shown in Figure 3-9 are used as inputs, while the seismic motions at the onshore site as shown in Figure 3-10 are used in the second case.

3.4.1.1 Parked condition

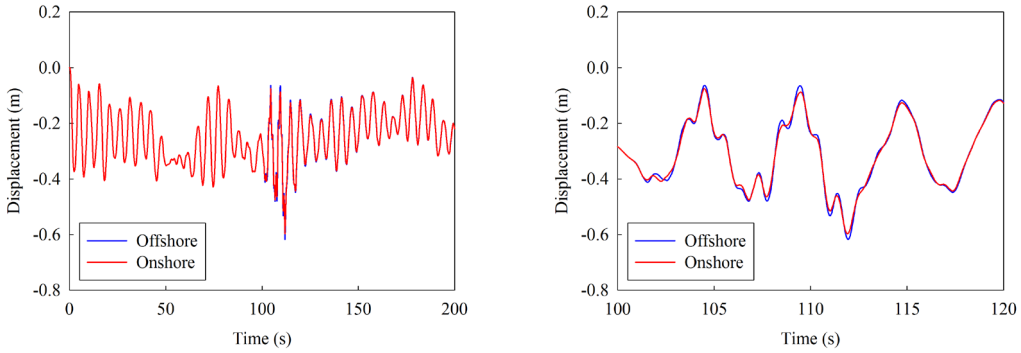

(a) within the whole time duration (b) within 100-120 s

Figure 3-13 Fore-aft displacements at the tower top of the parked wind turbine corresponding to offshore and onshore seismic motions

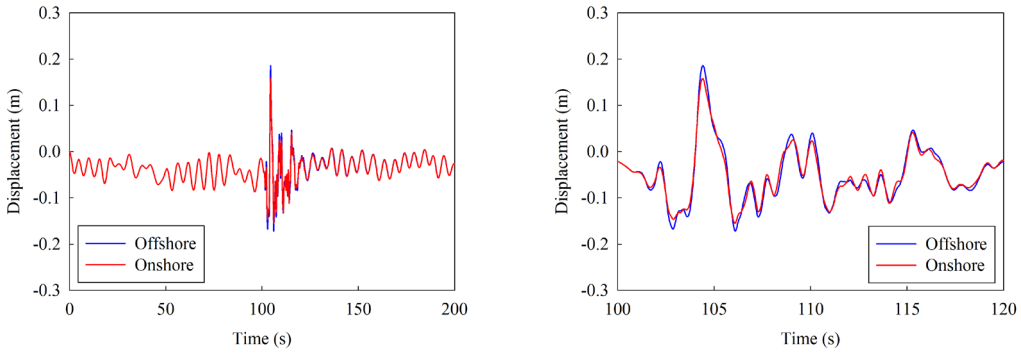

(a) within the whole time duration (b) within 100-120 s

Figure 3-14 Side-to-side displacements at the tower top of the parked wind turbine corresponding to offshore and onshore seismic motions

Table 3-4 Peak displacements and response ratios of the parked wind turbine subjected to offshore and onshore seismic motions

Component	Direction	Offshore seismic motions	Onshore seismic motions	Ratio
Tower	Fore-aft	0.617 m	0.597 m	0.97
	Side-to-side	0.186 m	0.158 m	0.85
Blade #1	Out-of-plane	1.511 m	1.466 m	0.97
	In-plane	0.814 m	0.621 m	0.75
Blade #2 (#3)	Out-of-plane	1.715 m	1.665 m	0.97
	In-plane	0.798 m	0.626 m	0.78

Figure 3-13 and Figure 3-14 show the displacements at the top of the tower in the fore-aft and side-to-side directions when the wind turbine is in the parked condition. Table 3-4 tabulates the peak displacements at the top of the tower and the corresponding response ratios between these two cases. As shown in Figure 3-13 and Figure 3-14, the maximum displacements of the tower subjected to the simultaneous wind, wave and offshore seismic loads in the fore-aft and side-to-side directions are 0.617 m and 0.186 m respectively, and they become 0.597 m and

0.158 m when the onshore seismic motions are considered. The corresponding response ratios obtained from the onshore and offshore sites are 0.97 and 0.85 respectively as tabulated in Table 3-4. These results are actually expected since the site transfer functions $|H_X(i\omega)|$ and $|H_Y(i\omega)|$ for the offshore site are generally larger than those for the onshore site especially at the seabed level as shown in Figure 3-8(a). The more obvious site amplification leads to the more violent seismic inputs as shown in Figure 3-9 and Figure 3-10, and thus the larger structural responses.

The results also show that the displacements of the tower in the side-to-side direction (X direction in Figure 3-7) are much smaller than those in the fore-aft direction (Y direction) though the PGAs of the earthquake motions in the X direction are actually slightly larger than those in the Y direction. This is because of the contributions from the wind and wave loads, which are acting in the fore-aft direction of the tower, while in the side-to-side direction only the seismic motions are applied.

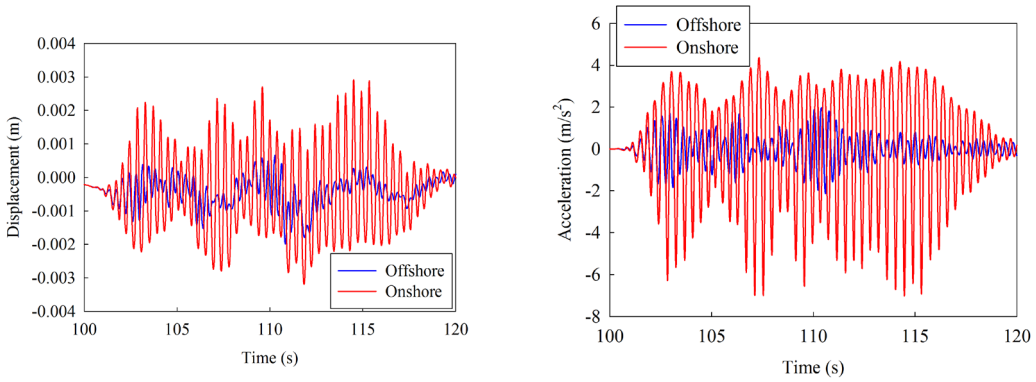

(a) displacement time history

(b) acceleration time history

Figure 3-15 Vertical responses at the tower top of the parked wind turbine corresponding to offshore and onshore seismic motions

Figure 3-15 shows the vertical displacement and acceleration time histories at the top of the tower when the wind turbine is in the parked condition. As shown, for both the displacements and accelerations, the offshore earthquake loadings lead to much smaller values compared to the onshore seismic motions due to the significant sea water suppression effect as discussed above. The results also show that the displacements at the tower top are very small under both the offshore and onshore earthquake motions, while the acceleration responses are large. As shown in Figure 3-15(b), the maximum acceleration reaches 7.021 m/s^2 when the onshore seismic motions are used as inputs. This is because the vertical vibration modes of the wind turbine have much higher frequencies compared to the modes in the horizontal directions. It should be noted that some equipment in the nacelle such as the yaw systems, mechanical control and brakes, gearboxes and connections to the power grid are sensitive to the acceleration responses, and they may be damaged if high acceleration levels are developed

(Dueñas-Osorio & Basu, 2008). From this point, using onshore earthquake ground motions as inputs may overestimate the damage level of these acceleration sensitive equipment of the OWTs.

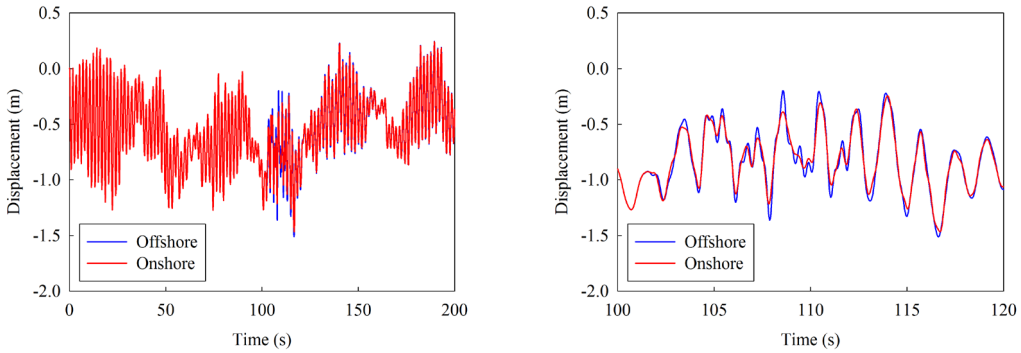

(a) within the whole time duration (b) within 100-120 s

Figure 3-16 Out-of-plane displacements at the tip of blade #1 of the parked wind turbine corresponding to offshore and onshore seismic motions

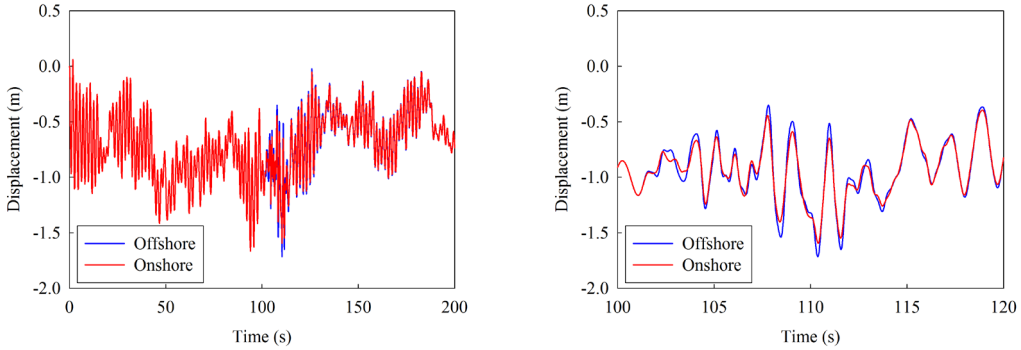

(a) within the whole time duration (b) within 100-120 s

Figure 3-17 Out-of-plane displacements at the tip of blade #2 (#3) of the parked wind turbine corresponding to offshore and onshore seismic motions

Figure 3-16 and Figure 3-17 show the displacements at the tips of blades #1 and #2 (#3) in the out-of-plane direction respectively when the wind turbine is in the parked condition. The peak displacements and the corresponding response ratios are also tabulated in Table 3-4. It should be noted that the displacements at the tip of blade #3 are the same as those at the tip of blade #2 due to the symmetric configuration. As presented in Table 3-4, the maximum out-of-plane displacements of blades #1 and #2 are 1.511 m and 1.715 m respectively when the wind turbine is subjected to the simultaneous wind, wave and offshore seismic loads, and these values slightly decrease to 1.466 m and 1.665 m when the onshore seismic motions are used. The corresponding response ratios are both 0.97. Comparing Figure 3-16 with Figure 3-17, the displacements of blade #2 are larger than those of blade #1 since its position are higher as

shown in Figure 3-1, and larger wind loads are applied on blade #2, which in turn lead to the larger displacement responses.

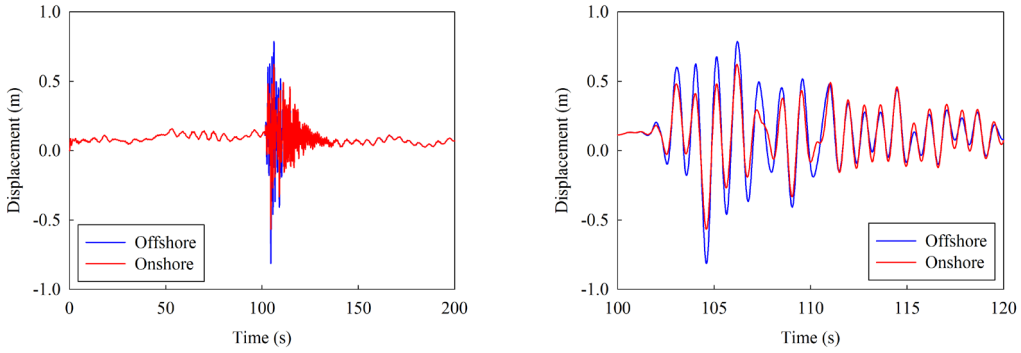

(a) within the whole time duration (b) within 100-120 s

Figure 3-18 In-plane displacements at the tip of blade #1 of the parked wind turbine corresponding to offshore and onshore seismic motions

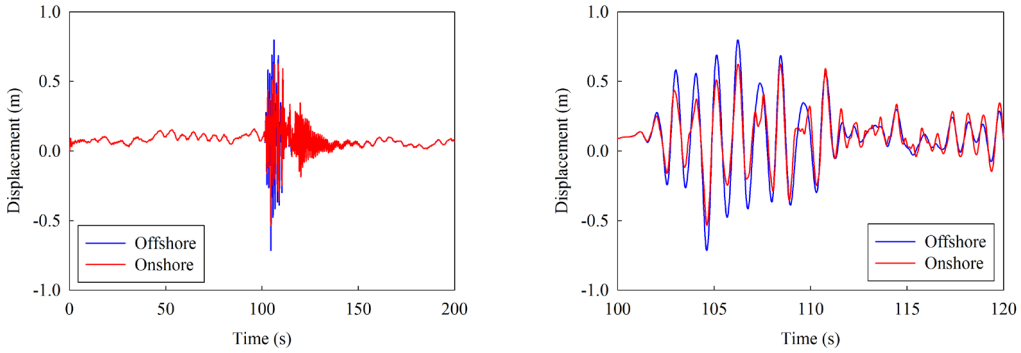

(a) within the whole time duration (b) within 100-120 s

Figure 3-19 In-plane displacements at the tip of blade #2 (#3) of the parked wind turbine corresponding to offshore and onshore seismic motions

Figure 3-18 and Figure 3-19 show the displacements at the tips of blades #1 and #2 (#3) in the in-plane direction when the blades are parked. As shown, the displacement responses within the duration of the earthquake are much larger than those when only the wind and wave loads are acting on the structure. The maximum in-plane displacements of blades #1 and #2 are 0.814 m and 0.798 m respectively with the offshore seismic motions, and they become 0.621 m and 0.626 m with the onshore inputs. The corresponding response ratios are 0.75 and 0.78 as given in Table 3-4. Compared to the out-of-plane responses, it is obvious that the in-plane responses are more evidently influenced by the types of seismic inputs. This is because besides the earthquake loadings in the X direction, the vertical seismic motions can also induce the in-plane displacements to the blades. Some obvious differences exist in the vertical ground motions for the offshore and onshore sites due to sea water suppression, the response differences in this direction are therefore more pronounced.

3.4.1.2 Operating condition

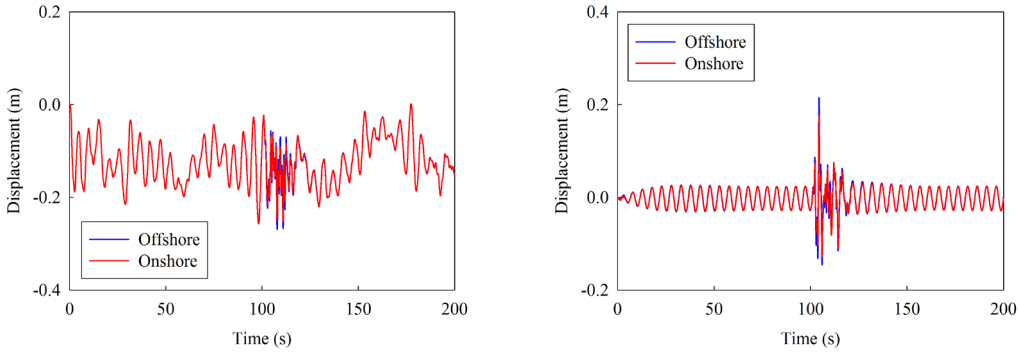

(a) fore-aft (b) side-to-side

Figure 3-20 Displacements at the tower top of the operating wind turbine corresponding to offshore and onshore seismic motions

Table 3-5 Peak displacements and response ratios of the operating wind turbine subjected to offshore and onshore seismic motions

Component	Direction	Offshore seismic motions	Onshore seismic motions	Ratio
Tower	Fore-aft	0.269 m	0.257 m	0.96
	Side-to-side	0.215 m	0.176 m	0.82
Blade #1		1.142 m	1.012 m	0.89
Blade #2	Out-of-plane	1.143 m	1.027 m	0.90
Blade #3		1.300 m	1.077 m	0.83
Blade #1 (#2, #3)	In-plane	2.643 m	2.617 m	0.99

The influence of the offshore and onshore seismic motions on the operating wind turbine is discussed in this section. Figure 3-20 shows the displacement time histories at the top of the tower in the fore-aft and side-to-side directions. The peak displacements and the corresponding response ratios are tabulated in Table 3-5. Similar to the parked condition, the onshore seismic motions lead to the smaller displacements at the tower top when the wind turbine is rotating. As shown, the maximum displacements of the tower in the fore-aft and side-to-side directions are 0.269 m and 0.215 m respectively when the wind turbine is subjected to the simultaneous wind, wave and offshore seismic loads, while they decrease to 0.257 m and 0.176 m when the onshore seismic motions are considered. Almost the same levels of response reduction are obtained compared to the parked condition, as shown in Table 3-5, the corresponding response ratios in the fore-aft and side-to-side directions are 0.96 and 0.82 respectively for the operating wind turbine. Comparing the results in Table 3-5 with those in Table 3-4, one can see that when the wind turbine is operating, the tower displacements in the fore-aft direction are much smaller than those in the parked condition. This is because the wind speeds for the operating and parked conditions are different, and they are 11.4 m/s and 25 m/s respectively as mentioned above. The larger wind speed results in larger wind and wave loads acting on the tower. For the side-to-side direction, the responses of the two operational conditions are at the

same level. This is because no wind and wave loadings are applied in this direction, the responses are generated by the earthquake excitation only. The slight differences are mainly because the wind loads on the rotating and parked blades are different as shown in Figure 3-5(b), which influence the interaction between the tower and blades and the responses of the tower.

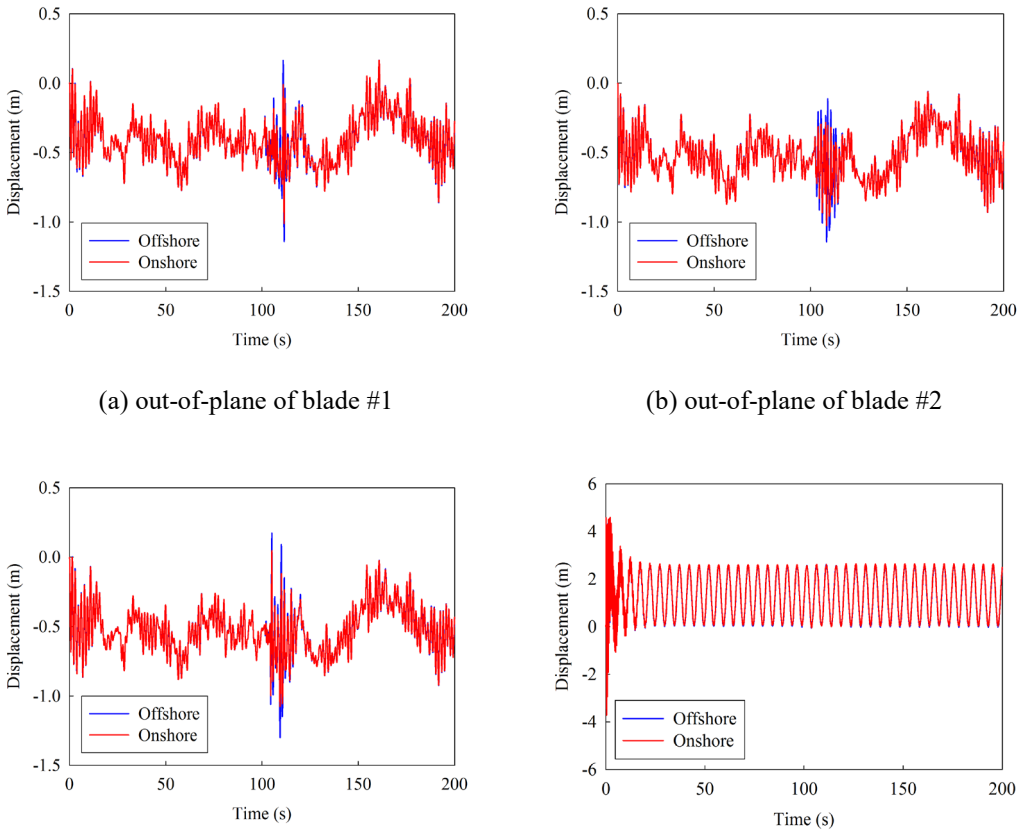

(a) out-of-plane of blade #1

(b) out-of-plane of blade #2

(c) out-of-plane of blade #3

(d) in-plane of blade #1

Figure 3-21 Displacements at the tips of blades of the operating wind turbine corresponding to offshore and onshore seismic motions

Figure 3-21 shows the displacements at the tips of the blades in the out-of-plane and in-plane directions when the wind turbine is in the operating condition. The peak displacements and the corresponding response ratios are also tabulated in Table 3-5. It should be noted that when the blades are rotating, the in-plane responses of the three blades are identical because of the same geometrical and structural parameters in the rotor plane. Only the in-plane displacements at the tip of blade #1 are presented in Figure 3-21(d) for simplicity. Figure 3-21 shows that the maximum out-of-plane displacements of the three blades are 1.142 m, 1.143 m and 1.300 m respectively with the offshore seismic motions as inputs, and the corresponding values are 1.012 m, 1.027 m and 1.077 m when the onshore seismic motions are considered. The corresponding response ratios are 0.89, 0.90 and 0.83 respectively. The out-of-plane displacement responses of the three blades are slightly different because of the initial locations

of the blades. Comparing the results in Table 3-5 with those in Table 3-4, it can be seen that using onshore and offshore ground motions results in more different the out-of-plane displacement responses when the wind turbine is in the operating condition compared to the parked condition. As shown, the average response ratios of the three blades for the parked and operating conditions are 0.97 and 0.87 respectively.

For the in-plane displacement time histories of the blades as shown in Figure 3-21(d), at the first 25 s, the responses are not stable (Zuo et al., 2018) since the blades rotate suddenly from the parked state at t=0 s. After about 25 s, the in-plane displacements at the tips of the blades become stable, and they show a sinusoidal shape in magnitude with the frequency of this variation corresponding to the rotor frequency of 1.27 rad/s. The peak in-plane displacements when the blades are stable are also tabulated in Table 3-5. It can be seen that the maximum displacements at the tips of the blades in the in-plane direction are 2.643 m and 2.617 m respectively when the offshore and onshore seismic motions are considered. The different types of seismic loadings have almost no influence on the in-plane responses of the blades. This is because the responses are governed by the rotation of the blades. This trend, on the other hand, is different from the parked condition. As shown in Table 3-4, the average response ratio of the three blades is 0.77 when the wind turbine is parked, and the obvious difference mainly results from the different vertical earthquake components as discussed.

3.4.2 Influence of depth-varying ground motions

The dynamic responses of the OWT under the depth-varying seismic motions are investigated in this section, and the results are compared with the case when the earthquake ground motions along the monopile foundation are the same with those at the seabed level (i.e. the uniform case). Again, both the parked and operating conditions are considered.

3.4.2.1 Parked condition

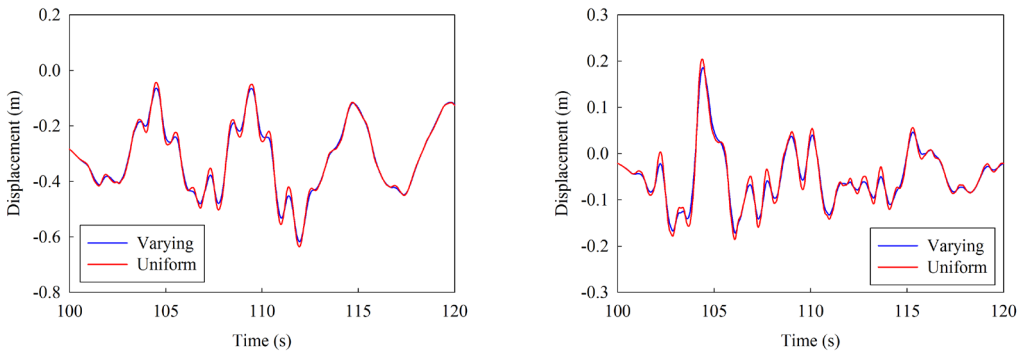

(a) fore-aft (b) side-to-side

Figure 3-22 Displacements at the tower top of the parked wind turbine with depth-varying and uniform seismic motions

Figure 3-22 shows the displacements at the top of the tower in the fore-aft and side-to-side directions when the wind turbine is in the parked condition. Since more severe responses occur when the earthquake comes in, only the displacement time histories within the duration of 100-120 s are shown here for more clear comparisons. The peak displacements and the corresponding response ratios between the depth-varying and uniform seismic motions are tabulated in Table 3-6. As shown, the maximum displacements of the tower in the fore-aft and side-to-side directions with the seismic motions varying with the depth are 0.617 m and 0.186 m respectively, and they become 0.635 m and 0.204 m when the uniform seismic motions are considered. The corresponding response ratios are 1.03 and 1.10 respectively. The responses of the OWT are larger by ignoring the seismic motions varying with the depth below the seabed. This is easy to understand because the seismic motions at the ground surface are the largest compared to other locations along the monopile foundation due to the amplification of the soil layers as shown in Figure 3-9, which in turn lead to the larger structural responses.

Table 3-6 Peak displacements and response ratios of the parked wind turbine subjected to depth-varying and uniform seismic motions

Component	Direction	Varying seismic motions	Uniform seismic motions	Ratio
Tower	Fore-aft	0.617 m	0.635 m	1.03
	Side-to-side	0.186 m	0.204 m	1.10
Blade #1	Out-of-plane	1.511 m	1.547 m	1.02
	In-plane	0.814 m	1.012 m	1.24
Blade #2 (#3)	Out-of-plane	1.715 m	1.835 m	1.07
	In-plane	0.798 m	0.978 m	1.23

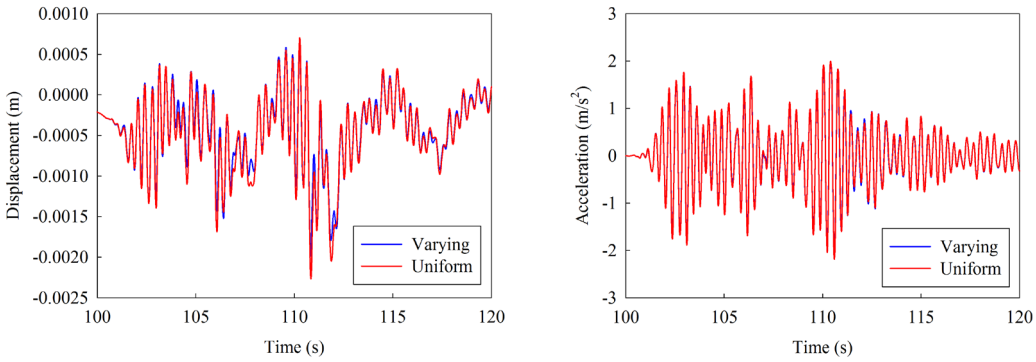

(a) displacement time history

(b) acceleration time history

Figure 3-23 Vertical responses at the tower top of the parked wind turbine with depth-varying and uniform seismic motions

Figure 3-23 shows the vertical displacement and acceleration time histories at the top of the tower when the depth-varying and uniform seismic motions are considered. Similar to the responses of the tower in the horizontal directions (fore-aft and side-to-side directions), the uniform seismic motions result in slightly larger vertical displacements and accelerations than those with the depth-varying earthquake motions. These results indicate that using the uniform

seismic motions as inputs can lead to the conservative design since the structural responses are larger. However, the design will be not economic.

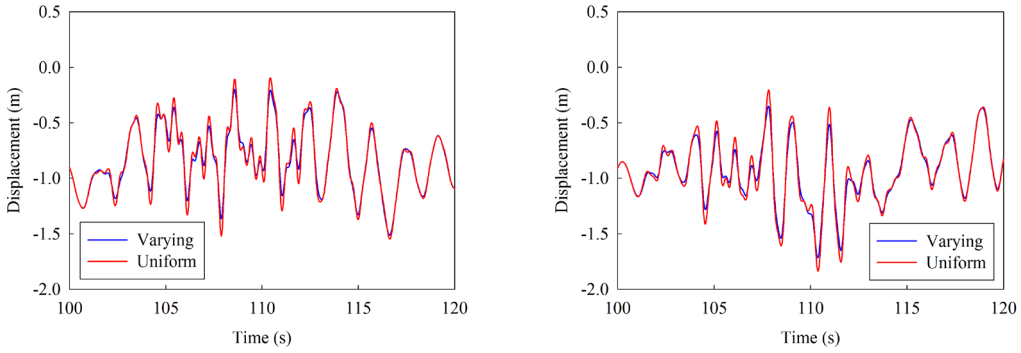

(a) blade #1 (b) blade #2 (#3)

Figure 3-24 Out-of-plane displacements at the tips of blades of the parked wind turbine with depth-varying and uniform seismic motions

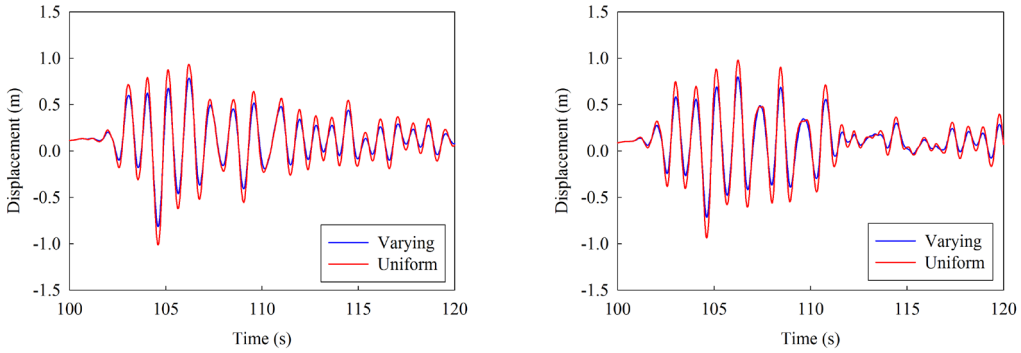

(a) blade #1 (b) blade #2 (#3)

Figure 3-25 In-plane displacements at the tips of blades of the parked wind turbine with depth-varying and uniform seismic motions

Figure 3-24 and Figure 3-25 show the displacements at the tips of blades #1 and #2 (#3) in the out-of-plane and in-plane directions respectively when the wind turbine is in the parked condition. The peak displacements and the corresponding response ratios are also tabulated in Table 3-6. As shown, the maximum displacements at the tip of blade #1 in the out-of-plane and in-plane directions are 1.511 m and 0.814 m respectively when the depth-varying seismic motions are considered, and the values become 1.547 m and 1.012 m with the uniform seismic motions. The corresponding response ratios are 1.02 and 1.24 respectively. For blade #2 (#3), the corresponding values are 1.715 m and 0.798 m respectively with the depth-varying seismic motions and they increase to 1.835 m and 0.978 m when the uniform seismic motions are considered. The corresponding response ratios become 1.07 and 1.23 respectively. Again, similar to the trend as observed in Table 3-4, different earthquake inputs have more obvious influence on the in-plane responses compared to the out-of-plane results due to the

contribution of the different vertical seismic components. As shown, the maximum difference can reach 24% for the in-plane displacement of blade #1.

3.4.2.2 Operating condition

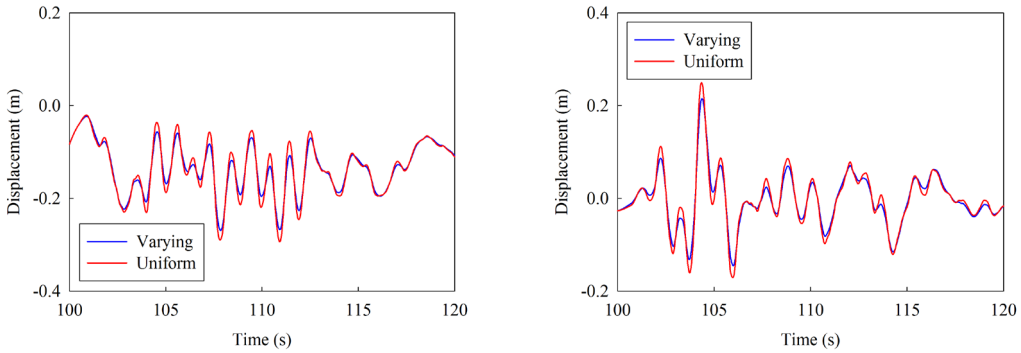

(a) fore-aft (b) side-to-side

Figure 3-26 Displacements at the tower top of the operating wind turbine with depth-varying and uniform seismic motions

Figure 3-26 shows the displacements at the top of the tower in the fore-aft and side-to-side directions when the wind turbine is in the operating condition. The peak displacements and the corresponding response ratios are tabulated in Table 3-7. As shown, the maximum displacements of the tower in the fore-aft and side-to-side directions are 0.269 m and 0.215 m respectively with the seismic motions varying with the depth, and they reach 0.293 m and 0.250 m with the uniform seismic motions. The corresponding response ratios are 1.09 and 1.16 respectively. Compared to the results in Table 3-6, it can be seen that the influence of depth-varying earthquake motions on the operating wind turbine is slightly more evident than the case when the wind turbine is parked.

Table 3-7 Peak displacements and response ratios of the operating wind turbine subjected to depth-varying and uniform seismic motions

Component	Direction	Varying seismic motions	Uniform seismic motions	Ratio
Tower	Fore-aft	0.269 m	0.293 m	1.09
	Side-to-side	0.215 m	0.250 m	1.16
Blade #1		1.142 m	1.365 m	1.20
Blade #2	Out-of-plane	1.143 m	1.261 m	1.10
Blade #3		1.300 m	1.446 m	1.11
Blade #1 (#2, #3)	In-plane	2.643 m	2.663 m	1.01

Figure 3-27 shows the displacements at the tips of the blades in the out-of-plane and in-plane directions when the blades are rotating with a uniform velocity of 1.27 rad/s. The peak displacements and the corresponding response ratios are tabulated in Table 3-7. As shown, the maximum out-of-plane displacements of the blades with the depth-varying seismic motions are 1.142 m, 1.143 m and 1.300 m respectively, and the corresponding values are 1.365 m, 1.261 m and 1.446 m when the uniform seismic motions are used. The corresponding response

ratios are 1.20, 1.10 and 1.11 respectively with an average of 1.14. Similar to the influence of offshore and onshore earthquake ground motions, the depth-varying seismic motions have more evident influence in the operating wind turbine compared to the parked condition, in which the average response ratio is 1.05 as can be calculated from Table 3-6.

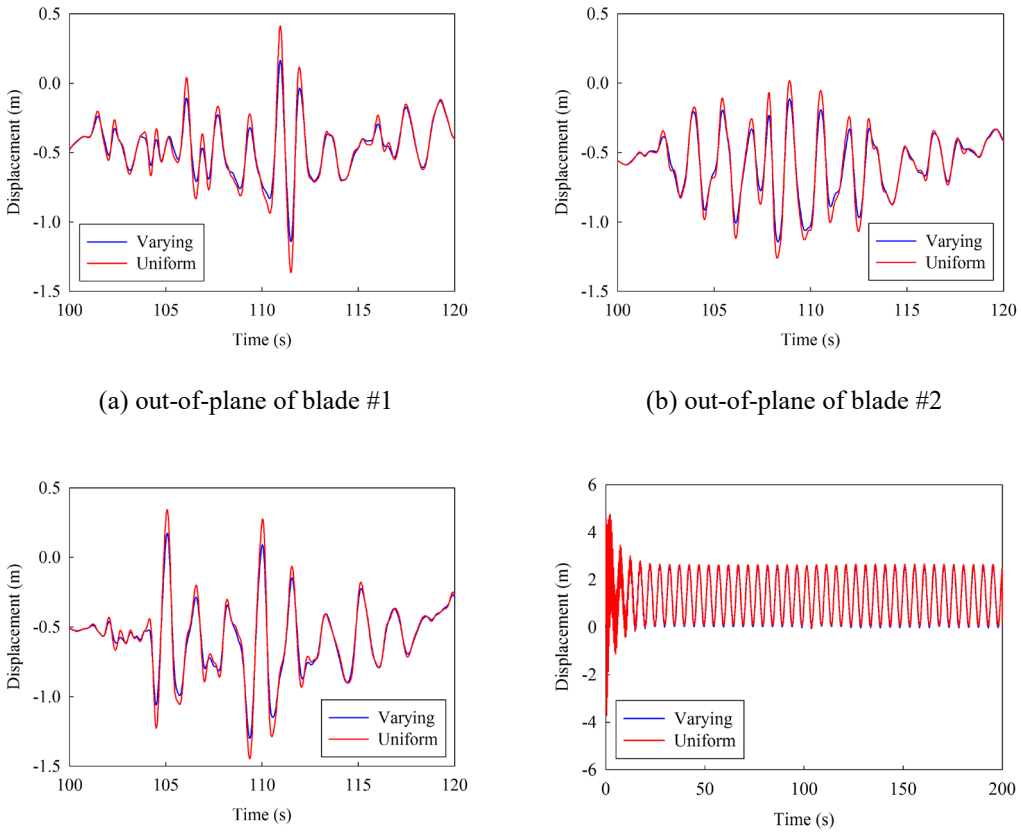

(a) out-of-plane of blade #1

(b) out-of-plane of blade #2

(c) out-of-plane of blade #3

(d) in-plane of blade #1

Figure 3-27 Displacements at the tips of blades of the operating wind turbine with depth-varying and uniform seismic motions

For the in-plane displacements of the blades, as shown in Figure 3-27(d) and Table 3-7, the maximum displacements at the tips of the blades are 2.643 m and 2.663 m respectively when the depth-varying and uniform seismic motions are considered, and the response ratio is 1.01. The results indicate again that the using different ground motion inputs considered in this study has almost no effect on the in-plane displacements of the rotating blades.

3.5 Conclusions

In this chapter, the dynamic behaviours of the NREL 5 MW wind turbine subjected to the combined actions of the wind, wave and earthquake excitations are numerically investigated in both the parked and operating conditions. The depth-varying offshore seismic motions are stochastically simulated by considering the direct and indirect effects of the sea water layer.

The influences of the offshore and onshore seismic motions and the depth-varying seismic motions on the dynamic responses of the wind turbine are systematically discussed. Numerical results show that:

(1) The earthquake ground motions at the offshore site are significantly different from those at the onshore site especially for the seismic motions in the vertical direction. Compared to the offshore earthquake ground motions, using onshore seismic motions as inputs in the analyses may underestimate out-of-plane and in-plane responses of the OWTs. For the investigated OWT, the difference can reach 25%. The vertical responses are however overestimated by adopting the onshore earthquake motions.

(2) Compared to the depth-varying earthquake motions, using the seismic motions at the seabed level as inputs can overestimate the dynamic responses of OWTs. The overestimation can reach 24% for the examined example.

(3) The influence of different earthquake ground motions (onshore/offshore and uniform/depth-varying) on the in-plane responses of the parked blades is more evident compared to the out-of-plane responses due to the vertical seismic components influence the displacement in the in-plane direction.

(4) The different seismic inputs have more obvious effect on the responses of the operating OWT than those when the OWT is in the parked condition except the in-plane responses of the rotating blades, which are governed by the rotation of the blades.

It should be noted that the simplified soil spring model adopted in the present study cannot consider the soil stiffness degradation and the gap between the monopile foundation and surrounding soil under cyclic loadings, and it might result in slight inaccurate structural responses as discussed in Section 3.3.2. However, the observations and conclusions on the influences of using onshore and offshore ground motions inputs in seismic response analysis would not change if more refined soil models were used. In addition, all the above conclusions are based on the NREL 5 MW OWT and the site conditions shown in Figure 3-7. To obtain more general conclusions, more comprehensive analyses are needed. The quantitative results cannot be extrapolated to other OWTs and site conditions. The results, however, demonstrate the importance and necessity of using proper earthquake ground motions in predicting responses of OWTs.

3.6 References

Alati, N., Failla, G., & Arena, F. (2015). Seismic analysis of offshore wind turbines on bottom-fixed support structures. *Philosophical Transactions Royal Society A*, *373*(2035), 20140086.

American Petroleum Institute (API). (2014). Petroleum and natural gas industries-specific requirements for offshore structures. Part 4-geotechnical and foundation design considerations ISO 19901-4:2003 (Modified); 2011.

Arany, L., Bhattacharya, S., Macdonald, J., & Hogan, S. (2017). Design of monopiles for offshore wind turbines in 10 steps. *Soil Dynamics and Earthquake Engineering*, *92*, 126-152.

Arany, L., Bhattacharya, S., Macdonald, J., & Hogan, S. (2016). Closed form solution of Eigen frequency of monopile supported offshore wind turbines in deeper waters incorporating stiffness of substructure and SSI. *Soil Dynamics and Earthquake Engineering*, *83*, 18-32.

Bhattacharya, S., & Adhikari, S. (2011). Experimental validation of soil-structure interaction of offshore wind turbines. *Soil Dynamics and Earthquake Engineering*, *31*(5), 805-816.

Bhattacharya, S., & Goda, K. (2016). Use of offshore wind farms to increase seismic resilience of Nuclear Power Plants. *Soil Dynamics and Earthquake Engineering*, *80*, 65-68.

Bi, K., & Hao, H. (2012). Modelling and simulation of spatially varying earthquake ground motions at sites with varying conditions. *Probabilistic Engineering Mechanics*, *29*, 92-104.

Bi, K., Hao, H., Li, C., & Li, H. (2017). Stochastic seismic response analysis of buried onshore and offshore pipelines. *Soil Dynamics and Earthquake Engineering*, *94*, 60-65.

Bisoi, S., & Haldar, S. (2014). Dynamic analysis of offshore wind turbine in clay considering soil-monopile-tower interaction. *Soil Dynamics and Earthquake Engineering*, *63*, 19-35.

Boulanger, R., Curras, C., Kutter, B., Wilson, D., & Abghari, A. (1999). Seismic soil-pile-structure interaction experiments and analyses. *Journal of Geotechnical and Geoenvironmental Engineering*, *125*(9), 750-759.

Dash, S., Rouholamin, M., Lombardi, D., & Bhattacharya, S. (2017). A practical method for construction of p-y curves for liquefiable soils. *Soil Dynamics and Earthquake Engineering*, *97*, 478-481.

Dash, S., Govindaraju, L., & Bhattacharya, S. (2009). A case study of damages of the Kandla Port and Customs Office tower supported on a mat-pile foundation in liquefied soils under the 2001 Bhuj earthquake. *Soil Dynamics and Earthquake Engineering*, *29*(2), 333-346.

De Risi, R., Bhattacharya, S., & Goda, K. (2018). Seismic performance assessment of monopile-supported offshore wind turbines using unscaled natural earthquake records. *Soil Dynamics and Earthquake Engineering*, *109*, 154-172.

Der Kiureghian, A. (1980). Structural response to stationary excitation. *Journal of the Engineering Mechanics Division*, *106*(6), 1195-1213.

Díaz, O., & Suárez, L. (2014). Seismic analysis of wind turbines. *Earthquake Spectra*, *30*(2), 743-765.

Det Norske Veritas (DNV). (2014). DNV-OS-J101: Design of offshore wind turbine structures. Copenhagen, Denmark: DNV.

Dueñas-Osorio, L., & Basu, B. (2008). Unavailability of wind turbines due to wind-induced accelerations. *Engineering Structures*, *30*(4), 885-893.

Fitzgerald, B., & Basu, B. (2016). Structural control of wind turbines with soil structure interaction included. *Engineering Structures*, *111*, 131-151.

Global Wind Energy Council (GWEC). (2018). Global wind report-Annual market update 2017.

Hacıefendioğlu, K. (2012). Stochastic seismic response analysis of offshore wind turbine including fluid-structure-soil interaction. *The Structural Design of Tall and Special Buildings*, *21*(12), 867-878.

Hansen, M. O. L. (2008). Aerodynamics of wind turbines 2nd ed. London: Earthscan.

Hao, H., Oliveira, C., & Penzien, J. (1989). Multiple-station ground motion processing and simulation based on SMART-1 array data. *Nuclear Engineering and Design*, *111*(3), 293-310.

IEC 61400-3. (2009). Wind turbines-Part 3: design requirements for offshore wind turbines 1st ed. Geneva (Switzerland): International Electrotechnical Commission.

Jonkman, J., Butterfield, S., Musial, W., & Scott, G. (2009). Definition of a 5-MW reference wind turbine for offshore system development. (Technical Report No. NREL/TP-500-38060). Golden, CO: National Renewable Energy Laboratory.

Katsanos, E., Thöns, S., & Georgakis, C. (2016). Wind turbines and seismic hazard: a state-of-the-art review. *Wind Energy*, *19*(11), 2113-2133.

Kaynia, A. M. (2018). Seismic considerations in design of offshore wind turbines. *Soil Dynamics and Earthquake Engineering*.

Kim, D. H., Lee, S. G., & Lee, I. K. (2014). Seismic fragility analysis of 5 MW offshore wind turbine. *Renewable Energy*, *65*, 250-256.

Kjørlaug, R. A., & Kaynia, A. M. (2015). Vertical earthquake response of megawatt-sized wind turbine with soil-structure interaction effects. *Earthquake Engineering & Structural Dynamics*, *44*(13), 2341-2358.

Kooijman, H., Lindenburg, C., Winkelaar, D., van der Hooft, E. (2003). Aero-elastic modelling of the DOWEC 6 MW pre-design in PHATAS DOWEC-F1W2-HJK-01-046/9.

Li, C., Hao, H., Li, H., & Bi, K. (2015). Theoretical modeling and numerical simulation of seismic motions at seafloor. *Soil Dynamics and Earthquake Engineering*, *77*, 220-225.

Li, C., Hao, H., Li, H., Bi, K., & Chen, B. (2017). Modeling and simulation of spatially correlated ground motions at multiple onshore and offshore sites. *Journal of Earthquake Engineering*, *21*(3), 359-383.

Li, C., Li, H., Hao, H., & Bi, K. (2018a). Simulation of spatially varying seafloor motions using onshore earthquake recordings. *Journal of Engineering Mechanics*, *144*(9), 04018085.

Li, C., Li, H., Hao, H., Bi, K., & Chen, B. (2018b). Seismic fragility analyses of sea-crossing cable-stayed bridges subjected to multi-support ground motions on offshore sites. *Engineering Structures*, *165*, 441-456.

Li, C., Li, H., Hao, H., Bi, K., & Tian, L. (2018c). Simulation of multi-support depth-varying earthquake ground motions within heterogeneous onshore and offshore sites. *Earthquake Engineering and Engineering Vibration*, *17*(3), 475-490.

Murtagh, P. J., Basu, B., & Broderick, B. M. (2005). Along-wind response of a wind turbine tower with blade coupling subjected to rotationally sampled wind loading. *Engineering Structures*, *27*(8), 1209-1219.

Wolf, J. (1985). Dynamic soil-structure interaction. New Jersey: Prentice Hall Inc.

Patil, A., Jung, S., & Kwon, O. (2016). Structural performance of a parked wind turbine tower subjected to strong ground motions. *Engineering Structures*, *120*, 92-102.

Prowell, I., Elgamal, A., Uang, C. M., Enrique Luco, J., Romanowitz, H., & Duggan, E. (2014). Shake table testing and numerical simulation of a utility-scale wind turbine including operational effects. *Wind Energy*, *17*(7), 997-1016.

Prowell, I., Veletzos, M., Elgamal, A., & Restrepo, J. (2009). Experimental and numerical seismic response of a 65 kW wind turbine. *Journal of Earthquake Engineering*, *13*(8), 1172-1190.

Rendon, E. A., & Manuel, L. (2014). Long-term loads for a monopile-supported offshore wind turbine. *Wind Energy*, *17*(2), 209-223.

Santangelo, F., Failla, G., Santini, A., & Arena, F. (2016). Time-domain uncoupled analyses for seismic assessment of land-based wind turbines. *Engineering Structures*, *123*, 275-299.

Sun, C., & Jahangiri, V. (2018). Bi-directional vibration control of offshore wind turbines using a 3D pendulum tuned mass damper. *Mechanical Systems and Signal Processing*, *105*, 338-360.

Valamanesh, V., & Myers, A. (2014). Aerodynamic damping and seismic response of horizontal axis wind turbine towers. *Journal of Structural Engineering*, *140*(11), 04014090.

Wang, P., Zhao, M., Du, X., Liu, J., & Xu, C. (2018). Wind, wave and earthquake responses of offshore wind turbine on monopile foundation in clay. *Soil Dynamics and Earthquake Engineering*, *113*, 47-57.

Witcher, D. (2005). Seismic analysis of wind turbines in the time domain. *Wind Energy*, *8*(1), 81-91.

Yang, J., & Sato, T. (2000). Interpretation of seismic vertical amplification observed at an array site. *Bulletin of the Seismological Society of America*, *90*(2), 275-285.

Zhang, Z., Staino, A., Basu, B., & Nielsen, S. R. K. (2016). Performance evaluation of full-scale tuned liquid dampers (TLDs) for vibration control of large wind turbines using real-time hybrid testing. *Engineering Structures*, *126*, 417-431.

Zhao, B., Gao, H., Wang, Z., & Lu, Z. (2018). Shaking table test on vibration control effects of a monopile offshore wind turbine with a tuned mass damper. *Wind Energy*, *21*(12), 1309-1328.

Zuo, H., Bi, K., & Hao, H. (2017). Using multiple tuned mass dampers to control offshore wind turbine vibrations under multiple hazards. *Engineering Structures*, *141*, 303-315.

Zuo, H., Bi, K., & Hao, H. (2018). Dynamic analyses of operating offshore wind turbines including soil-structure interaction. *Engineering Structures*, *157*, 42-62.

Zuo, H., Bi, K., & Hao, H. (2019). Mitigation of tower and out-of-plane blade vibrations of offshore monopile wind turbines by using multiple tuned mass dampers. *Structure and Infrastructure Engineering*, *15*(2):269-284.

CHAPTER 4 FRAGILITY ANALYSES OF OFFSHORE WIND TURBINES SUBJECTED TO AERODYNAMIC AND SEA WAVE LOADINGS

ABSTRACT[3]

To more effectively extract the vast wind energy in marine areas, offshore wind turbines have been constructed with slender tower and large rotor. External vibration sources such as aerodynamic, sea wave and seismic loadings can threaten the safety of these energy infrastructures. It is important to evaluate the reliability of offshore wind turbines subjected to external vibration sources. Previous research works on the wind turbine fragility analyses only considered the fragility of the tower by assuming the wind turbine was in the parked condition with the blade mass lumped at the top of the tower. The study of the fragility of the blade which is one of the most important components of a wind turbine has not been reported. In the present study, a detailed three-dimensional (3D) finite element (FE) model of the NREL 5 MW wind turbine is developed in ABAQUS and the tower and blades are explicitly modelled to realistically estimate the aerodynamic loads and structural behaviours of the wind turbine. The uncertainties of the structural mass, stiffness and damping are taken into account to develop the probabilistic wind-induced demand models for the tower and blades. The dynamic behaviours of the wind turbine subjected to the simultaneous aerodynamic and sea wave loadings are investigated in a probabilistic frame and the fragility curves for both the tower and blades under the parked and operating conditions are derived and discussed.

4.1 Introduction

Wind energy as one of the renewable energies is becoming a main contributor to the new electricity generation. The growth and expansion of wind farms increased rapidly in the past decade. As reported by the Global Wind Energy Council (GWEC), the worldwide installed capacity of wind power at the end of 2018 was 591 GW, with an increase of 9.6% compared to that at the end of 2017 (GWEC, 2018).

Due to the fact that the power generated by the wind turbine is proportional to the wind speed and rotor diameter, multi-megawatt wind turbines with slender tower and large rotor are widely constructed in the state-of-the-art designs. These wind turbines are very flexible and lightly damped since they are normally manufactured by the light-weight high-strength materials. They are thus susceptible to external vibration sources such as aerodynamic and sea

[3] Zuo, H., Bi, K., Hao, H., Li, J., Xin, Y. & Li, C. (2019). Fragility analyses of offshore wind turbines subjected to aerodynamic and sea wave loadings. (Under review).

wave loadings, which are experienced constantly during the whole lifetimes by offshore wind turbines. Moreover, many wind farms are located in the regions of high seismic activities such as western of United States, Japan and China (Katsanos et al., 2016), seismic loading is another possible vibration source during their lifetimes in these regions. The excessive vibrations may slow down the conversion of wind energy to electricity, reduce the fatigue life of the structural components or even lead to the structural collapse in extreme conditions.

Extensive research works have been carried out to investigate the dynamic behaviours of wind turbines subjected to aerodynamic, sea wave and/or seismic loadings (Bisoi & Haldar, 2014; Haldar et al., 2018; Zuo et al., 2018). Various control strategies have been proposed to mitigate these adverse vibrations (Colwell & Basu, 2009; Fitzgerald & Basu, 2016; Murtagh et al., 2008; Sun, 2018; Zhang et al., 2013; Zuo et al., 2017, 2019a). Since the vibration control of wind turbines is beyond the scope of the present study, only the previous studies on the dynamic response analyses of wind turbines are briefly reviewed here. In order to simplify the analysis, the wind turbines were generally assumed in the parked condition, and the blades were modelled as a lumped mass at the top of the tower (Bisoi & Haldar, 2014; Haldar et al., 2018; Zuo et al., 2017). In some literatures, the geometrical configurations of the blades were considered and explicitly developed in the finite element (FE) models (Kjørlaug & Kaynia, 2015; Prowell et al., 2009). However, the influence of the rotation of blades on the structural vibration characteristics was not considered in these studies since they only considered the parked condition. It is well known that the centrifugal stiffness will be generated by the rotating blades and the natural frequencies of the blades therefore increase as compared to the parked condition, which in turn affect the dynamic responses of wind turbines (Murtagh et al., 2005). Moreover, the aerodynamic loads acting on the blades are directly related to the geometrical characteristics and rotational velocity of the blades (Hansen, 2008). To more accurately estimate the dynamic behaviours of wind turbines, some researchers modelled the blade as a single or two degrees-of-freedom (DOF) (Fitzgerald et al., 2013; Harte et al., 2012) system and investigated the in-plane and/or out-of-plane responses of the blade by using the home-made codes. It should be noted that many mathematics are included in the calculations, and these methods are not convenient for other researchers/engineers to use. Moreover, aerodynamic loads acting along the height of the tower and the length of the blades are unavoidably different, the structural responses thus might not be realistically obtained by using these simplified lumped mass models. Some other researchers (Lackner & Rotea, 2011; Stewart & Lackner, 2014) modelled the wind turbines by using the open-source program such as FAST. The tower and blades were explicitly developed and the rotation of the blades was considered. However, as explained in the user's guide (Jonkman & Buhl Jr, 2005), FAST can only simulate the elastic behaviours of wind turbines. During strong wind events/earthquakes,

wind turbines may experience nonlinear deformations, which might not be accurately captured by FAST.

Besides these deterministic analyses, some researchers adopted the probabilistic approach by employing fragility analysis to further assess the reliability of wind turbines under aerodynamic, sea wave and/or seismic loadings. For example, Dueñas-Osorio and Basu (2008) investigated the unavailability of wind turbines as a function of wind speed. Their investigations indicated that the vibrations of the tower can lead to the malfunction of the acceleration sensitive equipment installed in the nacelle and reduce the annual wind turbine availability. Mensah and Dueñas-Osorio (2014) and Fitzgerald et al. (2018) proposed using tuned liquid column dampers (TLCDs) and active tuned mass dampers (ATMDs) to mitigate the tower vibrations and improve the reliability of wind turbine tower. Quilligan et al. (2012) performed fragility analysis on the performances of steel and concrete wind turbine towers. Analyses were performed for a range of typical tower heights varying from 88 to 120 m. Kim et al. (2014) analysed the seismic fragility of offshore wind turbines considering the interaction between the monopile foundation and surrounding soil. Patil et al. (2016) compared the influence of near- and far-fault ground motions on the seismic fragility of wind turbine tower. Mardfekri and Gardoni (2013) developed the probabilistic models to predict the deformation, shear and moment demands on the wind turbine tower subjected to aerodynamic and sea wave loadings. Asareh et al. (2016) and Yuan et al. (2017) carried out fragility analyses of wind turbine tower under the simultaneous aerodynamic and seismic loadings. However, it should be noted that in these studies the wind turbines were either assumed in the parked condition (Kim et al., 2014) and the mass of the blades was lumped at the top of the tower (Mardfekri & Gardoni, 2013; Patil et al., 2016) or the rotation of the blades was considered by the simplified 1- or 2-DOF system (Dueñas-Osorio & Basu, 2008; Fitzgerald et al., 2018; Mensah & Dueñas-Osorio, 2014; Quilligan et al., 2012). The influence of blades on the structural responses was therefore not necessarily realistically considered as discussed above. Moreover, all these researches focused on the reliability of wind turbine tower, to the best knowledge of the authors, no open literature reports the vulnerability of the blades under the external vibration sources.

In this chapter, the dynamic behaviours of the wind turbine subjected to the simultaneous aerodynamic and sea wave loadings are investigated in a probabilistic frame and the fragility curves for both the tower and blades under the parked and operating conditions are derived. In particular, the tower and blades of the modern NREL 5 MW wind turbine are explicitly modelled by using the commercially available FE code ABAQUS. The influence of the rotating blades on the aerodynamic loads and dynamic behaviours of the wind turbine is investigated. The uncertainties of the structural mass, stiffness and damping of the wind

turbine are considered to derive the probabilistic demand models of the wind turbine as a function of wind speed. The structure of this chapter is organized as follows: the properties of the wind turbine, the FE modelling and physical uncertainties are presented in Section 4.3; Section 4.4 introduces the external vibration sources, i.e. the aerodynamic and sea wave loadings; the fragility model and numerical results are systematically presented in Section 4.5 and some concluding remarks are summarized in Section 4.6.

4.2 Numerical model description

4.2.1 NREL 5 MW wind turbine

Table 4-1 Properties of the NREL 5 MW

NREL 5 MW baseline wind turbine properties		
Blade	Rotor diameter	126 m
	Hub height	90 m
	Cut-in, rated and cut-out wind speed	3 m/s, 11.4 m/s, 25 m/s
	Cut-in and rated rotor speed	6.9 rpm, 12.1 rpm
	Length	61.5 m
	Overall (integrated) mass	17,740 kg
	Structural damping ratio	0.5%
Hub and Nacelle	Hub diameter	3 m
	Hub mass	56,780 kg
	Nacelle mass	240,000kg
Tower	Height above water	87.6 m
	Top outer diameter and wall thickness	3.87 m, 0.019 m
	Bottom outer diameter and wall thickness	6 m, 0.027 m
	Overall (integrated) mass	347,460 kg
	Structural damping ratio	1%
Monopile	Total length	30 m
	Outer diameter and wall thickness	6 m, 0.027 m

The NREL 5 MW wind turbine is used as an example in the present study since its detailed information has been well documented and is available to the public. The detailed properties of this wind turbine is reported in (Jonkman et al., 2009), and they are tabulated in Table 4-1. For the monopile foundation, the total height is 30 m, in which 10 m is above the mean sea level and another 20 m is in the sea water. Previous studies revealed that soil-monopile interaction might influence the vibration frequencies of the wind turbine and thus the structural responses (e.g. Zuo et al., 2018, 2019b). The fragility curves obtained with and without considering soil-monopile interaction therefore might be slightly different neither. However, it is believed that these differences will not influence the general conclusions of the present study. In this work, not to fuether complicate the problem, the soil-monopile interaction is not considered and the monopile is assumed fully fixed at the seabed level.

In (Jonkman et al., 2019), the mass of each blade is defined, but the thickness of the blades is not explicitly given. In the present study, a uniform thickness is assumed fot the twisted blades,

and the mass of each blade is ensured to be the same as that in (Jonkman et al., 2019). This thickness is computed as 0.019 m.

4.2.2 FE modelling

The detailed three-dimensional (3D) FE model of the NREL 5 MW wind turbine is developed in ABAQUS. The tower and monopile are modelled by shell elements (S4 in ABAQUS). To ensure the same deformation at the connection between the tower and monopile, a tie constraint is applied to connect the cross sections at the bottom of the tower and the top of the monopile. The blades are also explicitly modelled by the shell elements to consider their influence on the structural dynamic behaviours. To simulate the operating condition (i.e. the blades are rotating), a hinge connection between the top of the tower and the root of the blades is defined and the rotational DOF along the out-of-rotor-plane direction is released. In the numerical simulations, a uniform annular velocity is applied to the blades as a boundary condition to consider the rotation of the blades. For the hub and nacelle, only the masses of them are considered and they are lumped at the top of the tower. A convergence test shows that the element sizes of 0.5 m and 1 m in the circumferential and axial directions of the blades, tower and monopile yield a good balance between the computational time and accuracy, thus these element sizes are adopted in the present model. Figure 4-1 shows the FE model of the wind turbine, in which the three blades are labelled as #1 to #3 in an anticlockwise direction.

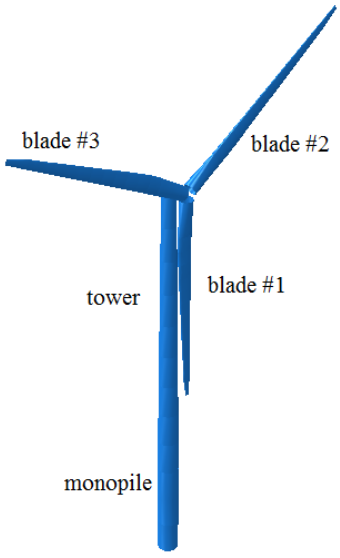

Figure 4-1 FE model of the wind turbine

The materials of the blades, tower and monopile are assumed as ideal elastic-plastic materials and the detailed properties are tabulated in Table 4-2. The density of the tower is taken as 8500 kg/m^3, which is higher than the standard steel to account for the paint, welds, bolts and flanges that are not explicitly included in the numerical model. For the monopile in the sea water, the

vibrating monopile can impart an acceleration to the surrounding sea water, and this interaction is considered by using the added mass model (Bi & Hao, 2016).

After developing the FE model of the wind turbine, an eigenvalue analysis is performed, and the natural frequencies and vibration modes of the wind turbine are calculated (Zuo et al., 2018). These results agree well with those given in (Jonkman et al., 2019), which demonstrates the accuracy of the FE model.

Table 4-2 Material properties of the wind turbine (Jonkman et al., 2009; Burton et al., 2011)

Component	Material	Density (kg/m^3)	Young's modulus (GPa)	Poisson's ratio	Yield strength (MPa)	Plastic strain
Blade	Polyester	1850	38	0.3	700	0.02
Tower	Steel	8500	210	0.3	235	0.01
Monopile	Steel	7850	210	0.3	235	0.01

4.2.3 Physical uncertainties

The structural behaviours of the wind turbine are sensitive not only to the variations of the external vibration sources, but also to the inherent uncertainties of the structural properties. In particular, uncertainties in the structural stiffness, masses and damping ratios of the tower and blades can significantly contribute to the variability in the dynamic responses of the wind turbine. In the present study, the variables considered in the simulations include the material (Young's modulus, density, wall thickness) and damping parameters of the tower and blades. The probability density function (PDF) and coefficient of variation (CoV) of the material parameters are tabulated in Table 4-3. The parameters related to the steel are directly adopted from (Quilligan et al., 2012). For the material of the blades (polyester), the same PDF and CoV are assumed as the steel due to the lack of data.

Table 4-3 Model input variables

Material	Variable	Unit	PDF	Mean (μ)	CoV (%)
Steel	Young's modulus	GPa	Lognormal	210	3
	Density	kg/m^3	Normal	8500	1
	Thickness	mm	Normal	30	2
Polyester	Young's modulus	GPa	Lognormal	38	3
	Density	kg/m^3	Normal	1850	1
	Thickness	mm	Normal	19	2

The damping mechanism of an offshore wind turbine is composed of structural damping, aerodynamic damping and hydrodynamic damping, which account for the contributions of the structure itself, wind and surrounding sea water respectively. The structural damping ratios of the tower and blades are 1% and 0.5% as reported in (Jonkman et al., 2009). Aerodynamic damping results from the relative velocity between the rotating blades and wind. As suggested by Bisoi and Haldar (2014), an aerodynamic damping ratio of 3.5% in the fore-aft direction

for an operating wind turbine is adopted. When the wind turbine is in the parked condition, previous studies (Arany et al., 2016) revealed that the aerodynamic damping is almost zero, and it is adopted in the present study. The hydrodynamic damping results from the drag between the monopile and surrounding sea water and its upper limit is about 0.23% (Arany et al., 2016). Summing all the components together, the damping ratio of the tower is 1.23%. For the rotating blades, it is 4% in the fore-aft direction and the value is 0.5% for the parked blades. In this study, a uniform distribution is assigned to the damping ratios of the tower and blades, and the variability is assumed as 50% with respect to their mean values (Dueñas-Osorio & Basu, 2008; Fitzgerald et al., 2018). The damping of the wind turbine is considered by means of Rayleigh damping and the damping ratio is assumed for the first two vibration modes of the tower and blades.

The Latin Hypercube sampling technique (Dueñas-Osorio & Basu, 2008) is adopted to obtain the random variables and they are then assigned to the numerical models subjected to different wind speeds within the range from 3 to 25 m/s (within which the wind turbine is allowed to operate).

4.3 Aerodynamic and sea wave loadings

In the present study, the wind turbine is subjected to the simultaneous aerodynamic and sea wave loadings, which are stochastically simulated according to the sophisticated simulation techniques. The detailed simulation techniques have been introduced in the authors' another paper (Zuo et al., 2018). For completeness of the present paper, they are briefly introduced in this section. Interested readers can refer to (Zuo et al., 2018) for more detailed information.

For the aerodynamic load acting on the tower, it can be decomposed into a mean and a fluctuating component. The fluctuating aerodynamic loads at different locations along the tower are different but with certain similarities, which is known as the spatial correlation effect. It can be described by a spatial coherency loss function. The power spectral density (PSD) of the fluctuating wind speed at any locations can be calculated by using the Kaimal spectrum (Murtagh et al., 2005),

$$S_{vv}(h,f) = \frac{v_*^2}{f}\frac{200c}{(1+50c)^{5/3}} \tag{4.1}$$

where

$$c = fh/\bar{v}(h) \tag{4.2}$$

and

$$\bar{v}(h) = v_* \ln(h/z_0)/K \tag{4.3}$$

in which h is the height of the location where aerodynamic load is calculated, f is the frequency in Hz, $\bar{v}$ is the mean wind speed, v_* is the friction velocity, c is the Monin coordinate, K is the von-Karman's constant and z_0 is the roughness length. For simplicity, the tower is divided into nine segments and the aerodynamic load is assumed to be the same within each segment. The lengths of the top and bottom segments are 5 and 15 m respectively and the other segments are 10 m. Figure 4-2 shows the fluctuating wind speed PSDs in the top segment (85-90 m along the tower) and the corresponding model values, which are calculated by Eq. (4.1), when the mean wind speeds at the hub height are 3 and 25 m/s respectively. As shown, the simulated results are in well agreement with the corresponding model values. For conciseness, not all the aerodynamic loads on the tower are shown, only the time histories in the top segment are shown in Figure 4-3 when the mean wind speeds at the hub height are 3 and 25 m/s respectively.

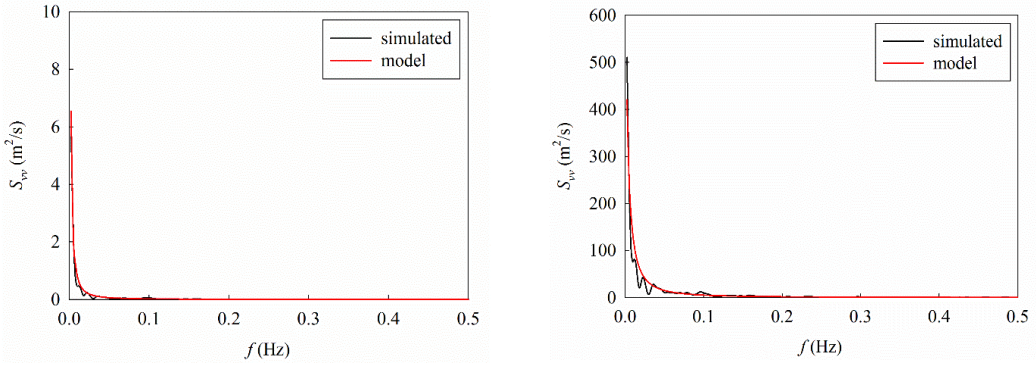

(a) v=3 m/s (b) v=25 m/s

Figure 4-2 Comparisons between the simulated and model PSDs of wind speed

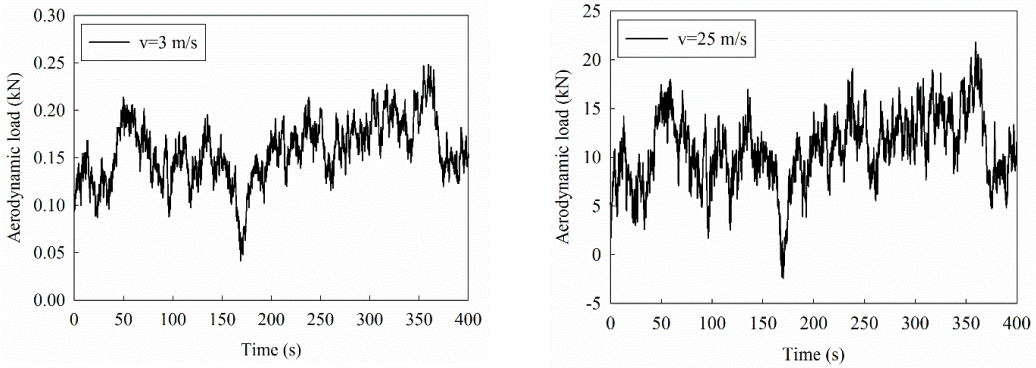

(a) v=3 m/s (b) v=25 m/s

Figure 4-3 Aerodynamic load time histories at the top of the tower

Different from the aerodynamic load on the tower, the aerodynamic loads on the blades are influenced by the wind speed, rotational velocity, pitch angle and geometrical characteristics of the blade. The blade element momentum (BEM) method (Hansen, 2008) is adopted in the

present study to estimate the aerodynamic loads on the blades. In this method, it is assumed that no aerodynamic interaction between different sections along the rotor, the blade therefore can be divided into several elements and the aerodynamic load acting on each element can be calculated separately.

The relative wind velocity on each element of the blade (v_{rel}) is given by

$$v_{rel}(r) = \sqrt{\left(\bar{v}(1-a) + v_f\right)^2 + \left(\Omega r(1+a')\right)^2} \tag{4.4}$$

where r is a radial distance of the element from the centre of the hub, a and a' are the axial and tangential induction factors respectively, Ω is the rotational velocity in rad/s and v_f is the fluctuating wind speed. It should be noted that the PSD of the fluctuating wind speed is a time-variant spectrum due to the height of the blade experiences a sinusoidal variation in magnitude with the rotation of the blades. Not to further complicate the problem, an isotropic, homogenous wind turbulence at the height of the hub is assumed to represent the wind turbulence over the rotor field in the present study. According to this assumption, the fluctuating wind speed in Eq. (4.4) can be easily calculated by using the PSD of wind velocity at the hub height defined in Eq. (4.1).

After the relative wind speed is determined, the local lift and drag forces on each element then can be computed as follows

$$p_l(r) = \frac{1}{2}\rho v_{rel}^2(r) l(r) C_{lb} \tag{4.5}$$

$$p_d(r) = \frac{1}{2}\rho v_{rel}^2(r) l(r) C_{db} \tag{4.6}$$

where ρ is the air density, l is the chord length and C_{lb} and C_{db} are the lift and drag coefficients of the blade respectively, which are related to the flow, pitch and pre-twist angles. Figure 4-4 shows the flap-wise and edgewise aerodynamic loads on the blade #2 when the mean wind speeds at the hub height are 3 and 25 m/s respectively.

For the sea wave loading acting on the monopile, the JONSWAP spectrum (Hasselmann et al., 1973) is used to simulate the sea surface elevation and it can be described as follows

$$S_{\eta\eta}(f) = \alpha_P g^2 (2\pi)^{-4} f^{-5} exp\left[-\frac{5}{4}\left(\frac{f_m}{f}\right)^4\right] \gamma^{exp\left[-\frac{(f-f_m)^2}{2\sigma^2 f_m^2}\right]} \tag{4.7}$$

in which g is the gravitational acceleration and γ is the peak enhancement factor and a value of 3.3 is used in the simulation. α_P, f_m and σ are three constants, which are

$$\alpha_P = 0.076(Fg/v_{10}^2)^{-0.22} \tag{4.8}$$

$$f_m = 11(v_{10}F/g^2)^{-1/3}/\pi \tag{4.9}$$

$$\sigma = \begin{cases} 0.07 & f \le f_m \\ 0.09 & f > f_m \end{cases} \tag{4.10}$$

where F is the fetch length and v_{10} is the mean wind speed at 10 m above the sea surface, which can be determined by Eq. (4.3).

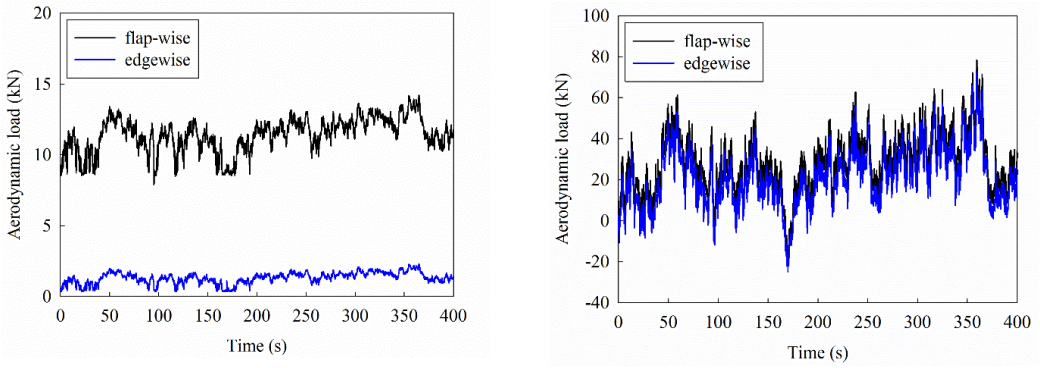

(a) v=3 m/s (b) v=25 m/s

Figure 4-4 Flap-wise and edgewise aerodynamic loads on the blade #2

The sea wave length is generally much larger than the dimension of the monopile, Morison equation therefore can be adopted to calculate the sea wave load on the monopile

$$F_w = \frac{1}{2}\rho_w C_{dp} d_p |v_x| v_x + \rho_w C_m A_p a_x \tag{4.11}$$

where F_w is the transverse sea wave load per unit length of the monopile, ρ_w is the sea water density, d_p, A_p are the outer diameter and cross section area of the monopile respectively, C_{dp}, C_m are the drag and inertia coefficients respectively, v_x and a_x are the velocity and acceleration of water particles respectively, and the detailed calculation of these two parameters can be found in (Zuo et al., 2018) and is not introduced herein. Similar to the tower, the monopile in the sea water is equally divided into two segments. Figure 4-5 shows the simulated sea wave load time histories at the mean sea level when the mean wind speeds at the hub height are 3 and 25 m/s respectively and Figure 4-6 compares the PSDs of the simulated sea surface elevation and the model. Good matches are observed as shown.

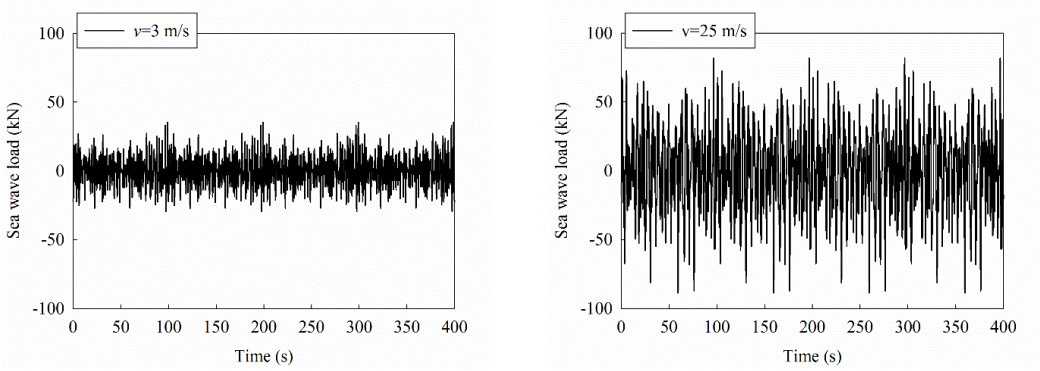

(a) v=3 m/s (b) v=25 m/s

Figure 4-5 Sea wave load time histories at the mean sea level

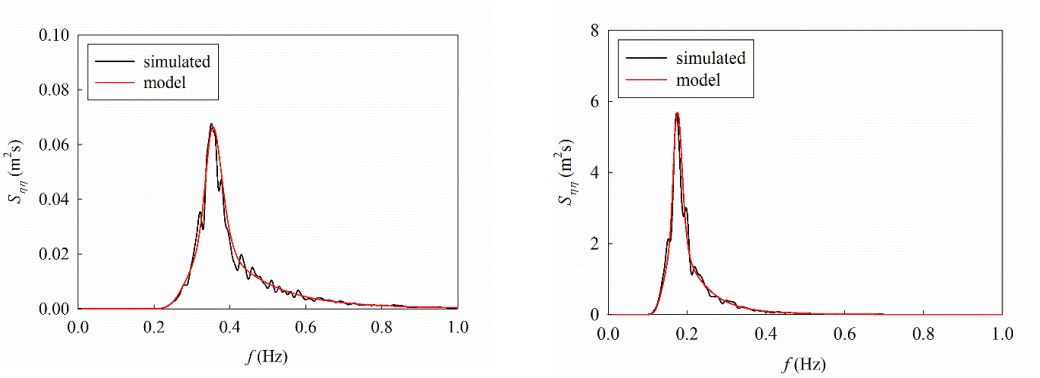

(a) v=3 m/s (b) v=25 m/s

Figure 4-6 Comparisons between the simulated and model PSDs of sea surface elevation

As introduced above, the tower, blade and monopile are divided into several segments in the simulation of the aerodynamic and sea wave loadings. In the FE model, a reference point is developed in each segment and coupled to the cross section of the corresponding segment, the simulated aerodynamic and sea wave loadings are applied to these reference points as the external loadings.

4.4 Fragility analysis of wind turbine

4.4.1 Fragility function

The structural fragility can be defined as the conditional probability of a structural demand to reach or exceed the structural capacity at a given excitation level. The present study constructs the fragility curves of the tower and blades by using the out-of-plane displacement responses obtained from the numerical simulations. For the fragility curve calculated based on the in-plane responses of the blades, they are not included in the present study due to the lack of data to define the corresponding limit state levels.

In seismic response analysis, fragility curves can normally be generated by using the incremental dynamic analysis (IDA) method or the probability seismic demand analysis (PSDA) method (Zhang & Huo, 2009). In the former approach, all motions are scaled to the selected intensity levels and IDA is performed at different hazard levels. A large amount of numerical simulations are needed in order to generate the fragility curve by using the IDA method. On the other hand, the PSDA approach uses unscaled earthquake ground motions and regression analysis to obtain the mean and standard deviation of the structural response at each intensity level by assuming a logarithmic correlation between the median engineering demand parameters and a selected intensity level. Compared to the IDA approach, the PSDA method requires much less computational effort, but can result in reasonable estimations of the fragility curve (Zhang & Huo, 2009). It is therefore widely used in the fragility analyses for engineering structures when they are subjected to the earthquake loadings. Recently, the PSDA method is also adopted in the wind-induced fragility analyses of wind turbines (Dueñas-Osorio & Basu, 2008; Fitzgerald et al., 2018; Mensah & Dueñas-Osorio, 2014). In the present study, the PSDA method is used and the mean wind speed at the hub height is selected as the fragility hazard parameter though the aerodynamic and sea wave loadings are considered in the analyses due to the fact that the structural responses induced by the sea wave load are much smaller than those induced by the aerodynamic load (Zuo et al., 2018). Similar to the seismic demand model developed in (Li et al., 2016, 2018), the structural demands for a wind turbine under the combined wind and sea wave excitations are estimated by using a power law functional form as

$$D_w = m(v_w)^n \; or \; ln(D_w) = lnm + nln(v_w) \tag{4.12}$$

where D_w is the median wind-induced out-of-plane displacement of the wind turbine, v_w is the mean wind speed at the hub height, and m and n are coefficients obtained from regression analysis.

The power law model (Eq. (4.12)) is used to develop the fragility curves by providing an estimation of the likelihood of displacement threshold exceedance as a function of wind speed. The conditional probability of exceeding a prescribed displacement is defined as a lognormal distribution:

$$P[D_w > D_{LS}|v_w] = \Phi\left(\frac{ln(D_w) - ln(D_{LS})}{\beta_{D_w|v_w}}\right) \tag{4.13}$$

in which D_{LS} represents the displacement threshold that initiates changes in the performance state of the wind turbine, $\Phi(\cdot)$ is the standard normal cumulative distribution function, $\beta_{D_w|v_w}$ is the dispersion of the logarithmic displacement response as a function of wind speed.

For simplicity, it is normally assumed that the parameter $\beta_{D_w|v_w}$ is independent of v_w and can be expressed as follows (Li et al., 2018)

$$\beta_{D_w|v_w} = \sqrt{\frac{\sum_{j=1}^{N}\left[ln(D_j) - ln(D_{wj})\right]^2}{N-2}} \tag{4.14}$$

where D_j is the jth realization of the wind-induced structural demand, D_{wj} is the median displacement of the wind turbine corresponding to the jth wind speed and can be calculated by Eq. (4.12), and N is the number of conducted nonlinear time history analyses. In the present study, 45 nominally identical but statistically different wind turbine models are generated based on the random variables defined in Section 4.3.3, and these 45 wind turbine models are paired with 45 different wind speeds to calculate the structural responses and further estimate the fragility curves.

4.4.2 Limit state levels

To assess the safety of the wind turbine subjected to the aerodynamic and sea wave loadings, limit states should be defined. Four limit states are widely adopted in the analyses of offshore wind turbines, which are the serviceability limit state (SLS), ultimate limit state (ULS), fatigue limit state (FLS) and accidental limit state (ALS) (DNV, 2014). The SLS and ULS are considered in the present study to determine the damage levels of the wind turbine. The SLS is the deformation tolerances to ensure the regular and normal operation of the wind turbine and the ULS corresponds to the maximum load-carrying capacity (e.g. yielding, buckling, overturning etc.) of a structure and structural components. In the present study, a damage criterion based on the displacements at the top of the tower and the tip of the blade is adopted and four damage states are defined depending on the different demand parameters of the wind turbine. These four damage states are introduced individually as follows:

Damage state one (DS_1) corresponds to the SLS. The deformation tolerance is usually defined in the design basis and it is often specified in terms of the maximum allowable rotation of the pile head at the seabed in a vertical plane. DNV (2014) specifies that the maximum allowable tilt of the tower should be less than 0.5°, which incorporates the error during the construction and it normally ranges from 0.2° to 0.25°. The maximum allowable tilt of the tower due to external vibration sources is therefore about 0.25°. In the present study, the height of the wind turbine is near 120 m, so the tilt of the tower can be converted to the displacement at the top of the tower, and it is 0.524 m.

To determine the other three damage states of the tower, pushover analysis is carried out to investigate the nonlinear deformation characteristics of the wind turbine tower and to find the corresponding critical displacement. This procedure is achieved by gradually increasing the

displacement applied in the fore-aft direction at the top of the tower and considering the first buckling mode as initial imperfection (Dimopoulos & Gantes, 2012). It is obvious that the maximum internal forces (bending moment and shear force) appear at the bottom of the monopile. The results from the pushover analysis can describe the relationship between the internal forces at the bottom of the monopile and the displacement at the top of the tower. The normal stress is adopted as the yield criterion for the wind turbine in the present study, which can be calculated by

$$\sigma = \frac{M}{W} - \frac{N}{A} \tag{4.15}$$

$$W = \frac{\pi d_1^3}{32}\left[1 - \left(\frac{d_2}{d_1}\right)^4\right] \tag{4.16}$$

$$A = \frac{\pi}{4}(d_1^2 - d_2^2) \tag{4.17}$$

in which M is the bending moment as shown in Figure 4-7(a), N is the axial force, d_1 and d_2 are the outer and internal diameters of the monopile respectively.

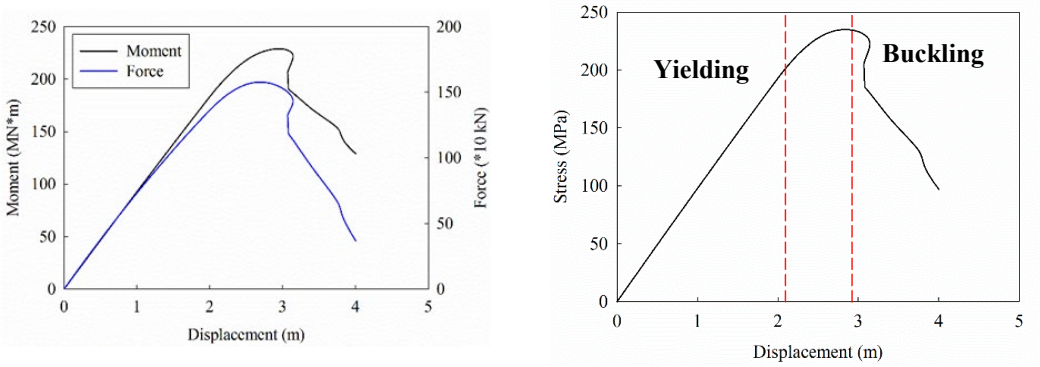

(a) bending moment and shear force (b) stress

Figure 4-7 Moment, shear force and stress and top displacement relationship from pushover analysis

Figure 4-7(a) shows the relationship between the bending moment/shear force at the bottom of the monopile and the displacement applied at the top of the tower. By substituting them into Eqs. (4.15), (4.16) and (4.17), the normal stress at the bottom of the monopile can be obtained and it is presented in Figure 4-7(b). As shown, nonlinear behaviour begins to occur at a displacement of 2.097 m, which indicates that the wind turbine tower starts to yield at this displacement. It also can be observed that the internal force/stress-displacement relationship shows a snap-back behaviour due to the local buckling of the tower when the displacement at the top of the tower reaches 2.922 m. Figure 4-8 shows the local buckling of the wind turbine from the pushover analysis, in which the blades are not presented to more clearly show the result. As shown, the buckling of the wind turbine appears at a point approximately 10 m above

the bottom of the monopile foundation, which is consistent with previous studies (e.g. Asareh et al., 2016).

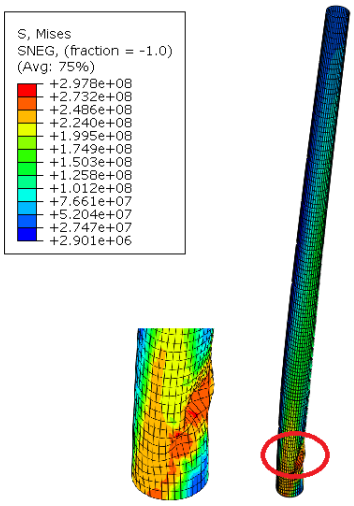

Figure 4-8 Buckling of the wind turbine tower (deformation is amplified three times)

The above results show that buckling occurs at a much larger displacement compared to the yielding. In the present study, wind and wave loadings are considered as excitations, buckling is very unlikely to appear, and it is not adopted as a damage state. Following the suggestions of many researchers (e.g. Mensah & Dueñas-Osorio, 2014; Kim et al., 2014), damage states DS_2-DS_4 are defined as 30%, 40% and 50% of the yielding displacement of the tower, which are 0.629 m, 0.839 m and 1.049 m respectively. Table 4-4 tabulates the four limit states of the wind turbine tower. However, it is worth noting that when the wind turbine has opening and stiffening (Dimopoulos & Gantes, 2012; Guo et al., 2013) or it is subjected to other vibration sources such as earthquake, buckling might occur, and it should be considered as a limit state in the analyses.

Table 4-4 Damage states of the wind turbine tower

Damage states	Critical displacement	Description
DS_1	0.524 m	SLS
DS_2	0.629 m	30% of yield stress
DS_3	0.839 m	40% of yield stress
DS_4	1.049 m	50% of yield stress

Different from the tower, it is not realistic to define the damage limit states (the critical displacement) of the blade by using the pushover method, since the blade is made of high-strength material (e.g. for the polyester, the yield strength is 700 MPa (Burton et al., 2011)), which is very difficult to yield. On the other hand, a minimum clearance between the tip of the blade and the tower should be specified to avoid the possible collision between the rotor and the tower during the extreme conditions. A tilt angle of 5° between the rotor axis and the horizontal plane is used in the design of the wind turbine (DNV, 2002). As shown in Table

4-1, the rotor radius is 63 m, so the maximum allowable displacement at the tip of the blade subjected to the external loads is 5.5 m. Similar to the limit states of the tower as defined above, the four limit states for the blade are defined as 20%, 30%, 40% and 50% of the maximum allowable displacement at the tip of the blade (i.e. 5.5 m), which are 1.100, 1.650, 2.200 and 2.750 m respectively.

4.4.3 Fragility curves of the wind turbine

Based on the prescribed damage states of the tower and blades, the fragility curves of the wind turbine can be calculated by using Eqs. (4.12) and (4.13). To examine the influence of operational conditions on the fragility curves of the wind turbine, two scenarios are considered. In the first scenario, the wind turbine is in the parked condition with the locations of the blades shown in Figure 4-1. In the second scenario, the blades are rotating at a uniform velocity, which is related to the wind speed. For the NREL 5 MW wind turbine, the blades start to rotate at a cut-in velocity of 6.9 rounds per minute (0.72 rad/s) when the wind speed is 3 m/s, and the maximum wind energy output will be achieved at a rated velocity of 12.1 rounds per minute (1.27 rad/s) when the wind speed is or above 11.4 m/s. The rotational velocity is assumed as a linear variation between the cut-in and rated velocities. In the present study, the wind speeds ranging from 3 to 25 m/s with an interval of 0.5 m/s are considered (in total 45 wind speeds, i.e. N=45 in Eq.(4.14)), which correspond to the normal operating range of the wind turbine. The aerodynamic and sea wave loads shown in Figure 4-3 and Figure 4-5 are applied to the tower. For the aerodynamic loads on the blades, they depend on the rotational velocity as introduced in Section 4.4. Different aerodynamic loads on the blades are simulated according to the different wind speeds and rotational velocities. It should be noted that the fragility of the wind turbine is related to the maximum structural response, which is influenced by the duration of the external excitations. All the numerical results in the present study are based on a relatively long duration of 400 s as shown in Section 4.4.

4.4.3.1 Parked condition

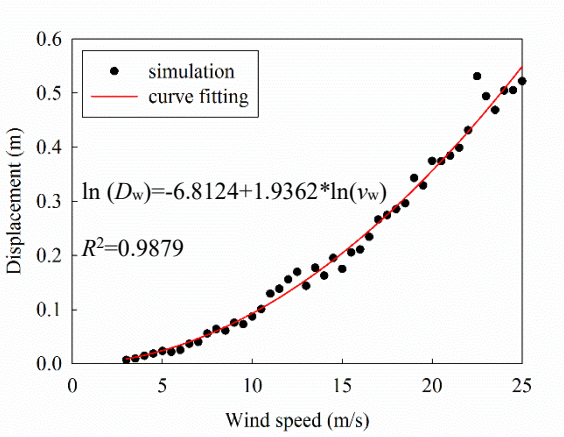

Figure 4-9 The maximum displacements at the tower top and the corresponding wind-induced demand model in the parked condition

It is obvious that the maximum responses of the tower and blades occur at the top of the tower and the tip of the blade when the wind turbine is subjected to the simultaneous aerodynamic and sea wave loadings. Here only the maximum responses of the tower and blades are used to develop the fragility curves. Figure 4-9 shows the peak displacements at the top of the tower under different wind speeds and the probabilistic wind-induced demand model (red curve) constructed based on the regression analysis (Eq. (4.12)) by using these maximum displacements. The values of the parameters m, n and $\beta_{D_w|v_w}$ are tabulated in Table 4-5. As shown in Figure 4-9, the power law model can well describe the relationship between the displacement response at the top of the tower and the wind speed with a coefficient of determination R^2 equalling to 0.9879. It also can be seen that the uncertainties in the Young's modulus, wall thickness, density and damping ratio of the tower marginally affect the displacement responses of the tower when the wind speed is below 10.5 m/s. This is because the displacements at the top of the tower are small when the wind speeds are low. With the increment of the wind speed, the uncertainties of these parameters have more obvious effect on the responses of the tower and the dispersion of the displacement responses becomes larger.

Table 4-5 Parameters to characterize wind-induced displacement fragility curves in the parked condition

Component	m	n	$\beta_{D_w\|v_w}$
Tower	0.0011	1.9362	0.1252
Blade #1	0.0017	2.1319	0.2479
Blade #2 (#3)	0.0021	2.1001	0.2115

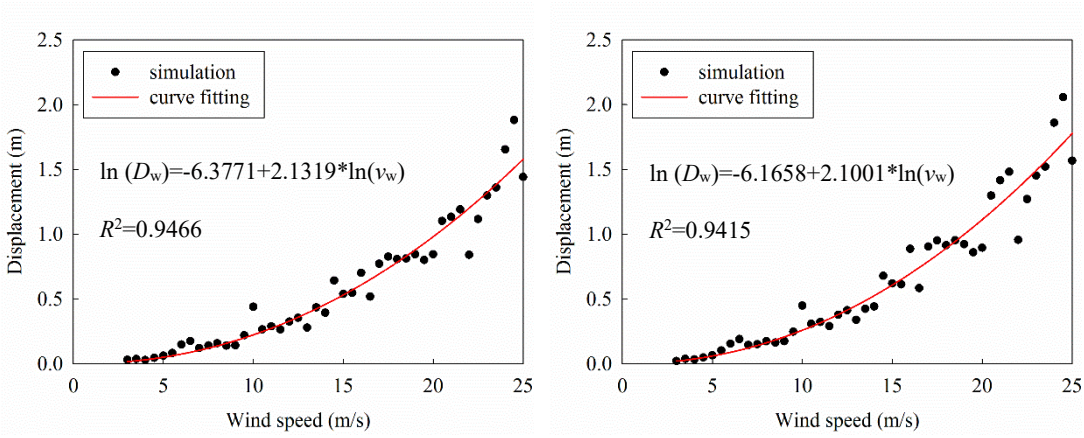

(a) blade #1 (b) blade #2 (#3)

Figure 4-10 The maximum displacements at the blade tips and the corresponding wind-induced demand models in the parked condition

Figure 4-10 shows the maximum displacements at the tips of the blades under different wind speeds and the corresponding probabilistic wind-induced demand models. The values of the parameters for the demand models are also tabulated in Table 4-5. It should be noted that the displacement responses of blade #3 are the same as those of blade #2 due to the fact that the geometrical configurations and locations of blades #2 and #3 are symmetric as shown in Figure 4-1, and the same excitations are applied on those two blades. As shown in Figure 4-10, the coefficients of determination R^2 in the probabilistic wind-induced demand models of blades #1 and #2 are 0.9466 and 0.9415 respectively, which again indicate the good fits of the model to the simulated responses of the blades. It also can be observed from Figure 4-10 that the maximum displacements at the tip of blade #1 are slightly smaller than those at the tip of blade #2 since blade #1 locates at a lower position than blade #2 and the aerodynamic loads acting on blade #1 are smaller than those on blade #2 for a particular wind speed. Comparing Figure 4-10 with Figure 4-9, it can be seen that the dispersion of the displacement responses of the blades is larger than that of the tower. This is because as tabulated in Table 4-3, although the PDF and CoV of the blade parameters are assumed the same as those of the tower, the mean value of the Young's modulus of the blade is 38 GPa, which is much smaller than that of the tower of 210 GPa. A small variation on the input values will result in more obvious structural response changes, which in turn leads to the larger dispersion of the displacement responses of the blades as compared to the tower.

After the probabilistic wind-induced demand models of the tower and blades are determined, the fragility curves of the tower and blades with respect to different damage states can be calculated by using Eq. (4.13). Figure 4-11 and Figure 4-12 show the fragility curves of the tower and blades respectively when the wind turbine is in the parked condition. For brevity,

only the fragilities of the wind turbine at the cut-in (3 m/s), rated (11.4 m/s) and cut-out (25 m/s) wind speeds are discussed below.

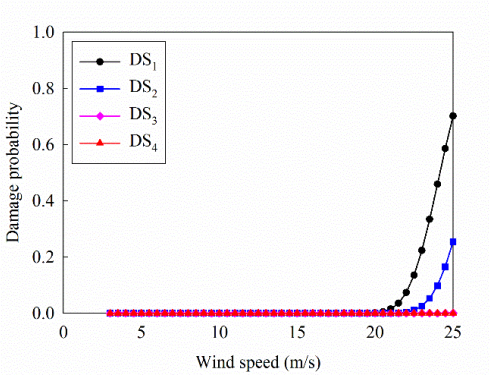

Figure 4-11 Wind-induced fragility curves for the tower in the parked condition.

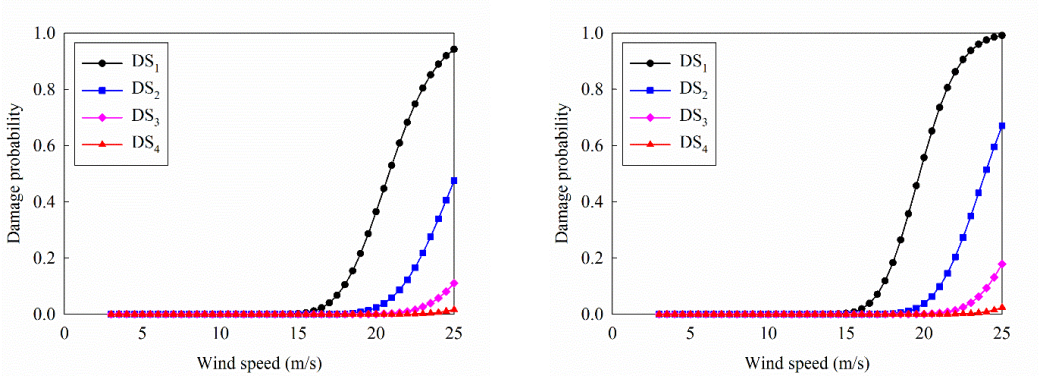

(a) blade #1 (b) blade #2 (#3)

Figure 4-12 Wind-induced fragility curves for the blades in the parked condition

As shown in Figure 4-11 and Figure 4-12, the likelihood of exceeding the four prescribed displacement levels is near zero for the tower and blades at cut-in and rated wind speeds of the parked wind turbine. When the wind speed is 25 m/s, Figure 4-11 shows that the damage probabilities of the tower are 70.2%, 25.5%, 0.2% and 0%, respectively for the four displacement thresholds, which indicates that the tower is very unlikely to yield under this wind condition. It might be worth reiterating that buckling occurs at a much larger displacement (2.922 m as shown in Figure 4-8) than that when yielding occurs (2.097 m), thus the wind turbine tower is also less likely to fail as a buckling damage, which supports the selection of limit states as presented in Section 4.5.2. For the blades, Figure 4-12 shows that the probabilities of the limit state exceedance for blade #1 are 94.2%, 47.5%, 11.1% and 1.7% respectively and they are 99.1%, 67.1%, 17.9% and 2.4% respectively for blade #2 when the wind speed reaches 25 m/s. The probabilities of exceeding the predefined displacement thresholds of blade #2 are higher than those of blade #1 since the displacement responses of blade #2 are larger as discussed above. The results also show that the potentials of the blade crossing the four limit states are all higher than the tower. This is actually deemed necessary

and reasonable, since the blades are supported by the tower, the damage of the tower will lead to the total malfunction of the wind turbine. The tower therefore can be regarded as a more important component than the blades, and it should be designed with higher reliability.

4.4.3.2 Operating condition

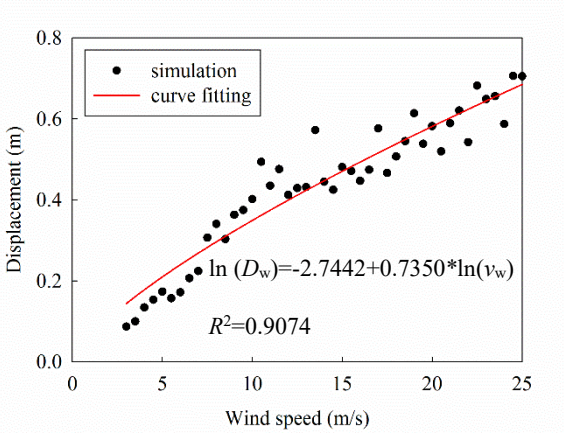

Figure 4-13 The maximum displacements at the tower top and the corresponding wind-induced demand model in the operating condition

This section presents the fragility of the operating wind turbine under the simultaneous aerodynamic and sea wave loadings. Figure 4-13 shows the peak displacements at the top of the tower under different wind speeds and the fitted probabilistic wind-induced demand models. Table 4-6 tabulates the values of the parameters m, n and $\beta_{D_w|v_w}$ from regression analyses. It can be seen that the dispersion of the maximum displacements at the top of the tower in the operating condition is larger than that of the parked wind turbine as shown in Figure 4-9. This is because the aerodynamic loads on the rotating blades are larger than those on the parked blades, which results in more severe interaction between the top of the tower and the root of the blades.

Table 4-6 Parameters to characterize wind-induced displacement fragility curves in the operating condition

Component	m	n	$\beta_{D_w\|v_w}$
Tower	0.0643	0.7350	0.1810
Blade #1	0.4420	0.4593	0.2075
Blade #2	0.5438	0.3989	0.1809
Blade #3	0.5816	0.3730	0.1874

Figure 4-14 shows the maximum displacements at the tips of the blades under different wind speeds and the corresponding probabilistic wind-induced demand models. The fitted values are also tabulated in Table 4-6. As shown in Figure 4-14 and Table 4-6, different from the displacement responses of the blades in the parked condition, when the blades are rotating, the displacements at the blade tips increases at a slow rate with the increasing of the wind speed, i.e. n<1 as tabulated in Table 4-6. This is because the aerodynamic damping in the parked

condition is about zero, however, as stated in Section 4.3.3, the aerodynamic damping appears due to the rotation of the blades, and this damping is related to the rotational velocity and wind speed. Large rotational velocity and wind speed result in large aerodynamic damping, which slows down the increasing rate of the displacement responses of the blades. Moreover, the pitch control mechanism in the blades is initiated when the wind speed is above the rated speed to limit the aerodynamic loads acting on the blades and maintain wind energy output by changing pitch angles during operation, which is considered in the simulation of the aerodynamic loads in the present study. As shown in Figure 4-14, the maximum displacement responses of the three blades are slightly different when the wind turbine is in the operating condition. This is because of the influence of the initial positions of the blades.

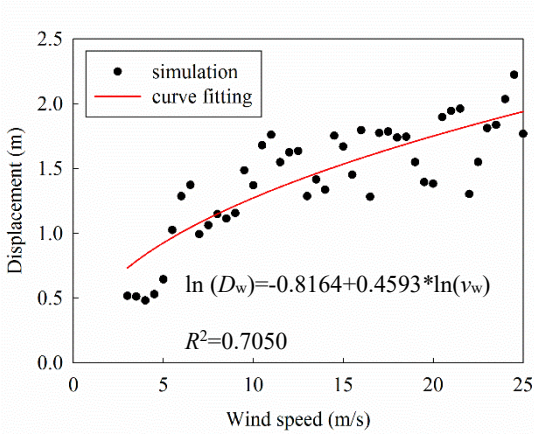

(a) blade #1

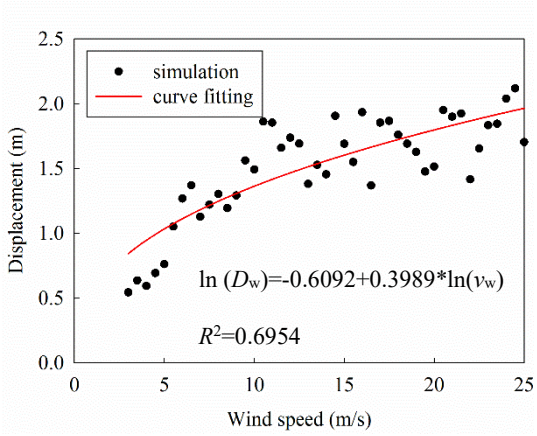

(b) blade #2

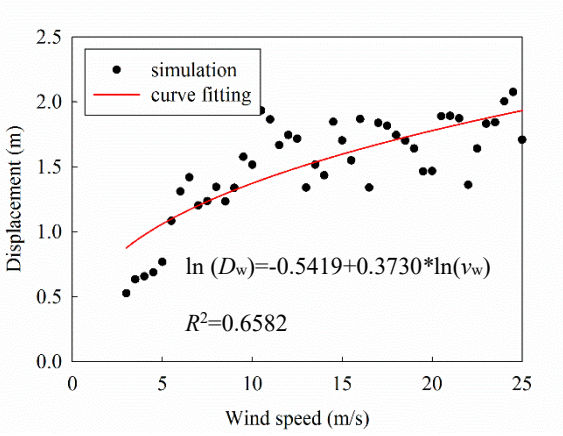

(c) blade #3

Figure 4-14 The maximum displacements at the blade tips and the corresponding wind-induced demand models in the operating condition

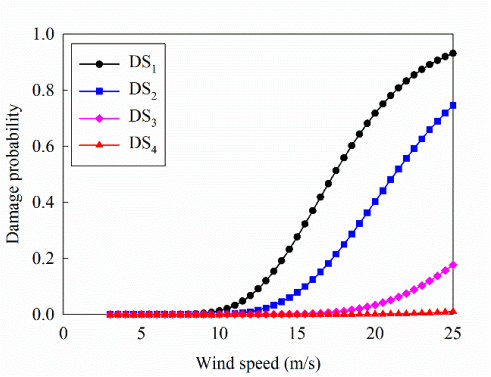

Figure 4-15 Wind-induced fragility curves for the tower in the operating condition

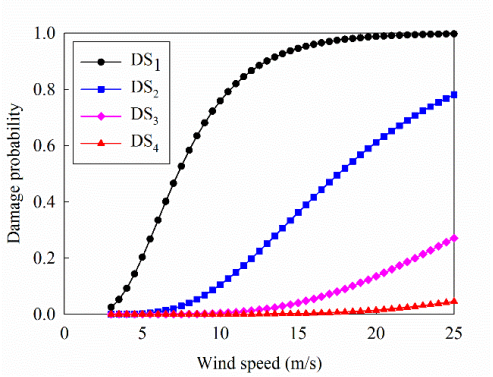

(a) blade #1

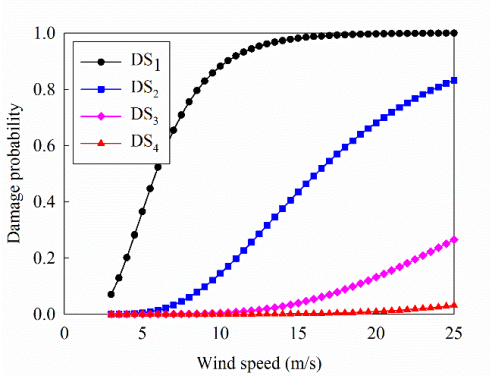

(b) blade #2

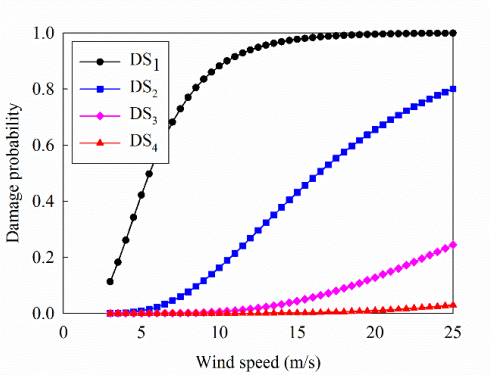

(c) blade #3

Figure 4-16 Wind-induced fragility curves for the blades in the operating condition

Figure 4-15 and Figure 4-16 show the fragility curves of the tower and blades respectively when the wind turbine is in the operating condition. As shown in Figure 4-15, the likelihood of exceeding the prescribed limit states of the tower is about zero when the wind speed is 3 m/s. When the wind turbine is subjected to the rated speed of 11.4 m/s, the damage probabilities of the tower are 4.7%, 0.6%, 0% and 0% respectively. When the wind speed increases to 25 m/s, they become 93.1%, 74.5%, 17.7% and 1.1% respectively. Compared to the parked condition, it can be seen that the probabilities of exceeding DS_1-DS_4 are larger in

the operating condition, this is because larger aerodynamic loads acting on the wind turbine lead to larger median displacement responses of the tower as shown in Figure 4-13.

As shown in Figure 4-16, when the wind speed is 3 m/s, the probability of reaching DS_1 for the three blades are 2.5%, 7.1% and 11.2% respectively and the likelihood of exceeding the other three states is near zero. When the wind turbine is operating under the rated speed of 11.4 m/s, the damage probabilities of blade #1 are 84.4%, 17.3%, 1.0% and 0% respectively for the four displacement thresholds defined above. For the blade #2, they are 93.2%, 22.7%, 1.0% and 0% respectively and the corresponding values are 92.8%, 24.1%, 1.3% and 0% for blades #3. When the wind speed is 25 m/s, the damage probabilities of blade #1 are 99.7%, 78.1%, 27.1% and 4.6% respectively. For blade #2, the corresponding values are 99.9%, 83.2%, 26.5% and 3.1% and they are 99.9%, 80.0%, 24.4% and 3.0% respectively for blade #3. Similar to the tower, the probabilities of DS_1-DS_4 exceedance of the rotating blades are larger than those of the parked blades, which can be explained again by the larger median displacement responses (refer to Figure 4-10 and Figure 4-14).

4.5 Conclusions

In this chapter, the dynamic behaviours of the NREL 5 MW wind turbine subjected to the simultaneous aerodynamic and sea wave loadings are investigated by taking the uncertainties of the material and damping into account. Different damage states for the tower and blades are defined based on the serviceability and ultimate limit states. The fragility curves of the tower and blades are developed. Numerical results show that:

(1) The uncertainties of the material and damping ratio have more obvious influence on the dynamic responses of the blades compared to the tower. The dispersion of the displacement responses is larger in the operating condition compared to the parked condition. The maximum displacements of the tower and blades are larger in the operating condition than those in the parked condition.

(2) The yielding of the wind turbine tower is very unlikely to occur when the wind speeds are within the cut-in and cut-out range in either the operating or parked conditions. However, the probabilities of the limit state exceedance of the blades are more apparent in both conditions.

(3) The aerodynamic damping and the pitch control system have a considerable influence on the wind-induced displacement responses of the wind turbine, which slow down the increasing rate of the displacement responses with the increasing of the wind speed.

It should be noted that the fragility of the wind turbine in the in-plane direction is not developed in this chapter due to the lack of an appropriate damage criterion of the in-plane response for the blades as discussed in the paper, which needs to be further investigated in the future.

4.6 References

Arany, L., Bhattacharya, S., Macdonald, J., & Hogan, S. (2016). Closed form solution of Eigen frequency of monopile supported offshore wind turbines in deeper waters incorporating stiffness of substructure and SSI. *Soil Dynamics and Earthquake Engineering*, *83*, 18-32.

Asareh, M., Schonberg, W., & Volz, J. (2016). Fragility analysis of a 5-MW NREL wind turbine considering aero-elastic and seismic interaction using finite element method. *Finite Elements in Analysis and Design*, *120*, 57-67.

Bi, K., & Hao, H. (2016). Using pipe-in-pipe systems for subsea pipeline vibration control. *Engineering Structures*, *109*, 75-84.

Bisoi, S., & Haldar, S. (2014). Dynamic analysis of offshore wind turbine in clay considering soil-monopile-tower interaction. *Soil Dynamics and Earthquake Engineering*, *63*, 19-35.

Burton, T., Jenkins, N., Sharpe, D., Bossanyi, E. (2011). Wind energy handbook 2nd ed. John Wiley & Sons.

Colwell, S., & Basu, B. (2009). Tuned liquid column dampers in offshore wind turbines for structural control. *Engineering Structures*, *31*(2), 358-368.

DNV/Risø National Laboratory. (2002). Guidelines for design of wind turbines 2nd ed. Denmark: DNV and Risø National Laboratory.

Det Norske Veritas (DNV). (2014). DNV-OS-J101: Design of offshore wind turbine structures. Copenhagen, Denmark: DNV.

Dimopoulos, C. A., & Gantes, C. J. (2012). Experimental investigation of buckling of wind turbine tower cylindrical shells with opening and stiffening under bending. *Thin-Walled Structures*, *54*, 140-155.

Dueñas-Osorio, L., & Basu, B. (2008). Unavailability of wind turbines due to wind-induced accelerations. *Engineering Structures*, *30*(4), 885-893.

Fitzgerald, B., & Basu, B. (2016). Structural control of wind turbines with soil structure interaction included. *Engineering Structures*, *111*, 131-151.

Fitzgerald, B., Basu, B., & Nielsen, S. R. K. (2013). Active tuned mass dampers for control of in-plane vibrations of wind turbine blades. *Structural Control and Health Monitoring*, *20*(12), 1377-1396.

Fitzgerald, B., Sarkar, S., & Staino, A. (2018). Improved reliability of wind turbine towers with active tuned mass dampers (ATMDs). *Journal of Sound and Vibration*, *419*, 103-122.

Global Wind Energy Council (GWEC). (2018). https://gwec.net/51-3-gw-of-global-wind-capacity-installed-in-2018/.

Guo, L., Yang, S., & Jiao, H. (2013). Behavior of thin-walled circular hollow section tubes subjected to bending. *Thin-Walled Structures*, *73*, 281-289.

Haldar, S., Sharma, J., & Basu, D. (2018). Probabilistic analysis of monopile-supported offshore wind turbine in clay. *Soil Dynamics and Earthquake Engineering*, *105*, 171-183.

Hansen, M. O. L. (2008). Aerodynamics of wind turbines 2nd ed. London: Earthscan.

Harte, M., Basu, B., & Nielsen, S. R. K. (2012). Dynamic analysis of wind turbines including soil-structure interaction. *Engineering Structures*, *45*, 509-518.

Hasselmann, K., Barnett, T., Bouws, E., Carlson, H., Cartwright, D., Enke, K., Walden, H. (1973). Measurements of wind-wave growth and swell decay during the Joint North Sea Wave Project (JONSWAP). Hamburg: Deutches Hydrographisches Institut.

Jonkman, J., Butterfield, S., Musial, W., & Scott, G. (2009). Definition of a 5-MW reference wind turbine for offshore system development. (Technical Report No. NREL/TP-500-38060). Golden, CO: National Renewable Energy Laboratory.

Jonkman, J., & Buhl Jr, M. L. (2005). FAST user's guide. Golden, CO: National Renewable Energy Laboratory.

Katsanos, E. I., Thöns, S., & Georgakis, C. T. (2016). Wind turbines and seismic hazard: a state-of-the-art review. *Wind Energy*, *19*(11), 2113-2133.

Kim, D. H., Lee, S. G., & Lee, I. K. (2014). Seismic fragility analysis of 5 MW offshore wind turbine. *Renewable Energy*, *65*, 250-256.

Kjørlaug, R. A., & Kaynia, A. M. (2015). Vertical earthquake response of megawatt-sized wind turbine with soil-structure interaction effects. *Earthquake Engineering & Structural Dynamics*, *44*(13), 2341-2358.

Lackner, M. A., & Rotea, M. A. (2011). Passive structural control of offshore wind turbines. *Wind Energy*, *14*(3), 373-388.

Li, C., Hao, H., Li, H., & Bi, K. (2016). Seismic fragility analysis of reinforced concrete bridges with chloride induced corrosion subjected to spatially varying ground motions. *International Journal of Structural Stability and Dynamics*, *16*(5), 1550010.

Li, C., Li, H., Hao, H., Bi, K., & Chen, B. (2018). Seismic fragility analyses of sea-crossing cable-stayed bridges subjected to multi-support ground motions on offshore sites. *Engineering Structures*, *165*, 441-456.

Mardfekri, M., & Gardoni, P. (2013). Probabilistic demand models and fragility estimates for offshore wind turbine support structures. *Engineering Structures*, *52*, 478-487.

Mensah, A. F., & Dueñas-Osorio, L. (2014). Improved reliability of wind turbine towers with tuned liquid column dampers (TLCDs). *Structural Safety*, *47*, 78-86.

Murtagh, P. J., Basu, B., & Broderick, B. M. (2005). Along-wind response of a wind turbine tower with blade coupling subjected to rotationally sampled wind loading. *Engineering Structures*, *27*(8), 1209-1219.

Murtagh, P. J., Ghosh, A., Basu, B., & Broderick, B. M. (2008). Passive control of wind turbine vibrations including blade/tower interaction and rotationally sampled turbulence. *Wind Energy*, *11*(4), 305-317.

Patil, A., Jung, S., & Kwon, O. (2016). Structural performance of a parked wind turbine tower subjected to strong ground motions. *Engineering Structures*, *120*, 92-102.

Prowell, I., Veletzos, M., Elgamal, A., & Restrepo, J. (2009). Experimental and numerical seismic response of a 65 kW wind turbine. *Journal of Earthquake Engineering*, *13*(8), 1172-1190.

Quilligan, A., O'Connor, A., & Pakrashi, V. (2012). Fragility analysis of steel and concrete wind turbine towers. *Engineering Structures*, *36*, 270-282.

Stewart, G. M., & Lackner, M. A. (2014). The impact of passive tuned mass dampers and wind-wave misalignment on offshore wind turbine loads. *Engineering Structures*, *73*, 54-61.

Sun, C. (2018). Semi-active control of monopile offshore wind turbines under multi-hazards. *Mechanical Systems and Signal Processing*, *99*, 285-305.

Yuan, C., Chen, J., Li, J., & Xu, Q. (2017). Fragility analysis of large-scale wind turbines under the combination of seismic and aerodynamic loads. *Renewable Energy*, *113*, 1122-1134.

Zhang, J., & Huo, Y. (2009). Evaluating effectiveness and optimum design of isolation devices for highway bridges using the fragility function method. *Engineering Structures*, *31*(8), 1648-1660.

Zhang, Z., Chen, J., & Li, J. (2013). Theoretical study and experimental verification of vibration control of offshore wind turbines by a ball vibration absorber. *Structure and Infrastructure Engineering*, *10*(8), 1087-1100.

Zuo, H., Bi, K., & Hao, H. (2017). Using multiple tuned mass dampers to control offshore wind turbine vibrations under multiple hazards. *Engineering Structures*, *141*, 303-315.

Zuo, H., Bi, K., & Hao, H. (2018). Dynamic analyses of operating offshore wind turbines including soil-structure interaction. *Engineering Structures*, *157*, 42-62.

Zuo, H., Bi, K., & Hao, H. (2019a). Mitigation of tower and out-of-plane blade vibrations of offshore monopile wind turbines by using multiple tuned mass dampers. *Structure and Infrastructure Engineering*, *15*(2), 269-284.

Zuo, H., Bi, K., Hao, H., & Li, C. (2019b).Influence of earthquake ground motion modelling on the dynamic responses of offshore wind turbines. *Soil Dynamics and Earthquake Engineering*, *121*:151-167.

CHAPTER 5 USING MULTIPLE TUNED MASS DAMPERS TO CONTROL OFFSHORE WIND TURBINE VIBRATIONS UNDER MULTIPLE HAZARDS

ABSTRACT[4]

Offshore wind turbines can be built larger and lighter than they used to be due to the application of new materials. These large and flexible structures are vulnerable to external vibration sources such as wind, sea wave and earthquake excitations. It is necessary to mitigate the dynamic responses of offshore wind turbines to ensure the safety of these structures. Extensive research works have been carried out to mitigate the vibrations of the tower and/or blades of offshore wind turbines. Almost all the previous studies on the offshore wind turbine tower vibration control propose installing the control device at the top of the tower, i.e. in the nacelle. This method is effective to suppress the fundamental vibration mode of the tower, in which the maximum displacement occurs at the top of the tower. This practice is reasonable when wind and/or sea wave loadings are of interest since the energies of these vibration sources are concentrated in the low frequency range, and normally only the fundamental vibration mode of the tower is excited. On the other hand, offshore wind turbines may locate in the seismic prone areas, earthquake loading can be another vibration source during their lifetimes. When offshore wind turbines are subjected to earthquake excitation, higher vibration modes might be also excited. These higher vibration modes can further contribute to the structural responses and in certain circumstances they may even dominate the structural responses. In this case, installing the control device only in the nacelle will not be effective and more control devices should be installed at certain locations along the tower. In other words, one single control device will not be effective to control the tower vibrations if both the fundamental and higher vibration modes are of interest. This chapter proposes using multiple tuned mass dampers (MTMDs) to control vibrations from the fundamental and higher modes of offshore wind turbine tower under multiple hazards, i.e. under the combined wind, sea wave and earthquake excitations. The effectiveness of the proposed method is numerically investigated. It should be noted that only the vibration of the tower is of interest in the present study. The vibration control of the blades is out of the scope of this chapter, which will be further investigated.

[4] This chaper was published in *Engineering Structures* with the full bibliographic citation as follows: Zuo, H., Bi, K. & Hao, H. (2017). Using multiple tuned mass dampers to control offshore wind turbine vibrations under multiple hazards. *Engineering Structures*, *141*, 303-315. https://doi.org/10.1016/j.engstruct.2017.03.006.

5.1 Introduction

Wind turbines are becoming an attractive way to produce electrical energy nowadays. To more effectively extract the vast wind resources throughout the lifetimes of wind turbines, larger rotor and slender tower are adopted in the current designs with the development of new technologies and materials. For example, the rotor diameter and tower height of the latest NREL 5 MW three-bladed wind turbine reach 126 m and 87.6 m respectively, while the maximum wall thickness of the tower is only 0.027 m (Jonkman et al., 2009). These thin-walled wind turbines are vulnerable to external vibration sources such as wind and sea wave loadings, which are the constant vibration sources that offshore wind turbines experience during their whole lifetimes irrespective of their locations. Moreover, many wind turbines are located in the earthquake prone areas such as China, USA, Japan and New Zealand (Katsanos et al., 2016). Seismic loading is another possible vibration source during their lifetimes (Katsanos et al., 2016). In this case, the offshore wind turbine is subjected to simultaneous wind, sea wave and earthquake loads and the influence of earthquake loading on the structural responses of offshore wind turbine should be considered. Actually many guidelines and standards (DNV, 2014; IEC, 2005, 2009) clearly state that the wind turbine needs to be designed to resist seismic load when it is located in the seismic prone area. The simultaneous wind, sea wave and seismic loadings can lead to excessive vibrations to the tower and blades of wind turbines, which in turn can compromise the wind energy output and even result in the collapse of the tower (Chou & Tu, 2011). It is therefore important to mitigate these adverse vibrations to protect wind turbines and to improve their overall dynamic performances.

Extensive research works have been carried out by different researchers to mitigate the vibrations of tower and/or blades of a wind turbine by using different vibration control devices (Rahman et al., 2015). Since the aim of this study is to propose a method to mitigate the tower vibration, only the previous works on the tower vibration control are summarized here. These devices can be generally divided into passive (Chen et al., 2015; Colwell & Basu, 2009; Lackner & Rotea, 2011; Mensah & Dueñas-Osorio, 2014; Murtagh et al., 2008; Stewart & Lackner, 2014) and active (Zhang et al., 2014) categories depending on whether external power is needed. Compared to the active control devices, passive vibration control methods need no external power. They are therefore more widely used in engineering practices. For example, Lackner and Rotea (2011), Murtagh et al. (2008) and Stewart and Lackner (2014) proposed using tuned mass dampers (TMDs) to control tower vibrations; Colwell and Basu (2009), Mensah and Dueñas-Osorio (2014) and Chen et al. (2015) suggested using tuned liquid column dampers (TLCDs); Chen and Georgakis proposed a rolling-ball damper (2013a) and a spherical tuned liquid damper (2013b); Zhang et al. (2013) suggested a ball vibration absorber. The effectiveness of these proposed dampers were either numerically (Colwell & Basu, 2009;

Lackner & Rotea, 2011; Mensah & Dueñas-Osorio, 2014; Murtagh et al., 2008; Stewart & Lackner, 2014) or experimentally (Chen & Georgakis, 2013a, 2013b; Chen et al., 2015; Zhang et al., 2013) studied. The results confirmed these dampers can be used to mitigate the adverse vibrations for wind turbine towers.

Almost all the previous studies on the tower vibration control suggested installing the control devices at the top of the tower, i.e. in the nacelle. In reality, there is very limited space in the nacelle, which makes the installation of the dampers not straightforward. More importantly, previous studies mainly consider wind (Mensah & Dueñas-Osorio, 2014; Murtagh et al., 2008) and/or sea wave (Colwell & Basu, 2009; Stewart & Lackner, 2014) as the vibration sources. The energies of these loadings are concentrated in the low frequency range, hence they normally excite the fundamental vibration mode of the tower only, and the maximum displacement occurs at the top of the tower. Installing the control devices in the nacelle is therefore effective. However, when a wind turbine is subjected to earthquake shaking (Alati et al., 2015; Prowell et al., 2009, 2014), the higher vibration modes might be also excited since the energy of an earthquake loading is within a broader frequency range. These higher vibration modes can further contribute to the structural responses and may even govern the total structural responses in certain cases. In this case, installing the control device at the top of the tower may not be effective, and multiple dampers are necessary to effectively mitigate the tower vibrations under the wind, sea wave and earthquake excitations.

Applying multiple tuned mass dampers (MTMDs) to mitigate the unwanted vibrations of engineering structures has been reported by some researchers (Abe & Fujino, 1994; Kareem & Kline, 1995; Moon, 2010; Elias et al., 2016). Their studies revealed that MTMDs could effectively control the multiple vibration modes of engineering structures. Moreover, another two obvious merits can be appreciated by adopting this method. Firstly, this method can significantly facilitate the TMD installation since the mass of each TMD is much smaller compared to the single large TMD. The reliability of the control system can be significantly enhanced in case some of the MTMDs do not function properly. However, to the best knowledge of the authors, no open literature reports the study of the effectiveness of using MTMDs to control the tower vibrations of wind turbines.

This chapter proposes using MTMDs to control the tower vibrations of wind turbines when they are subjected to the simultaneous wind, sea wave and earthquake excitations. The effectiveness of the proposed method is numerically investigated by using the finite element code ABAQUS. The tower responses of the original wind turbine (without control devices) are compared with those controlled by STMD and MTMDs. The robustness of the proposed method is also discussed by arbitrarily assuming some dampers do not work properly.

5.2 Optimization of STMD/MTMD systems

STMD/MTMD systems have been widely used to control the vibrations of engineering structures due to the simplicity and effectiveness of the systems. Figure 5-1(a) shows a standard STMD system, in which an auxiliary mass (m_T) is attached to the vibrating main structure by a spring and a dashpot. The natural frequency of the TMD is tuned to the vibration frequency of the main structure so that the damper will resonate out of phase with the main structure and a large amount of structural vibrating energy is transferred to the TMD and dissipated by the damper. For a MTMD system, as implied by the name, multiple TMDs instead of a single TMD are attached to the main structure by the springs and dashpots. Figure 5-1(b) shows a structure-MTMD system with n TMDs. Again the springs are used to tune the frequency of the MTMD system and the energy is dissipated by the multiple dashpots.

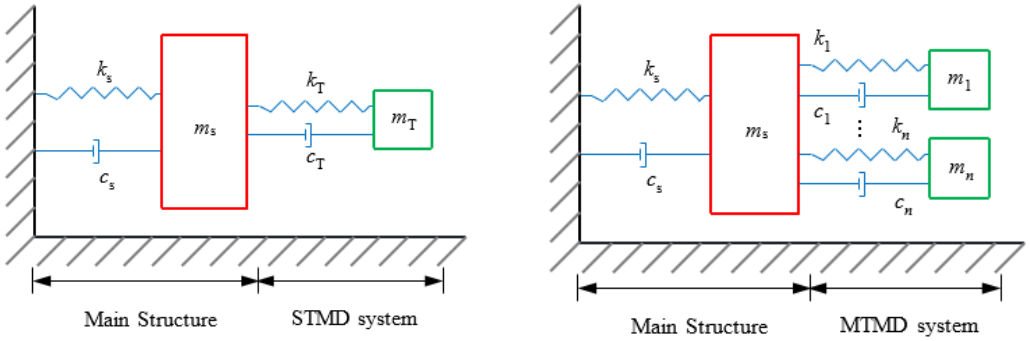

(a) STMD system (b) MTMD system

Figure 5-1 Structure-TMD systems (a) STMD system and (b) MTMD system

The tuned frequency ratios and damping ratios of the dampers are the key parameters that can significantly influence the effectiveness of the STMD/MTMD systems. Numerous methods have been proposed by different researchers (Abe & Fujino, 1994; Bakre & Jangid, 2004, 2007; Bi & Hao, 2016; Hoang et al., 2008; Jangid, 1999; Li, 2002; Sadek et al., 1997; Warburton, 1982; Yamaguchi & Harnpornchai, 1993) to obtain the optimal TMD parameters after the pioneering work done by Den Hartog (1985). In the present study, the displacement response of the tower is of interest and numerical searching technique is used to minimize the mean square displacement of the tower under a given mass ratio.

As will be presented in Section 5.4, the natural frequencies of different modes of the example wind turbine are well separated with each other, the springs and dashpots used to control different vibration modes of the tower therefore can be optimised separately. To further facilitate the optimization, the following two assumptions are made (Li & Liu, 2003): (1) the natural frequencies of MTMDs are uniformly distributed around their average natural frequency; (2) each TMD has the same mass and damping coefficient to achieve a better effectiveness on the vibration control of the tower.

For a structure-MTMD system as shown in Figure 5-1(b), the vibration frequency of the main structure can be calculated as $\omega_S = \sqrt{k_S/m_S}$, where m_S and k_S are the mass and stiffness of the main structure respectively. For a MTMD system with n TMDs, the frequency of the jth TMD in the MTMD system can be estimated based on the first assumption as (Joshi & Jangid, 1997)

$$\omega_j = \omega_T \left[1 + \left(j - \frac{n+1}{2}\right)\frac{\beta}{n-1}\right] \quad j = 1, 2, \ldots, n \tag{5.1}$$

where $\omega_T = \sum_{j=1}^{n} \omega_j/n$ is the average frequency of MTMDs and $\beta = (\omega_n - \omega_1)/\omega_T$ is the non-dimensional frequency interval.

By defining the mass ratio of the system as $\mu = \sum_{j=1}^{n} m_j/m_S$, the mass of each TMD can be calculated as follows based on assumption 2:

$$m_j = \mu m_S/n \tag{5.2}$$

The stiffness and damping coefficient of each TMD are therefore

$$k_j = m_j\omega_j^2 \tag{5.3}$$

$$c_j = 2nm_j\zeta_T \Big/ \sum_{j=1}^{n} 1/\omega_j \tag{5.4}$$

in which $\zeta_T = \sum_{j=1}^{n} \zeta_j/n$ is the average damping ratio of MTMDs and ζ_j is the damping ratio of the jth TMD.

For a main structure-STMD system, the corresponding values can be simplified by substituting n=1 into Eqs. (5.2), (5.3) and (5.4).

As mentioned above, the displacement response of the main system (tower) is of interest in the present study. The mean square displacement of the main system can be defined as (Xu & Igusa, 1992)

$$\sigma^2 = \int_0^\infty |H_S(\omega)|^2 S(\omega) d\omega \tag{5.5}$$

in which $S(\omega)$ is the power spectral density of the excitation and $H_S(\omega)$ is the transfer function.

In the present study, the combined wind, sea wave and earthquake loadings are considered. Wind and sea wave act on the wall of the main structure, and they excite the fundamental vibration mode, while earthquake loading acts at the base of the tower, and it mainly excites the second vibration mode of the tower as will be seen in Section 5.6. For the base excitation and the dynamic pressures acting on the main structure, the transfer functions are different.

For the base acceleration excitation, the transfer function can be expressed as (Xu & Igusa, 1992)

$$H_S(\omega) = \frac{1 - (i\omega m_S)^{-1} Z(\omega)}{\omega_S^2 - 2i\omega\omega_S\zeta_S - \omega^2 - i\omega m_S^{-1} Z(\omega)} \tag{5.6}$$

where

$$Z(\omega) = -i\omega \sum_{j=1}^{n} \frac{m_j\left(\omega_j^2 - 2i\omega\omega_j\zeta_j\right)}{\omega_j^2 - 2i\omega\omega_j\zeta_j - \omega^2} \tag{5.7}$$

in which $\zeta_S = c_S/2m_S\omega_S$ is the damping ratio of the main structure.

For the dynamic pressure on the main structure, the transfer function is (Xu & Igusa, 1992)

$$H_S(\omega) = \left[\omega_S^2 - 2i\omega\omega_S\zeta_S - \omega^2 - i\omega m_S^{-1} Z(\omega)\right]^{-1} \tag{5.8}$$

Substituting Eqs. (5.6) and (5.8) into Eq. (5.5), the optimal frequency bandwidth β, tuned frequency ratio $\gamma = \omega_T/\omega_S$ and average damping ratio ζ_T can be obtained through a numerical searching technique by minimizing the mean square displacement of the tower under an assumed mass ratio μ.

5.3 Numerical model

5.3.1 NREL 5 MW wind turbine

The modern NREL 5 MW three-bladed horizontal axis wind turbine is used as an example in the present study. This wind turbine is selected simply because the properties are well defined in many previous studies (Jonkman et al., 2009). The tower height above the water level is 87.6 m and the length of the hollow monopile foundation in the water (between the water level and the ground level) is 20 m. As indicated in (Jonkman, et al., 2009), a length of about 30-45 m of the monopile is normally buried in the soil. Previous studies revealed that soil-structure (monopile) interaction (SSI) can further change the vibration characteristics of the structure and therefore the structural responses (Bhattacharya & Adhikari, 2011; Bi et al., 2011; Damgaard et al., 2014). Not to further complicate the problem, SSI is, however, not considered in the present study and the pile is assumed fully fixed at the ground level. This simplification might slightly change the optimal spring stiffness and damping coefficient(s) of the STMD/MTMD systems, it will not influence the conclusions of the present study. Figure 5-2 shows the main dimensions of the tower and the detailed information of the wind turbine can be found in Table 5-1.

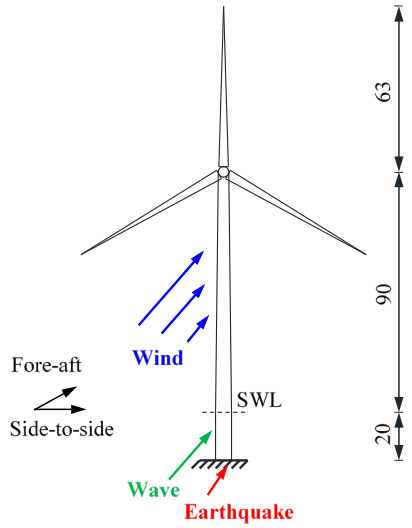

Figure 5-2 Offshore wind turbine model (Front view, dimensions in m)

For the monopile in the sea water, the vibrating monopile can impart an acceleration to the surrounding sea water. The water-monopile interaction is modelled by the added mass method (Bi & Hao, 2016) in the present study, in which the effective mass m_e of the monopile can be calculated as (Bi & Hao, 2016)

$$m_e = m_p + m_a \tag{5.9}$$

where m_p is the monopile physical mass and m_a denotes the added mass which can be calculated as (Bai & Bai, 2014)

$$m_a = C_a \frac{\pi}{4} d_p^2 \rho_w \tag{5.10}$$

where d_p is the outer diameter of the monopile, which is 6 m in the present study, ρ_w=1030 kg/m^3 is the sea water density and C_a is the added mass coefficient. C_a is related to many parameters including Keulegan-Carpenter (KC) number, surface roughness, the proximity of the structure to the seabed and the cross section shape of the structure (DNV, 2010). C_a=1.0 is assumed in the present study (DNV, 2010).

Table 5-1 Properties of NREL 5 MW wind turbine (Jonkman et al., 2009)

Wind turbine properties	Value	Wind turbine properties	Value
Max. rated power	5 MW	Rotor diameter	126 m
Tower height	87.6 m	Bottom section diameter	6 m
Top section diameter	3.87 m	Tower wall thickness	27-19 mm
Rotor hub height	90 m	Hub diameter	3 m
Tower mass	347,460 kg	Nacelle mass	240,000 kg
Rotor mass (with hub)	110,000 kg	Monopile height	20 m
Monopile diameter	6 m	Monopile wall thickness	27 mm

5.3.2 Finite element model

The detailed three-dimensional (3D) finite element (FE) model of the NREL 5 MW wind turbine is developed by using the finite element code ABAQUS. Both the tower and monopile are modelled by shell elements (S4 in ABAQUS). The geometry of the rotor can influence the vibration characteristics of the wind turbine especially when it is in operational condition since the locations of the blades are changing periodically and moreover the centrifugal stiffness generated by the rotating blades can increase the stiffness and thus the natural frequencies of the blades (Murtagh et al., 2005). Murtagh et al. (2005) further indicated that the rotation of the blades mainly affect the vibration characteristics of the blades themselves, its influence on the tower is relatively less. As mentioned above, the aim of the present study is to investigate the effectiveness of using MTMDs to control the tower vibration of wind turbines and only the parked condition is considered. The influence of the geometries of the nacelle and blades is believed not significant and therefore neglected in the present study. Only the masses of the nacelle and blades are considered in the numerical model, and they are modelled by a lumped mass element (point mass in ABAQUS) located at the top of the tower. The TMD(s) are modelled by the mass, spring and dashpot elements in ABAQUS. The material properties of the tower and monopile are tabulated in Table 5-2. The cross sections of the tower and monopile are divided into 24 elements (Bi & Hao, 2016), and a convergence test shows that an element size of 1 m along the height of the tower yields a good balance between the computational time and accuracy, an element size of 1 m is therefore used in the axial direction of the wind turbine.

Table 5-2 Material properties of tower and monopile

Density (kg/m^3)	Young's modulus (GPa)	Poisson's ratio
7850	210	0.3

The vibration frequencies and vibration modes of the wind turbine can be calculated by carrying out an eigenvalue analysis. Table 5-3 tabulates the first five natural frequencies and the corresponding vibration modes of the wind turbine. As shown in Table 5-3, the vibration frequencies in the two horizontal directions (fore-aft and side-side directions) for the same vibration mode are the same due to the simplification that the blades and nacelle are modelled by a lumped mass at the top of the tower and the numerical model is symmetric. The modal participation factors for the fundamental and the second vibration modes are 91.15% and 8.66% respectively for the wind turbine. The tower response will be mainly determined by the first two vibration modes. Only the first two vibration modes of the tower are therefore controlled in this study. Figure 5-3 shows the fundamental and the second mode shapes of the wind turbine in the fore-aft direction. The corresponding vibration frequencies are 0.232 and

2.021 Hz respectively. It is obvious that the largest amplitude of the first mode shape is at the top of the tower (location A). For the second mode shape the maximum amplitude occurs at around 40 m below the tower top (location B) as shown in Figure 5-3.

Table 5-3 Natural frequencies and vibration modes

Mode	Type	f (Hz)
1st	Fore-aft	0.232
1st	Side-side	0.232
2nd	Fore-aft	2.021
2nd	Side-side	2.021
3rd	Fore-aft	5.926
3rd	Side-side	5.926
4th	Vertical	6.775
5th	Torsion	9.462

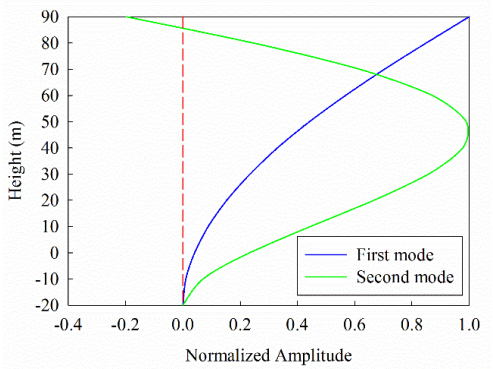

Figure 5-3 First two mode shapes of the tower in the fore-aft direction

Table 5-4 Optimal values of different TMD systems

TMD	Controlled mode	β_{opt}	γ_{opt}	ζ_{Topt}	m (kg)	k_{opt} (N/m)	c_{opt} (N s/m)
STMD1	First	-	0.96	0.11	36,096	70,909	11,130
Two TMDs	First	-	0.98	0.08	18,048	36,947	4132
	Second	-	0.96	0.08	18,048	2.68×10^6	35,206
Six TMDs	First	0.16	0.99	0.04	6016	10,638	693
					6016	12,568	693
					6016	14,660	693
					6016	7.57×10^5	5843
	Second	0.16	0.96	0.04	6016	8.94×10^5	5843
					6016	1.04×10^6	5843

The damping mechanism of the wind turbine is quite complicated and it normally comprises aerodynamic damping, structural damping, hydrodynamic damping and soil damping, which account for the contributions of the wind, tower itself, surrounding sea water and supporting soil respectively (Arany et al., 2016). Koukoura et al. (2015) carried out experimental studies to identify the damping ratio of a wind turbine in standstill condition and found that the value is 1.93%. Katsanos et al. (2016) reported that the damping ratio of a parked wind turbine is normally between 0.5% and 2%. For simplicity, the damping of the tower is considered by

means of Rayleigh damping and a 2% damping ratio is assumed for the first two vibration modes without loss of generality. The mass and stiffness coefficients are therefore 0.052 and 0.003 respectively (Chopra, 2012). In the present study, the total tuned mass is assumed to be 5.18% of the wind turbine, and it is 36,096 kg based on the information in Table 5-1.

With all the parameters defined above, the optimal parameters for the STMD/MTMD systems can be estimated. Table 5-4 tabulates the calculated values according to the optimised method summarized in Section 5.3. In the first column of the table, STMD1 means single TMD is placed at location A to control the fundamental vibration mode only (Figure 5-4(a)); two TMDs indicates two TMDs are used simultaneously to control both the first and second vibration modes of the tower (Figure 5-4(b)), and they are placed at locations corresponding to the maximum amplitudes of these two vibration modes, i.e., the locations A and B as shown in Figure 5-3. To investigate the robustness of the proposed method, another case with six TMDs used to control the first two vibration modes are also considered, with three TMDs applied to control the first mode and another three used to control the second mode (Figure 5-4(c)). The distance between each TMD is assumed as 10 m and the six TMDs are labelled as #1 to #6 from the tower top.

In the numerical simulation, the external excitations are assumed acting in the fore-aft direction of the tower (x direction in Figure 5-4) only. The control devices are therefore only applied in the x direction. It should be noted that the values in Table 5-4 are calculated based on the mathematic model shown in Figure 5-1, in which a single spring/dashpot is used to connect a TMD mass and the main structure. In the numerical simulation, two springs and two dashpots are installed in the $+x$ and $-x$ directions to connect a TMD and the tower as shown in Figure 5-4, the spring stiffness and damping coefficient are therefore equal to half of those given in Table 5-4.

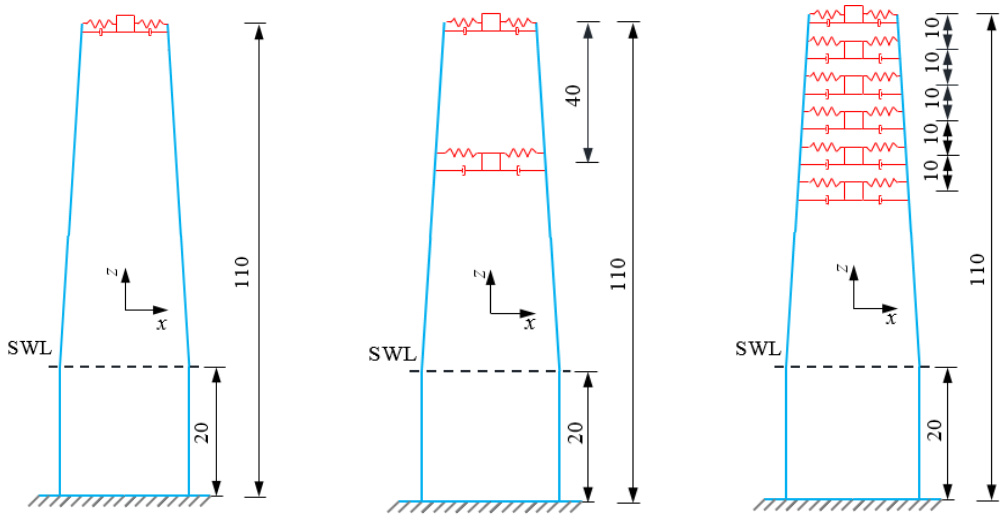

(a) STMD1 (b) two TMDs (c) six TMDs

Figure 5-4 Different TMD arrangements (Side view, not to scale, dimensions in m)

5.4 Vibration sources

The responses of the wind turbine under the combined wind, sea wave and earthquake loadings as shown in Figure 5-2 are calculated in the present study. All these external vibration sources are stochastically simulated based on the sophisticated simulation techniques. For completeness of the paper, these techniques are briefly introduced in this section.

5.4.1 Wind load

The wind loads along the height of the tower are different and the wind load can be decomposed into a constant mean wind load and a fluctuating component. The Kaimal spectrum (Murtagh et al., 2005) is used to model the power spectral density (PSD) function of the fluctuating wind velocity along the tower, which can be expressed as

$$S_{vv}(z,f) = \frac{v_*^2}{f}\frac{200c}{(1+50c)^{5/3}} \tag{5.11}$$

in which

$$c = fz/\bar{v}(z) \tag{5.12}$$

and

$$\bar{v}(z) = v_* \ln(z/z_0)/K \tag{5.13}$$

where z is the vertical coordinate, f is the frequency (Hz), v_* is the friction velocity, c is the Monin coordinate, K is the von-Karman's constant (typically 0.4 (Benowitz & Deodatis, 2015)) and z_0 is the roughness length.

For a continuous line-like structure, like the tower, the wind loads at different locations along the tower are different but with certain similarities, which is known as the spatial correlation effect. A spatial coherency loss function is generally used to describe this effect. The modal fluctuating drag force power spectrum (Murtagh et al., 2005), which includes the influence of spatial correlation effect, is given by

$$S_{f,j}(f) = (C_D\rho)^2 \sum_{k=1}^{N}\sum_{l=1}^{N} S_{v_k v_l}(f) A_k A_l \bar{v}_k \bar{v}_l \phi_j(k)\phi_j(l) \tag{5.14}$$

where C_D is the drag coefficient, ρ is the air density, A_k, A_l and $\bar{v}_k$, $\bar{v}_l$ are the areas exposed to the wind and the mean wind velocities at locations k and l respectively, $\phi_j(k)$ and $\phi_j(l)$ are the jth mode shape at locations k and l. $S_{v_k v_l}$is the cross PSD function of wind velocity between locations k and l, which can be formulated as

$$S_{v_k v_l}(f) = \sqrt{S_{v_k v_k}(f) S_{v_l v_l}(f)}\, coh(k,l;f) \tag{5.15}$$

in which $S_{v_k v_k}$ and $S_{v_l v_l}$ are the wind velocity auto PSDs as expressed by Eq. (5.11), and $coh(k, l; f)$ is the spatial coherency loss function between locations k and l, the formula proposed by Huang et al. (2013) is used in the present study

$$coh(k,l;f) = exp\left(-\frac{D\omega|k-l|}{2\pi\hat{v}}\right) exp\left(-i\frac{k-l}{v_{app}}\omega\right) \quad (k>l) \tag{5.16}$$

where $|k\text{-}l|$ and $\hat{v}$ are the distance and average mean wind velocity between locations k and l respectively, D is a decay constant and v_{app} is the apparent wave velocity. For $k<l$, the spatial coherency loss function is the complex conjugate of that with $k>l$.

In the simulation, the tower is divided into nine segments, and the drag force is assumed to be the same within each segment. Moreover, as will be confirmed in the following analysis, wind load will mainly excite the fundamental vibration mode of the tower, the contribution from the higher modes can be neglected, j=1 (Eq. (5.14)) is thus assumed in the wind load simulation. After the PSD of the drag force is determined, the fluctuating wind drag force time histories with zero mean (f_i(t) in Eq. (5.18)) then can be generated based on the Inverse Fast Fourier Transform (IFFT) technique (see details in (Bi & Hao, 2012; Hao et al., 1989)).

The mean component of the wind drag force can be calculated as

$$\bar{f}_{mean,i} = \frac{1}{2} C_D A_i \rho \bar{v}_i^2 \tag{5.17}$$

where A_i and $\bar{v}_i$ denote the area associated with location i and the mean wind velocity at location i.

The total wind drag force is therefore

$$F_i(t) = \bar{f}_{mean,i} + f_i(t) \tag{5.18}$$

In the simulation, the roughness length, air density, drag coefficient and apparent wave velocity are 0.005, 1.2 kg/m^3, 1.2 and 10 m/s respectively, and the mean wind velocity at the top of the tower is taken as 18 m/s. Figure 5-5 shows the fluctuating wind velocity PSDs at locations A and B and the corresponding model values. The model and simulated coherency loss functions between segments S1 (85-90 m along the tower), S2 (75-85 m) and S3 (65-75 m) are shown in Figure 5-6. Good matches are observed as shown in Figure 5-5 and Figure 5-6. Figure 5-7 shows the simulated total drag forces applied to the tower within the height range of 85-90 m (a) and 45-55 m (b). The drag forces at other locations on the tower are not shown for conciseness.

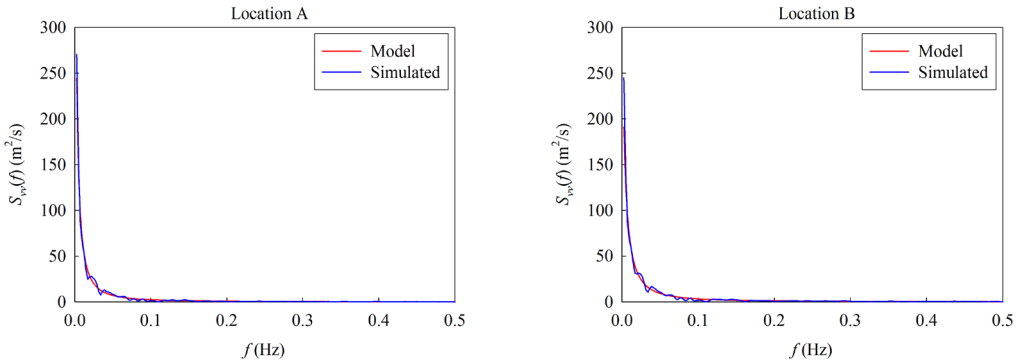

Figure 5-5 Comparisons of the simulated wind velocity PSD with the model PSD

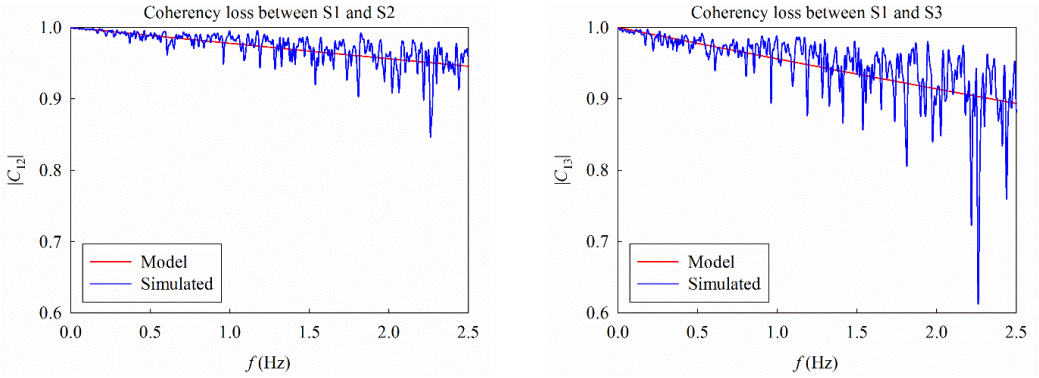

Figure 5-6 Comparisons of coherency loss of the simulated wind velocity with the model coherency loss function

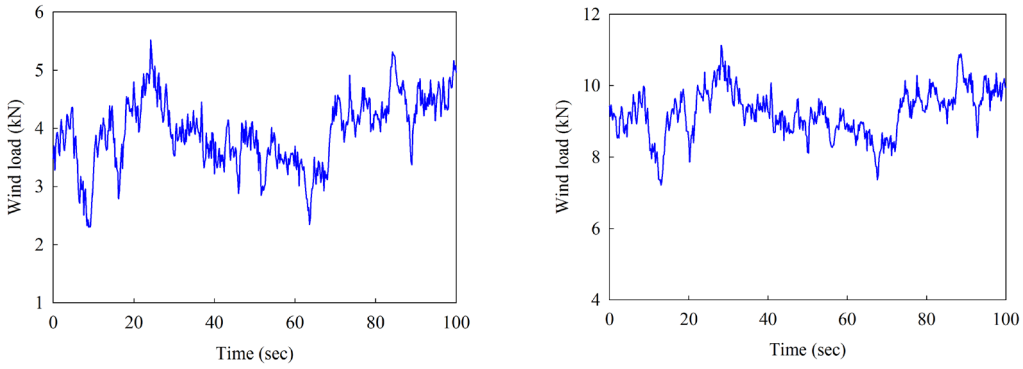

(a) the height range of 85-90 m (b) the height range of 45-55 m

Figure 5-7 Total wind loads within the height range of (a) 85-90 m and (b) 45-55 m

5.4.2 Sea wave load

To calculate the sea wave load acts on the monopile, the Joint North Sea Wave Observation Project (JONSWAP) spectrum (Hasselmann et al., 1973) is used to simulate the sea surface elevation, this spectrum has the form

$$S_{\eta\eta}(f) = \alpha g^2 (2\pi)^{-4} f^{-5} exp\left[-\frac{5}{4}\left(\frac{f_m}{f}\right)^4\right] \gamma^{exp\left[-\frac{(f-f_m)^2}{2\sigma^2 f_m^2}\right]} \tag{5.19}$$

in which, η is the sea surface elevation, γ is the peak enhancement factor (generally taken to be 3.3), g is gravitational acceleration and f is the wave frequency (Hz). The values of the constants in this equation are (Colwell & Basu, 2009)

$$\alpha = 0.076(Fg/v_{10}^2)^{-0.22} \tag{5.20}$$

$$f_m = 11(v_{10}F/g^2)^{-1/3}/\pi \tag{5.21}$$

and

$$\sigma = \begin{cases} 0.07 & f \le f_m \\ 0.09 & f > f_m \end{cases} \tag{5.22}$$

where F is the fetch length and v_{10} is the mean wind velocity at 10 m above the sea surface.

After obtaining the sea surface elevation spectrum $S_{\eta\eta}(f)$, $\eta(t)$ can be simulated in the time domain as

$$\eta(t) = \sum_{i=1}^{n} \sqrt{2d\omega S_{\eta\eta}(\omega_i)}\cos\left(\omega_i t + \varphi_{nn}(\omega_i)\right) \tag{5.23}$$

in which $\varphi_{nn}(\omega_i)$ is the random phase angles uniformly distributed over the range of [0, 2π].

The velocity potential of water particles is (Sorensen, 2005)

$$\phi(x,z,t) = \frac{gH}{2\omega}\frac{\cosh k(d+z)}{\cosh kd}\sin(kx-\omega t) \tag{5.24}$$

where x and z denote the horizontal and vertical directions, respectively, H is the wave height, which is two times of the amplitude of the sea surface elevation $\eta(t)$, d is water depth, ω is the sea wave angular frequency (rad/s) and k is the sea wave number, which can be estimated from (Sorensen, 2005)

$$\omega^2 = gk\tanh(kd) \tag{5.25}$$

By differentiating the velocity potential, the velocity and acceleration of water particles in the horizontal direction can be obtained as (Sorensen, 2005)

$$v_x = \partial\phi/\partial x = \frac{H\omega}{2}\frac{\cosh k(d+z)}{\sinh kd}\cos(kx-\omega t+\varphi) \tag{5.26}$$

$$a_x = \partial v_x/\partial t = \frac{H\omega^2}{2}\frac{\cosh k(d+z)}{\sinh kd}\sin(kx-\omega t+\varphi) \tag{5.27}$$

The wave load generated between the monopile and the surrounding water is mainly due to the inertia and pressure drag effects. In the present study, the following parameters are used: g=9.8 m/s^2, v_{10}=14 m/s and F=20,000 m. f_m is therefore 0.245 Hz based on Eq. (5.21); the wave period is $T=1/f_m$= 4.08 s and the wave length is $\lambda=gT^2/2\pi$=26 m (Sorensen, 2005). The wave length is nearly five times of the monopile diameter, the Morison equation can be used to calculate the sea wave force based on the specifications in (DNV, 2010). The transverse sea wave force per unit length of the monopile can be expressed as (DNV, 2010)

$$F = \frac{1}{2}\rho_w C_d d_p |v_x| v_x + \rho_w C_m A_p a_x \tag{5.28}$$

$$C_m = C_a + 1 \tag{5.29}$$

where A_p is the cross section area of the monopile, C_d, C_m are the drag and inertia coefficients respectively, and C_d=1.2, C_m=2.0 in the sea wave simulation. It should be noted that the first term represents the contribution of the quadratic drag force, and the second term is the inertia force.

Figure 5-8 shows the PSDs of the simulated sea surface elevation time history and the given model, good match is observed. Figure 5-9 shows the sea wave load time history at the mean water level based on Eq. (5.28).

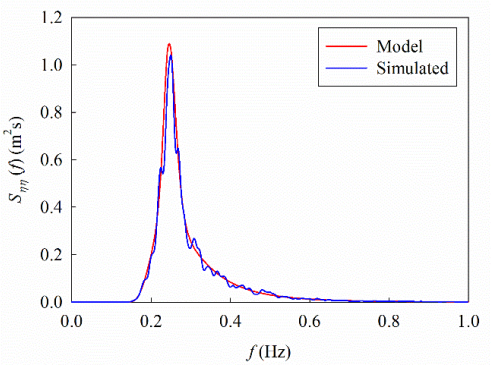

Figure 5-8 Comparison of the simulated sea surface elevation PSD with the model PSD

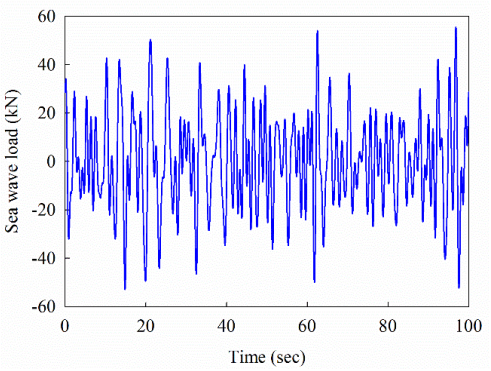

Figure 5-9 Sea wave load time history at mean sea water level

5.4.3 Seismic load

For the offshore wind turbine as shown in Figure 5-2, the sea water will influence the earthquake motions especially the vertical component (Li et al., 2015). Earthquake time histories at the seafloor should therefore be selected as the inputs. However, very limited seafloor recordings are available. Moreover, only the horizontal input is considered in the present study as mentioned above, and the influence of sea water on the earthquake horizontal component is relatively less (Li et al., 2015). The earthquake simulation technique for the onshore site is therefore adopted in the present study.

The spectral representation method proposed in (Bi & Hao, 2012) is used to simulate the earthquake motion in this chapter. Figure 5-10 shows the simulated acceleration time history. This earthquake ground motion time history is generated to be compatible with the design spectrum for shallow soil site (Class C) specified in the New Zealand seismic design code. In the simulation, the peak ground acceleration (PGA) is set as 0.25g and the time duration is 40.96 s. The sampling frequency and upper cut off frequency are 100 and 25 Hz respectively. Figure 5-11 shows the response spectra of the generated time history and the given model. Good match is observed.

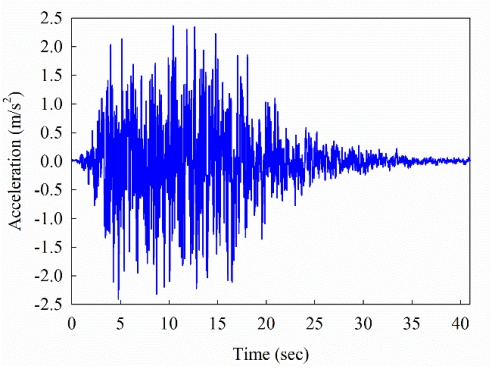

Figure 5-10 Simulated earthquake acceleration time history

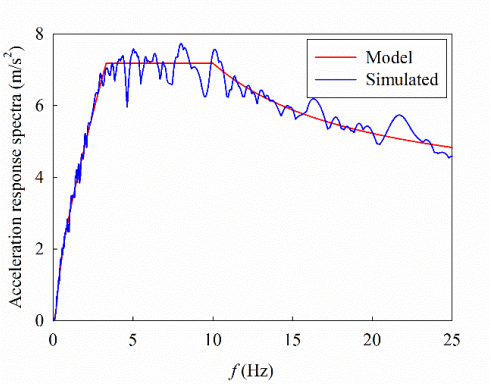

Figure 5-11 Comparison of the generated earthquake acceleration and the target response spectra

It should be noted that under the earthquake loading, the water surrounding the tower might be excited. Since the vibration periods of the water and the wind turbine are different, impacts from the surrounding water may be imposed to the tower, which will further influence the tower response. Moreover, seismic loading may result in the sloshing of the water, which can lead to different water pressure at different locations of the tower and therefore influence the structural responses. Detailed modelling on this phenomenon should adopt the computational fluid dynamics (CFD) method, which will significantly increase the computational effort and it is out of the scope of the paper. In other words, the additional wave force induced by earthquake excitations is neglected in this study. This simplification is justifiable because only P-wave can propagate through the water layer, but usually most seismic ground motion energy is associated with S-wave. Therefore the additional sea wave force acting on wind turbine due to seismic excitation is believed relatively small.

5.5 Numerical results

5.5.1 Dynamic responses of the original tower

To examine the effectiveness of the proposed method, two excitation scenarios are considered. In the first scenario, the wind and sea wave loads shown in Figure 5-7 and Figure 5-9 are

assumed as the excitation sources, and they are applied to the tower in a period of 100 s. In the second scenario, seismic load is also considered and earthquake loading comes in at the instant of 30 s, i.e., the earthquake excitation starts at 30 s and ends at 70.96 s in the simulation. The responses of the original structure (without control devices) and the structure with different control arrangements (Figure 5-4) are investigated.

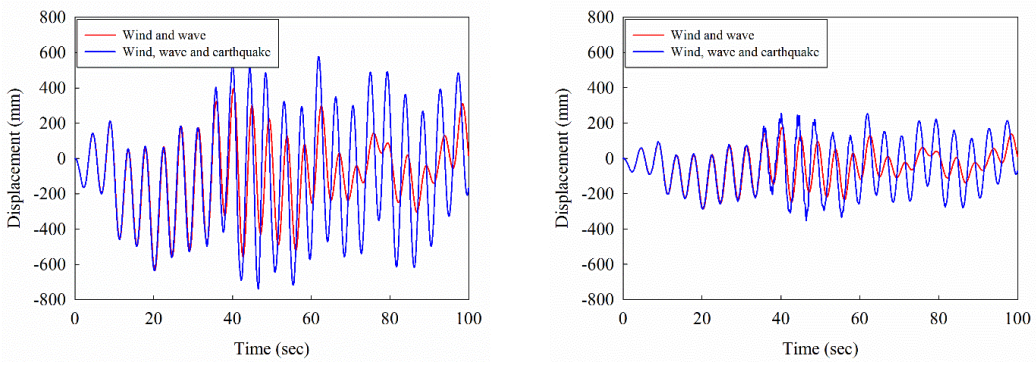

(a) location A (b) location B

Figure 5-12 Displacement time histories at (a) location A and (b) location B under different excitation scenarios

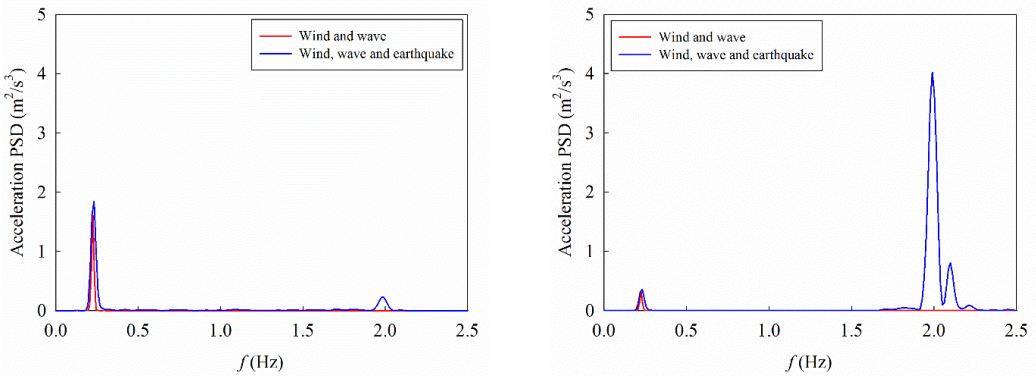

(a) location A (b) location B

Figure 5-13 Acceleration PSDs at (a) location A and (b) location B under different excitation scenarios

Figure 5-12 shows the displacement time histories at the tower top (location A in Figure 5-3) and 40 m below the top of the tower (location B) when the wind turbine is subjected to different excitation scenarios. The red curves are the results under the actions of wind and sea wave loads, and the blue curves are from the combined wind, sea wave and earthquake excitations. It is observed that the maximum displacement at location A is 635 mm occurring at t=20 s when wind and sea wave loads act on the tower. When earthquake loading is applied, larger maximum displacement (739 mm) occurring at t=47 s is obtained (Figure 5-12(a)). For the displacement at location B, the maximum values are 286 mm and 352 mm respectively under different excitation scenarios (Figure 5-12(b)). These results are actually expected since when

earthquake is considered, more energy comes in, which in turn leads to larger structural responses. Figure 5-12 also shows that the additional earthquake loading does not have significant influence on the tower displacements in the period of 30 to 35 s. This is because earthquake loading comes in at 30 s, and the tower responses during this period are still dominated by the inertia from the wind and sea wave.

Figure 5-13 shows the PSDs of the acceleration responses at locations A and B. The figure clearly shows that wind and sea wave only excite the fundamental vibration mode of the tower, only one peak corresponding to the fundamental vibration frequency of 0.232 Hz is obtained from the PSD curves (the red curves). This is because the energies of the wind and sea wave mainly concentrate in the low frequency range. As shown in Figure 5-5 and Figure 5-8, the energies can be neglected when the frequencies are larger than 0.2 and 0.8 Hz for the wind and sea wave loads respectively. When earthquake loading is also considered, another peak corresponding to the second vibration frequency of the tower (2.021 Hz) appears due to the broader frequency range of earthquake loading, which means the second vibration mode of the tower is also excited. It should be noted that a Hamming window is used in MATLAB to smooth the PSD curves to more clearly present the dominant frequencies of structural responses in this study. The third peak occurs in Figure 5-13(b) is caused by the large window number used.

The results indicate that when wind, sea wave and earthquake loadings are acting together on the wind turbine, higher vibration modes besides the fundamental vibration mode can also be excited. As discussed in Section 5.4.2, the first two modes contribute to 99.8% of the total structural responses for the example wind turbine. In this case, at least two TMDs are necessary to effectively control the fundamental and second vibration modes of the tower, with one installed at location A and another at location B based on the vibration modes shown in Figure 5-3. In certain cases, the contributions from the even higher modes may not be neglected, and more TMDs are therefore needed.

5.5.2 Dynamic responses of the tower with TMD(s)

To control the vibrations of the wind turbine under the combined wind, sea wave and earthquake excitations, the influences of different TMD arrangements on the structural responses are investigated in this section. Figure 5-14 and Figure 5-15 show the displacement time histories at locations A and B respectively when one TMD (case STMD1 in the figures), two TMDs and six TMDs are installed. As shown, at the first 7 s, the installation of TMD(s) seems not effective. This is because TMD system becomes effective only after the relative displacement develops between the main structure and the TMD(s). It takes time for the TMD(s) to react and therefore develop relative displacements. After about 7 s, TMD(s) can

effectively mitigate the vibrations of the tower. To more clearly demonstrate the control effect, the structural responses are discussed within two time periods, i.e. with (t=30-70.96 s) and without (the rest of the simulation time) earthquake loading. The peak displacement responses at locations A and B of the tower of different systems are tabulated in Table 5-5. The corresponding ratios between the peak responses of the systems with TMD(s) and without TMD are also given in the table.

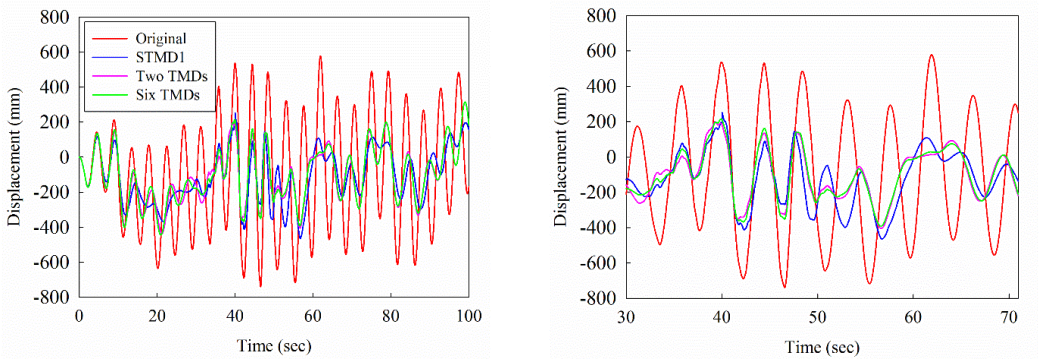

(a) within the whole time duration (b) within 30-70.96 s

Figure 5-14 Displacement time histories at location A (a) within the whole time duration and (b) within 30-70.96 s

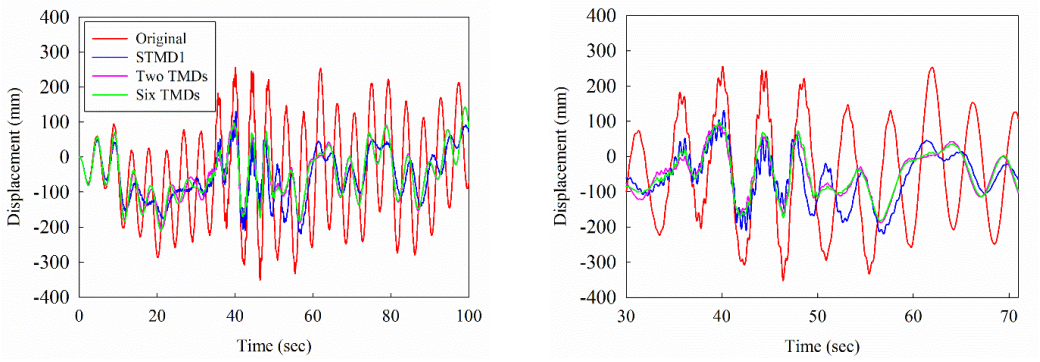

(a) within the whole time duration (b) within 30-70.96 s

Figure 5-15 Displacement time histories at location B (a) within the whole time duration and (b) within 30-70.96 s

Table 5-5 Peak displacements at locations A and B of the tower without and with TMD(s) and the corresponding response ratios

Type	t=0-30, 70.96-100 s				t=30-70.96 s			
	Disp. (mm)		Ratio (%)		Disp. (mm)		Ratio (%)	
	A	B	A	B	A	B	A	B
Original	635	286	-	-	739	352	-	-
STMD1	367	176	42.20	38.46	464	220	37.21	37.50
Two TMDs	437	205	31.18	28.32	405	188	45.20	46.59
Six TMDs	444	209	30.08	26.92	393	183	46.82	48.01

Table 5-5 shows that when only wind and sea wave loadings act on the tower, i.e. during t=0-30 s and 70.96-100 s, the maximum displacements for the uncontrolled system are 635 mm and 286 mm respectively at locations A and B. When STMD1 is applied at location A, the peak displacements reduce to 367 mm and 176 mm respectively with the vibration reduction ratios reaching 42.20% and 38.46%. This is because wind and sea wave excite the first vibration mode of the tower as mentioned above. When STMD1 is installed, the energy at the fundamental vibration frequency is significantly suppressed by the TMD as shown in Figure 5-16 (the blue curve).

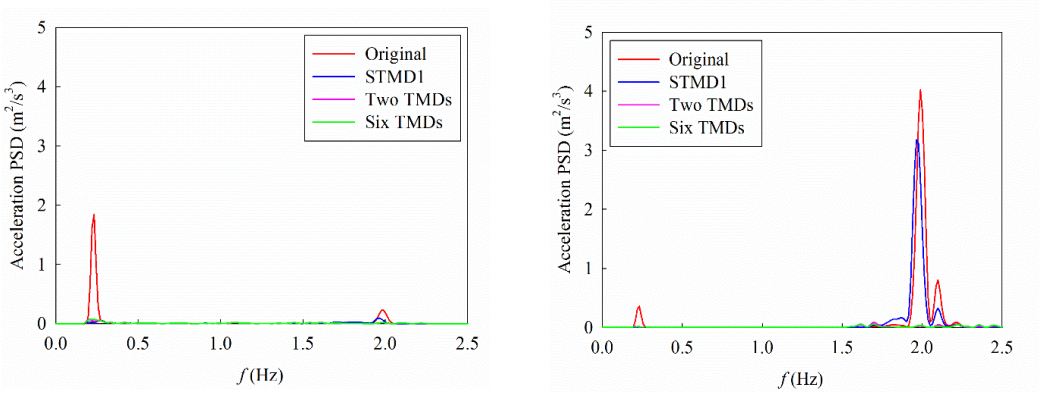

(a) location A (b) location B

Figure 5-16 Acceleration PSDs at (a) location A and (b) location B without and with TMD(s)

When two TMDs are applied, the peak displacements are 437 mm and 205 mm at locations A and B respectively, and the corresponding reduction ratios are 31.18% and 28.32%. Dividing one large TMD into two smaller TMDs slightly decreases the control effectiveness. This conclusion can also be drawn from the displacement time histories shown in Figure 5-14(a) and Figure 5-15(a), in which it is shown that installation of two TMDs results in slightly larger displacements compared to the case with STMD1 during most of the time duration (0-30 s and 70.96-100 s). The results can be explained by the PSD curves again shown in Figure 5-16 (especially Figure 5-16(a)). As shown, when two TMDs are applied, the energy at the fundamental vibration frequency is slightly larger than the case with STMD1 applying at location A, which in turn results in the slightly larger displacements. Further dividing two TMDs into six even smaller TMDs, the control effectiveness is marginally decreased compared to the case with two TMDs. As shown in Table 5-5, the reduction ratios are 30.08% and 26.92% at locations A and B respectively when six TMDs are installed. This is because the control effectiveness will be most evident when the TMDs are installed at the maximum amplitudes of the corresponding mode shapes (locations A and B). When six TMDs are applied, only TMDs #1 and #5 (Figure 5-4(c)) are installed at the maximum mode amplitudes, which in turn slightly decreases the control effectiveness. These results are consistent with

those reported by Moon (2010), in which it was concluded that applying MTMDs to control one certain vibration mode will slightly decrease the control effectiveness.

When earthquake comes in, i.e. within the time duration of 30-70.96 s, the control effectiveness is different from the results discussed above. As shown in Table 5-5, when no control device is applied, the maximum displacements are 739 mm and 352 mm respectively at locations A and B. Earthquake loading clearly excites the second vibration mode of the tower as demonstrated by the multiple spikes in the displacement time histories clearly shown in Figure 5-15(b). When STMD1 is installed, the fundamental vibration mode is significantly suppressed as discussed above, the peak displacements therefore reduce to 464 mm and 220 mm respectively and the displacement reduction ratios reach 37.21% and 37.50%. Figure 5-15(b) and Figure 5-16 also show that when STMD1 is installed, the second vibration mode cannot be obviously suppressed, multiple spikes still exist in the displacement curve (the blue curve) as shown in Figure 5-15(b). When two TMDs are applied, the displacements can be further reduced compared to the case with STMD1 installed as shown in Figure 5-14(b) and Figure 5-15(b). The peak displacements decrease to 405 mm and 188 mm respectively and the displacement reduction ratios reach 45.20% and 46.59%. This is because the second vibration mode is obviously controlled by applying another TMD at location B as shown in Figure 5-16. The spikes in Figure 5-15(b) therefore disappear and the displacement curve becomes smoother. When six TMD are applied, the second vibration modes are also controlled as shown in Figure 5-16, although the peak displacements are marginally decreased compared to the case with two TMDs, the displacements at other time are slightly larger as shown in Figure 5-14(b) and Figure 5-15(b) due to the reason that only TMDs #1 and #5 are installed at the maximum amplitudes of the vibration modes.

The above results indicate that dividing a single large TMD into multiple smaller TMDs slightly decreases the control effectiveness when wind and sea wave are the vibration sources. When earthquake is also considered, higher vibration modes are excited, applying MTMDs can obviously suppress these high modes of vibrations and further reduce the structural responses and increase the control effectiveness. Moreover, by dividing one large TMD into MTMDs will significantly facilitate the installation of TMDs since the mass for each TMD becomes smaller. Furthermore, as will be demonstrated in Section 5.6.3, the robustness of the control system can be significantly enhanced by using MTMDs. Balancing the pros and cons, the proposed system is believed more practicable to control the wind turbine vibrations especially when these wind turbines are located in the seismic active areas.

5.5.3 Robustness of MTMD system

When only one TMD (the STMD1 case) or two TMDs are installed, the effectiveness of the control system will be significantly influenced if the TMD(s) do not function properly. By dividing the single large TMD into multiple smaller TMDs, the control effectiveness might not be obviously influenced if one or more TMDs do not function well. To demonstrate the robustness of the proposed MTMD system for vibration control, some TMDs are assumed not function properly in this section. Without loss of generality, following three cases are considered. In Case 1, TMD #1 is not functioning; TMDs #2 and #5 are malfunctioning in Case 2 and in Case 3, three TMDs (#2, 3 and 4) lose their control capabilities. In the numerical simulation, the masses of the malfunctioned TMDs are kept and they are lumped to the corresponding locations of the tower, i.e., the total mass of the system in different cases is the same.

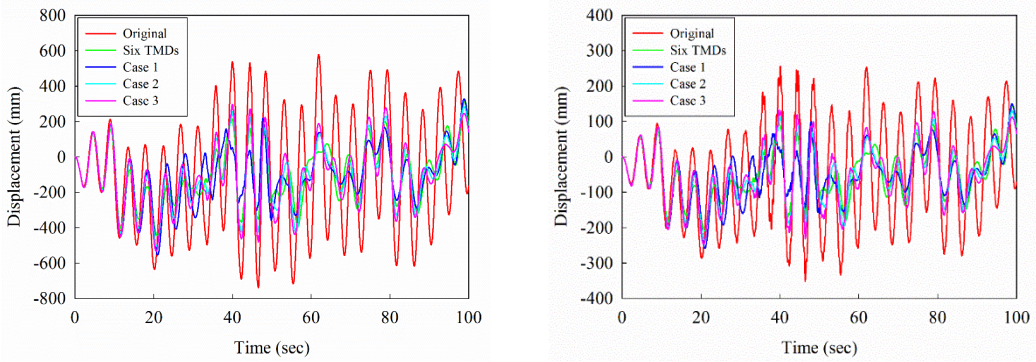

(a) location A (b) location B

Figure 5-17 Displacement time histories at (a) location A and (b) location B with some TMDs not working

Figure 5-17 shows the displacement time histories for different cases. For comparison, the results for the original structure and the structure controlled by six well-functioning TMDs are also plotted. Table 6 tabulates the peak displacements at locations A and B for different cases. The reduction ratios are also given in the table. As shown in Table 5-6 and Figure 5-17, the control effectiveness decreases, as expected when some TMDs do not work properly as compared to the case with all the TMDs functioning. However, due to the contributions of other functioning TMDs, the displacements are still much smaller than the uncontrolled case. These results demonstrate the robustness of the control system. Particularly, among these three cases, Case 1 is least effective and the peak displacements are 554 mm and 259 mm respectively at locations A and B with the reduction ratios are 25.03% and 26.42%. This is because TMD #1 is installed at the location with the maximum modal amplitude. The malfunction of this TMD will evidently influence the control effectiveness as mentioned above. The control effectiveness is least affected in Case 2 though two TMDs do not work properly

and TMD#5 locates at another maximum modal amplitude location (location B). However, the modal contribution of mode 2 is only 8.66% as mentioned above. The malfunction of this TMD is less evident compared to Case 1. For Case 3, the maximum displacements are between Cases 1 and 2, the displacements during most of the whole simulation time duration are actually slightly larger than other two cases as shown in Figure 5-17. These results can be further observed by the corresponding acceleration PSD curves shown in Figure 5-18.

Table 5-6 Peak displacements of the tower with some TMDs not working and the corresponding response ratios

Type	Disp. (mm)		Ratio (%)	
	A	B	A	B
Original	739	352	-	-
Six TMDs	444	209	39.92	40.63
Case 1	554	259	25.03	26.42
Case 2	505	235	31.66	33.24
Case 3	532	246	28.01	30.11

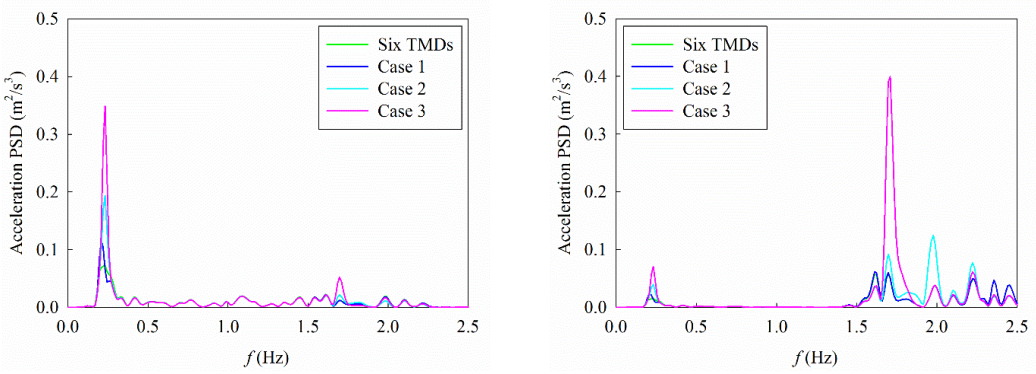

(a) location A (b) location B

Figure 5-18 Acceleration power spectral densities at (a) location A and (b) location B with some TMDs not working

5.6 Conclusions

Previous studies on the wind turbine tower vibration control proposed installing control device at the top of the tower. This application is reasonable when the external vibration sources are wind and/or sea wave since the energy of these loadings mainly concentrate in the low frequency range and normally only the fundamental vibration mode of the tower is excited. When wind turbines are located in the seismic prone areas, higher vibration modes of the tower might be also excited, and putting the control device at the top of the tower is not necessarily effective to control the seismic induced vibrations. To control both the fundamental and higher vibration modes of the tower, MTMDs are necessary. This chapter proposes using MTMDs to control the tower vibration of offshore wind turbines when they are subjected to the combined

wind, sea wave and earthquake excitations. Numerical analyses are carried out to examine the effectiveness of the proposed method. Numerical results reveal that:

(1) When only the fundamental vibration mode is excited by the external vibration sources, dividing the single TMD into smaller MTMDs may slightly decrease the control effectiveness compared to the case with a single TMD installed at the top of the tower.

(2) When both the fundamental and higher vibration modes of the tower are excited by the external vibration sources, MTMDs can effectively control both the fundamental and higher vibration modes and increase the control effectiveness. The control effectiveness is most evident when MTMDs are applied at the locations with the largest mode amplitudes.

(3) Using smaller MTMDs can significantly improve the robustness of the control system and facilitate the installations.

It should be noted that the primary contribution of the present study is the demonstration of using MTMDs, as compared to using a single TMD, in controlling the vibrations from multiple vibration sources. To apply the proposed method in engineering practice and to guide the designs, more comprehensive studies like the experimental investigations are needed.

5.7 References

Abe, M., & Fujino, Y. (1994). Dynamic characterization of multiple tuned mass dampers and some design formulas. *Earthquake Engineering & Structural Dynamics*, *23*(8), 813-835.

Alati, N., Failla, G., & Arena, F. (2015). Seismic analysis of offshore wind turbines on bottom-fixed support structures. *Philosophical Transactions Royal Society A*, *373*(2035), 20140086.

Arany, L., Bhattacharya, S., Macdonald, J., & Hogan, S. (2016). Closed form solution of Eigen frequency of monopile supported offshore wind turbines in deeper waters incorporating stiffness of substructure and SSI. *Soil Dynamics and Earthquake Engineering*, *83*, 18-32.

Bai, Q., & Bai, Y. (2014). Subsea pipeline design, analysis, and installation. Oxford: Gulf Professional Publishing.

Bakre, S., & Jangid, R. (2004). Optimum multiple tuned mass dampers for base-excited damped main system. *International Journal of Structural Stability and Dynamics*, *4*(4), 527-542.

Bakre, S., & Jangid, R. (2007). Optimum parameters of tuned mass damper for damped main system. *Structural Control and Health Monitoring*, *14*(3), 448-470.

Benowitz, B., & Deodatis, G. (2015). Simulation of wind velocities on long span structures: A novel stochastic wave based model. *Journal of Wind Engineering and Industrial Aerodynamics*, *147*, 154-163.

Bhattacharya, S., & Adhikari, S. (2011). Experimental validation of soil-structure interaction of offshore wind turbines. *Soil Dynamics and Earthquake Engineering*, *31*(5), 805-816.

Bi, K., & Hao, H. (2012). Modelling and simulation of spatially varying earthquake ground motions at sites with varying conditions. *Probabilistic Engineering Mechanics*, *29*, 92-104.

Bi, K., & Hao, H. (2016). Using pipe-in-pipe systems for subsea pipeline vibration control. *Engineering Structures*, *109*, 75-84.

Bi, K., Hao, H., & Chouw, N. (2011). Influence of ground motion spatial variation, site condition and SSI on the required separation distances of bridge structures to avoid seismic pounding. *Earthquake Engineering & Structural Dynamics*, *40*(9), 1027-1043.

Chen, J., & Georgakis, C. T. (2013a). Tuned rolling-ball dampers for vibration control in wind turbines. *Journal of Sound and Vibration*, *332*(21), 5271-5282.

Chen, J., & Georgakis, C. T. (2013b). Spherical tuned liquid damper for vibration control in wind turbines. *Journal of Vibration and Control*, *21*(10), 1875-1885.

Chen, J., Liu, Y., & Bai, X. (2015). Shaking table test and numerical analysis of offshore wind turbine tower systems controlled by TLCD. *Earthquake Engineering and Engineering Vibration*, *14*(1), 55-75.

Chopra, A. K. (2012). Dynamics of structures 4th ed. New Jersey: Prentice Hall.

Chou, J., & Tu, W. (2011). Failure analysis and risk management of a collapsed large wind turbine tower. *Engineering Failure Analysis*, *18*(1), 295-313.

Colwell, S., & Basu, B. (2009). Tuned liquid column dampers in offshore wind turbines for structural control. *Engineering Structures*, *31*(2), 358-368.

Damgaard, M., Zania, V., Andersen, L., & Ibsen, L. (2014). Effects of soil-structure interaction on real time dynamic response of offshore wind turbines on monopiles. *Engineering Structures*, *75*, 388-401.

Den Hartog, J. P. (1956). Mechanical vibrations. New York: McGraw-Hill.

Det Norske Veritas (DNV). (2010). DNV-RP-C205: Environmental conditions and environmental loads. Norway: DNV.

Det Norske Veritas (DNV). (2014). DNV-OS-J101: Design of offshore wind turbine structures. Copenhagen, Denmark: DNV.

Elias, S., Matsagar, V., & Datta, T. (2016). Effectiveness of distributed tuned mass dampers for multi-mode control of chimney under earthquakes. *Engineering Structures*, *124*, 1-16.

Hao, H., Oliveira, C., & Penzien, J. (1989). Multiple-station ground motion processing and simulation based on SMART-1 array data. *Nuclear Engineering and Design*, *111*(3), 293-310.

Hasselmann, K., Barnett, T., Bouws, E., Carlson, H., Cartwright, D., Enke, K., Walden, H. (1973). Measurements of wind-wave growth and swell decay during the Joint North Sea Wave Project (JONSWAP). Hamburg: Deutches Hydrographisches Institut.

Hoang, N., Fujino, Y., & Warnitchai, P. (2008). Optimal tuned mass damper for seismic applications and practical design formulas. *Engineering Structures*, *30*(3), 707-715.

Huang, G., Liao, H., & Li, M. (2013). New formulation of Cholesky decomposition and applications in stochastic simulation. *Probabilistic Engineering Mechanics*, *34*, 40-47.

IEC 61400-1. (2005). Wind turbines-Part 1: design requirements 3rd ed. Geneva (Switzerland): International Electrotechnical Commission.

IEC 61400-3. (2009). Wind turbines-Part 3: design requirements for offshore wind turbines 1st ed. Geneva (Switzerland): International Electrotechnical Commission.

Jangid, R. (1999). Optimum multiple tuned mass dampers for base-excited undamped system. *Earthquake Engineering & Structural Dynamics*, *28*(9), 1041-1049.

Jonkman, J., Butterfield, S., Musial, W., & Scott, G. (2009). Definition of a 5-MW reference wind turbine for offshore system development. (Technical Report No. NREL/TP-500-38060). Golden, CO: National Renewable Energy Laboratory.

Joshi, A., & Jangid, R. (1997). Optimum parameters of multiple tuned mass dampers for base-excited damped systems. *Journal of Sound and Vibration*, *202*(5), 657-667.

Kareem, A., & Kline, S. (1995). Performance of multiple mass dampers under random loading. *Journal of Structural Engineering*, *121*(2), 348-361.

Katsanos, E. I., Thöns, S., & Georgakis, C. T. (2016). Wind turbines and seismic hazard: a state-of-the-art review. *Wind Energy*, *19*(11), 2113-2133.

Koukoura, C., Natarajan, A., & Vesth, A. (2015). Identification of support structure damping of a full scale offshore wind turbine in normal operation. *Renewable Energy*, *81*, 882-895.

Lackner, M. A., & Rotea, M. A. (2011). Passive structural control of offshore wind turbines. *Wind Energy*, *14*(3), 373-388.

Li, C. (2002). Optimum multiple tuned mass dampers for structures under the ground acceleration based on DDMF and ADMF. *Earthquake Engineering & Structural Dynamics*, *31*(4), 897-919.

Li, C., Hao, H., Li, H., & Bi, K. (2015). Theoretical modeling and numerical simulation of seismic motions at seafloor. *Soil Dynamics and Earthquake Engineering*, *77*, 220-225.

Li, C., & Liu, Y. (2003). Optimum multiple tuned mass dampers for structures under the ground acceleration based on the uniform distribution of system parameters. *Earthquake Engineering & Structural Dynamics*, *32*(5),

Mensah, A. F., & Dueñas-Osorio, L. (2014). Improved reliability of wind turbine towers with tuned liquid column dampers (TLCDs). *Structural Safety*, *47*, 78-86.

Moon, K. S. (2010). Vertically distributed multiple tuned mass dampers in tall buildings: performance analysis and preliminary design. *The Structural Design of Tall and Special Buildings*, *19*(3), 347-366.

Murtagh, P. J., Basu, B., & Broderick, B. M. (2005). Along-wind response of a wind turbine tower with blade coupling subjected to rotationally sampled wind loading. *Engineering Structures*, *27*(8), 1209-1219.

Murtagh, P. J., Ghosh, A., Basu, B., & Broderick, B. M. (2008). Passive control of wind turbine vibrations including blade/tower interaction and rotationally sampled turbulence. *Wind Energy*, *11*(4), 305-317.

Prowell, I., Elgamal, A., Uang, C. M., Enrique Luco, J., Romanowitz, H., & Duggan, E. (2014). Shake table testing and numerical simulation of a utility-scale wind turbine including operational effects. *Wind Energy*, *17*(7), 997-1016.

Prowell, I., Veletzos, M., Elgamal, A., & Restrepo, J. (2009). Experimental and numerical seismic response of a 65 kW wind turbine. *Journal of Earthquake Engineering*, *13*(8), 1172-1190.

Rahman, M., Ong, Z. C., Chong, W. T., Julai, S., & Khoo, S. Y. (2015). Performance enhancement of wind turbine systems with vibration control: A review. *Renewable and Sustainable Energy Reviews*, *51*, 43-54.

Sadek, F., Mohraz, B., Taylor, A. W., & Chung, R. M. (1997). A method of estimating the parameters of tuned mass dampers for seismic applications. *Earthquake Engineering & Structural Dynamics*, *26*(6), 617-636.

Sorensen, R. M. (2005). Basic coastal engineering. New York: Springer Science & Business Media.

Stewart, G. M., & Lackner, M. A. (2014). The impact of passive tuned mass dampers and wind-wave misalignment on offshore wind turbine loads. *Engineering Structures*, *73*, 54-61.

Warburton, G. (1982). Optimum absorber parameters for various combinations of response and excitation parameters. *Earthquake Engineering & Structural Dynamics*, *10*(3), 381-401.

Xu, K., & Igusa, T. (1992). Dynamic characteristics of multiple substructures with closely spaced frequencies. *Earthquake Engineering & Structural Dynamics*, *21*(12), 1059-1070.

Yamaguchi, H., & Harnpornchai, N. (1993). Fundamental characteristics of multiple tuned mass dampers for suppressing harmonically forced oscillations. *Earthquake Engineering & Structural Dynamics*, *22*(1), 51-62.

Zhang, Z., Chen, J., & Li, J. (2013). Theoretical study and experimental verification of vibration control of offshore wind turbines by a ball vibration absorber. *Structure and Infrastructure Engineering*, *10*(8), 1087-1100.

Zhang, Z., Nielsen, S. R. K., Blaabjerg, F., & Zhou, D. (2014). Dynamics and control of lateral tower vibrations inoffshore wind turbines by means of active generator torque. *Energies*, *7*(11), 7746-7772.

CHAPTER 6 MITIGATION OF TOWER AND OUT-OF-PLANE BLADE VIBRATIONS OF OFFSHORE MONOPILE WIND TURBINES BY USING MULTIPLE TUNED MASS DAMPERS

ABSTRACT[5]

Offshore wind turbines are vulnerable to external vibration sources such as wind and wave excitations due to the increasing size and flexibility. It is necessary to mitigate the excessive vibrations of offshore wind turbines to ensure the safety and serviceability during their operations. Some research works have been carried out to control the excessive vibrations of the tower and the in-plane vibrations of blades. Very limited study focuses on the out-of-plane vibration mitigation of blades. In the present study, a detailed finite element (FE) model of the latest NREL 5 MW wind turbine is developed by using the FE code ABAQUS. The tower and blades are explicitly modelled, and the rotating of the blades is considered. Multiple tuned mass dampers (MTMDs) are proposed to be installed in the tower and each blade to simultaneously mitigate the out-of-plane vibrations of the tower and blades when the wind turbine is subjected to the combined wind and wave loadings. The effectiveness and robustness of the proposed method are systematically investigated. Numerical results show that MTMDs can effectively mitigate the out-of-plane vibrations of the tower and blades when the wind turbine is in either the operational or parked condition.

6.1 Introduction

Offshore wind turbines are becoming an attractive means to produce electricity recently. In the current design, slender tower and larger rotor are normally adopted in order to more effectively extract the vast wind resources in the marine area. For example, the tower height and rotor diameter of the NREL 5 MW wind turbine reach 87.6 m and 126 m respectively, while the maximum wall thickness of tower is only 0.027 m (Jonkman et al., 2009). These tall and thin-walled structures are vulnerable to the external vibration sources such as wind and wave excitations. These external excitations can result in excessive vibrations of the wind turbines, which in turn may compromise wind energy output or even lead to the fatigue damages of the structural components. It is therefore necessary to mitigate the adverse

[5] This chaper was published in *Structure and Infrastructure Engineering* with the full bibliographic citation as follows:
Zuo, H., Bi, K. & Hao, H. (2019). Mitigation of tower and out-of-plane blade vibrations of offshore monopile wind turbines by using multiple tuned mass dampers. *Structure and Infrastructure Engineering*, *15*(2):269-284. https://doi.org/10.1080/15732479.2018.1550096.

vibrations of offshore wind turbines to ensure the safety and serviceability during their operations.

Extensive research works have been carried out by different researchers to suppress the excessive vibrations of wind turbines, and the majority works focused on the vibration control of the tower by installing a single vibration control device at the top of the tower. For example, Murtagh et al. (2008), Lackner and Rotea (2011), Altay et al. (2014), Stewart and Lackner (2014) and Zheng et al. (2017) installed tuned mass dampers (TMDs) in the nacelle to mitigate the tower vibrations; Sun and Jahangiri (2018) proposed using a three dimensional (3D) pendulum TMD; Colwell and Basu (2009), Mensah and Dueñas-Osorio (2014) and Chen et al. (2015a) investigated the effectiveness of using tuned liquid column dampers (TLCDs); Chen and Georgakis suggested using rolling-ball dampers (2013a) and spherical tuned liquid dampers (2013b); Van der Woude and Narasimhan (2014) installed vibration isolators at the tower top; a ball vibration absorber (BVA) (Zhang et al., 2013) and a tuned liquid damper (TLD) (Zhang et al., 2016) were used as well; a semi-active MR-TLCD and -TMD were proposed by Sarkar and Chakraborty (2018) and Sun (2018) respectively; Stewart and Lackner (2011) and Brodersen et al. (2016) suggested using active control techniques and an active TMD was installed in the nacelle. The effectiveness of the proposed control devices were either numerically (Altay et al., 2014; Brodersen et al., 2016; Colwell & Basu, 2009; Lackner & Rotea, 2011; Mensah & Dueñas-Osorio, 2014; Murtagh et al., 2008; Sarkar & Chakraborty, 2018; Stewart & Lackner, 2011, 2014; Sun, 2018; Sun & Jahangiri, 2018; Van der Woude & Narasimhan, 2014; Zheng et al., 2017) or experimentally (Chen & Georgakis, 2013a, 2013b; Chen et al., 2015a; Zhang et al., 2013, 2016) investigated. The results showed that these dampers can be used to effectively control the adverse vibrations of the tower of the wind turbine when it is subjected to wind and/or wave loadings.

It is well known that the energies of wind and wave concentrate in the low frequency range, in general only the fundamental vibration mode of the tower would be mostly excited, the largest displacement therefore occurs at the tower top. On the other hand, many wind turbines are located in the seismic prone areas, severe earthquakes can also endanger the safety of these wind turbines. Compared to the wind and wave, the energy of an earthquake loading is within a broader frequency range, and higher vibration modes of the tower might also be well excited by the earthquake loading. In such a case, the maximum displacement does not necessarily occur at the tower top but at certain locations along the tower depending on which vibration mode dominates the total structural response.

Moreover, there is limited space in the nacelle, which makes the installation of a large control device in the nacelle not straightforward. The authors (Zuo et al., 2017) therefore proposed using multiple TMDs (MTMDs) to control the tower vibrations under the combined wind,

wave and seismic loadings. It was observed that MTMDs can effectively mitigate the vibrations and significantly increase the robustness of the wind turbine system. Using MTMDs is also more practical compared to the application of a single TMD at the tower top considering the limited space in the nacelle. It also makes the installation, maintenance and replacement of TMDs easier because of the smaller size and mass of each TMD.

Compared to the vibration of the tower, the blade vibrations might be even more serious (Zuo et al., 2018). The blade vibrations can occur in both the flap-wise (out-of-plane) and edgewise (in-plane) directions. The studies on the edgewise vibration control of the blades are relatively extensive. Zhang et al. (2014) proposed using roller dampers to suppress the edgewise vibrations of the blades. Motivated by the concept of TLCD (Zhang et al., 2015a), two new types of liquid damper, namely the tuned rectangular (Zhang et al., 2015b) and circular (Basu et al., 2016) liquid dampers were proposed recently. It should be noted that the theoretical model of the rotating blade-damper system is very complex and probably for this reason the interaction between the tower and rotating blades was not considered in these studies (Basu et al., 2016; Zhang et al., 2014, 2015a, 2015b). Semi-active and active control techniques have also been investigated by different researchers to mitigate the edgewise vibrations of the blades. Chen et al. (2015b) proposed a semi-active fuzzy control strategy for controlling the edgewise vibrations when the wind turbine is under extreme wind, i.e. the wind turbine stops working and it is in the parked condition. The use of active tendons installed inside the blades was suggested by Staino et al. (2012) and Staino and Basu (2013) for the active control of the edgewise vibrations, in which a variable control force, which was manipulated according to a prescribed law, was applied in the rotor plane. Fitzgerald et al. (2013) and Fitzgerald and Basu (2014) studied using active TMDs and cable connected active TMDs to mitigate the edgewise vibrations in the rotating blades. The effectiveness of these control methods was demonstrated through numerical investigations.

Compared to the edgewise vibration mitigation, very limited research works on the flap-wise vibration control were performed. Arrigan et al. (2011) proposed using semi-active TMDs to control the flap-wise vibrations of the blades. Significant reduction was achieved for both the steady and turbulent wind loadings, which highlighted the viability of TMDs in mitigating the vibrations of the blades in the flap-wise direction. Using semi-active and active control strategies can achieve reasonable structural response reduction, however, both semi-active and active control methods need relatively complicated controller configurations and external power input, which impedes their applications in the blades since the space in the blades is even smaller than that in the nacelle. Therefore using multiple smaller TMDs will be more practical. This chapter proposes using MTMDs to control the out-of-plane vibrations of the blades of the wind turbine.

On the other hand, the stiffness of the operational wind turbines is time dependent due to the time varying centrifugal stiffness generated by the rotation of the blades, which can alter the vibration characteristics of the wind turbines and in turn affect the dynamic responses of the structure. Moreover, the wind loads acting on the blades are directly influenced by their geometrical configurations (Hansen, 2008). However, most previous studies assumed the wind turbines were in the parked condition and the blades were considered as a lumped mass located at the tower top by neglecting the interaction between the tower and blades and the geometrical characteristics of the blades (Colwell & Basu, 2009; Zheng et al., 2017; Zuo et al., 2017). Some researchers considered the operational condition of the blade, but each blade was simplified as a few degrees of freedom (DOFs) system (Fitzgerald & Basu, 2016; Harte et al., 2012; Quilligan et al., 2012), the influence of geometrical configurations on the wind loads acting on the blades therefore could not be realistically considered. These simplified models, therefore, might not be able to accurately capture the responses of the wind turbine.

This chapter is an extension of the authors' recent study (Zuo et al., 2017), in which MTMDs are used to control the vibrations of the wind turbine tower. The NREL 5 MW wind turbine is taken as the example again, and the detailed finite element (FE) model of this wind turbine is developed by using the commercially available FE code ABAQUS. Compared to the previous study (Zuo et al., 2017), not only the tower, but also the blades are explicitly modelled in the numerical model. The influences of the geometrical configurations and rotor velocity on the wind loads acting on the blades, the centrifugal stiffness generated by the blades rotation, and the interaction between the tower and blades are realistically considered. In the present study, MTMDs are installed in the tower and each blade to simultaneously control the out-of-plane vibrations of the tower and blades. The responses of the parked and operational wind turbine when they are subjected to the combined actions of wind and wave loadings are compared and discussed, the effectiveness and robustness of the proposed method are investigated.

6.2 Numerical model

In the present study, the NREL 5 MW three-bladed wind turbine is used as an example since its detailed properties are well reported (Jonkman et al., 2009). Figure 6-1 shows the main dimensions of the wind turbine and the detailed information is tabulated in Table 6-1. As shown, the height of the tower is 87.6 m, and the outer diameters at the tower top and base are 3.87 m and 6 m respectively and the corresponding wall thickness are 0.019 m and 0.027 m. The outer diameter and wall thickness decrease linearly from the base to the top of the tower. A monopile is designed as the foundation of the wind turbine and the total length of the hollow monopile is 30 m, in which 10 m is above the mean sea level and another 20 m is in the sea

water. The outer diameter and wall thickness of the monopile are the same as those of the base cross section of the tower.

Previous studies revealed that soil-structure (monopile) interaction (SSI) can alter the vibration characteristics of the structure and therefore the structural responses (Bi et al., 2011; Zuo et al., 2018). Not to further complicate the problem, SSI is, however, not considered in the present study and the monopile is fully fixed at the seabed level.

The length of each blade is 61.5 m and the hub radius is 1.5 m. The rotor radius is therefore 63 m. Each blade is composed of eight unique airfoil sections and the detailed geometries can be found in (Jonkman et al., 2009). It should be noted that the wall thickness of each blade is not defined in (Jonkman et al., 2009), and a uniform thickness is assumed to ensure the mass of the blade is the same as that reported in (Jonkman et al., 2009), which is calculated as 0.019 m.

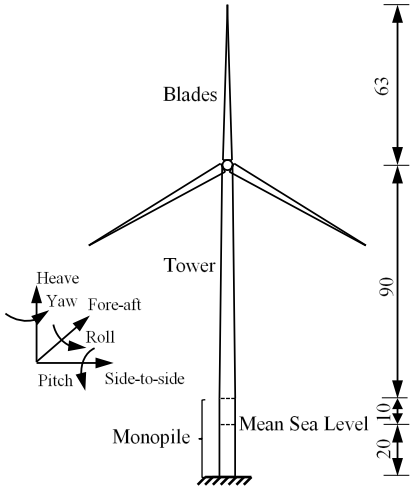

Figure 6-1 Offshore wind turbine model (Front view, dimensions in m)

Table 6-1 Properties of NREL 5 MW wind turbine

NREL 5 MW baseline wind turbine properties		
	Rotor diameter	126 m
	Hub height	90 m
	Cut-in, rated, cut-out wind speed	3 m/s, 11.4 m/s, 25 m/s
Blade	Cut-in, rated rotor speed	6.9 rpm, 12.1 rpm
	Length	61.5 m
	Overall (integrated) mass	17,740 kg
	Structural damping ratio	0.48%
	Hub diameter	3 m
Hub and Nacelle	Hub mass	56,780 kg
	Nacelle mass	240,000kg
	Height above water	87.6 m
Tower	Overall (integrated) mass	347,460 kg
	Structural damping ratio	1%

The detailed 3D FE model of the NREL 5 MW wind turbine is developed by using the commercially available FE code ABAQUS. The blades, tower and monopile are modelled by shell elements (S4 in ABAQUS). To ensure the same deformation at the connection between the tower and monopile, the cross sections of the base of the tower and the top of the monopile are tied with each other. To simulate the blades rotation, a hinge connection between the top of the tower and the root of the blades is defined and the rotational DOF along the out-of-plane direction is released. A convergence test shows that the element sizes of 0.5 m and 1 m in the circumferential and axial directions of the blades, tower and monopile yield a good balance between the computational time and accuracy, these element sizes are therefore adopted in the present numerical model. Figure 6-2 shows the FE model of the wind turbine.

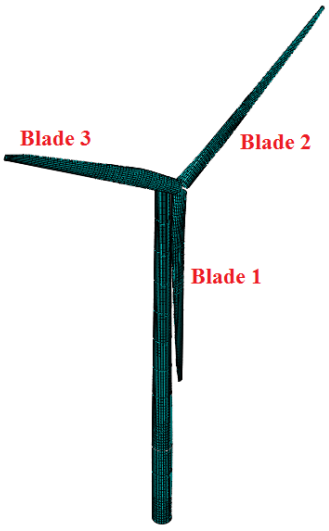

Figure 6-2 FE model of the wind turbine

Table 6-2 Material properties of the wind turbine

Component	Material	Density (kg/m^3)	Elastic modulus (MPa)	Poisson's ratio	Yield strength (MPa)	Plastic strain
Blade	Polyester	1850	3.8×10^4	0.3	700	0.02
Tower	Steel	8500	2.1×10^5	0.3	235	0.01
Monopile	Steel	7850	2.1×10^5	0.3	235	0.01

Table 6-2 tabulates the material properties of the blades, tower and monopile. The density of the tower is taken as 8500 kg/m^3 in the present study to account for the welds and bolts that are not directly included in the numerical model (Jonkman et al., 2009). For the monopile in the sea water, the interaction between the monopile and surrounding water is modelled by the added mass (Zuo et al., 2017). The polyester and steel are assumed as ideal elastic-plastic materials and the stress-strain relationship is shown in Figure 6-3, where f_y is the yield strength, ε_1 is the elastic strain and ε_2 is the strain which equals to the sum of the elastic and plastic strains.

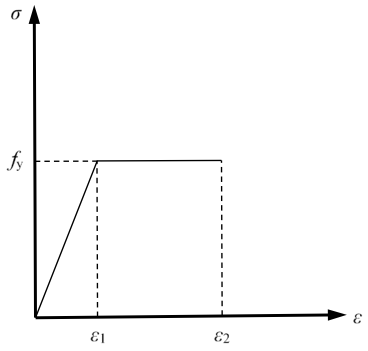

Figure 6-3 Ideal elastic-plastic stress-strain relationship of wind turbine materials: polyester (blade) and steel (tower and monopile)

6.3 Optimization of TMD system

In the present study, MTMDs are proposed to be installed in the tower and each blade to control their out-of-plane vibrations. Figure 6-4 shows a main structure-MTMD system with n TMDs, in which each auxiliary mass (m_i, i=1⋯n) is attached to the vibrating main structure by a spring (k_i) and a dashpot (c_i). The natural frequency of each TMD is tuned to the vibration frequency of the main structure so that the dampers will resonate out of phase with the main structure and a large amount of structural vibrating energy is transferred to the TMD system and dissipated by the dashpots. If n=1, it becomes a single TMD (STMD) system.

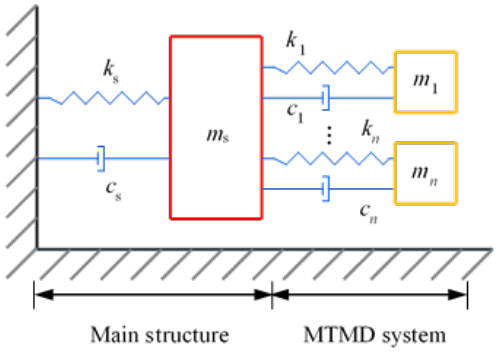

Figure 6-4 Main structure-MTMD system

Two key parameters of each TMD, namely the vibration frequency and damping ratio, can significantly influence the control effectiveness of the system. Various methods have been proposed by different researchers (Hoang et al., 2008; Nikoo et al., 2017; Sadek et al., 1997) to optimize these parameters after the pioneering work done by Den Hartog (1956). In the present study, the displacement response is of interest and numerical searching technique is used to obtain the optimal values by minimizing the mean square displacement of the main structure under a given mass ratio. To simplify the optimization analysis, the following two assumptions are made (Li & Liu, 2003): (1) each TMD has the same mass and damping

coefficient; (2) the natural frequencies of MTMDs are uniformly distributed around their average natural frequency.

For the system shown in Figure 6-4, the vibration frequency of the main structure can be calculated as $\omega_S = \sqrt{k_S/m_S}$, in which m_s and k_s are the structural mass and stiffness respectively. For the MTMD system, the mass ratio is defined as $\mu = \sum_{i=1}^{n} m_i/m_S$, the mass of each TMD can be therefore calculated based on the first assumption as follows

$$m_i = \mu m_S/n \quad i = 1, 2, \dots, n \tag{6.1}$$

The frequency of the *i*th TMD can be estimated based on the second assumption as (Joshi & Jangid, 1997)

$$\omega_i = \omega_T \left[1 + \left(i - \frac{n+1}{2}\right)\frac{\beta}{n-1}\right] \quad i = 1, 2, \dots, n \tag{6.2}$$

in which $\omega_T = \sum_{i=1}^{n} \omega_i/n$ is the average frequency of the TMDs and $\beta = (\omega_n - \omega_1)/\omega_T$ is the non-dimensional frequency interval. The stiffness and damping coefficient of each TMD are therefore

$$k_i = m_i \omega_i^2 \quad i = 1, 2, \dots, n \tag{6.3}$$

$$c_i = 2n m_i \zeta_T \Big/ \sum_{i=1}^{n} 1/\omega_i \quad i = 1, 2, \dots, n \tag{6.4}$$

where $\zeta_T = \sum_{i=1}^{n} \zeta_i/n$ is the average damping ratio of MTMDs and ζ_i is the damping ratio of the *i*th TMD.

As mentioned above, the displacement response of the wind turbine is of interest in the present study. The mean square displacement of the wind turbine can be expressed as (Xu & Igusa, 1992)

$$\sigma^2 = \int_0^{\infty} |H_S(\omega)|^2 S(\omega) d\omega \tag{6.5}$$

where $S(\omega)$ is the power spectral density (PSD) of the excitation and $H_S(\omega)$ is the transfer function, which can be calculated as (Xu & Igusa, 1992)

$$H_S(\omega) = \left[\omega_S^2 - 2i\omega\omega_S\zeta_S - \omega^2 - i\omega m_S^{-1} Z(\omega)\right]^{-1} \tag{6.6}$$

in which $\zeta_S = c_S/2m_S\omega_S$ is the damping ratio of the main structure and $Z(\omega)$ is given by

$$Z(\omega) = -i\omega \sum_{i=1}^{n} \frac{m_i\left(\omega_i^2 - 2i\omega\omega_i\zeta_i\right)}{\omega_i^2 - 2i\omega\omega_i\zeta_i - \omega^2} \tag{6.7}$$

Substituting Eq. (6.6) into Eq. (6.5), the optimal frequency bandwidth β, tuned frequency ratio $\gamma = \omega_{\mathrm{T}}/\omega_{\mathrm{S}}$ and average damping ratio ζ_T can be obtained through a numerical searching technique by minimizing the mean square displacement of the main structure under an assumed mass ratio μ.

For the STMD system, the corresponding values can be obtained by substituting n=1 into the above equations.

6.4 Vibration sources

In the present study, the wind and wave loadings are considered as the external vibration sources. They are stochastically simulated in the present study and briefly introduced in this section.

6.4.1 Wind load on the tower

The wind load acting on the tower is composed of a constant mean and a fluctuating term. The mean wind drag force can be calculated by

$$\bar{f}_{mean,i} = \frac{1}{2} C_{dt} A_i \rho \bar{v}_i^2 \tag{6.8}$$

where C_{dt} is the drag coefficient of the tower and a value of 1.2 is assumed (Colwell & Basu, 2009), ρ is the air density, which is 1.2 kg/m^3, A_i is the area associated with location i and $\bar{v}$ is the mean wind velocity in the present study.

The fluctuating wind loads at different locations along the tower are different but with certain similarities, which is known as the spatial correlation effect and can be described by a spatial coherency loss function. The modal fluctuating drag force power spectrum including the spatial correlation effect can be calculated by (Murtagh et al., 2005)

$$S_{f,j}(f) = (C_{dt}\rho)^2 \sum_{k=1}^{N}\sum_{l=1}^{N} \sqrt{S_{v_k v_k}(f) S_{v_l v_l}(f)}\, coh(k,l;f) A_k A_l \bar{v}_k \bar{v}_l \phi_j(k) \phi_j(l) \tag{6.9}$$

where A_k, A_l and $\bar{v}_k$, $\bar{v}_l$ are the areas exposed to the wind and the mean wind velocities at locations k and l respectively, $\phi_j(k)$ and $\phi_j(l)$ are the coordinates of the jth mode shape of the tower at locations k and l. S_{vkvk} and S_{vlvl} are the auto PSDs of the fluctuating wind velocity at locations k and l and can be described by the Kaimal spectrum (Murtagh et al., 2005), which is defined as

$$S_{vv}(h,f) = 200 v_*^2 \frac{h}{\bar{v}(h)} \frac{1}{\left(1 + 50\frac{fh}{\bar{v}(h)}\right)^{5/3}} \tag{6.10}$$

in which

$$\bar{v}(h) = v_* \ln(h/z_0)/K \tag{6.11}$$

where h is the height of the location where the wind load is calculated, f is the frequency in Hz, v_* is the friction velocity and z_0 and K are the roughness length and von-Karman's constant respectively, which are 0.005 and 0.4 respectively in the present study.

$coh(k, l; f)$ is the spatial coherency loss function between locations k and l, which can be expressed as (Huang et al., 2013)

$$coh(k,l;f) = exp\left(-\frac{D\omega|k-l|}{2\pi\hat{v}}\right)exp\left(-i\frac{k-l}{v_{app}}\omega\right) \quad (k > l) \tag{6.12}$$

where D is a decay constant, ω is the angular frequency in rad/s, $|k\text{-}l|$ and $\hat{v}$ are the distance and average mean wind velocity between locations k and l respectively and v_{app} is the apparent wave velocity and a value of 10 m/s is adopted in the simulation (Huang et al., 2013). For $k<l$, the spatial coherency loss function is the complex conjugate of that with $k>l$. The fluctuating drag force with zero mean in the time domain then can be simulated by using the Inverse Fast Fourier Transform (IFFT) technique (Bi & Hao, 2012; Hao et al., 1989).

To simplify the simulation, the tower is divided into nine segments and the drag force is assumed to be the same in each segment. The lengths of the top (S1) and bottom (S9) segments are 5 m and 15 m respectively and the others are 10 m. Figure 6-5 shows the fluctuating wind velocity PSDs in segments S1 (85-90 m along the tower) and S5 (45-55 m) and the corresponding model values when the mean wind velocity at the tower top is 15 m/s. The model and simulated coherency loss functions between S1 and S5 are shown in Figure 6-6. As shown, the simulated results agree well with the corresponding model values. For conciseness, not all the wind loads acting on the tower are presented, only the drag forces in S1 and S5 are shown in Figure 6-7. The extreme case of the mean wind velocity at the tower top (25 m/s) is also considered in the present study, and the wind loads are also shown in Figure 6-7. It is obvious that large wind velocity results in large wind loads on the tower.

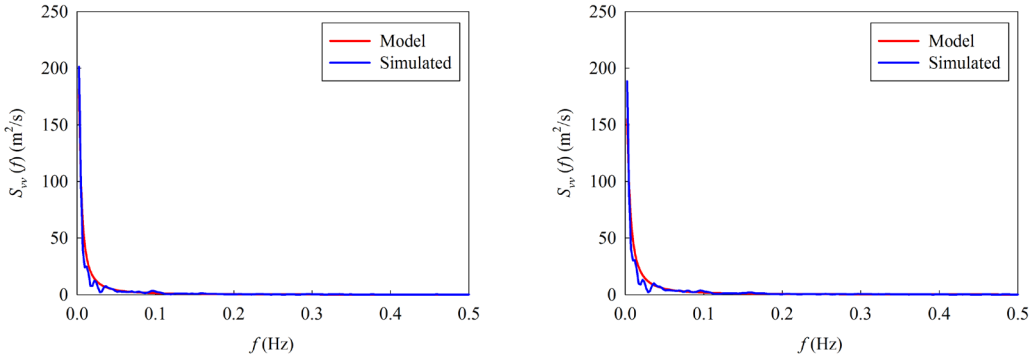

Figure 6-5 PSDs of the simulated wind velocity and the model values in S1and S5

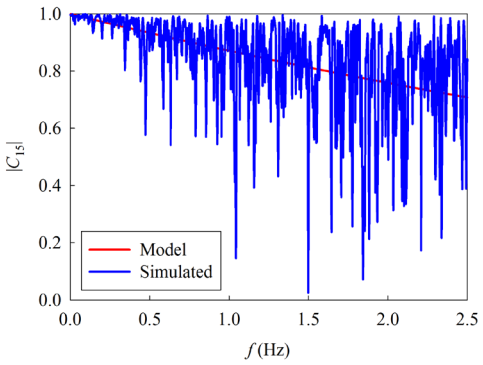

Figure 6-6 Coherency loss functions between S1 and S5

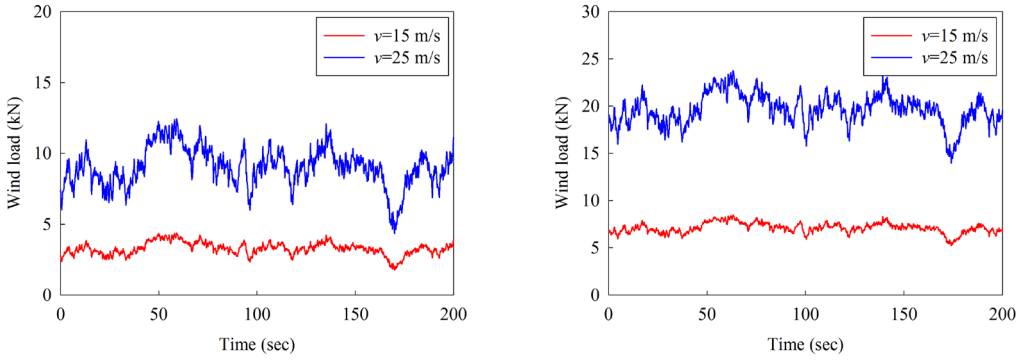

Figure 6-7 Wind load time histories in S1 and S5

6.4.2 Wind load on the blades

Different from the wind load on the tower, the wind loads acting on the blades are influenced by the wind velocity, rotor velocity, pitch angle and geometrical characteristics of the blade (Hansen, 2008). The blade element momentum (BEM) method (Hansen, 2008) is adopted in the present study to estimate the wind loads on the blades. In the BEM method, it is assumed that no aerodynamic interaction between different sections along the rotor. Each blade therefore can be divided into several elements and wind load acting on each element can be calculated separately.

The relative wind velocity v_{rel} on each element of the blade is given by

$$v_{rel}(r) = \sqrt{\left(\bar{v}(r)(1-a) + v_f\right)^2 + \left(\Omega r(1+a')\right)^2} \tag{6.13}$$

where r is the radial distance, a and a' are the axial and tangential induction factors respectively, Ω is the rotor velocity and v_{f} is the fluctuating wind velocity. Note that the PSD of the fluctuating wind velocity v_{f} is a time-variant rotational sample spectrum due to the rotation of the blades. However, not to further complicate the problem, an isotropic, homogeneous turbulence at the hub height is assumed to represent the turbulence over the rotor field in the

present study as suggested in (Harte et al., 2012). The fluctuating wind velocity v_f therefore can be obtained by using the PSD of wind velocity at the hub height defined in Eq. (6.10).

After the relative wind velocity is defined, the lift and drag forces on each element of the blade can be calculated by

$$p_l(r) = \frac{1}{2}\rho v_{rel}^2(r) l(r) C_{lb} \tag{6.14}$$

$$p_d(r) = \frac{1}{2}\rho v_{rel}^2(r) l(r) C_{db} \tag{6.15}$$

where l is the chord length and C_{lb} and C_{db} are the lift and drag coefficients of the blade respectively. More detailed information regarding these two parameters can be found in (Jonkman et al., 2009). By projecting the lift and drag forces in the directions parallel and perpendicular to the rotor plane respectively as shown in Figure 6-8, the local wind loads can be calculated by

$$\begin{Bmatrix} p_t(r) \\ p_n(r) \end{Bmatrix} = \begin{bmatrix} \sin(\varphi) & -\cos(\varphi) \\ \cos(\varphi) & \sin(\varphi) \end{bmatrix} \begin{Bmatrix} p_l(r) \\ p_d(r) \end{Bmatrix} \tag{6.16}$$

where φ is the flow angle and it can be calculated as

$$\varphi(r) = \tan^{-1}\left(\frac{(1-a)\bar{v}(r) + v_f}{(1+a')\Omega r}\right) \tag{6.17}$$

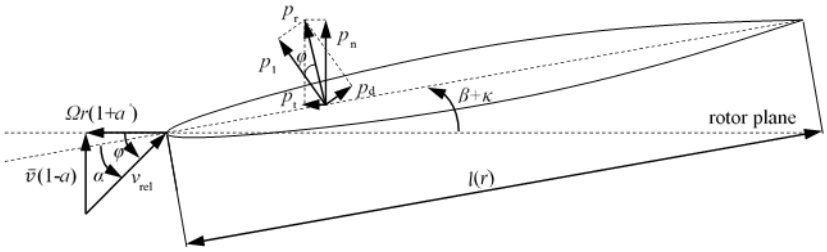

Figure 6-8 Wind loads acting on the blade element

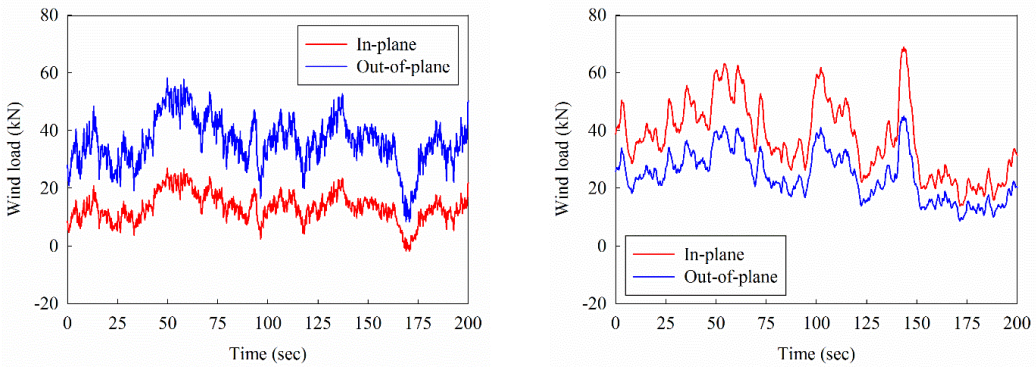

(a) Operational condition with v=15 m/s (b) Parked condition with v=25 m/s

Figure 6-9 In-plane and out-of-plane wind loads on blade 2

When the parked condition is of interest, the above formulas can be simplified by substituting Ω=0 into Eqs. (6.13) and (6.17). Figure 6-9(a) shows the total in-plane and out-of-plane wind loads on blade 2 by integrating the wind loads on each blade element over the entire rotor length when the rotor speed is 12.1 rounds per minute (rpm) and the mean wind velocity at the tower top is 15 m/s. Figure 6-9(b) shows the corresponding wind loads when the wind turbine is in the parked condition and wind velocity is 25 m/s. For brevity, the wind loads acting on the other two blades are not shown.

6.4.3 Wave load on the monopile

The JONSWAP spectrum is used to simulate the sea surface elevation in the present study, which has the following form (Hasselmann et al., 1973)

$$S_{\eta\eta}(f) = \alpha_P g^2 (2\pi)^{-4} f^{-5} exp\left[-\frac{5}{4}\left(\frac{f_m}{f}\right)^4\right] \gamma^{exp\left[-\frac{(f-f_m)^2}{2\sigma^2 f_m^2}\right]} \tag{6.18}$$

in which g is the gravitational acceleration and γ is the peak enhancement factor and a value of 3.3 is used in the simulation. α_P, f_m and σ are three constants, which are

$$\alpha_P = 0.076(Fg/v_{10}^2)^{-0.22} \tag{6.19}$$

$$f_m = 11(v_{10}F/g^2)^{-1/3}/\pi \tag{6.20}$$

$$\sigma = \begin{cases} 0.07 & f \le f_m \\ 0.09 & f > f_m \end{cases} \tag{6.21}$$

where F is the fetch length and v_{10} is the mean wind velocity at 10 m above sea surface.

In the simulation, the following parameters are used: g=9.8 m/s^2, v_{10}=11.5 m/s and F=40,000 m. The wave frequency f_m is therefore 0.208 Hz based on Eq. (6.20) and the wave period is T=1/f_m= 4.81 s. The wave length can be calculated as λ=gT^2/2π=36 m (Sorensen, 2005), which is larger than five times of the diameter of the monopile. Based on the specifications reported in DNV (2010), the Morison formula can be used to calculate the wave load on the monopile, which is given by

$$F_w = \frac{1}{2}\rho_w C_{dp} d_p |v_x| v_x + \rho_w C_m A_p a_x \tag{6.22}$$

where F_w is the transverse wave load per unit length of the monopile, ρ_w=1030 kg/m^3 is the sea water density, d_p, A_p are the outer diameter and cross section area of the monopile respectively and C_{dp}, C_m are the drag and inertia coefficients respectively, which are 1.2 and 2.0 respectively in the present study, v_x and a_x are the velocity and acceleration of water particles respectively, the detailed calculation of these two parameters can be found in (Zuo et al., 2018).

The monopile in the water is divided into two segments and the length of each segment is 10 m. The comparison between the PSD of the simulated sea surface elevation and the corresponding model values is shown in Figure 6-10. Figure 6-11(a) shows the simulated wave load at the mean sea level when the mean wind velocity at the tower top is 15 m/s. When the extreme case of the mean wind velocity equalling 25 m/s is considered, the corresponding curves are shown in Figure 6-11(b). The wave loads at other locations are not presented for brevity.

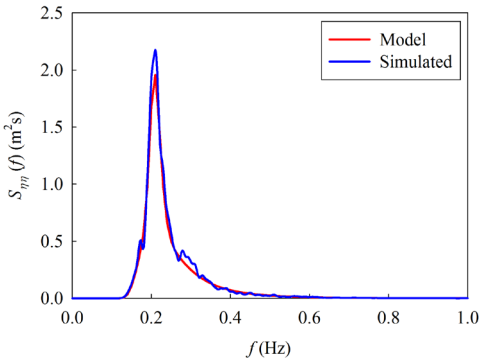

Figure 6-10 PSD of the simulated sea surface elevation and the model values (v=15 m/s)

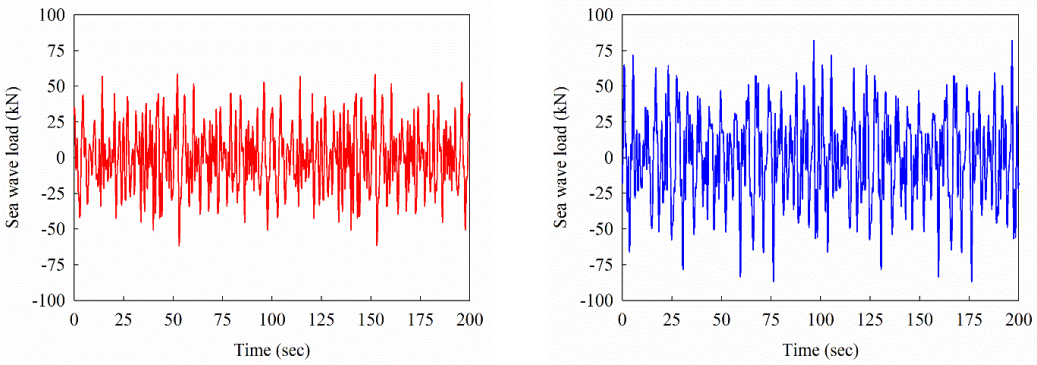

(a) v=15 m/s (b) v=25 m/s

Figure 6-11 Wave load time histories at mean sea level

As indicated above, the tower, blade and monopile in the water are divided into several segments in the simulation. In the present FE model, a reference point is developed in each segment and coupled with the cross section of the corresponding segment, the simulated wind and wave loads are applied to these reference points as the external vibration sources.

6.5 Numerical results

To examine the effectiveness of the proposed vibration control method, two scenarios are considered in the present study. In the first scenario, the wind turbine is in the operational condition with the blades rotating at a uniform angular velocity of Ω=1.27 rad/s, which

corresponds to the rated rotor speed of the NREL 5 MW wind turbine (12.1 rpm), and the mean wind velocity at the hub height is taken as 15 m/s. In the second scenario, the wind turbine is in the parked condition with the locations of the blades shown in Figure 6-2. The wind turbine normally stops working when the wind velocity above a certain value (the cut-out wind velocity) in order to protect the electrical and mechanical components. The cut-out wind speed of the NREL 5 MW wind turbine is 25 m/s (Jonkman et al., 2009), and it is adopted in this section, i.e. the mean wind velocity of 25 m/s and the rotor velocity of Ω=0 rad/s are used to simulate the wind loads in the parked condition. In both scenarios, a duration of 200 s is considered for all the external vibration sources, and the input time histories are shown in Figure 6-7, Figure 6-9 and Figure 6-11 respectively.

To compare the control effectiveness, the reduction ratio δ is defined as

$$\delta = \frac{SD_1 - SD_2}{SD_1} \tag{6.23}$$

in which SD_1 and SD_2 are the standard deviations of the out-of-plane displacements of the wind turbine without and with control respectively.

6.5.1 Parameters of TMD systems

To optimize the parameters for each TMD, the vibration frequency of the main structure (ω_S) should be known in advance. This chapter proposes using MTMDs to control the out-of-plane vibrations of the tower and blades, the tower and blades are therefore the main structures. Table 6-3 tabulates the fundamental vibration frequencies of the tower and the rotating and parked blades in the out-of-plane direction. It can be seen that the vibration frequency of the rotating blades is slightly larger than that of the parked blades. This is because the rotating blades result in the centrifugal stiffness to the system. The vibration frequencies of the tower and blades in the parked condition can be obtained by carrying out an eigenvalue analysis. The vibration frequency of the rotating blades, however, cannot be directly obtained by using ABAQUS, this is because the rotation of the blades cannot be considered in the modal analysis in ABAQUS. They are indirectly estimated in the present study based on the structural responses (e.g. the displacement or acceleration) by carrying out a Fourier Transform to the responses (Zuo et al., 2018).

Table 6-3 Fundamental vibration frequencies of the tower and blades in the out-of-plane direction

Component	Vibration mode description	Frequency (Hz)
Tower	First tower fore-aft	0.207
Blade	First blade collective flap	0.647 (Rotating), 0.603 (Parked)

To estimate the optimal damping for each TMD (c_i), the damping ratio of the main structure (ζ_S) should be known in advance as well. The damping mechanism of an offshore wind turbine is quite complicated and it is normally composed of structural damping, aerodynamic damping and hydrodynamic damping, which account for the contributions of the structure itself, wind and surrounding sea water respectively (Arany et al., 2016). The structural damping ratios of the tower and blades are 1% and 0.48% as reported in (Jonkman et al., 2009). Aerodynamic damping results from the relative velocity between the rotating blades and the surrounding wind. Without loss of generality, an aerodynamic damping ratio of 3.5% in the fore-aft direction for an operational wind turbine is adopted as suggested in (Bisoi & Haldar, 2014). For a parked wind turbine, a previous study (Arany et al., 2016) revealed that the aerodynamic damping ratio is almost zero, which is therefore assumed in the present study. The hydrodynamic damping results from the drag between the monopile and the surrounding sea water, and its upper limit is about 0.23% (Arany et al., 2016). This value is adopted in this study. Summing all the components together, the damping ratio is 3.98% in the fore-aft direction for the rotating blades; for the parked blades, the value is 0.48%, and for the tower, the corresponding value is 1.23%.

Table 6-4 Optimal values of different TMD systems

TMD	Component	β_{opt}	γ_{opt}	ζ_{Topt}	m (kg)	k_{opt} (N/m)	c_{opt} (Ns/m)
STMD	Tower	–	0.98	0.09	24816	40341	5695
	Rotating blade		0.97	0.09	532	8196	376
	Parked blade		0.98	0.09	532	6376	332
Three TMDs	Tower	0.17	0.99	0.04	8272	11499 13744 16190	849
	Rotating blade	0.18	0.99	0.04	177	2357 2847 3383	57
	Parked blade	0.17	0.99	0.04	177	1817 2169 2554	49
Five TMDs	Tower	0.22	0.99	0.03	4963	6529 7363 8246 9180 10163	381
	Rotating blade	0.23	0.99	0.03	106	1332 1511 1701 1902 2115	25
	Parked blade	0.22	0.99	0.03	106	1031 1158 1302 1449 1604	22

With all the parameters defined above, the optimal parameters for the MTMD system can be estimated based on the method presented in Section 6.4. Table 6-4 tabulates the estimated values by assuming a mass ratio (μ) of 3%. In the present study, three cases are considered. In the first case, a single TMD is installed at the top of the tower and the tip of each blade. In the second and third cases, three and five TMDs are placed from the tower top with a 10 m interval; for the blades, they are installed in the first three and five segments from each blade tip, i.e. 0 m, 6.2 m, 10.3 m, 14.4 m and 18.5 m from the blade tip (Jonkman et al., 2009). MTMDs installed along the tower are labelled as #TT1 to #TT*N* from the tower top, and those applied in each blade are labelled as #BT1 to #BT*N* from the blade tip, in which *N* is the number of TMDs.

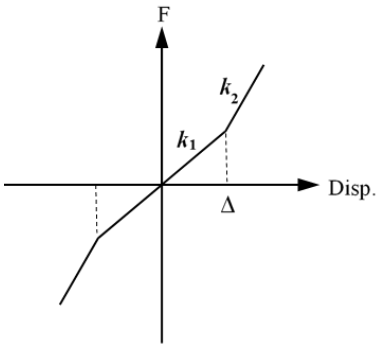

Figure 6-12 Force-displacement relationship of the springs in the blades and tower

The TMD(s) are modelled by the mass, spring and dashpot elements in ABAQUS. In the blades, the space in the out-of-plane direction is limited, TMD mass may penetrate the corresponding blade in the numerical simulation when the relative displacement between the TMD(s) and blade is larger than the chord length of the blade. To avoid this unreasonable penetration, a bi-linear force-displacement relationship as shown in Figure 6-12 is considered for the spring elements in the blades (Bi & Hao, 2016), where Δ is the chord length of the blade in the out-of-plane direction, which is taken from (Jonkman et al., 2009). When the relative displacement between the TMD(s) and blade is smaller than Δ, the stiffness is the optimum value as tabulated in Table 6-4, i.e. $k_1=k_{opt}$. On the other hand, when the relative displacement is larger than Δ, the spring becomes quite rigid and a large stiffness k_2 is defined. A very large k_2 can result in the simulation difficult to converge, $k_2=1\times10^6$ N/m is found to have a good balance between the effectiveness and efficiency, and this value is adopted in the simulations. For the TMD(s) in the tower, the same force-displacement relationship is adopted.

6.5.2 Dynamic responses of the operational wind turbine

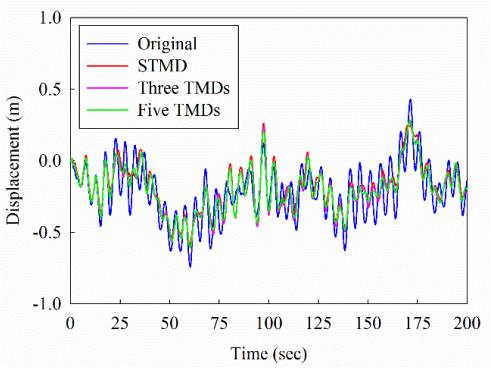

Figure 6-13 Fore-aft displacement time histories at the tower top under the operational condition

Table 6-5 Standard deviations of the displacements of the operational wind turbine without and with TMD(s) and the reduction ratios

Location	Original	STMD		Three TMDs		Five TMDs	
	SD (m)	SD (m)	δ	SD (m)	δ	SD (m)	δ
Tower top	0.1892	0.1606	15.1%	0.1618	14.5%	0.1623	14.2%
Tip of Blade 1	0.2924	0.2407	17.7%	0.2431	16.9%	0.2432	16.8%
Tip of Blade 2	0.2948	0.2443	17.1%	0.2548	13.6%	0.2583	12.4%
Tip of Blade 3	0.2998	0.2446	18.4%	0.2469	17.6%	0.2479	17.3%

The dynamic responses of the operational wind turbine are investigated first. It is obvious that the responses along the tower and blades are different, and the maximum responses occur at the top of the tower and the tip of each blade under the excitations of wind and wave. For conciseness, only the maximum responses are discussed in the present study. Figure 6-13 shows the fore-aft displacement time histories at the tower top without and with different numbers of TMDs. As shown, the installation of TMD(s) is not effective in the first 15 s. This is because TMD system becomes effective only after the relative displacement develops between the main structure and TMD(s). It takes time for the TMD(s) to react and therefore develop relative displacements. After about 15 s, TMD(s) can effectively mitigate the vibrations of the tower. To compare the overall control effectiveness, the standard deviations of the fore-aft displacements at the tower top and the corresponding reduction ratios are summarized in Table 6-5. It can be seen that when TMD is not installed, the standard deviation is 0.1892 m. When STMD is used, it becomes 0.1606 m with a reduction ratio of 15.1%. When three and five TMDs are installed along the tower, the standard deviations of the displacements are 0.1618 m and 0.1623 m respectively and the corresponding reduction ratios are 14.5% and 14.2%. The results reveal that the reduction ratios decrease slightly by dividing a single large TMD into three or five smaller ones to control the tower vibrations. This is because STMD is installed at the top of the tower, where the amplitude of the first vibration mode of the tower is the maximum. The control effectiveness is most evident when the TMD is installed at the

maximum amplitude of the corresponding vibration mode shape. When MTMDs are applied, only TMD #TT1 is installed at the maximum modal response point while the others are not, which in turn slightly decreases the control effectiveness. These results are consistent with those reported by Moon (2010), in which it was concluded that applying MTMDs to control one certain vibration mode will slightly decrease the control effectiveness. On the other hand, as discussed above, these wind turbines may be subjected to earthquake excitations during their whole lifetimes. When earthquake is considered, higher vibration modes might be excited, applying MTMDs can obviously suppress these higher modes induced vibrations and further increase the control effectiveness (Zuo et al., 2017). Moreover, dividing a single large TMD into multiple smaller TMDs will significantly facilitate the installation of TMDs since the mass of each TMD is smaller. Furthermore, as will be demonstrated in Section 6.6.4, the robustness of the control system can be significantly enhanced by using MTMDs. This control strategy is believed worthwhile and more practical though the control effectiveness is reduced marginally.

Figure 6-14 shows the influence of TMD numbers on the displacement time histories at the blade tips in the flap-wise direction. Wind load acting on the blade can be decomposed into a constant mean and a fluctuating component as discussed in Section 6.5. The mean value of the fluctuating term is zero. However, the total wind load on the blade has a non-zero mean because of the constant component of the wind pressure as shown in Figure 6-9, which results in the non-zero baseline of the structural responses as shown in Figure 6-14. The standard deviations of the fore-aft displacements at the blade tips and the corresponding reduction ratios are also tabulated in Table 6-5. As shown, the standard deviations at the tips of blades 1, 2 and 3 without TMD are 0.2924 m, 0.2948 m and 0.2998 m respectively. When STMD is applied, these values are reduced to 0.2407 m, 0.2443 m and 0.2446 m respectively and the corresponding reduction ratios are 17.7%, 17.1% and 18.4%. When three TMDs are installed in each blade, the standard deviations of the flap-wise displacements at the tips of blades 1, 2 and 3 become 0.2431 m, 0.2548 m and 0.2469 m with the reduction ratios of 16.9%, 13.6% and 17.6% respectively. When five TMDs are applied, the standard deviations are 0.2432 m, 0.2583 m and 0.2479 m respectively and the corresponding reduction ratios reduce to 16.8%, 12.4% and 17.3%. Similar to the tower, the control effectiveness slightly decreases by using MTMDs in each blade, this is because the maximum displacement occurs at the tip of the blade and it is most evident by installing the control device at the blade tip.

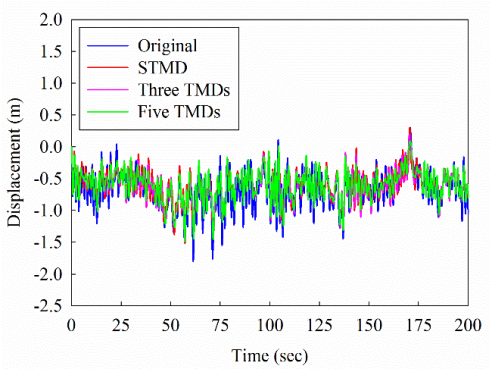

(a) blade 1

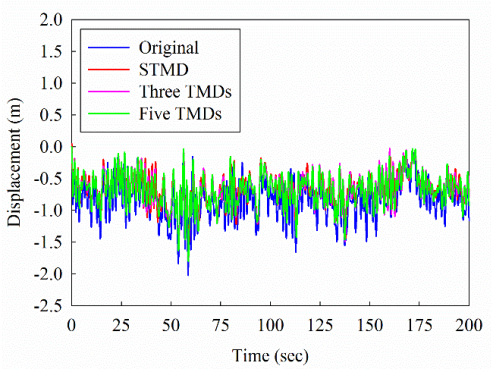

(b) blade 2

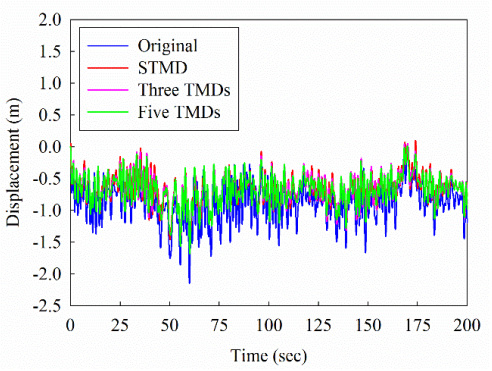

(c) blade 3

Figure 6-14 Flap-wise displacement time histories at the blade tips under the operational condition

6.5.3 Dynamic responses of the parked wind turbine

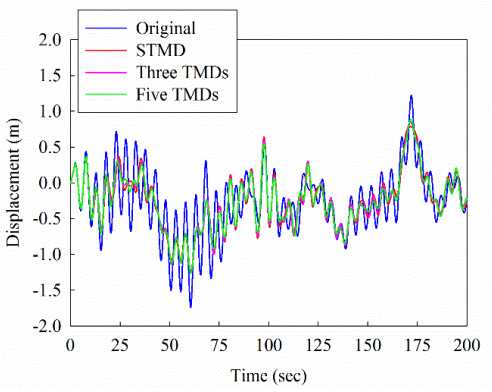

Figure 6-15 Fore-aft displacement time histories at the tower top under the parked condition

Under the extreme case, the operation of wind turbine will stop and it will be in the parked condition. The corresponding wind and wave loads when the wind turbine is in the parked condition are also shown in Figure 6-7, Figure 6-9 and Figure 6-11. As shown in Figure 6-2, blades 2 and 3 are in symmetric position, the wind loads and thus the responses of these two blades will be the same when the wind turbine is in the parked condition.

Figure 6-15 shows the fore-aft displacement time histories at the top of the tower without and with TMD(s) when the wind turbine is in the parked condition. Comparing Figure 6-15 with Figure 6-13, the fore-aft displacement responses at the tower top without TMD are larger than those when the wind turbine is in the operational condition. This is because the mean wind velocity at the tower top is 25 m/s in the parked condition, which is larger than that of the operational condition (15 m/s). Larger wind velocity leads to larger wind load as shown in Figure 6-7, which in turn results in the larger structural responses. Table 6-6 tabulates the standard deviations of the fore-aft displacements at the top of the tower and the corresponding reduction ratios. As shown, the standard deviation of the fore-aft displacements at the tower top without TMD is 0.4619 m. When STMD is used, it becomes 0.3801 m with a reduction ratio of 17.7%. When three and five TMDs are installed along the tower, the standard deviations of the displacements are 0.3825 m and 0.3830 m respectively and the corresponding reduction ratios are 17.2% and 17.1%. Again using smaller MTMDs slightly decreases the control effectiveness due to the reason discussed above.

Table 6-6 Standard deviations of the displacements of the parked wind turbine without and with TMD(s) and the reduction ratios

Location	Original	STMD		Three TMDs		Five TMDs	
	SD (m)	SD (m)	δ	SD (m)	δ	SD (m)	δ
Tower top	0.4619	0.3801	17.7%	0.3825	17.2%	0.3830	17.1%
Tip of Blade 1	0.4200	0.2819	32.9%	0.2850	32.1%	0.2860	31.9%
Tip of Blade 2/3	0.4333	0.3307	23.7%	0.3360	22.5%	0.3428	20.9%

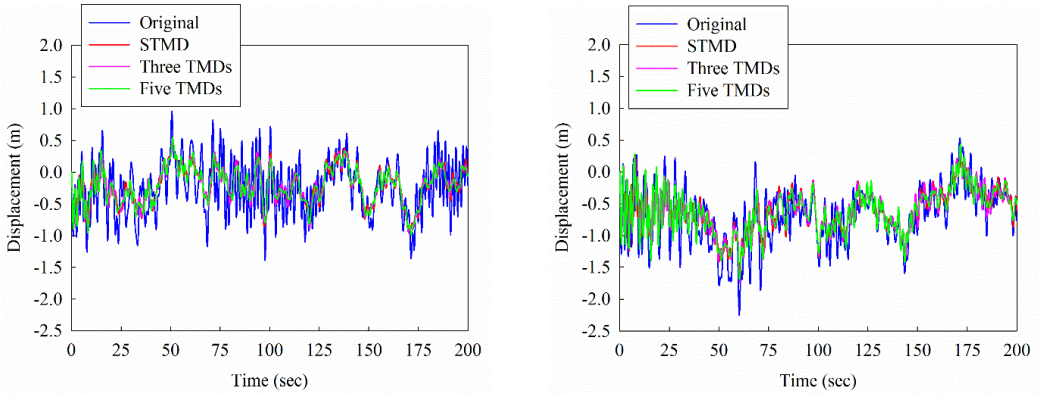

(a) blade 1 (b) blade 2/3

Figure 6-16 Flap-wise displacement time histories at the blade tips under the parked condition

Figure 6-16 shows the displacement time histories in the flap-wise direction at the blade tips without and with TMD(s). Again, the non-zero baseline of the flap-wise displacements is due to the contribution of the mean term of the wind loads acting on the blades. The responses of blades 2 and 3 are the same in the parked condition as discussed above, only the displacement time history at the tip of blade 2 is presented in Figure 6-16. The standard deviations of the

displacement responses together with the corresponding reduction ratios are tabulated in Table 6-6. As shown, the standard deviations of the flap-wise displacements at the tips of blades 1 and 2 without TMD are 0.4200 m and 0.4333 m respectively. When STMD is applied, these values are reduced to 0.2819 m and 0.3307 m respectively and the corresponding reduction ratios are 32.9% and 23.7%. When three TMDs are installed in each blade, the standard deviations of the flap-wise displacements at the tips of blades 1 and 2 are 0.2850 m and 0.3360 m with the reduction ratios of 32.1% and 22.5% respectively. When five smaller TMDs are used, the standard deviations are 0.2860 m and 0.3428 m respectively and the corresponding reduction ratios are 31.9% and 20.9%. These results indicate that MTMD system slightly decrease the control effectiveness, but it can make the control more practical and robust as will be discussed in Section 6.6.4.

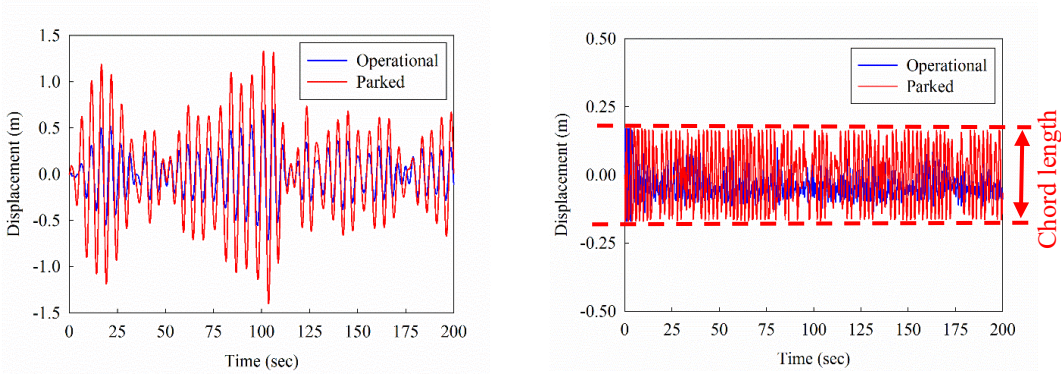

(a) tower (b) blade 2

Figure 6-17 Relative displacement time histories between STMD and the tower and blade 2

Compare the results in Table 6-6 with those in Table 6-5, it can be seen that the control effectiveness for the parked condition is more evident compared to the operational condition. This is because the wind velocity in the parked condition is larger and the larger wind velocity results in the larger structural responses as illustrated above, which in turn lead to the larger relative displacement between the TMD(s) and the main structure. Figure 6-17 shows the relative displacement time histories between STMD and the tower and blade 2 when the wind turbine is in the operational and parked conditions, and the relative displacements in other cases are not presented for conciseness. The blue curves are the relative displacements of the operational wind turbine and the red curves are those of the parked wind turbine. As shown in Figure 6-17, the relative displacements between the TMD and the tower and blade 2 when the blades in the parked condition are much larger than those when the blades are rotating. In other words, the function of the TMD is more evidently developed in the parked condition. In fact, the relative displacement between the STMD and the blade can reach the chord length in the parked condition as shown in Figure 6-17(b). The control effectiveness can be more evident if the chord length becomes larger.

It should be noted that the performances of the MTMD systems are obtained based on the particular wind turbine and the limited wind-wave configurations, more comprehensive experimental/numerical studies are necessary to obtain more general conclusions on the MTMD performances.

6.5.4 Robustness of MTMD system

When only one TMD is installed at the tower top and blade tip, the effectiveness of the control system will be lost partially or even totally if the TMD does not function properly. By dividing the single large TMD into multiple smaller ones, the control system will still work if one or more TMDs do not function well since the other TMD(s) can still control the vibrations. To demonstrate the robustness of the proposed MTMD system for vibration control, some TMDs are assumed not functioning in the present study. The wind turbine with five TMDs in the tower and each blade is taken as an example and the wind turbine is assumed in the operational condition with a rotor velocity of 1.27 rad/s. Without loss of generality, following three cases are considered, and they are tabulated in Table 6-7. In Case 1, TMDs #TT1 installed at the tower top and #BT3 applied in each blade are not working; TMDs #TT1 in the tower and #BT2 and #BT3 in each blade lose their control capabilities in Case 2; and in Case 3, TMDs #TT2 and #TT3 in the tower and #BT2 and #BT3 in each blade are not working. In the numerical simulation, the masses of the malfunctioned TMDs are kept and they are lumped to the corresponding locations of the tower and blade, i.e. the total mass of the system in different cases is the same.

Table 6-7 Different cases of the malfunctioned TMDs

Cases	Malfunctioned TMDs	
	Tower	Blade
1	#TT1	#BT3
2	#TT1	#BT2,3
3	#TT2,3	#BT2,3

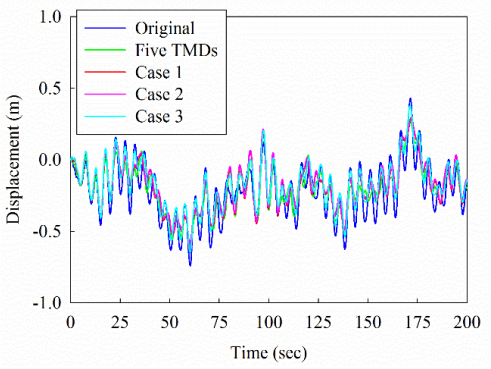

Figure 6-18 Fore-aft displacement time histories at the tower top with some TMDs not working

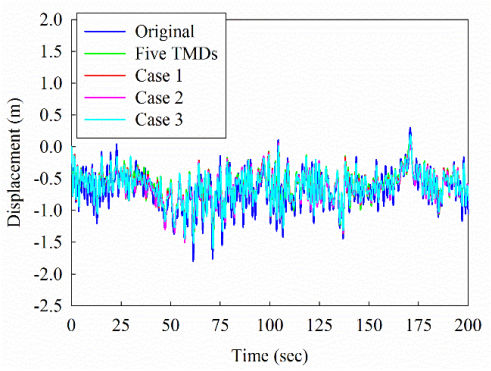

(1) blade 1

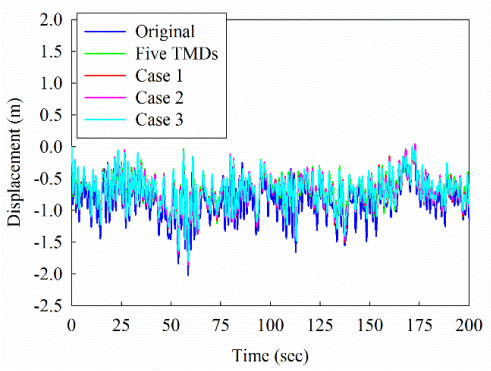

(b) blade 2

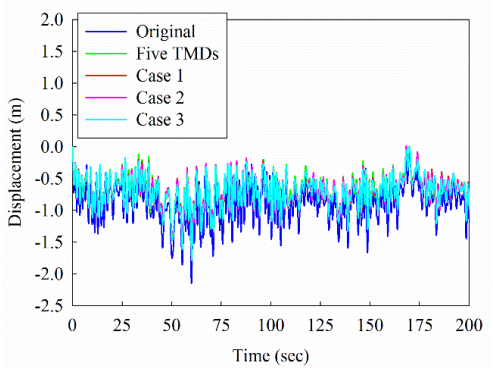

(c) blade 3

Figure 6-19 Flap-wise displacement time histories at the blade tips with some TMDs not working

Table 6-8 Standard deviations of the displacements of the operational wind turbine with some TMDs not working and the reduction ratios

Location	Original	Five TMDs		Case 1		Case 2		Case 3	
	SD (m)	SD (m)	δ	SD (m)	δ	SD (m)	δ	SD (m)	δ
Tower top	0.1892	0.1623	14.2%	0.1657	12.4%	0.1658	12.4%	0.1708	9.7%
Tip of blade 1	0.2924	0.2432	16.8%	0.2449	16.2%	0.2462	15.8%	0.2473	15.4%
Tip of blade 2	0.2948	0.2583	12.4%	0.2592	12.1%	0.2621	11.1%	0.2626	10.9%
Tip of blade 3	0.2998	0.2448	18.3%	0.2453	18.2%	0.2456	18.1%	0.2497	16.7%

Figure 6-18 and Figure 6-19 show the out-of-plane displacement time histories at the top of the tower and the tip of each blade respectively for different cases. For comparison, the results for the original structure and the tower and each blade controlled by five well-functioning TMDs are also plotted. Table 6-8 tabulates the standard deviations of the out-of-plane displacements at the tower top and blade tips and the corresponding reduction ratios. It can be seen that when five TMDs are working properly, the reduction ratio at the tower top reaches 14.2%. When the TMD at the tower top (#TT1) is malfunctioning (Cases 1 and 2), the control effectiveness decreases slightly and the reduction ratio is 12.4%. The results clearly indicate

the benefit of this design concept, namely although the TMD at the maximum amplitude of the first mode shape of the tower does not work, the contributions of other TMDs make the control system still effective. When two TMDs (#TT2, 3) stop working (Case 3), the reduction reduces to 9.7%. It should be noted that #TT2 and 3 are close to the tower top, the malfunctioning of these two TMDs can obviously influence the control effectiveness. When the TMDs that are far from the tower top (e.g. #TT4, 5) are not working, the influence will not be so evident. The numerical results also indicate that the control effectiveness of the tower is mainly governed by the TMDs in the tower. As shown in Table 6-8, the reduction ratios for Cases 1 and 2 are almost the same though one more TMD (#BT2) is not working in the blade of Case 2.

For the vibration mitigation of the blades, the malfunctioning of #BT3 only slightly decreases the control effectiveness. As shown in Table 6-8, when the five TMDs are working properly, the reduction ratios of the standard deviations of the flap-wise displacements at the three blade tips are 16.8%, 12.4% and 18.3% respectively. When #BT3 does not function, the reduction ratios reduce marginally to 16.2%, 12.1% and 18.2%. When one more TMD (#BT2) is malfunctioning as well (Case 2), the control effectiveness further decreases, and the corresponding reduction ratios are 15.8%, 11.1% and 18.1% respectively. Table 6-8 also shows that the control effectiveness in Case 3 is less than that in Case 2 although the same TMDs #BT2, 3 are not working in both Cases 2 and 3. This is because TMDs #TT2, 3 do not function properly in Case 3, which leads to larger responses of the tower as shown in Figure 6-18 and severe interaction between the tower and blades.

It should be noted that all the numerical results presented in this section are based on the optimized MTMD/STMD systems, i.e. different TMD parameters are adopted for the parked and operational wind turbines. In practice, it is obvious that the TMD system is designed based on one condition only (i.e. either parked or operational condition). For example, if the TMD system is designed based on the parked condition, it may not most effective for the operational wind turbine, and this effect may be more evident if only a single TMD is installed in each blade. The semi-active strategy can be a good alternative to solve problem (Altay et al., 2014). On the other hand, the numerical results show that the MTMD system is robust compared to the STMD system, the malfunction of one or some TMDs (i.e. partially mistune) only slightly decreases the control effectiveness as discussed, which is a beneficial aspect of the proposed vibration control method. In other words, the MTMD system designed based on one operational condition will be more effective for the other condition compared to the STMD system.

6.6 Conclusions

In this chapter, MTMDs are proposed to be installed in the tower and each blade to simultaneously mitigate the out-of-plane vibrations of the tower and blades when they are subjected to the combined wind and wave loadings. To examine the effectiveness of the proposed vibration control system, the tower and blades are directly modelled in the FE model by using ABAQUS. Numerical results show that MTMDs can effectively control both the out-of-plane vibrations of the tower and blades when the wind turbine is in the operational and parked conditions. The reduction ratio of the displacement responses slightly decreases compared to the case with a single TMD installed at the tower top and blade tips. The reliability of the control system can be significantly improved in case some of the tuned mass do not function well. Another obvious merit of this control method is that it can significantly facilitate the TMD installations since the mass of each TMD is much smaller compared to the single large TMD.

It is worth reiterating again that all the numerical results are obtained based on the example wind turbine and the limited wind-wave configurations. To obtain more general conclusions on the MTMD performances, further studies are necessary.

6.7 References

Altay, O., Taddei, F., Butenweg, C., & Klinkel, S. (2014). Vibration mitigation of wind turbine towers with tuned mass dampers. *Wind Turbine Control and Monitoring* (pp. 337-373). Berlin, Germany: Springer.

Arany, L., Bhattacharya, S., Macdonald, J. H., & Hogan, S. J. (2016). Closed form solution of Eigen frequency of monopile supported offshore wind turbines in deeper waters incorporating stiffness of substructure and SSI. *Soil Dynamics and Earthquake Engineering*, *83*, 18-32.

Arrigan, J., Pakrashi, V., Basu, B., & Nagarajaiah, S. (2011). Control of flap-wise vibrations in wind turbine blades using semi-active tuned mass dampers. *Structural Control and Health Monitoring*, *18*(8), 840-851.

Basu, B., Zhang, Z., & Nielsen, S. R. K. (2016). Damping of edgewise vibration in wind turbine blades by means of circular liquid dampers. *Wind Energy*, *19*(2), 213-226.

Bi, K., & Hao, H. (2012). Modelling and simulation of spatially varying earthquake ground motions at sites with varying conditions. *Probabilistic Engineering Mechanics*, *29*, 92-104.

Bi, K., & Hao, H. (2016). Using pipe-in-pipe systems for subsea pipeline vibration control. *Engineering Structures*, *109*, 75-84.

Bi, K., Hao, H., & Chouw, N. (2011). Influence of ground motion spatial variation, site condition and SSI on the required separation distances of bridge structures to avoid seismic pounding. *Earthquake Engineering & Structural Dynamics*, *40*(9), 1027-1043.

Bisoi, S., & Haldar, S. (2014). Dynamic analysis of offshore wind turbine in clay considering soil-monopile-tower interaction. *Soil Dynamics and Earthquake Engineering*, *63*, 19-35.

Brodersen, M. L., Bjørke, A. S., & Høgsberg, J. (2016). Active tuned mass damper for damping of offshore wind turbine vibrations. *Wind Energy*, *20*, 783-796.

Chen, J., & Georgakis, C. T. (2013a). Tuned rolling-ball dampers for vibration control in wind turbines. *Journal of Sound and Vibration*, *332*(21), 5271-5282.

Chen, J., & Georgakis, C. T. (2013b). Spherical tuned liquid damper for vibration control in wind turbines. *Journal of Vibration and Control*, *21*(10), 1875-1885.

Chen, J., Liu, Y., & Bai, X. (2015a). Shaking table test and numerical analysis of offshore wind turbine tower systems controlled by TLCD. *Earthquake Engineering and Engineering Vibration*, *14*(1), 55-75.

Chen, J., Yuan, C., Li, J., & Xu, Q. (2015b). Semi-active fuzzy control of edgewise vibrations in wind turbine blades under extreme wind. *Journal of Wind Engineering and Industrial Aerodynamics*, *147*, 251-261.

Colwell, S., & Basu, B. (2009). Tuned liquid column dampers in offshore wind turbines for structural control. *Engineering Structures*, *31*(2), 358-368.

Den Hartog, J. P. (1956). Mechanical vibrations. New York, NY: McGraw-Hill.

Det Norske Veritas (DNV). (2010). DNV-RP-C205: Environmental conditions and environmental loads. Norway: DNV.

Fitzgerald, B., & Basu, B. (2014). Cable connected active tuned mass dampers for control of in-plane vibrations of wind turbine blades. *Journal of Sound and Vibration*, *333*(23), 5980-6004.

Fitzgerald, B., & Basu, B. (2016). Structural control of wind turbines with soil structure interaction included. *Engineering Structures*, *111*, 131-151.

Fitzgerald, B., Basu, B., & Nielsen, S. R. K. (2013). Active tuned mass dampers for control of in-plane vibrations of wind turbine blades. *Structural Control and Health Monitoring*, *20*(12), 1377-1396.

Hansen, M. O. L. (2008). Aerodynamics of wind turbines. London, UK: Earthscan.

Hao, H., Oliveira, C., & Penzien, J. (1989). Multiple-station ground motion processing and simulation based on SMART-1 array data. *Nuclear Engineering and Design*, *111*(3), 293-310.

Harte, M., Basu, B., & Nielsen, S. R. K. (2012). Dynamic analysis of wind turbines including soil-structure interaction. *Engineering Structures*, *45*, 509-518.

Hasselmann, K., Barnett, T., Bouws, E., Carlson, H., Cartwright, D., Enke, K., Walden, H. (1973). Measurements of wind-wave growth and swell decay during the Joint North Sea Wave Project (JONSWAP). Hamburg: Deutches Hydrographisches Institut.

Hoang, N., Fujino, Y., & Warnitchai, P. (2008). Optimal tuned mass damper for seismic applications and practical design formulas. *Engineering Structures*, *30*(3), 707-715.

Huang, G., Liao, H., & Li, M. (2013). New formulation of Cholesky decomposition and applications in stochastic simulation. *Probabilistic Engineering Mechanics*, *34*, 40-47.

Jonkman, J., Butterfield, S., Musial, W., & Scott, G. (2009). Definition of a 5-MW reference wind turbine for offshore system development. (Technical Report No. NREL/TP-500-38060). Golden, CO: National Renewable Energy Laboratory.

Joshi, A., & Jangid, R. (1997). Optimum parameters of multiple tuned mass dampers for base-excited damped systems. *Journal of Sound and Vibration*, *202*(5), 657-667.

Lackner, M. A., & Rotea, M. A. (2011). Passive structural control of offshore wind turbines. *Wind Energy*, *14*(3), 373-388.

Li, C., & Liu, Y. (2003). Optimum multiple tuned mass dampers for structures under the ground acceleration based on the uniform distribution of system parameters. *Earthquake Engineering & Structural Dynamics*, *32*(5), 671-690.

Mensah, A. F., & Dueñas-Osorio, L. (2014). Improved reliability of wind turbine towers with tuned liquid column dampers (TLCDs). *Structural Safety*, *47*, 78-86.

Moon, K. S. (2010). Vertically distributed multiple tuned mass dampers in tall buildings: performance analysis and preliminary design. *The Structural Design of Tall and Special Buildings*, *19*(3), 347-366.

Murtagh, P. J., Basu, B., & Broderick, B. M. (2005). Along-wind response of a wind turbine tower with blade coupling subjected to rotationally sampled wind loading. *Engineering Structures*, *27*(8), 1209-1219.

Murtagh, P. J., Ghosh, A., Basu, B., & Broderick, B. M. (2008). Passive control of wind turbine vibrations including blade/tower interaction and rotationally sampled turbulence. *Wind Energy*, *11*(4), 305-317.

Nikoo, H. M., Bi, K., & Hao, H. (2017). Passive vibration control of cylindrical offshore components using pipe-in-pipe (PIP) concept: An analytical study. *Ocean Engineering*, *142*, 39-50.

Quilligan, A., O'Connor, A., & Pakrashi, V. (2012). Fragility analysis of steel and concrete wind turbine towers. *Engineering Structures*, *36*, 270-282.

Sadek, F., Mohraz, B., Taylor, A. W., & Chung, R. M. (1997). A method of estimating the parameters of tuned mass dampers for seismic applications. *Earthquake Engineering & Structural Dynamics*, *26*(6), 617-636.

Sarkar, S., & Chakraborty, A. (2018). Optimal design of semiactive MR-TLCD for along-wind vibration control of horizontal axis wind turbine tower. *Structural Control and Health Monitoring*, *25*(2), 1-18.

Sorensen, R. M. (2005). Basic coastal engineering. New York, NY: Springer Science & Business Media.

Staino, A., & Basu, B. (2013). Dynamics and control of vibrations in wind turbines with variable rotor speed. *Engineering Structures*, *56*, 58-67.

Staino, A., Basu, B., & Nielsen, S. R. K. (2012). Actuator control of edgewise vibrations in wind turbine blades. *Journal of Sound and Vibration*, *331*(6), 1233-1256.

Stewart, G. M., & Lackner, M. A. (2011). The effect of actuator dynamics on active structural control of offshore wind turbines. *Engineering Structures*, *33*(5), 1807-1816.

Stewart, G. M., & Lackner, M. A. (2014). The impact of passive tuned mass dampers and wind-wave misalignment on offshore wind turbine loads. *Engineering Structures*, *73*, 54-61.

Sun, C. (2018). Mitigation of offshore wind turbine responses under wind and wave loading: Considering soil effects and damage. *Structural Control and Health Monitoring*, *25*(3), 1-22.

Sun, C., & Jahangiri, V. (2018). Bi-directional vibration control of offshore wind turbines using a 3D pendulum tuned mass damper. *Mechanical Systems and Signal Processing*, *105*, 338-360.

Van der Woude, C., & Narasimhan, S. (2014). A study on vibration isolation for wind turbine structures. *Engineering Structures*, *60*, 223-234.

Xu, K., & Igusa, T. (1992). Dynamic characteristics of multiple substructures with closely spaced frequencies. *Earthquake Engineering & Structural Dynamics*, *21*(12), 1059-1070.

Zhang, Z., Basu, B., & Nielsen, S. R. K. (2015a). Tuned liquid column dampers for mitigation of edgewise vibrations in rotating wind turbine blades. *Structural Control and Health Monitoring*, *22*(3), 500-517.

Zhang, Z., Chen, J., & Li, J. (2013). Theoretical study and experimental verification of vibration control of offshore wind turbines by a ball vibration absorber. *Structure and Infrastructure Engineering*, *10*(8), 1087-1100.

Zhang, Z., Li, J., Nielsen, S. R. K., & Basu, B. (2014). Mitigation of edgewise vibrations in wind turbine blades by means of roller dampers. *Journal of Sound and Vibration*, *333*(21), 5283-5298.

Zhang, Z., Nielsen, S. R. K., Basu, B., & Li, J. (2015b). Nonlinear modeling of tuned liquid dampers (TLDs) in rotating wind turbine blades for damping edgewise vibrations. *Journal of Fluids and Structures*, *59*, 252-269.

Zhang, Z., Staino, A., Basu, B., & Nielsen, S. R. K. (2016). Performance evaluation of full-scale tuned liquid dampers (TLDs) for vibration control of large wind turbines using real-time hybrid testing. *Engineering Structures*, *126*, 417-431.

Zheng, M., Yang, Z. J., Yang, S., & Still, B. (2017). Modeling and mitigation of excessive dynamic responses of wind turbines founded in warm permafrost. *Engineering Structures*, *148*, 36-46.

Zuo, H., Bi, K., & Hao, H. (2017). Using multiple tuned mass dampers to control offshore wind turbine vibrations under multiple hazards. *Engineering Structures*, *141*, 303-315.

Zuo, H., Bi, K., & Hao, H. (2018). Dynamic analyses of operating offshore wind turbines including soil-structure interaction. *Engineering Structures*, *157*, 42-62.

CHAPTER 7 SIMULTANEOUS OUT-OF-PLANE AND IN-PLANE VIBRATION MITIGATIONS OF OFFSHORE MONOPILE WIND TURBINES BY TUNED MASS DAMPERS

ABSTRACT[6]

Extensive research efforts have been made to mitigate the adverse vibrations of offshore wind turbines to ensure their serviceability and safety in the normal working condition. However, most previous studies focused on the vibration control in either the in-plane or out-of-plane direction only. In reality, wind turbines inevitably vibrate in both directions when they are subjected to external excitations. In the present study, the NREL 5 MW wind turbine is taken as an example, the detailed three-dimensional (3D) finite element (FE) model of the wind turbine is developed in ABAQUS. To simultaneously control the in-plane and out-of-plane vibrations induced by the combined wind and wave loads, another carefully designed (i.e. tuned) spring and dashpot are added to the perpendicular direction of each tuned mass damper (TMD) system that is used to control the vibrations of the tower and blades in one particular direction. With this simple modification, a bi-directional TMD system is formed and the vibrations in both the out-of-plane and in-plane directions are simultaneously controlled. To examine the control effectiveness, the responses of the wind turbine without control, with separate TMD system and the proposed bi-directional TMD system are calculated and compared. Numerical results show that the bi-directional TMD system can simultaneously control the out-of-plane and in-plane vibrations of the wind turbine without changing too much of the conventional design of the control system. The bi-directional control system therefore could be a cost-effective solution to mitigate the bi-directional vibrations of offshore wind turbines.

7.1 Introduction

Offshore wind energy, as one of the renewable energies, experienced rapid development in the last decade and is becoming a main contributor to the new electricity generation. As reported by the Global Wind Energy Council (GWEC) (GWEC, 2018), a historical record of 4,334 MW of new offshore wind power was installed worldwide in 2017, an 87% increase compared to that in 2016, and the cumulative offshore wind capacity in 2017 reached 18,814 MW. To maximize the wind energy extraction in marine areas, offshore wind turbines are erected with slender tower and large rotors. For example, the tower height and rotor diameter of the

[6] Zuo, H., Bi, K., & Hao, H. (2019). Simultaneous out-of-plane and in-plane vibration mitigations of offshore monopile wind turbines by tuned mass dampers. (Under review).

conceptual Haliade-X 12 MW offshore wind turbine reach 150 m and 220 m, respectively (GWEC, 2018). These high-rise and flexible structures are susceptible to the external excitations such as wind and wave loads, and the excessive vibrations can compromise the wind energy output and decrease the fatigue life and may even lead to the catastrophic collapse of wind turbines in the harsh environmental conditions. It is imperative to mitigate the excessive vibrations of offshore wind turbines by using vibration control techniques to ensure their safety and serviceability and to lower the maintenance cost when they are in the normal parked and operating conditions.

The vibration issue of offshore wind turbine has received extensive attentions. Various control devices have been proposed to suppress the adverse vibrations induced by wind, wave and/or seismic loads. These control devices can be generally divided into passive, semi-active and active categories depending on whether external power is needed. Compared to the semi-active and active strategies, passive control methods need no power input and they have been widely applied to mitigate the vibrations of wind turbines especially the tower vibrations. For example, tuned mass dampers (TMDs) were adopted by Murtagh et al. (2008), Lackner and Rotea (2011), Zhao et al. (2018) and Ghassempour et al. (2019). Colwell and Basu (2009), Mensah and Dueñas-Osorio (2014) and Chen et al. (2015) proposed using tuned liquid column dampers (TLCDs). Very recently, some new techniques have been developed to further improve the performance of conventional TMD systems. For example, it is well known that the control performance of TMD is influenced by the mass ratio of the control device to the main structure, and larger mass ratio generally results in better and more robust control effect. Hu et al. (2018) and Zhang et al. (2019) proposed using inerter-based TMD systems to amplify the physical mass of TMD in order to increase the control effectiveness. Considering the limited space in the nacelle, Zuo et al. (2017) suggested installing multiple small TMDs (MTMDs) to mitigate the tower vibrations under the combined wind, wave and earthquake loads. It was observed that, besides controlling the vibration associated with the fundamental vibration mode, MTMDs can effectively mitigate high-mode vibrations with improved robustness.

It should be noted that, in the previous studies, wind was assumed as the main driving force for the wave, and wind and wave loads were assumed acting on the tower in the same direction, i.e. the out-of-plane direction of the wind turbine. Only the out-of-plane vibration of the tower was therefore controlled. However, recorded metocean data indicate that the directions of wind and wave are not necessarily always aligned (Stewart & Lackner, 2014). The wind-wave misalignment could lead to the tower vibrates in both the in-plane and out-of-plane directions simultaneously. Moreover, the wind loads acting on the blades can result in the in-plane vibration of the tower since the blades are with twisted shape and the wind loads on the blades

can have a component in the in-plane direction. Since the aerodynamic damping in the in-plane direction is very low, large tower responses thus might appear in this direction and need be suppressed. In order to control the in-plane vibration of the tower, Zhang et al. (2016) used a tuned liquid damper (TLD). A three-dimensional (3D) pendulum TMD was developed by Sun and Jahangiri (2018, 2019a, 2019b), and two linear TMDs were proposed by Stewart and Lackner (2014) to simultaneously mitigate the out-of-plane and in-plane vibrations of the tower. It was found that the dual TMDs reduced the out-of-plane and in-plane fatigue loads by approximately 5% and 40%, respectively.

Compared to the wind turbine tower, the research works on the vibration mitigation of blades are relatively scarce. Similarly, the vibrations of blades occur in both the in-plane and out-of-plane directions and they are usually coupled with each other due to the twisted shape of the blades. However, this coupling effect was not considered in the previous studies, and the out-of-plane and in-plane vibrations of the blades were controlled separately. Arrigan et al. (2011) and Zuo et al. (2019) used semi-active TMDs and MTMDs respectively to control the out-of-plane vibrations of the blades, which highlighted the feasibility of using TMDs in supressing the vibrations of the blades. Zhang et al. developed roller dampers (2014), TLCDs (2015a), TLDs (2015b) and Basu et al. (2016) used circular liquid column dampers (CLCDs) to enhance the damping of the blades in the in-plane direction. In these studies, the mass of the control device was set very small by taking advantage of the centrifugal acceleration. These control methods are therefore more effective when the wind turbine is in the operating condition.

Besides these passive control methods, active control techniques have also been used to mitigate the in-plane vibrations of the blades. Active tendons were installed inside the blades as suggested by Staino et al. (2012); Fitzgerald et al. (2013) and Fitzgerald and Basu (2014) proposed using active TMDs and cable connected active TMDs respectively. Although the effectiveness of these active control strategies were numerically confirmed and reasonable structural response reductions were achieved, these active control techniques need relatively complex control configurations and external power input, the practical application of these active control strategies might be an issue since the internal space of the blades is even smaller than that in the nacelle.

The above literature review reveals that most previous studies on the vibration control of offshore wind turbines focused on the out-of-plane (fore-aft) vibration of the tower. Very limited studies, to the best knowledge of the authors only (Stewart & Lackner, 2014; Sun & Jahangiri, 2018, 2019a, 2019b), considered the simultaneous control of the out-of-plane and in-plane vibrations of the tower though the coupling are inevitable, yet the bi-directional vibration mitigation of the blades was not addressed in (Stewart & Lackner, 2014; Sun & Jahangiri, 2018, 2019a, 2019b). For the blades, controlling the out-of-plane and in-plane

vibrations are investigated by some researchers. However, the vibrations were controlled separately in all these studies, i.e. when the vibration in one direction was of interest, the vibration in the other direction was not considered.

This chapter proposes using bi-directional TMD systems, a system that can be conveniently achieved by perpendicularly adding another properly designed (i.e. tuned) spring and dashpot to each of the TMD system that is used to control the vibration of the wind turbine in one particular direction (refer to Figure 7-5) to simultaneously control the out-of-plane and in-plane vibrations of both the tower and blades of offshore wind turbines. The NREL 5 MW wind turbine is taken as an example, and the detailed 3D finite element (FE) model is developed in ABAQUS. The tower and blades are explicitly modelled. The combined wind and wave loads are considered as external vibration sources, and the responses of the parked and operating wind turbines without control, with separate control device and the proposed bi-directional control system are calculated and systematically compared. The structure of this chapter is organized as follows: the detailed information of the FE model is given in Section 7.3; Section 7.4 briefly introduces the simulation methods of wind and wave loads; the parameters of the TMD system are calculated in Section 7.5; Section 7.6 discusses the dynamic responses of the wind turbine without and with different control strategies, and some concluding remarks are given in Section 7.7.

7.2 FE model

The NREL 5 MW wind turbine is chosen as an example in the present study since its geometrical configurations were given in detail in (Jonkman et al., 2009). Figure 7-1(a) shows the main dimensions of the wind turbine, and the detailed information are tabulated in Table 7-1. As shown, the total length of the monopile is 30 m, in which 10 m is above the mean sea level and another 20 m is in the sea water. The outer diameter and wall thickness of the tower are linearly decreased from the base to the top, and they are 6 m and 0.027 m respectively at the tower base, and the corresponding values are 3.87 m and 0.019 m at the tower top. For the twisted blades, except the thickness, all other information can be found in (Jonkman et al., 2009). In the present study, a uniform thickness is assumed and the mass of the blades is ensured to be the same as that in (Jonkman et al., 2009). With this assumption, the thickness of the blades is computed as 0.019 m.

The FE model of the wind turbine has been presented in detail in one of the authors' previous studies (Zuo et al., 2019). For completeness of the paper, it is briefly introduced in this section. More detailed information can be found in (Zuo et al., 2019). The monopile, tower and blades are modelled by shell elements (S4) in ABAQUS. For the hub and nacelle, only the masses are considered, which are modelled by a point mass element lumped at the tower top. To

consider the rotation of the blades, a hinge connection between the tower and blades is defined and the rotational degree-of-freedom (DOF) in the out-of-plane direction is released. A convergence test is used to identify the most appropriate element sizes of the numerical model, and the results show that the element sizes of 1 m along the length of monopile, tower and blades and 0.5 m in the circumferential direction yield a good balance between the computational time and accuracy, these element sizes are therefore adopted in the numerical model. Figure 7-1(b) shows the developed FE model.

Table 7-1 Properties of the NREL 5 MW wind turbine

Blade	Rotor diameter	126 m
	Hub height	90 m
	Cut-in, rated and cut-out wind speed	3 m/s, 11.4 m/s, 25 m/s
	Cut-in and rated rotor speed	6.9 rpm, 12.1 rpm
	Length	61.5 m
	Overall (integrated) mass	17,740 kg
	Structural damping ratio	0.5%
Hub and Nacelle	Hub diameter	3 m
	Hub mass	56,780 kg
	Nacelle mass	240,000kg
	Height above water	87.6 m
Tower	Bottom and top outer diameters	6 m, 3.87 m
	Bottom and top wall thicknesses	0.027 m, 0.019 m
	Overall (integrated) mass	347,460 kg
	Structural damping ratio	1%
Monopile	Total length	30 m
	Outer diameter	6 m
	Wall thickness	0.060 m

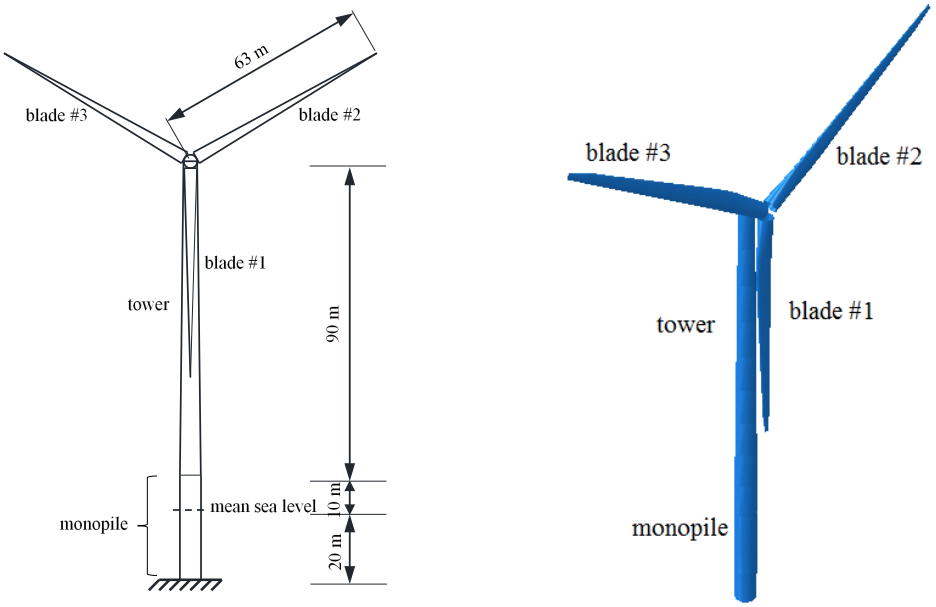

(a) the NREL 5 MW wind turbine (b) FE model

Figure 7-1 Offshore wind turbine model

The monopile, tower and blades are made of steel and polyester respectively, which are assumed as ideal elastic-plastic materials, and the detailed properties are tabulated in Table 7-2. For the monopile in the sea water, the vibrating monopile can impart an acceleration to the surrounding sea water, and this interaction is considered by using the added mass method in the present study.

Table 7-2 Material properties of steel and polyester

Component	Material	Density (kg/m^3)	Young's modulus (GPa)	Poisson's ratio	Yield strength (MPa)	Plastic strain
Blade	Polyester	1850	38	0.3	700	0.02
Tower	Steel	8500	210	0.3	235	0.01
Monopile	Steel	7850	210	0.3	235	0.01

For the damping of an offshore wind turbine, it normally consists of structural, aerodynamic and hydrodynamic damping, which account for the contributions of the structure itself, wind and surrounding sea water respectively. The structural damping ratios of the tower and blades are 1% and 0.5% respectively as recommended in (Jonkman et al., 2009). The aerodynamic damping results from the relative velocity between the rotational blades and wind, and is assumed as 3.5% in the out-of-plane direction as advised by Bisoi and Haldar (2014). For a parked wind turbine or in the in-plane direction, previous studies (e.g. (Arany et al., 2016)) revealed that the aerodynamic damping is negligible and therefore is not considered in the present study. The hydrodynamic damping is induced by the drag between the monopile and surrounding sea water and the value of 0.23% is adopted (Arany et al., 2016). Add all the components together, the damping ratio of the tower is 1.23%. The value is 4% in the out-of-plane direction for the rotating blades; for the parked blades or in the in-plane direction, it is 0.5%.

Table 7-3 The fundamental vibration frequencies and modes of the wind turbine in the in-plane and out-of-plane directions (parked condition)

Mode description	Frequency (rad/s)
1st tower in-plane	1.514
1st tower out-of-plane	1.516
1st blade out-of-plane	3.763
1st blade in-plane	7.774

After the FE model is developed, an eigenvalue analysis is carried out to calculate the vibration frequencies and mode shapes of the wind turbine. It should be noted that, in the modal analysis, the rotation of the blades cannot be explicitly considered by using ABAQUS, and only the parked condition is considered when these vibration characteristics (vibration frequencies and modes) are calculated. Since the energies of wind and wave loads considered in the present study concentrate in the low frequency range, normally only the fundamental vibration modes

of the tower and blades can be excited, the fundamental modes are thus mitigated in the present study. Table 7-3 tabulates the first vibration frequencies and the corresponding vibration modes of the tower and blades in the in-plane and out-of-plane directions.

7.3 Wind and wave loads

In the present study, the wind turbine is subjected to the combined wind and wave loads, which are constantly experienced by offshore wind turbines during their lifetimes. The wind and wave loads are stochastically simulated based on the sophisticated simulation techniques and are briefly introduced in this section for completeness. Detailed information regarding the wind and wave simulation can be found in (Zuo et al., 2018).

The wind loads on the tower are composed of a mean and a fluctuating component, and the fluctuating wind loads at different locations along the tower are different. For simplicity, the tower is divided into nine segments in the present study and the wind load within each segment is assumed the same. The Kaimal spectrum (Murtagh et al., 2005) is adopted to represent the power spectral density (PSD) of the fluctuating wind speed in each segment. On the other hand, the wind loads between different segments are with certain similarities, which is normally known as the spatial correlation effect (Huang et al., 2013), and this effect is considered in the wind load simulations and described by a spatial coherency loss function in the present study.

As tabulated in Table 7-1, the maximum energy output of wind turbine will be achieved when the mean wind speed at the hub height is 11.4 m/s, and the wind turbine stops rotating when the wind speed is above 25 m/s in order to protect the electrical and mechanical components. In the present study, two operational conditions (i.e. the operating and parked conditions) are considered, and the mean wind speed of 11.4 m/s and 35 m/s is used in each condition. Figure 7-2 shows the wind loads at the top segment when the NREL 5 MW wind turbine is in the operating and parked conditions respectively. The wind loads in the other segments are not presented for conciseness.

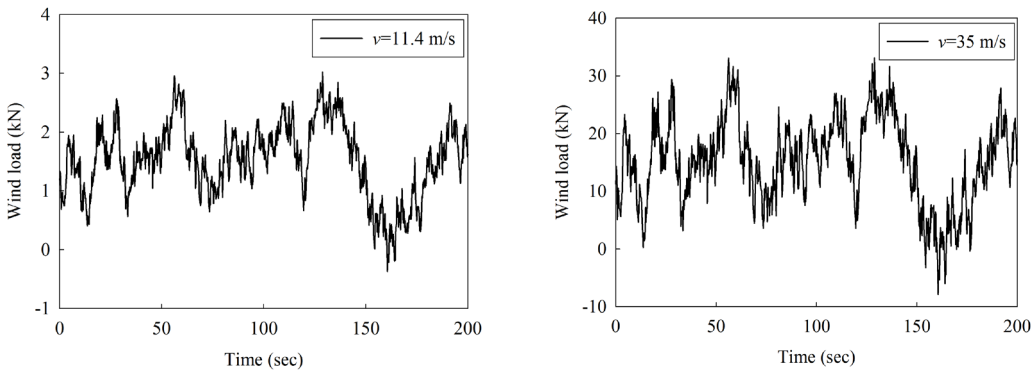

(a) v=11.4 m/s (b) v=35 m/s

Figure 7-2 Wind loads at the tower top when the wind turbine is in the (a) operating and (b) parked conditions

The wind loads on the blades are different from those on the tower, and they are related to various parameters such as wind speed, rotational velocity, number of the blades and the geometrical characteristics of the blade. In the present study, the blade element momentum (BEM) method (Hansen, 2008) is used to estimate the wind loads on the rotating blades. In this method, similar to the tower, each blade is divided into several segments, but the interaction between different segments along the length of the rotor is not considered, the wind load on each segment is thus simulated separately. For the parked condition, the same method is used but the rotational velocity is set to zero. Figure 7-3(a) shows the in-plane and out-of-plane wind loads on the three blades when the wind turbine rotates at a rated velocity of 12.1 rpm, and the corresponding wind loads for the parked condition (in which the mean wind speed is 35 m/s) are shown in Figure 7-3(b). As shown in Figure 7-1, the locations of the blades #2 and #3 are symmetric when the wind turbine is in the parked condition, the wind loads on these two blades are therefore the same. Only the wind loads on blade #2 are presented in Figure 7-3(b) for conciseness.

As shown in Figure 7-1, part of the monopile is in the sea water, the wave load acting on the monopile is considered, and the JONSWAP spectrum (Hasselmann et al., 1973) is used to simulate the sea surface elevation. Then the wave load is calculated by the Morison formula. Similar to the tower, the monopile in the sea water is equally divided into two segments and the wave load in each segment is assumed the same. Figure 7-4 shows the wave loads at the mean sea level when the mean wind speeds at the hub height are 11.4 m/s and 35 m/s, respectively.

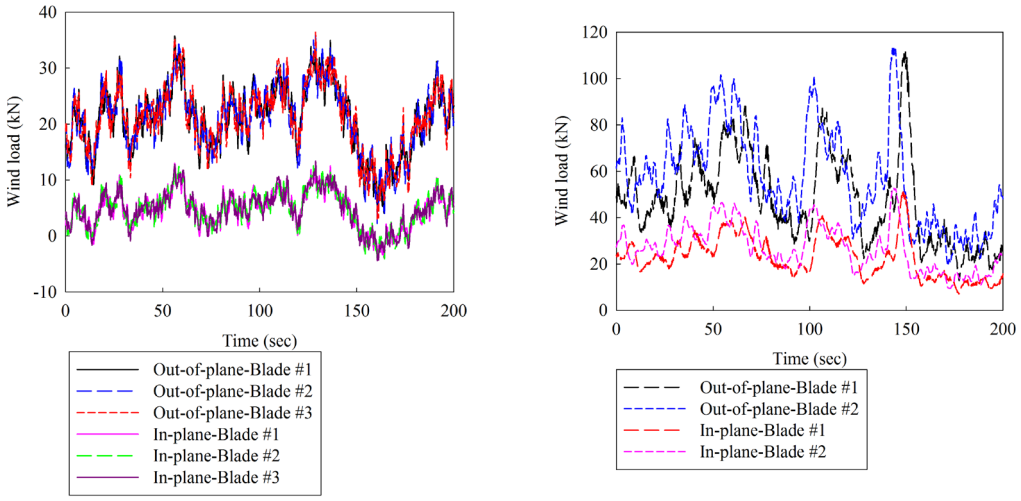

(a) operating condition (b) parked condition

Figure 7-3 Wind loads on the blades under different operational conditions

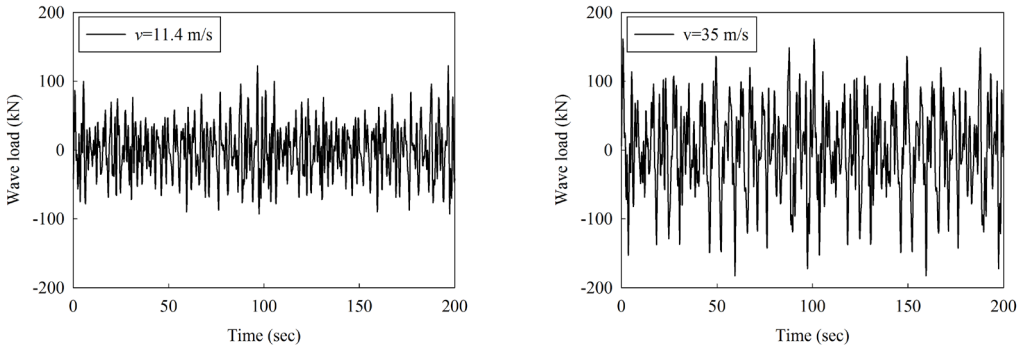

(a) v=11.4 m/s (b) v=35 m/s

Figure 7-4 Wave loads at the mean sea level

In the wind and wave load simulations, the blades, tower and monopile are divided into a few segments as mentioned above. In the FE model, a reference point is developed in each segment and coupled with the cross section of the corresponding segment, the simulated wind and wave loads are applied to these reference points as the external vibration sources.

7.4 Bi-directional TMD system and parameters

As discussed above, the vibrations of the tower and blades of offshore wind turbines were normally considered separately, and a TMD system was generally used to control the vibration in one direction. For example, if the vibration in the out-of-plane direction is of interest, the spring and dashpot will be installed in the out-of-plane direction. Literature review also indicates that the out-of-plane and in-plane vibrations of offshore wind turbine are inevitably coupled with each other, and the vibrations in both directions may significantly influence the

performance of the wind turbines, thus they should be controlled simultaneously. In the present study, instead of installing spring and dashpot in one direction, another properly designed spring and dashpot are installed in the perpendicular direction of the original TMD system to form a bi-directional TMD system as shown in Figure 7-5. By doing so, the vibrations in both directions can be controlled simultaneously as will be demonstrated in the numerical results. It should be noted that, compared to the conventional uniaxial TMD system, only another spring and dashpot need to be added, which will not change too much of the conventional design. The bi-directional control system therefore could be a cost-effective solution to mitigate the bi-directional vibrations of offshore wind turbines.

Figure 7-5 shows the sketch of the bi-directional TMD system, in which the auxiliary mass (m_t) is attached to the vibrating main structure (i.e. tower and blade) by two perpendicular springs ($k_{t\text{-}in}$ and $k_{t\text{-}out}$) and dashpots ($c_{t\text{-}in}$ and $c_{t\text{-}out}$). As demonstrated in many previous studies, the springs and dashpots should be carefully selected in order to make the system effective, and this is normally dubbed tune. In the present study, the displacement responses of the tower and blades are of interest, and the numerical searching technique is then used to obtain the corresponding optimal values by minimizing the mean square displacements of the tower and blades under an assumed mass ratio, which is briefly introduced in this section.

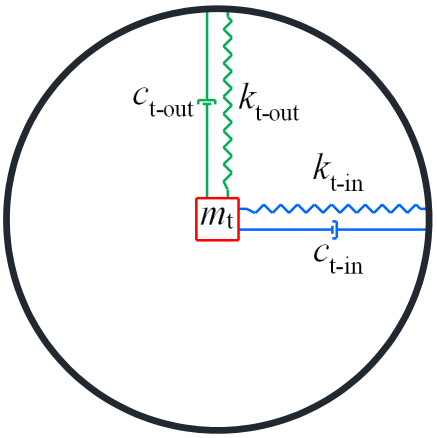

Figure 7-5 Main structure-bi-directional TMD system

To optimize the TMD systems, two parameters are defined:

$$\gamma = \frac{\omega_t}{\omega_s} \tag{7.1}$$

$$\mu = \frac{m_t}{m_s} \tag{7.2}$$

in which γ and μ are the frequency (ω) and mass (m) ratios of the TMD to the main structure, respectively, with the subscripts t and s denoting the TMD and the main structure. The stiffness (k_t) and damping coefficient (c_t) of the TMD then can be estimated as

$$k_t = m_t\omega_t^2 = \mu m_s \gamma^2 \omega_s^2 \tag{7.3}$$

$$c_t = 2\zeta_t m_t \omega_t = 2\zeta_t \mu m_s \gamma \omega_s \tag{7.4}$$

where ζ_t is the damping ratio of the TMD.

As discussed above, the displacements of the tower and blades in the in-plane and out-of-plane directions are aimed to be controlled. The mean square displacement of the wind turbine in a particular direction can be expressed as

$$\sigma^2 = \int_0^\infty |H_s(\omega)|^2 S(\omega) d\omega \tag{7.5}$$

in which

$$H_s(\omega) = [\omega_s^2 - 2i\omega\omega_s\zeta_s - \omega^2 - i\omega m_s^{-1} Z(\omega)]^{-1} \tag{7.6}$$

$$Z(\omega) = -i\omega \frac{m_t(\omega_t^2 - 2i\omega\omega_t\zeta_t)}{\omega_t^2 - 2i\omega\omega_t\zeta_t - \omega^2} \tag{7.7}$$

where ζ_s is the damping ratio of the main structure as given in Section 7.3.

Substituting Eqs. (7.6) and (7.7) into Eq. (7.5), the optimal frequency ratio γ and damping ratio ζ_t can be obtained via the numerical searching technique by minimizing the mean square displacement of the main structure under a given mass ratio μ.

It should be noted that the vibration characteristics (frequency ω_s and damping ratio ζ_s) of the tower and blades in the in-plane and out-of-plane directions are different as indicated in Section 7.3, the stiffness and damping coefficients in these two directions are optimized separately considering the different frequencies ($\omega_{s\text{-in}}$ and $\omega_{s\text{-out}}$) and damping ratios ($\zeta_{s\text{-in}}$ and $\zeta_{s\text{-out}}$) in the corresponding direction. Moreover, the vibration frequencies of the parked and rotating blades are also slightly different (Zuo et al., 2018, 2019) due to the centrifugal stiffness generated by rotation. In practice, however, it is not feasible to change the parameters of the control devices during its service life. In the present study, the vibration frequencies of the parked condition (i.e. Table 7-3) are used to estimate the parameters of the bi-directional TMD systems in both the parked and operating conditions. Table 7-4 tabulates the optimal values of the TMD systems in different directions by assuming a mass ratio of 3%.

The bi-directional TMD as shown in Figure 7-5 are modelled by the mass, spring and dashpot elements in ABAQUS. However, it should be noted that the space in the tower and blades is limited, and the TMDs might penetrate the tower and blades in the numerical simulations, which is obviously not realistic, therefore the deformations of TMDs should be restrained in the numerical simulations. To avoid this unreasonable phenomenon, a nonlinear force-displacement relationship as shown in Figure 7-6 is defined for the spring elements in the

tower and blades, in which Δ is the allowable displacement. When the relative displacement between the TMDs and the tower/blade is smaller than Δ, the stiffness equals to the optimal value in Table 7-4, i.e. $k_1=k_t$. If the relative displacement is larger than Δ, the spring becomes hard to be compressed and a stiffness k_2 is defined. $k_2=1\times10^6$ N/m is found to have a good balance between the effectiveness and efficiency (Zuo et al., 2019), and this value is adopted in the simulations.

Table 7-4 Optimal stiffness and damping coefficients of the bi-directional TMD systems

Component		γ	ζ_t	m_t (kg)	k_t (kN/m)	c_t (kNs/m)
Tower	In-plane	0.98	0.09	10424	23.63	2.83
	Out-of-plane	0.98	0.09		23.02	2.79
Blade	In-plane	0.97	0.09	532	30.25	0.72
	Out-of-plane	0.97	0.09		7.09	0.35

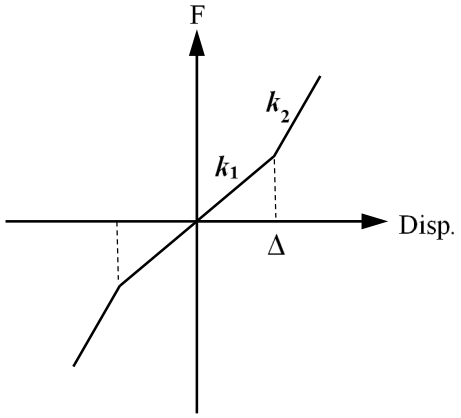

Figure 7-6 Nonlinear force-displacement relationship of the spring element

7.5 Results and discussions

To examine the effectiveness of the proposed simultaneous control method, two operational scenarios are considered in the present study. In the first scenario, the wind turbine is in the parked condition with the mean wind speed of 35 m/s at the hub height. In the second scenario, the wind turbine is in the operating condition with the blades rotating at a uniform velocity of 1.27 rad/s, which corresponds to the rated rotor speed of the NREL 5 MW wind turbine (12.1 rpm) as tabulated in Table 7-1, and the mean wind speed is taken as 11.4 m/s. To mitigate the in-plane and out-of-plane vibrations of the tower, the bi-directional TMD system is installed at the tower top, where the allowable displacement in both directions is 1.916 m. The TMD system installed at the tower top is because, as mentioned in Section 7.3, only the fundamental vibration mode of the tower is normally excited by the wind and wave loads, in which the maximum displacement occurs at the tower top. The most effective control can be achieved by placing the TMD at the location with the maximum displacement. For the blades, similar

to the tower, the maximum displacements appear at the corresponding tips. It is however not practical to install the TMD at the blade tip since the space at the tip is very limited. In the present study, a bi-directional TMD system is installed in each blade at the location with a distance of $L/6$ from the tip of the blade (where L is the length of the blade, i.e. L=61.5 m). At this location, the allowable displacements of the TMD in the out-of-plane and in-plane directions are 0.324 m and 1.259 m respectively. For comparison, the responses of the wind turbine without any control device and with separate TMD are also calculated. In particular, in the case of separate TMD, a single TMD is installed in either the out-of-plane or in-plane direction of the tower and blades to control the vibration in the corresponding direction.

To more straightforwardly show the control effectiveness, the following reduction ratio is defined

$$R = \frac{sd_1 - sd_2}{sd_1} \times 100\% \tag{7.8}$$

where sd_1 and sd_2 are the standard deviations of the in-plane and out-of-plane responses of the wind turbine without and with different control devices, respectively. It is obvious that the displacement responses along the height of the tower and the length of the blades are different and the largest responses occur at the top of the tower and the tip of the blades under the combined wind and wave loads as discussed. For conciseness, only the largest responses are examined to demonstrate the control effectiveness in the present study.

7.5.1 Parked condition

In this section, the wind turbine is assumed in the parked condition. In the numerical simulations, the external loads are applied to the wind turbine at t=0 s. Owing to the dynamic effect onto the structure, the responses in the initial stage are not stable (Clough & Penzien, 2003). The results in the first 10 s are therefore not analysed in this section, namely the discussions are based on the structural responses in the time period of 10-200 s during the stable response phase, not the initial transient response phase to better demonstrate the vibration control effectiveness.

Figure 7-7 shows the bi-directional motions at the top of the tower without and with the bi-directional TMD system when the wind turbine is in the parked condition. It can be seen that when the bi-directional TMD system is installed, the vibrations of the tower in the both directions are obviously reduced, which demonstrates the effectiveness of the proposed method. It should be noted that only the results of the cases with and without the bi-directional TMD system are shown in Figure 7-7, the trajectories of the tower with the uniaxial TMD (i.e. the cases of separate control) are not presented in the figure since when this case is considered,

another two curves should be added to the figure, which makes the figure very difficult to read. The control effectiveness are presented and discussed in more detail by comparing the results in the out-of-plane and in-plane directions separately.

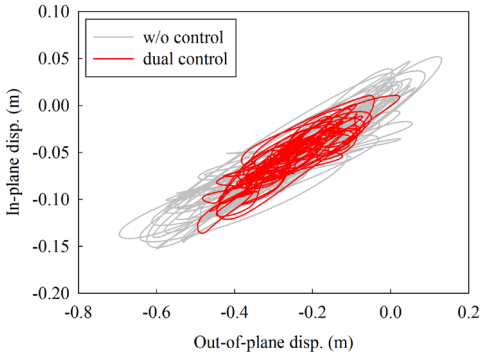

Figure 7-7 Influence of bi-directional TMD system on the tower displacements when the wind turbine is in the parked condition

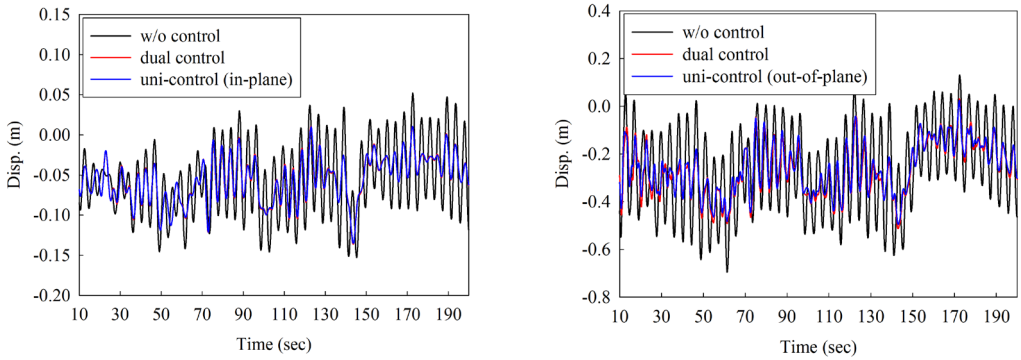

(a) in-plane (b) out-of-plane

Figure 7-8 In-plane and out-of-plane displacements at the tower top under parked condition

Figure 7-8 shows the displacement time histories at the top of the tower in the in-plane and out-of-plane directions without and with different control methods. To straightforwardly compare the overall control effectiveness, the standard deviations of the in-plane and out-of-plane displacements at the top of the tower and the corresponding reduction ratios are summarized in Table 7-5. As shown, for the wind turbine without any control device, the standard deviations of the in-plane and out-of-plane displacements are 0.0440 m and 0.1790 m respectively. When the bi-directional TMD system is installed to simultaneously mitigate the in-plane and out-of-plane vibrations, these values become 0.0276 m and 0.1074 m and the reduction ratios are 37.3% and 40.0% respectively. When the vibrations are controlled by the separate TMD, the standard deviations are 0.0274 m and 0.1038 m and the reduction ratios are 37.7% and 42.0% respectively. It can be seen that the control effectiveness of the bi-directional TMD system is slightly less than that of the uniaxial TMD system. This is because, in the bi-directional vibration control system, the displacement of the TMD in one direction (e.g. the

out-of-plane direction) is influenced by the spring and dashpot in the other direction (the in-plane direction), such that the axes of these two springs are no longer perpendicular as shown in Figure 7-9. The stiffness and damping components of the TMD in the in-plane and out-of-plane directions of the tower are therefore slightly different from the optimal values, and the control effectiveness are thus marginally decreased. However, it should be noted that, in the separate control case, only the vibration in one particular direction can be controlled. For the proposed method, the vibrations in both the in-plane and out-of-plane directions are mitigated simultaneously, and more importantly, the control effectiveness does not decrease too much compared to the uniaxial control system, which demonstrates the advantage of the proposed method.

Table 7-5 Standard deviations of the in-plane and out-of-plane displacements and the corresponding reduction ratios under parked condition

Direction	Location	W/o control	Dual control		Uni-control	
		sd (m)	*sd* (m)	*R*	*sd* (m)	*R*
In-plane	Tower top	0.0440	0.0276	37.3%	0.0274	37.7%
	Tip of blade #1	0.0649	0.0566	12.8%	0.0563	13.6%
	Tip of blade #2 (#3)	0.0788	0.0699	11.3%	0.0697	11.5%
Out-of-plane	Tower top	0.1790	0.1074	40.0%	0.1038	42.0%
	Tip of blade #1	0.6887	0.5502	20.1%	0.5159	25.1%
	Tip of blade #2 (#3)	0.6542	0.5855	10.5%	0.5736	12.3%

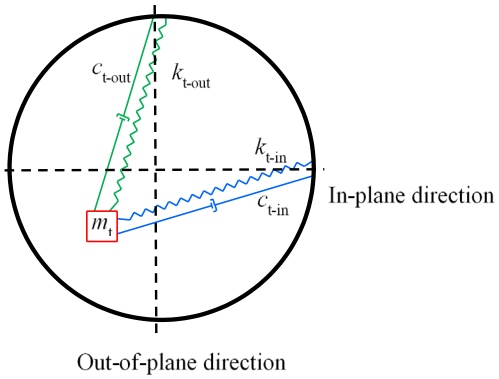

Figure 7-9 Deformations of bi-directional TMD system

Figure 7-10 shows the displacement time histories of the in-plane and out-of-plane TMDs at the tower top in the bi-directional and uniaxial control systems when the wind turbine is in the parked condition. It can be seen that the displacements of the TMDs in the uniaxial control systems are marginally smaller than those in the bi-directional control system though the control effectiveness of the uniaxial control systems is more evident as discussed above. This is because, as mentioned above, the bi-directional TMD can move in both the in-plane and out-of-plane directions, which leads to the deformations of the TMDs neither aligned with the in-plane nor out-of-plane direction of the tower. For the uniaxial control systems, the TMD however only moves in the in-plane or out-of-plane direction. If the in-plane and out-of-plane

displacement components are compared, larger relative displacements in the uniaxial TMDs are expected. Since the in-plane and out-of-plane displacement components of the bi-directional TMD cannot be directly extracted from ABAQUS, only the deformations of the TMDs are compared in this figure.

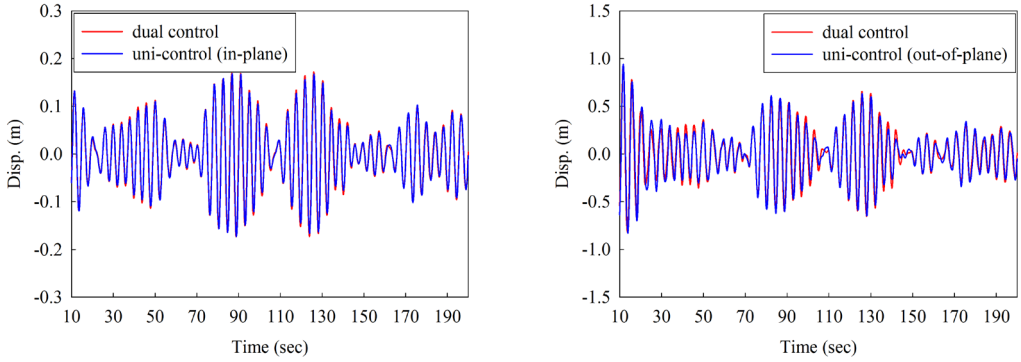

(a) in-plane TMD (b) out-of-plane TMD

Figure 7-10 Displacements of the in-plane and out-of-plane TMDs in the tower under parked condition

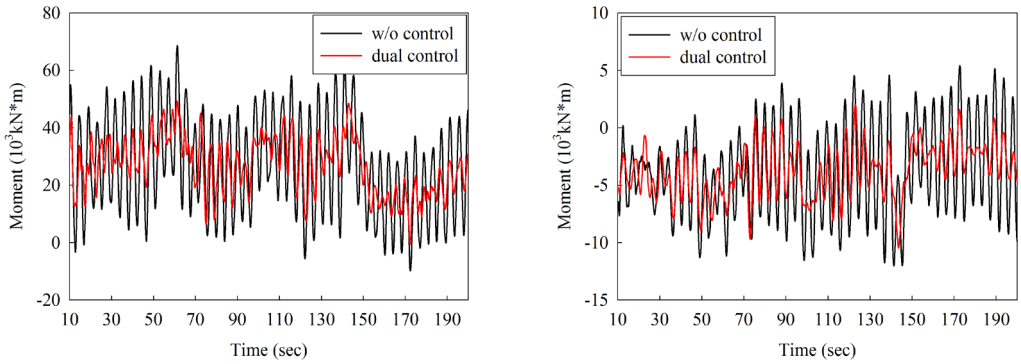

(a) in-plane (b) out-of-plane

Figure 7-11 In-plane and out-of-plane bending moments at the tower bottom under parked condition

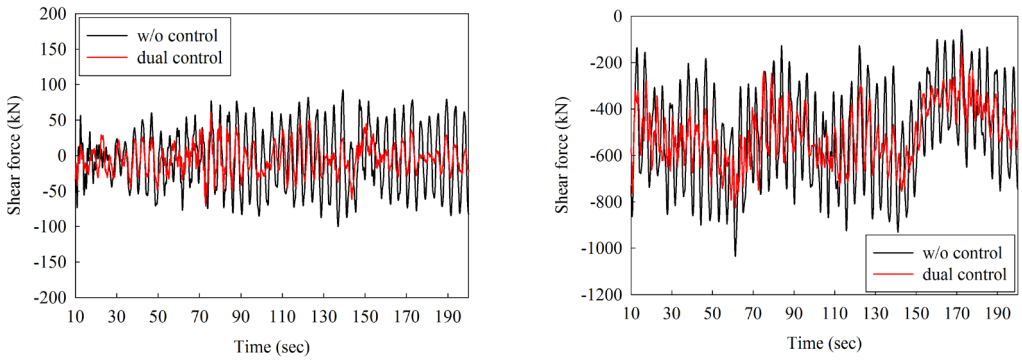

(a) in-plane (b) out-of-plane

Figure 7-12 In-plane and out-of-plane shear forces at the tower bottom under parked condition

Due to the high-rise and thin-walled geometrical characteristics of the wind turbine tower, it is vulnerable to fatigue damage or buckling under cyclic loads (e.g. wind and wave), and these calculations are related to the internal forces developed in the wind turbine, they are thus also discussed herein though the investigation on the fatigue damage or buckling is out of the scope of the present study.

The tower can be assumed as a cantilever beam, and it is obvious that the maximum internal forces appear at the bottom of the tower. Figure 7-11 and Figure 7-12 show the in-plane and out-of-plane bending moments and shear forces at this location without and with the bi-directional TMD system, respectively, and Table 7-6 summarizes the standard deviations in different cases and the corresponding reduction ratios. For the uniaxial TMD systems, since similar displacement control effectiveness is observed compared to the bi-directional control system as discussed above, the control effectiveness for the internal forces of these two systems should be similar as well. To more clearly show the curves, the results from the uniaxial control systems are not presented. It can be seen that the bi-directional TMD system can obviously mitigate the internal forces developed in the tower. As shown in Table 7-6, the reduction ratios for the shear forces and bending moments in the in-plane and out-of-plane directions vary from about 40% to 54%. This obvious reduction can significantly increase the fatigue life (Sun & Jahangiri, 2018) and buckling capacity (DNV & Risø, 2002) of the wind turbine.

Table 7-6 Standard deviations of the in-plane and out-of-plane bending moments and shear forces at the tower base and the corresponding reduction ratios under parked condition

Internal forces	Direction	W/o control	Dual control	
		sd	*sd*	*R*
Bending moment	In-plane	16830 kN·m	9786 kN·m	41.9%
	Out-of-plane	3909 kN·m	2235 kN·m	42.8%
Shear force	In-plane	43 kN	20 kN	53.5 %
	Out-of-plane	202 kN	121 kN	40.1%

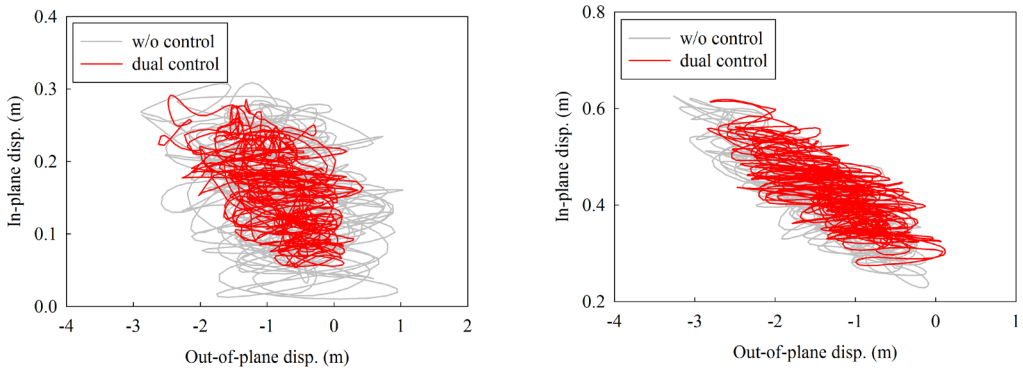

(a) blade #1 (b) blade #2 (#3)

Figure 7-13 Influence of bi-directional TMD system on the blade displacements when the wind turbine is in the parked condition

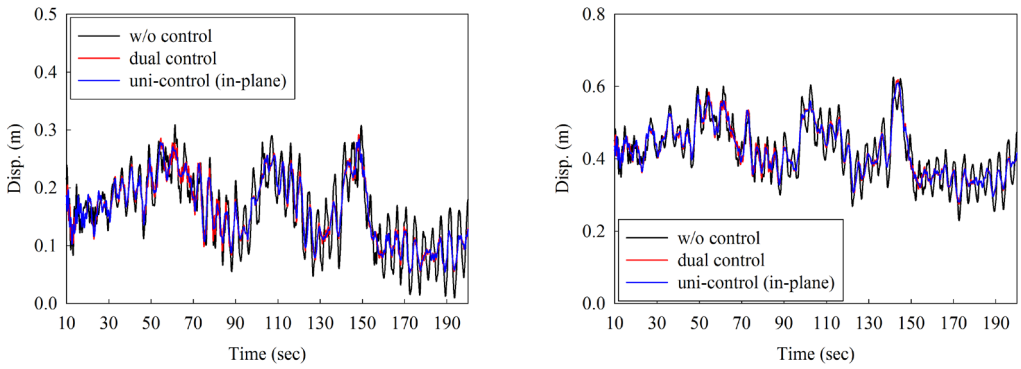

(a) blade #1 (b) blade #2 (#3)

Figure 7-14 In-plane displacements at the blade tips under parked condition

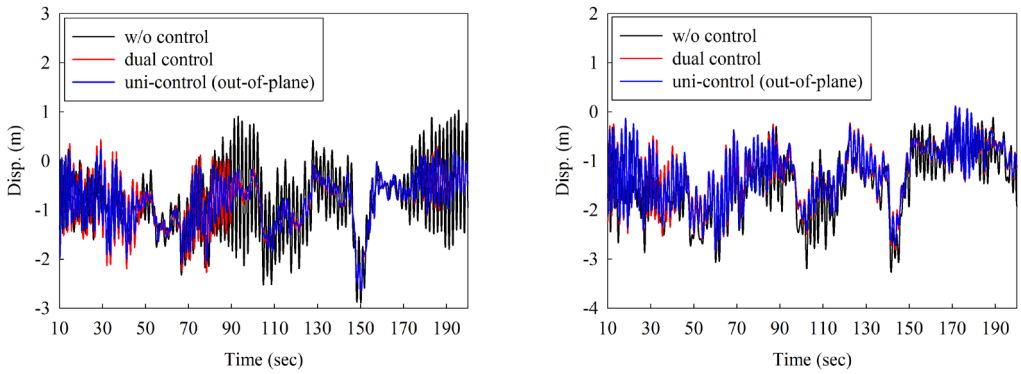

(a) blade #1 (b) blade #2 (#3)

Figure 7-15 Out-of-plane displacements at the blade tips under parked condition

As for the blade responses, Figure 7-13 shows the bi-directional motions at the tips of the three blades without and with the bi-directional TMDs when the wind turbine is in the parked condition. Figure 7-14 and Figure 7-15 respectively show the displacement time histories at the tips of the three blades in the in-plane and out-of-plane directions without and with different control systems. In the parked condition, the displacement responses of blade #3 are the same as those of blade #2 because the locations of blades #2 and #3 are symmetrical and the same wind loads are applied to these two blades as mentioned in Section 7.4. The standard deviations of the in-plane and out-of-plane displacements at the tips of the three blades and the corresponding reduction ratios are also tabulated in Table 7-5. Again, similar to the tower, using the bi-directional TMD system slightly decreases the control effectiveness compared to the uniaxial TMD system due to the reason explained above. For the in-plane vibrations, it can be seen from Table 5 that the TMD has the similar control effectiveness on blades #1 and #2. For the out-of-plane vibrations, the control effectiveness is, however, more evident for blade #1 compared to blade #2 for both control systems. The reason is that the wind loads on blade #2 are larger than those on blade #1, which result in larger displacement responses of blade #2 (see Figure 7-15) and also larger relative displacements of the TMD in the blade. Figure 7-16

and Figure 7-17 show the relative displacements of the in-plane and out-of-plane TMDs in blades #1 and #2, respectively. It can be seen that in the in-plane direction, both the TMDs in blades #1 and #2 can vibrate freely in the blades, while in the out-of-plane direction, the vibration for both TMDs are restrained by the limited space, and the relative displacements of the TMDs reach the allowable displacement (the red dashed lines in Figure 7-17). As shown, the restraints for blade #2 are more evident compared to blade #1, which means the function of TMD in blade #2 is less developed, leading to the control effectiveness of TMD in blade #2 less evident. It should be noted that in Figure 7-16 the displacements of the in-plane TMDs in the uniaxial control system are smaller than those in the bi-directional control system, but the effectiveness of the uniaxial control system is more evident. This is because the figure shows the total deformations of the springs of the damper but not the component in the in-plane direction as discussed above. The displacement components of bi-directional TMDs in the in-plane and out-od-plane directions are smaller than the corresponding displacement of the uniaxial TMDs.

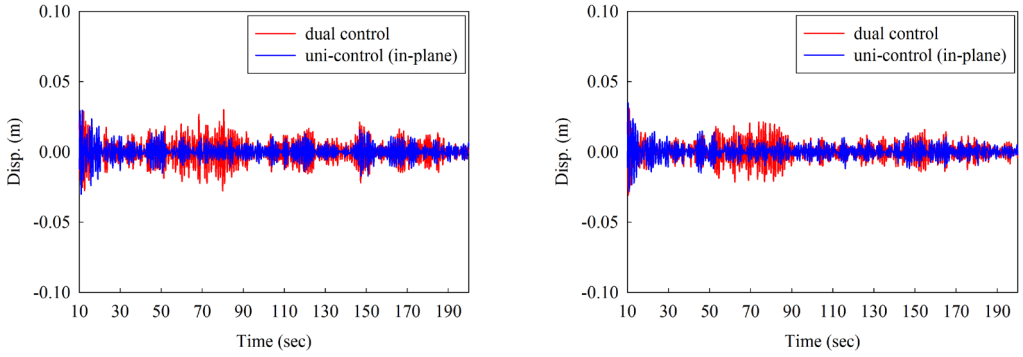

(a) blade #1 (b) blade #2

Figure 7-16 Displacements of the in-plane TMDs in blades #1 and #2 under parked condition

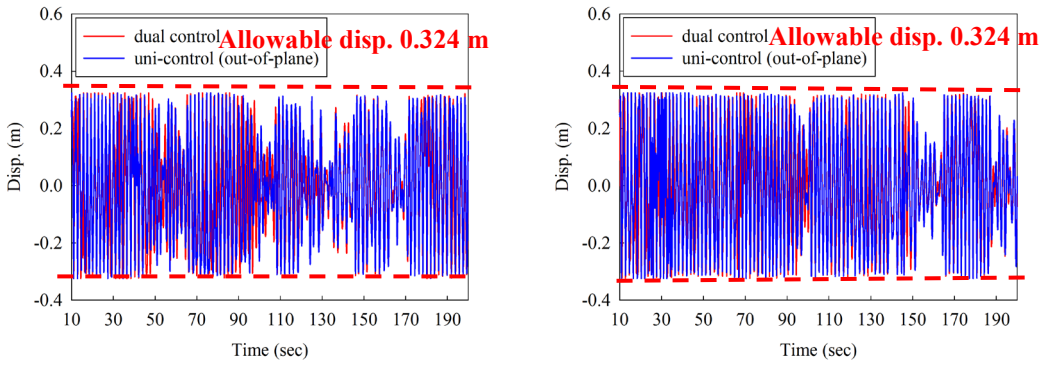

(a) blade #1 (b) blade #2

Figure 7-17 Displacements of the out-of-plane TMDs in blades #1 and #2 under parked condition

The results in Table 7-5 also show that the control effectiveness for the blades is less than that for the tower. This is because, as discussed above, the TMD should install at the location with

the maximum displacement to obtain the most effective control. In the tower, the TMD is installed at the tower top, while the TMD in each blade is installed at the location with a distance of $L/6$ from the tip of the blade, which impairs the control effectiveness for the blades.

7.5.2 Operating condition

In this section, the responses and control effectiveness of different control systems are compared and discussed when the wind turbine is in the operating condition. Similar to the application of external loads to the parked wind turbine, the response of the wind turbine system is unstable in the initial transient phase when the load is first applied (Zuo et al., 2018). To remove the influence of this effect, the blades are rotating without any external load at the first 30 s to make sure the system reaches a stable status, and then the wind and wave loads are applied. Again, the results of the first 10 s after the application of the external loads are not analysed. All the results and discussions in this section are based on the numerical results within the time period of t=40-230 s.

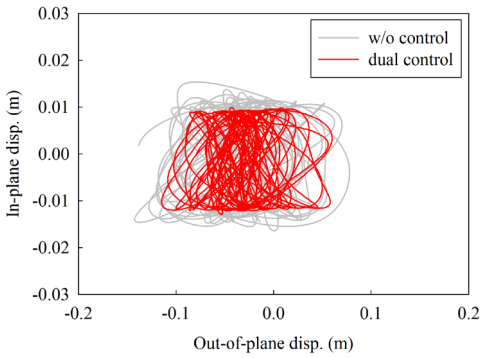

Figure 7-18 Influence of bi-directional TMD system on the tower displacements when the wind turbine is in the operating condition

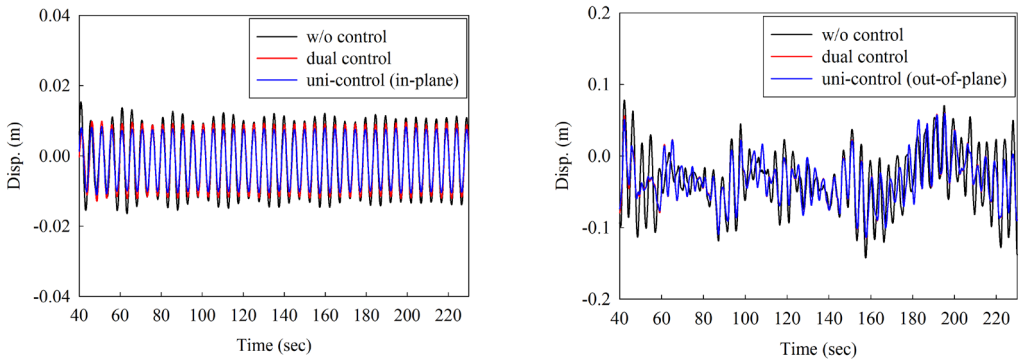

(a) in-plane (b) out-of-plane

Figure 7-19 In-plane and out-of-plane displacements at the tower top under operating condition

Figure 7-18 shows the bi-directional motions at the top of the tower without and with the bi-directional TMD when the wind turbine is in the operating condition. Be more specific, the

displacement time histories at the top of the tower in the in-plane and out-of-plane directions without and with different control methods are shown in Figure 7-19. It should be noted that no external excitation is acting in the in-plane direction of the tower, its in-plane responses are induced by the interaction between the tower and blades. Table 7-7 tabulates the standard deviations of the in-plane and out-of-plane displacements at the top of the tower and the corresponding reduction ratios. As shown, for the wind turbine without any control device, the standard deviations of the in-plane and out-of-plane displacements are 0.0089 m and 0.0405 m respectively. When the bi-directional TMD system is installed, these values reduce to 0.0074 m and 0.0312 m, respectively and the corresponding reduction ratios are 16.9% and 23.0%. When the uniaxial TMD is used, the standard deviations of the displacements decrease to 0.0064 m and 0.0310 m and the reduction ratios are 28.1% and 23.5%, respectively. Again the bi-directional TMD system moving in both the in-plane and out-of-plane directions slightly decreases the control effectiveness compared to the uniaxial TMDs.

Table 7-7 Standard deviations of the in-plane and out-of-plane displacements and the corresponding reduction ratios under operating condition

Direction	Location	W/o control	Dual control		Uni-control	
		sd (m)	*sd* (m)	*R*	*sd* (m)	*R*
In-plane	Tower top	0.0089	0.0074	16.9%	0.0064	28.1%
	Tip of blade #2	0.1404	0.0885	37.0%	0.0666	52.6%
Out-of-plane	Tower top	0.0405	0.0312	23.0%	0.0310	23.5%
	Tip of blade #1	0.1646	0.1481	10.0%	0.1476	10.3%
	Tip of blade #2	0.1632	0.1481	9.3%	0.1475	9.6%
	Tip of blade #3	0.1567	0.1471	6.1%	0.1463	6.6%

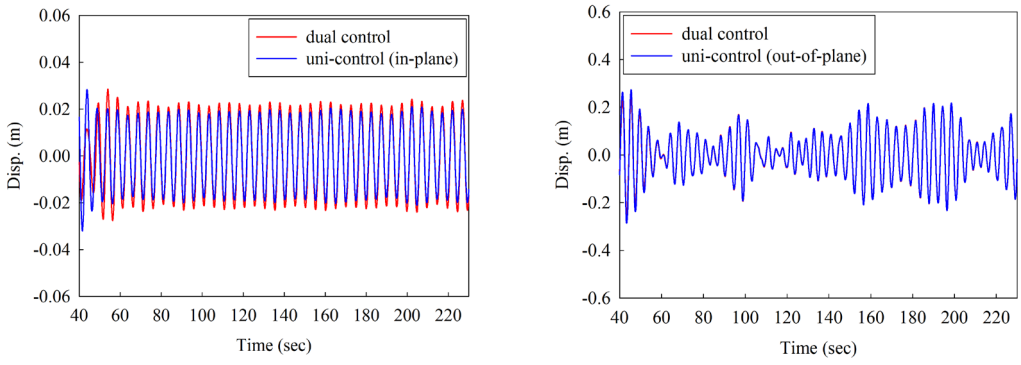

(a) in-plane TMD (b) out-of-plane TMD

Figure 7-20 Displacements of the in-plane and out-of-plane TMDs in the tower under operating condition

Figure 7-20 shows the displacements of the in-plane and out-of-plane TMDs in the bi-directional and uniaxial control systems. As shown, the displacements of the in-plane TMD are quite small compared to the out-of-plane TMD because no external load is directly applied in the in-plane direction as discussed above. Due to the relatively small motions in the in-plane

direction, the displacements of the out-of-plane TMD in the two control systems (i.e. the bi-directional and uniaxial control systems) are almost the same as shown in Figure 7-20(b), which results in the similar control effectiveness in the out-of-plane direction as shown in Figure 7-19(b) and Table 7-7.

Figure 7-21 and Figure 7-22 show the in-plane and out-of-plane bending moments and shear forces respectively at the tower bottom without and with the bi-directional TMD system when the wind turbine is in the operating condition. The standard deviations of the bending moments and shear forces and the corresponding reduction ratios are summarized in Table 7-8. Again, as shown in the table, the bending moments and shear forces can be obviously mitigated by using the bi-directional TMD system and the reduction ratios are within the range of 22% to 27%.

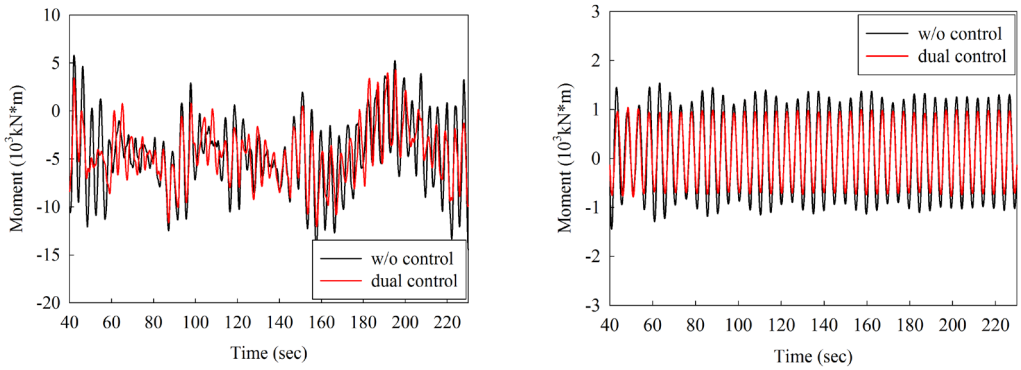

(a) in-plane (b) out-of-plane

Figure 7-21 In-plane and out-of-plane bending moments at the tower bottom under operating condition

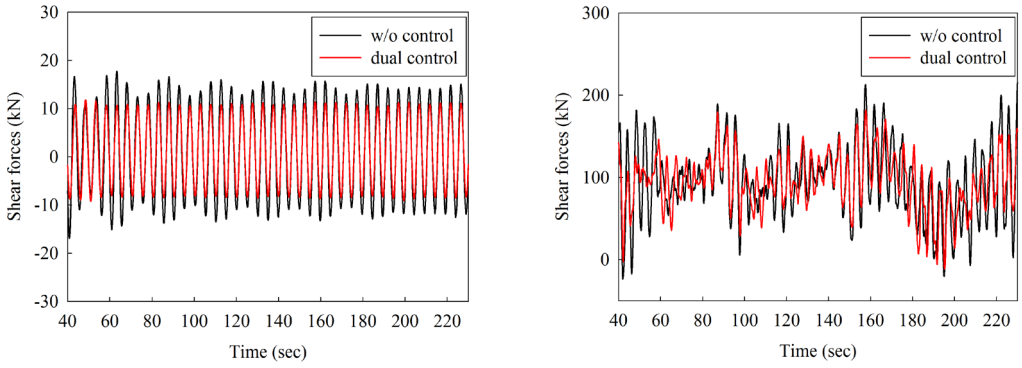

(a) in-plane (b) out-of-plane

Figure 7-22 In-plane and out-of-plane shear forces at the tower bottom under operating condition

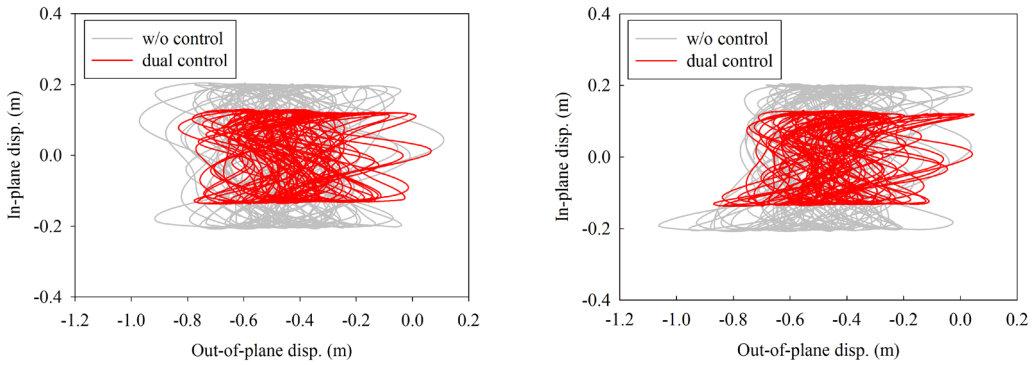

(a) blade #1

(b) blade #2

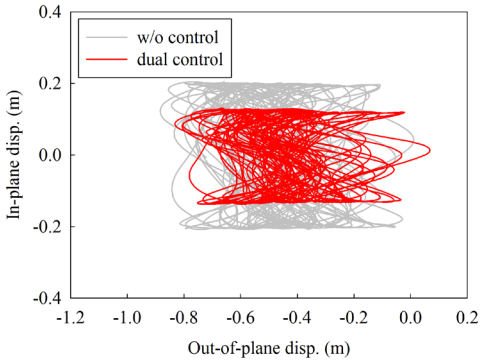

(c) blade #3

Figure 7-23 Influence of bi-directional TMD system on the blade displacements when the wind turbine is in the operating condition

Table 7-8 Standard deviations of the in-plane and out-of-plane bending moments and shear forces at the tower base and the corresponding reduction ratios under operating condition

Inertial forces	Direction	W/o control	Dual control	
		sd	*sd*	*R*
Bending moment	In-plane	3780 kN·m	2901 kN·m	23.3%
	Out-of-plane	819 kN·m	598 kN·m	27.0%
Shear force	In-plane	9 kN	7 kN	22.2%
	Out-of-plane	44 kN	34 kN	22.7%

Figure 7-23 show the bi-directional motions at the tips of the three blades without and with the bi-directional TMDs when the wind turbine is in the operating condition, and Figure 7-24 and Figure 7-25 respectively show the displacement time histories at the tips of the three blades in the in-plane and out-of-plane directions without and with different control systems. The in-plane responses of the rotating blades are governed by the gravity load, and the geometrical and structural parameters of the three blades in the rotor plane are the same, thus their responses in the in-plane direction are identical. Only the in-plane displacement responses of blade #2 are shown for conciseness. The standard deviations of the in-plane and out-of-plane displacements of the blades and the corresponding reduction ratios are also tabulated in Table 7-7. As shown, when the bi-directional system is installed, the standard deviation of the in-

plane displacements at the tip of the blade decreases from 0.1404 m to 0.0885 m with a reduction ratio of 37.0%. For the uniaxial TMD system, the control effectiveness is more evident, and the reduction ratio reaches 52.6%. For the out-of-plane vibration, the control effectiveness is less evident compared to the in-plane motions, and the reduction ratios for the three blades vary from about 6% to 10%, which are at the same level as reported by (Zuo et al., 2019). The effectiveness of the out-of-plane vibration control for the blades are different since the out-of-plane responses are influenced by the initial positions of the blades.

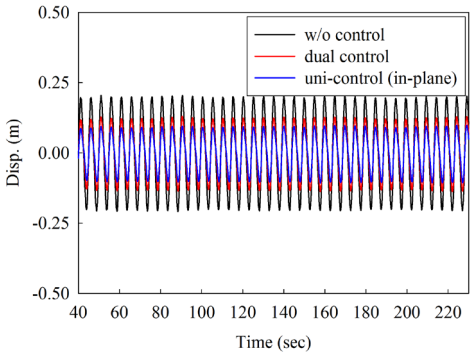

Figure 7-24 In-plane displacements at the tip of blade #2 under operating condition

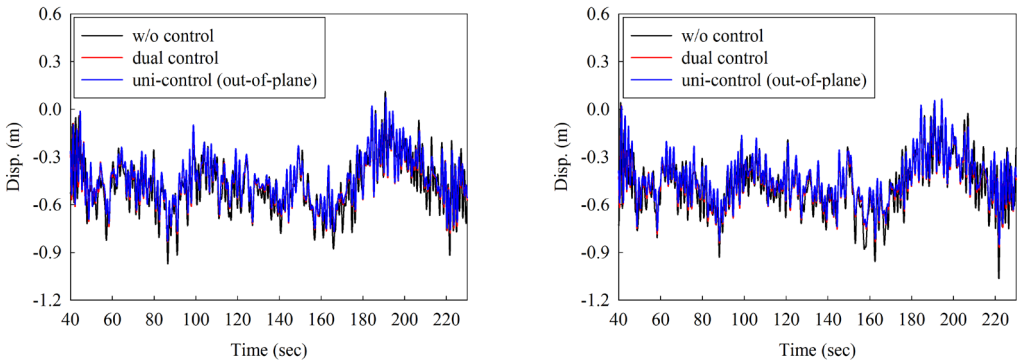

(a) blade #1 (b) blade #2

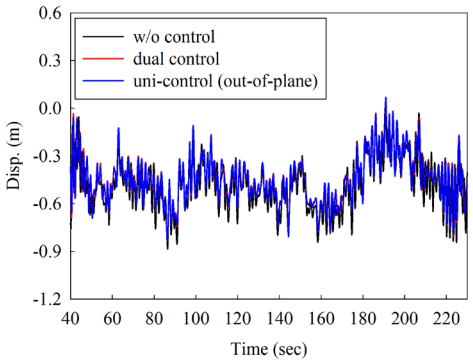

(c) blade #3

Figure 7-25 Out-of-plane displacements at the tips of the three blades under operating condition

7.6 Conclusions

In this chapter, the bi-directional TMD system is proposed to be installed in the tower and blades to simultaneously control the in-plane and out-of-plane vibrations of wind turbines when it is subjected to the combined wind and wave loads. Numerical results indicate that the bi-directional TMD system can effectively mitigate the in-plane and out-of-plane vibrations of the tower and blades at both the parked and operating conditions. Numerical results also reveal that the control effectiveness is marginally decreased compared to the commonly used uniaxial vibration control method. However, since the proposed method does not need to change too much of the original design but can simultaneously control both the in-plane and out-of-plane vibrations, it could have great application potentials in the vibration control of offshore wind turbines.

7.7 References

Arany, L., Bhattacharya, S., Macdonald, J. H., & Hogan, S. J. (2016). Closed form solution of Eigen frequency of monopile supported offshore wind turbines in deeper waters incorporating stiffness of substructure and SSI. *Soil Dynamics and Earthquake Engineering*, *83*, 18-32.

Arrigan, J., Pakrashi, V., Basu, B., & Nagarajaiah, S. (2011). Control of flapwise vibrations in wind turbine blades using semi-active tuned mass dampers. *Structural Control and Health Monitoring*, *18*(8), 840-851.

Basu, B., Zhang, Z., & Nielsen, S. R. K. (2016). Damping of edgewise vibration in wind turbine blades by means of circular liquid dampers. *Wind Energy*, *19*(2), 213-226.

Bisoi, S., & Haldar, S. (2014). Dynamic analysis of offshore wind turbine in clay considering soil-monopile-tower interaction. *Soil Dynamics and Earthquake Engineering*, *63*, 19-35.

Chen, J., Liu, Y., & Bai, X. (2015). Shaking table test and numerical analysis of offshore wind turbine tower systems controlled by TLCD. *Earthquake Engineering and Engineering Vibration*, *14*(1), 55-75.

Clough, R., & Penzien, J. (2003). Dynamics of structures 3rd ed. Computer & Structures, Inc.

Colwell, S., & Basu, B. (2009). Tuned liquid column dampers in offshore wind turbines for structural control. *Engineering Structures*, *31*(2), 358-368.

Det Norske Veritas (DNV). (2014). DNV-OS-J101: Design of offshore wind turbine structures. Copenhagen, Denmark: DNV.

Det Norske Veritas (DNV)/Risø National Laboratory. (2002). Guidelines for design of wind turbines 2nd ed. Denmark: DNV and Risø National Laboratory.

Fitzgerald, B., & Basu, B. (2014). Cable connected active tuned mass dampers for control of in-plane vibrations of wind turbine blades. *Journal of Sound and Vibration*, *333*(23), 5980-6004.

Fitzgerald, B., Basu, B., & Nielsen, S. R. K. (2013). Active tuned mass dampers for control of in-plane vibrations of wind turbine blades. *Structural Control and Health Monitoring*, *20*(12), 1377-1396.

Ghassempour, M., Failla, G., & Arena, F. (2019). Vibration mitigation in offshore wind turbines via tuned mass damper. *Engineering Structures*, *183*, 610-636.

Global Wind Energy Council. (2018). Global wind report-Annual market update 2017.

Hansen, M. O. L. (2008). Aerodynamics of wind turbines 2nd ed. London, UK: Earthscan.

Hasselmann, K., Barnett, T., Bouws, E., Carlson, H., Cartwright, D., Enke, K., Walden, H. (1973). Measurements of wind-wave growth and swell decay during the Joint North Sea Wave Project (JONSWAP). Hamburg: Deutches Hydrographisches Institut.

Hu, Y., Wang, J., Chen, M. Z., Li, Z., & Sun, Y. (2018). Load mitigation for a barge-type floating offshore wind turbine via inerter-based passive structural control. *Engineering Structures*, *177*, 198-209.

Huang, G., Liao, H., & Li, M. (2013). New formulation of Cholesky decomposition and applications in stochastic simulation. *Probabilistic Engineering Mechanics*, *34*, 40-47.

Jahangiri, V., & Sun, C. (2019a). Integrated bi-directional vibration control and energy harvesting of monopile offshore wind turbines. *Ocean Engineering*, 178, 260-269.

Jonkman, J., Butterfield, S., Musial, W., & Scott, G. (2009). Definition of a 5-MW reference wind turbine for offshore system development. (Technical Report No. NREL/TP-500-38060). Golden, CO: National Renewable Energy Laboratory.

Lackner, M. A., & Rotea, M. A. (2011). Passive structural control of offshore wind turbines. *Wind Energy*, *14*(3), 373-388.

Mensah, A. F., & Dueñas-Osorio, L. (2014). Improved reliability of wind turbine towers with tuned liquid column dampers (TLCDs). *Structural Safety*, *47*, 78-86.

Murtagh, P. J., Basu, B., & Broderick, B. M. (2005). Along-wind response of a wind turbine tower with blade coupling subjected to rotationally sampled wind loading. *Engineering Structures*, *27*(8), 1209-1219.

Murtagh, P. J., Ghosh, A., Basu, B., & Broderick, B. M. (2008). Passive control of wind turbine vibrations including blade/tower interaction and rotationally sampled turbulence. *Wind Energy*, *11*(4), 305-317.

Staino, A., Basu, B., & Nielsen, S. R. K. (2012). Actuator control of edgewise vibrations in wind turbine blades. *Journal of Sound and Vibration*, *331*(6), 1233-1256.

Stewart, G. M., & Lackner, M. A. (2014). The impact of passive tuned mass dampers and wind-wave misalignment on offshore wind turbine loads. *Engineering Structures*, *73*, 54-61.

Sun, C., & Jahangiri, V. (2018). Bi-directional vibration control of offshore wind turbines using a 3D pendulum tuned mass damper. *Mechanical Systems and Signal Processing*, *105*, 338-360.

Sun, C., & Jahangiri, V. (2019b). Fatigue damage mitigation of offshore wind turbines under real wind and wave conditions. *Engineering Structures*, *178*, 472-483.

Zhang, R., Zhao, Z., & Dai, K. (2019). Seismic response mitigation of a wind turbine tower using a tuned parallel inerter mass system. *Engineering Structures*, *180*, 29-39.

Zhang, Z., Basu, B., & Nielsen, S. R. K. (2015a). Tuned liquid column dampers for mitigation of edgewise vibrations in rotating wind turbine blades. *Structural Control and Health Monitoring*, *22*(3), 500-517.

Zhang, Z., Li, J., Nielsen, S. R. K., & Basu, B. (2014). Mitigation of edgewise vibrations in wind turbine blades by means of roller dampers. *Journal of Sound and Vibration*, *333*(21), 5283-5298.

Zhang, Z., Nielsen, S. R. K., Basu, B., & Li, J. (2015b). Nonlinear modeling of tuned liquid dampers (TLDs) in rotating wind turbine blades for damping edgewise vibrations. *Journal of Fluids and Structures*, *59*, 252-269.

Zhang, Z., Staino, A., Basu, B., & Nielsen, S. R. K. (2016). Performance evaluation of full-scale tuned liquid dampers (TLDs) for vibration control of large wind turbines using real-time hybrid testing. *Engineering Structures*, *126*, 417-431.

Zhao, B., Gao, H., Wang, Z., & Lu, Z. (2018). Shaking table test on vibration control effects of a monopile offshore wind turbine with a tuned mass damper. *Wind Energy*, *21*(12), 1309-1328.

Zuo, H., Bi, K., & Hao, H. (2017). Using multiple tuned mass dampers to control offshore wind turbine vibrations under multiple hazards. *Engineering Structures*, *141*, 303-315.

Zuo, H., Bi, K., & Hao, H. (2018). Dynamic analyses of operating offshore wind turbines including soil-structure interaction. *Engineering Structures*, *157*, 42-62.

Zuo, H., Bi, K., & Hao, H. (2019). Mitigation of tower and out-of-plane blade vibrations of offshore monopile wind turbines by using multiple tuned mass dampers. *Structure and Infrastructure Engineering*, *15*(2):269-284.

CHAPTER 8 CONCLUSIONS AND RECOMMENDATIONS

8.1 Main findings

This research develops sophisticated numerical models to more accurately capture the dynamic responses of offshore wind turbines and proposes practical passive control strategies to mitigate their excessive vibrations under wind, wave and/or seismic loads. The major contributions and findings in this thesis are briefly summarized below:

1. Chapter 2 presents the influences of operational conditions (i.e. parked and operating), SSI and rotational velocity on the dynamic responses of offshore wind turbines. Numerical results reveal that: (1) The dynamic responses of the tower and blades in the operating condition are much larger than those in the parked condition, which indicates that assuming the wind turbines in the parked condition may lead to non-conservative structural response estimations and unsafe design of structural components; (2) The vibration frequencies of the tower are decreased when SSI is considered, but SSI only marginally affects the natural frequencies of the blades. The displacement responses of the tower and blades in the out-of-plane direction are substantially influenced by SSI. However, SSI has a negligible effect on the in-plane displacements of the blades; (3) The out-of-plane displacements of the tower and blades increase with the increment of the rotational velocity. The displacements of the blades in the in-plane direction increase slightly when the rotational velocity becomes larger.
2. Chapter 3 investigates the influences of offshore and depth-varying ground motions on the seismic responses of offshore wind turbines. Numerical results show that: (1) The earthquake ground motions at the offshore site are significantly different from those at the onshore site especially for the seismic motions in the vertical direction, thetrefore using onshore seismic motions as inputs in the analyses may underestimate the out-of-plane and in-plane responses of offshore wind turbines. For the investigated offshore wind turbine, the difference can reach 25%. The vertical responses are however overestimated by adopting the onshore earthquake motions; (2) Compared to the depth-varying earthquake motions, using the seismic motions at the seabed level as inputs can overestimate the dynamic responses of offshore wind turbines. The overestimation can reach 24% for the examined example; (3) The influence of different earthquake ground motions (onshore/offshore and uniform/depth-varying) on the in-plane responses of the parked blades is more evident compared to the out-of-plane responses due to the vertical seismic components influence the displacement in the in-plane direction; (4) The different seismic inputs have more obvious effect on

the responses of the operating offshore wind turbine than those when the offshore wind turbine is in the parked condition except the in-plane responses of the rotating blades, which are governed by the rotation of the blades.

3. Chapter 4 analyses the fragilities of the wind turbine under the combined wind and wave loads. The uncertainties of the material and damping are considered and different damage states for the tower and blades are defined based on the serviceability and ultimate limit state levels. It was observed that: (1) The yielding of the wind turbine tower is very unlikely to occur when the wind speeds are within the cut-in and cut-out range in either the operating or parked conditions. However, the probabilities of the limit state exceedance of the blades are more apparent in both conditions; (2) The aerodynamic damping and the pitch control system have a considerable influence on the wind-induced displacement responses of the wind turbine, which slow down the increasing rate of the displacement responses with the increasing of the wind speed.
4. Chapter 5 proposes using MTMDs to control the vibrations of the tower induced by the first and higher vibration modes when the offshore wind turbine is subjected to the combined wind, wave and earthquake excitations. Numerical analyses are carried out to examine the control effectiveness of the proposed method and it was found that: (1) When only the fundamental vibration mode is excited by the external vibration sources, dividing the single TMD into smaller MTMDs may slightly decrease the control effectiveness compared to the case with a single TMD installed at the top of the tower; (2) When both the fundamental and higher vibration modes of the tower are excited by the external vibration sources, MTMDs can effectively control both the fundamental and higher vibration modes and increase the control effectiveness. The control effectiveness is most evident when MTMDs are applied at the locations with the largest mode amplitudes.
5. As an extension of Chapter 5, MTMDs are also installed in the blades in Chapter 6 to control their out-of-plane vibrations. Numerical results show that MTMDs can effectively control both the out-of-plane vibrations of the tower and blades when the wind turbine is in the operating and parked conditions though the reduction ratio of the displacement responses slightly decreases compared to the case with a single TMD installed at the tower top and blade tips. The reliability of the control system can be significantly improved in case some of the tuned masses do not function well. Another obvious merit of this control method is that it can significantly facilitate the TMD installations since the mass of each TMD is much smaller compared to a single large TMD.
6. In Chapter 7, the bi-directional TMD system is proposed to be installed in the tower and blades to simultaneously control the in-plane and out-of-plane vibrations of wind

turbines when they are subjected to the combined wind and wave loads. Numerical results indicate that the bi-directional TMD system can effectively mitigate the in-plane and out-of-plane vibrations of the tower and blades at both the parked and operating conditions. Numerical results also reveal that the control effectiveness is marginally decreased compared to the commonly used uniaxial vibration control method. However, since the proposed method does not need to change too much of the original design but can simultaneously control both the in-plane and out-of-plane vibrations, it could have great application potentials in the vibration control of offshore wind turbines.

8.2 Recommendations for future works

In the present study, extensive numerical analyses have been performed to investigate the dynamic responses of offshore wind turbines subjected to the combined wind, wave and/or seismic loads, and practical passive vibration control methods have also been explored to mitigate the vibrations of the tower and blades. Following investigations could be further made in the future studies:

1. This study carries out numerical analyses on the dynamic responses and vibration control of offshore monopile wind turbines. Experimental studies are needed to further validate the observations in the present thesis.
2. It is well known that larger mass ratio between the TMD device and the primary structure generally leads to better control performance. Instead of using TMDs, inerter-based control system, which can significantly amplify the physical mass of the control device and thus the mass ratio might be an effective solution to further improve the control effectiveness and can be investigated.
3. More and more offshore wind turbines are constructed far away from the coast line to more effectively extract the wind resources, the monopile foundation may not be feasible in the deep water. In this case, floating wind turbines might be more practical. The dynamic responses and vibration control of floating offshore wind turbines could be an interesting topic.
4. Due to the high-rise and thin-walled geometrical characteristics of the tower and blades, they are susceptible to the fatigue damage and buckling problem. Fatigue and buckling analyses should be performed to ensure the serviceability and safety of offshore wind turbines.
5. Offshore wind turbines may be collided by the commercial ships or infield support vessels. The collisions between ships or vessels and offshore wind turbines has received very limited attention, which could be further investigated

APPENDIX I ATTRIBUTION OF AUTHORSHIP

To whom it may concern

I, Haoran Zuo, contributed (carried out numerical simulations, analysed numerical results and wrote the manuscript which was revised and edited by other co-authors) to the papers entitled below.

Dynamic analyses of operating offshore wind turbines including soil-structure interaction

Using multiple tuned mass dampers to control offshore wind turbine vibrations under multiple hazards

Mitigation of tower and out-of-plane blade vibrations of offshore monopile wind turbines by using multiple tuned mass dampers

Simultaneous out-of-plane and in-plane vibration mitigations of offshore monopile wind turbines by tuned mass dampers

(……..……...)

I, as a co-author, endorse that this level of contribution by the candidate indicated above is appropriate.

(Dr. Kaiming Bi) (……..……...)

(Prof. Hong Hao) (……..……...)

To whom it may concern

I, Haoran Zuo, contributed (carried out numerical simulations, analysed numerical results and wrote the manuscript which was revised and edited by other co-authors) to the paper entitled (**Influence of earthquake ground motion modelling on the dynamic responses of offshore wind turbines**).

(……..……...)

I, as a co-author, endorse that this level of contribution by the candidate indicated above is appropriate.

(Dr. Kaiming Bi) (……..……...)

(Prof. Hong Hao) (……..……...)

(Dr. Chao Li) (……..……...)

To whom it may concern

I, Haoran Zuo, contributed (carried out numerical simulations, analysed numerical results and wrote the manuscript which was revised and edited by other co-authors) to the paper entitled (**Fragility analyses of offshore wind turbines subjected to aerodynamic and sea wave loadings**).

(……..……...)

I, as a co-author, endorse that this level of contribution by the candidate indicated above is appropriate.

(Dr. Kaiming Bi) (……..……...)

(Prof. Hong Hao) (……..……...)

(Dr. Jun Li) (……..……...)

(Mr. Yu Xin) (……..……...)

(Dr. Chao Li) (……..……...)

APPENDIX Ⅱ COPYRIGHT CLEARANCE

The proof of the rights, granted by publishers for the publication that forms the chapters of this thesis, to reproduce the contribution in the thesis are attached below.

Zuo, H., Bi, K. & Hao, H. (2018). Dynamic analyses of operating offshore wind turbines including soil-structure interaction. *Engineering Structures*, *157*, 42-62. https://doi.org/10.1016/j.engstruct.2017.12.001

Copyright Clearance Center RightsLink®

Home | Account Info | Help | LIVE CHAT

Title: Dynamic analyses of operating offshore wind turbines including soil-structure interaction

Author: Haoran Zuo,Kaiming Bi,Hong Hao

Publication: Engineering Structures

Publisher: Elsevier

Date: 15 February 2018

Logged in as:
Haoran Zuo
LOGOUT

BACK | CLOSE WINDOW

Zuo, H., Bi, K., Hao, H. & Li, C. (2019). Influence of earthquake ground motion modelling on the dynamic responses of offshore wind turbines. *Soil Dynamics and Earthquake Engineering*, *121*, 151-167. https://doi.org/10.1016/j.soildyn.2019.03.008.

Copyright Clearance Center RightsLink®

Home | Account Info | Help | LIVE CHAT

Title: Influence of earthquake ground motion modelling on the dynamic responses of offshore wind turbines

Author: Haoran Zuo,Kaiming Bi,Hong Hao,Chao Li

Publication: Soil Dynamics and Earthquake Engineering

Publisher: Elsevier

Date: June 2019

Logged in as:
Haoran Zuo
LOGOUT

BACK | CLOSE WINDOW

Zuo, H., Bi, K. & Hao, H. (2017). Using multiple tuned mass dampers to control offshore wind turbine vibrations under multiple hazards. *Engineering Structures*, *141*, 303-315. https://doi.org/10.1016/j.engstruct.2017.03.006.

Copyright Clearance Center RightsLink®

Home | Account Info | Help | LIVE CHAT

Title: Using multiple tuned mass dampers to control offshore wind turbine vibrations under multiple hazards
Author: Haoran Zuo,Kaiming Bi,Hong Hao
Publication: Engineering Structures
Publisher: Elsevier
Date: 15 June 2017
© 2017 Elsevier Ltd. All rights reserved.

Logged in as:
Haoran Zuo
LOGOUT

Please note that, as the author of this Elsevier article, you retain the right to include it in a thesis or dissertation, provided it is not published commercially. Permission is not required, but please ensure that you reference the journal as the original source. For more information on this and on your other retained rights, please visit: https://www.elsevier.com/about/our-business/policies/copyright#Author-rights

BACK | CLOSE WINDOW

Copyright © 2019 Copyright Clearance Center, Inc. All Rights Reserved. Privacy statement. Terms and Conditions.
Comments? We would like to hear from you. E-mail us at customercare@copyright.com

Zuo, H., Bi, K. & Hao, H. (2019). Mitigation of tower and out-of-plane blade vibrations of offshore monopile wind turbines by using multiple tuned mass dampers. *Structure and Infrastructure Engineering*, *15*(2):269-284. https://doi.org/10.1080/15732479.2018.1550096.

Copyright Clearance Center RightsLink®

Home | Account Info | Help | LIVE CHAT

Taylor & Francis
Taylor & Francis Group

Title: Mitigation of tower and out-of-plane blade vibrations of offshore monopile wind turbines by using multiple tuned mass dampers
Author: Haoran Zuo, , , et al
Publication: Structure & Infrastructure Engineering
Publisher: Taylor & Francis
Date: Feb 1, 2019
Rights managed by Taylor & Francis

Logged in as:
Haoran Zuo
LOGOUT

Thesis/Dissertation Reuse Request

Taylor & Francis is pleased to offer reuses of its content for a thesis or dissertation free of charge contingent on resubmission of permission request if work is published.

BACK | CLOSE WINDOW

Copyright © 2019 Copyright Clearance Center, Inc. All Rights Reserved. Privacy statement. Terms and Conditions.
Comments? We would like to hear from you. E-mail us at customercare@copyright.com

BIBLIOGRAPHY DISCLAIMER

Every reasonable effort has been made to acknowledge the owners of copyright material. I would be pleased to hear from any copyright owner who has been omitted or incorrectly acknowledged.